Winter 12-15-2015

Copper and Zinc Oxide Composite Nanostructures for Solar Energy Harvesting

Fei Wu
Washington University in St. Louis

WASHINGTON UNIVERSITY IN ST LOUIS

School of Engineering and Applied Science

Department of Mechanical Engineering and Materials Science

Dissertation Examination Committee:
Parag Banerjee, Chair
Pratim Biswas
Viktor Gruev
Shankar Sastry
Srikanth Singamaneni
Li Yang

Copper and Zinc Oxide Composite Nanostructures for Solar Energy Harvesting

by

Fei Wu

A dissertation presented to the
Graduate School of Arts & Sciences
of Washington University in
complete fulfillment of the
requirements for the degree
of Doctor of Philosophy

December 2015
St. Louis, Missouri

Table of Contents

List of Figures

List of Tables

List of Abbreviations

Atomic force microscopy	AFM
Atomic layer deposition	ALD
Angle resolved X-ray photoelectron spectroscopy	ARXPS
$CuInGaSe_2$	CIGS
Cupric oxide	CuO
Cuprous oxide	Cu_2O
Dimethylzinc	DMZ
Dyethylzinc	DEZ
Dye-sensitized solar cells	DSSC
Energy dispersive X-ray	EDX
Fast Fourier transformation	FFT
High resolution transmission electron microscopy	HRTEM
Kolmogorov–Johnson–Mehl–Avrami	KJMA
Nanowires	NWs
Near band emission	NBE
Numerical aperture	N.A.
Nucleation and growth	N&G
One dimension	1D
Photoluminescence	PL
Polydimethylsiloxane	PDMS
Polymethylmethacrylate	PMMA
Power conversion efficiency	PCE
Root mean square	RMS

Rutherford backscattering spectrometry	RBS
Scanning electron microscopy	SEM
Scanning transmission electron spectroscopy	STEM
Thermogravimetric	TGA
Transmission electron microscopy	TEM
Transient absorption spectroscopy	TAS
X-ray diffraction	XRD
X-ray photoelectron spectroscopy	XPS
Zn acetate	ZnAc
Zinc oxide	ZnO

Acknowledgements

I would like to thank my adviser Dr. Parag Banerjee who provided me opportunities and supports to make me go deep into this research area to know how to be a great engineer and scientist. His knowledge, expertise, and great personality guide and inspire me to build clear plan for the future career. None of my work would be possible without his help. I would also like to thank all my collaboration partners Dr. Pratim Biswas, Dr. Weining Wang, Dr. Srikanth Singanameni, Dr. Limei Tian, and Dr. Huafang Li for sharing their knowledge and background to design and finish the amazing and interdisciplinary experiments. There are many thanks to my colleges: Dr. Yoon Myung, Ms. Sriya Banerjee, Mr. Zhengning Gao, Ms. Junting Yang, and Ms. Andreea Stoica for helps during my research. I would like to thank my academic committee members: Dr. Pratim Biswas, Dr. Srikanth Singanameni, Dr. Yang Li, Dr. Shnkar Sastry, Dr. Viktor Gruev for their time and insightful comments to my work. I would like thank my family members for their long time supports and encouragement and all my friends for kindness help. I would like to thank the funding groups: MAGEEP and I-CARES and nanoresearch facilities, institute of materials science and engineering, and XRD lab in department of earth and planetary for providing all kinds of characterizations.

Fei Wu

Washington University in St. Louis

December 2015

ABSTRACT OF THE DISSERTATION

Copper and Zinc Oxide Composite Nanostructures for Solar Energy Harvesting

by

Fei Wu

Doctor of Philosophy in Mechanical Engineering

Washington University in St. Louis, 2015

Professor Parag Banerjee, Chair

Solar energy is a clean and sustainable energy source to counter global environmental issues of rising atmospheric CO_2 levels and depletion of natural resources. To extract useful work from solar energy, silicon-based photovoltaic devices are extensively used. The technological maturity and the high quality of silicon (Si) make it a material of choice. However limitations in Si exist, ranging from its indirect band gap to low light absorption coefficient and energy and capital intensive crystal growth schemes. Therefore, alternate materials that are earth-abundant, benign and simpler to process are needed for developing new platforms for solar energy harvesting applications.

In this study, we explore oxides of copper (CuO and Cu_2O) in a nanowire morphology as alternate energy harvesting materials. CuO has a bandgap of 1.2 eV whereas Cu_2O has a bandgap of 2.1 eV making them ideally suited for absorbing solar radiation. First, we develop a method to synthesize vertical, single crystalline CuO and Cu_2O nanowires of ~50 μm length and aspect ratios of ~200. CuO nanowire arrays are synthesized by thermal oxidation of Cu foils. Cu_2O nanowire arrays are synthesized by thermal reduction of CuO nanowires.

Next, surface engineering of these nanowires is achieved using atomic layer deposition (ALD) of ZnO. By depositing 1.4 nm of ZnO, a highly defective surface is produced on the CuO nanowires.

These defects are capable of trapping charge as is evident through persistent photoconductivity measurements of ZnO coated CuO nanowires. The same nanowires serve as efficient photocatalysts reducing CO_2 to CO with a yield of 1.98 mmol/g-cat/hr. Finally, to develop a robust platform for flexible solar cells, a protocol to transfer vertical CuO nanowires inside flexible polydimethylsiloxane (PDMS) is demonstrated. Embedded CuO nanowires-ZnO pn junctions show a V_{OC} of 0.4 V and a J_{SC} of 10.4 $\mu A/cm^2$ under white light illumination of 5.7 mW/cm^2. Thus, this research provides broad guidance to develop copper oxide nanowires as efficient platforms for a variety of solar energy harvesting applications.

Chapter 1 Introduction

1.1 Motivation and significance

Development of a sustainable and renewable energy source is one of the largest scientific and engineering challenges of our times. Among all the renewables, solar energy has gained much research interest due to its potential for providing an inexhaustive source of energy, which does not degrade the environment. An ideal photovoltaic material should satisfy several criteria: 1) the material should be abundant and inexpensive, 2) it should be nontoxic and environmentally friend, 3) it should have an optimal band gap to absorb visible light, 4) the electron-hole recombination rate should be low and the carrier diffusion length should be long enough to diffuse to material surfaces and conduct out through electrodes.[1] Traditionally, high purity single crystal silicon satisfies all these requirements. However, the purification processes for silicon is too complicated and expensive. In order to combat the high cost, both academia and industry have made great efforts to look for some new substitutes. In the past few decades, metal oxides have begun to attract research due to the wide range of oxides, some of which are earth abundant and exist as minerals in nature.

Metal oxides are a class of materials which are made up of positive metallic and negative oxygen ions. The electrostatic interaction bounds the metallic and oxygen ions together, resulting in a very firm ionic bond. Most of the metal oxides showed excellent thermal and chemical stability.[2] The partially or fully filled d-shells of metal oxides give them a variety of unique properties for all kinds of electronic device applications, including solar cells,[3] photoelectrochemical cells,[4] thin film transistors,[5] photocatalysts,[6] and sensors.[7, 8] It is reported that when the materials size and dimensionality are decreased to nanoscale level, the electronic

structures of nanomaterials are different from the bulk materials.[9] These changes make them exhibit some promising electronic properties, such as enhanced light absorption and rapid light response.[3, 10] Among all kinds of nanomaterials, one dimensional materials have attracted the most attention in electronic device application because they are easy to fabricate into building blocks and easy to test with two terminals at two ends.[11-13] Therefore, metal oxidize nanorods[14], nanowires[15], nano-needles[16] and nanotubes[17] are synthesized by different methods because they are suitable for a wide range of applications, such as biosensors[18], smart windows[19], solar cells[20], supercapacitors, photodetectors[21], light-emitting diodes[22] and field effect transistors[23].

Among the metal oxides, copper oxides showed promising solar energy harvesting potential because they have two different types of sub-oxides: cupric oxide [24] and cuprous oxide (Cu_2O) which have a narrow band gap[25, 26] of 1.2 eV and 2.2 eV, respectively. Until now, a lot of work has been reported on solar applications using CuO and Cu_2O as electrodes. However, they all showed low energy conversion efficiencies (0.1% for CuO and 2% for Cu_2O),[27, 28] even though they have a very high theoretical solar cell efficiency, for example, 30% for CuO,[29] 20% for Cu_2O.[30]

To improve the efficiency, a better design and combination of materials at nanoscale level is required. Single crystal nanostructure materials, especially single crystal nanowires (NWs), are reported to have several advantages in solar energy application, including reduced reflection, enhanced light absorption, improved band gap tunneling, facile strain relaxation, increased defects tolerance, and longer exaction lifetime.[1, 31] What's more, NWs with a high aspect ratio sufficiently allows sufficient light absorption in moderate thicknesses while providing short photo-excited carriers collection lengths. The short carrier collection lengths, as a result, improve the collection efficiency of photogenerated carriers in the oxides with a low minority diffusion lengths.[32]

Therefore, single crystalline CuO NWs and Cu_2O NWs arrays are promising for the applications of solar energy harvesting.

Single crystalline CuO NWs can be synthesized by thermal oxidation of pure commercial Cu foils.[33, 34] However, the NWs array with an average aspect ratio higher than 100 and a density higher than $10^8/cm^2$ have not been reported yet. To synthesize dense Cu_2O NW arrays, reduction of CuO NW arrays was usually used. However, the synthesized Cu_2O NW arrays suffers from either the simultaneously produced Cu or the porous structure.[35, 36] Thus, synthesis of pure Cu_2O NW arrays with a good crystallinity, a high density, and a high aspect ratio is required.

Zinc oxide (ZnO) is another metal oxide with an n-type conductivity and 3.3 eV band gap,[37] which is widely used in solar energy harvesting, such as, solar cells,[38] photoelectrochemical cells,[39] and CO_2 photoreduction.[40, 41] It has a high exciton binding energy of 60 meV, which makes the excitons stable at room temperature.[37] Generally speaking, the large band gap of ZnO makes it transparent to visible light. However, surface defects lead to blue, green and red light emissions, which are found in photoluminescence tests.[42, 43] Moreover, the surface to volume ratio is even more pronounced in a nanostructure, resulting in an enhanced defect band emission.[41] Understanding the role of defects on electrons generation and recombination processes are important for designing optoelectronic devices with a high efficiency.

Solar energy is one of the sustainable energy sources, provided by sun in large amounts between 125 W/m^2 and 305 W/m^2 every day by latitude dependent incidence, seasonal variation, and diurnal variation.[44] It is renewable and can be collected by solar cells, photoelectrochemical [45] cells and photocatalysts. The working mechanisms of the devices are illustrated in **Figure 1.1**. When light shines on the device, electrons from the valence band are excited to the conduction

band. The electrons are collected by an n-type semiconductor, and holes are collected by a p-type semiconductor. The electrons are conducted by circuits, which all together work as a solar cell device (**Figure 1.1a**). Both the photo-excited electrons collected by photocathode used to split water and generate H_2, and holes at photoanode used to generate O_2, work together as a PEC cell (**Figure 1.1b**). The prototypical mechanism to reduce CO_2 is shown in **Figure 1.1c**. Photons excite electrons and leave holes behind in valence band. These holes react with H_2O to form protons. Protons react with photo-excited electrons and the absorbed CO_2 to produce CO, CH_4OH, and H_2. Holes left in the valence band reacts with H_2O to produce protons and oxygen. Based on these mechanisms, we know that solar energy can be easily transferred to electrical or chemical energy. Thus, solar power would be the most promising energy source to fulfill the growing demands. Examining the photovoltaic performances of these copper oxides and ZnO nanostructures is main focus of this study.

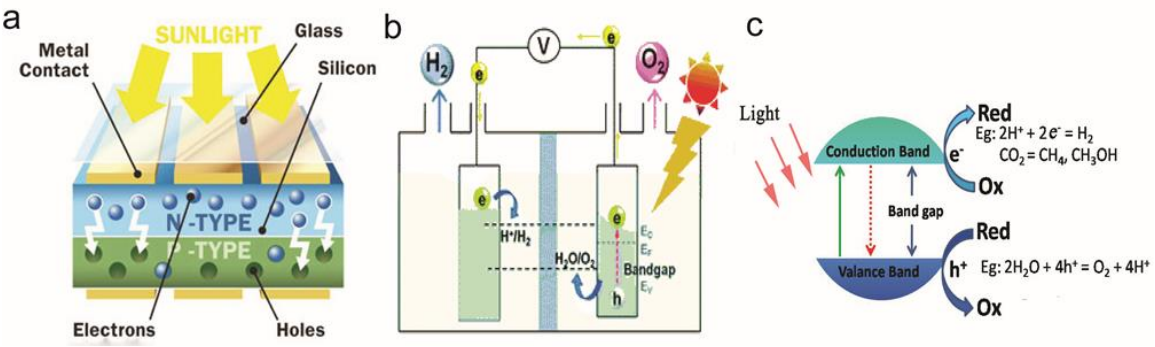

Figure 1.1. The diagram of **a)** solar cell; **b)** PEC cell[46]; **c)** photocatalyst for CO_2 degradation.

1.2 Goals and objectives

In this thesis, our goal is to synthesize dense crystalline CuO and Cu_2O NWs with an aspect ratio of more than 100 by thermal oxidation and thermal reduction methods, which can be used to convert solar energy into electrical or chemical energy.

The key technique objectives are summarized as following:

1. Grow CuO NWs with an average aspect ratio more than 100 and oxidize the whole Cu foils into pure CuO with dense CuO NWs on surface by thermal oxidation of commercial pure Cu foils.
2. Reduce the CuO NWs to pure Cu_2O NWs with an average aspect ratio more than100 and a high crystallinity. Synthesize various CuO/Cu_2O core/shell NWs and Cu_2O NWs with tunable surface morphologies by controlling thermodynamic and thermal kinetic processes.
3. Characterize the effect of surface defects of CuO NWs on the optoelectronic properties in air and vacuum.
4. Apply CuO NWs-ZnO nanocomposites for CO_2 photoreduction to harvest solar energy by controlling the exposed surfaces and surface defect densities.
5. Extract CuO NW arrays by polydimethylsiloxane (PDMS) without bundling and crashing. Use these NW arrays as light absorber to make CuO NWs based flexible solar cells.

1.3 Overview

Chapter 1 provides the necessary background of this work and describes the motivations and objectives.

Chapter 2 provides a literature review of fundamentals of CuO, Cu_2O, and ZnO and the current research status of these metal oxides on solar energy harvesting.

Chapter 3 describes the single crystalline CuO NWs growth and the NW length and density control.

Chapter 4 describes the thermal reduction of CuO NWs to synthesize CuO/Cu_2O core/shell NWs and Cu_2O NWs with controllable surface morphologies and provides a general protocol to grow complex core/shell NWs by controlling the kinetics of phase transformation.

Chapter 5 characterizes the optoelectronic properties of ZnO coated CuO NWs. The surface defects density is highly dependent on the ZnO thickness. Thus, the photocurrent decay processes are studied to discover the effect of the surface defect on the decay processes of ZnO coated CuO NWs both in air and vacuum.

Chapter 6 investigates the CO_2 photoreduction performance of these CuO NWs-ZnO nanocomposites to show that CO yields from CO_2 photoreduction significantly depend on the surface structures CuO NWs-ZnO nanocomposites.

Chapter 7 shows a technique developed to transfer vertical CuO NWs arrays, which are used as light absorber for a CuO NWs based solar cell.

Chapter 8 shows the conclusions and future work.

Chapter 2 Literature review

2.1 CuO and Cu_2O based photovoltaic applications

2.1.1 Fundamental properties of CuO and Cu_2O

The crystal structure of CuO is monoclinic with C2/c symmetry and a cell volume of 81.08 $Å^3$.[47] CuO is proven to be stable at a pressure below 700 kbar and a temperature below 3000 K, in contrast to other metal oxides, in which phase transitions can occur during annealing and cooling.[48] First principle calculation results indicate that CuO is an indirect band gap semiconductor with a band gap of 1 eV. The calculation results also demonstrate that CuO is intrinsically a p-type semiconductor because Cu vacancies were found to be the most stable defects in CuO in Cu and O rich environments by studying the point defect formation energy in CuO.[49]

Table 2.1. The surface free energies (γ, in unit of J/m^2) and work function (ϕ, in unit of eV) of stoichiometric CuO.[50] Copyright 2010 American Chemical Society.

	(111)	$(\bar{1}11)$	(011)	(110)	(101)	(010))	(100)
γ	0.74	0.86	0.93	1.16	1.29	1.37	2.28
ϕ	5.8	5.8	5.6	5.3	6.3	5.6	7.6

The stability of various CuO surfaces were systematically studied by first principle calculations. The results are shown in **Table 2.1**. The calculation results show that CuO (111) is the most stable surface with a surface energy of 0.74 J/m^2, and the $(\bar{1}11)$ plane is the second most stable surface with a surface energy of 0.86 J/m^2 under ambient conditions.[50] The calculation results also indicate that O and Cu terminated (110) and (100) planes showed different surface energies with Cu or O to end the surface. By comparison, the O terminated CuO (110) plane is even more stable than the CuO (111) plane in a very narrow range near the limit of O-rich condition.[50] The hole mobility of CuO films is around 0.134 $cm^2/V{\cdot}s$ and a hole concentration of

1.29×10^{18}/cm^3 at room temperature.[51] However, the single crystalline CuO films synthesized by the floating zone method shows a hole mobility of 11000 cm^2/V·s at 4.2 K.[52]

Cu_2O is a p-type semiconductor with a simple cubic crystal structure. The cell volume is 77.8 Å^3 and the crystal structure shows a symmetry of $pn\bar{3}m$.[53] First principle investigations indicate that Cu_2O has three low index surfaces, namely, (100), (110), and (111). Each surface can be terminated with O, and Cu. The Cu_2O (110) surface can contain both O and Cu on the outmost layer, which was defined as Cu_2O(110):CuO. These surfaces display different stabilities because of the different surface energies caused by the termination atoms.[53] The calculation results indicate that Cu_2O(110):CuO is the most stable surface in both O poor and rich conditions with a surface energy of 0.048 J/m^2. The hole mobility of Cu_2O films is 130 cm^2/V·s and a hole concentration of 6.51×10^{18}/cm^3 at room temperature.[54, 55] The single crystalline Cu_2O films synthesized by the floating zone method was reported to show a maximum hole mobility of 179000 cm^2/V·s at 4.2 K.[52]

2.1.2 CuO and Cu_2O NWs synthesis

CuO and Cu_2O nanowires can be synthesized by varied approaches using different concepts and materials, such as, wet chemistry, electrochemical methods, hydrothermal methods, thermal oxidation or reduction methods. These NWs can be single crystalline, bi-crystalline or polycrystalline. To synthesize desirable NWs, an optimal method should be selected, for example, solution based methods or solid based methods.

Solution based wet-chemical methods. Generally, copper hydroxide ($Cu(OH)_2$) NW precipitant is formed by adding sodium hydroxide (NaOH) to $CuCl_2\cdot2H_2O$ and polyethylene glycol (PEG2000) solution under rigorous stirring.[56] Then, the $Cu(OH)_2$ transforms to CuO precipitates in a steam

trace for 30 minutes. The obtained precipitates are washed and filtered several times to remove chlorine ions (Cl^-), followed by drying in an oven at 80 ^oC for 5 hours. The synthesized CuO NWs display a length of 400 nm with a diameter ranging from 5 to 15 nm. ($Cu(OH)_2$) NWs can also be synthesized by dropping ammonia solution into potassium hydroxide [57] and copper sulfate ($CuSO_4$) solution under vigorous stirring.[58] Then, the ($Cu(OH)_2$) NW precipitates are heated at 120 ^oC for 2 hours and at 180 ^oC for another 3 hours to form resulting CuO NWs. The NW has a length around 20 μm and a diameter around 10 nm. Organic molecular thioglycerol (TG) was used as a stabilizer to synthesize CuO NWs. TG was added to copper acetate ($Cu(CH_3COO)_2$) solution under stirring, followed by dropping NaOH solution to the mixture solution.[59] After that process, a little deionized water was immediately added to the solution under continuous stirring for several minutes. The precipitates were washed, filtered, and dried. The length and diameter of the CuO NWs are 2 to 5 μm and 90 nm, respectively.

The wet-chemical method was also used to synthesize Cu_2O NWs. PEG20000 and $CuCl_2 \cdot 2H_2O$ were dissolved into deionized water under stirring for 13 minutes. NaOH was added dropwise into the PEG20000 and $CuCl_2 \cdot 2H_2O$ solution to produce $Cu(OH)_2$. The $Cu(OH)_2$ precipitates were reduced by hydrazine (N_2H_4), followed by washing, filtering and drying processes. The synthesized Cu_2O NWs show a length around 10 to 20 μm and a diameter about 8 nm.[60] $CuSO_4 \cdot 5H_2O$, NaOH, and sodium tartrate were used as precursors and glucose was used as surfactants to produce Cu_2O NWs in a glass vial. The glass vial was heated at 95 ^oC in an oven for 60 to 90 minutes to grow NWs. The resulting NWs showed a length around 15 to 30 μm with a diameter of 40 to 100 nm.[61]

Thermal oxidation methods. Among many CuO NWs synthesis methods, thermal oxidation of copper foil was considered to be the easiest and simplest way to get high quality, long, and vertical CuO arrays.[7, 62, 63] CuO oxide whiskers were first observed on thermal oxidized copper foil by Pfefferkorn et al. in 1953.[64] However, the whiskers density was fairly low and the length was short. When Jiang, X. et al. reported that oxidation of TEM copper grids can obtain dense and long CuO NWs on the surface of grids.[65] The CuO NW was found to grow along [111] twin boundaries separating $(\bar{1}11)$ and (111) on both sides. Following this work, the thermal oxidation method was commonly used to synthesize single crystalline CuO NWs by directly heating Cu foils in air.[34] Typically, high purity commercial Cu foils were cut into desirable sample sizes. Then, the foils were cleaned by 1 mol/L HCl to remove surface native oxides. Then, the foils were put into a furnace at 400 ^{o}C for several hours. The NWs length is in a range from 2 to 10 μm. The longer the heat treatment time, the longer the NWs.[66] The NW length vs. oxidation time was found to follow the parabolic low.[67] It was found that CuO NW density depended on the heating temperature. The temperature in a range of 600 to 700 ^{o}C, the densest CuO NWs were observed.[63] The temperature window for CuO NW growth is 400 to 700 ^{o}C.[63, 68] The presence of oxygen flow or electrical fields during the oxidation process was reported to increase the CuO NWs yield and reduce the necessary oxidation time compared with the direct oxidation processes in air.[69, 70] Cu_2O NW growth through thermal oxidation process has not been reported yet.

2.1.3 The applications of CuO NWs and Cu_2O NWs for solar energy harvesting

2.1.3.1 Application for photocatalysts

The narrow band gap of CuO makes it promising for photocatalytic applications. Various CuO nanostrucutres, i.e. nanoleaves, nanoflowers, and nanoribbons, were synthesized by the wet-chemical method to examine the effect of the morphology and exposed surfaces on photocatalytic

performance.[71] The morphology of nanostructures showed negligible effect on Rhodamine B (RhB) photodecomposition under UV light. However, the exposed surfaces of the nanostructures significantly affected the photodecomposition properties, indicating the high photocatalytic performance was observed on the high surface energy plane. The photocatalytic property of CuO NWs synthesized at different temperatures by the thermal oxidation method in air was examined to degrade Congo red dye in a home-made photodetector, showing that NWs with a higher surface area exhibited better dye degradation performance.[72]

Truncated Cu_2O nanocubes with mostly {100} surfaces and octahedral with entirely {111} surfaces were synthesized by the wet chemical method to investigate the photocatalytic properties of these different surfaces.[73] The reported results indicated that {111} surfaces were principally responsible for the photocatalytic activity of Cu_2O nanoparticles in photocomposition of RhB. Hollow porous sphere Cu_2O nanoparticles were synthesized by soft-template method at room temperature.[74] These hollow nanoparticles was reported to be active to photodegradation of methyl orange (MO) under visible light irradiation. An enhanced photocatalytic activity of Cu_2O NWs was observed by decorating the NWs with Au nanoparticles to enhance light absorption., The Au decorated Cu_2O NWs showed 3 times higher catalytic performance, compared with the photocatalytic performance of Cu_2O NWs by photodegradation of methylene blue.[75]

2.1.3.2 Application in photocathodes to split water

CuO has a small band gap of 1.2 eV, which is suitable for all the visible light absorption. However, the drawbacks of CuO are low photocurrent density and instability in aqueous solutions.[76, 77] Strategies are employed to increase the photocurrent density and stability. Titanium (Ti) alloyed CuO was deposited on the F-doped tin oxide (FTO) by radiofrequency (RF) magnetron cosputtering to increase the stability of CuO. The reported results indicated that 10% of Ti in the

alloyed CuO thin film kept the photocathode without corrosion for 2 hours.[78] CuO/Cu_2O composites synthesized by annealing Cu foils via H_2-O_2 flame were used as photocathodes to split water to increase the stability. After a 10 minute test, the best sample showed a photocurrent density decay around 40%.[79]

Cu_2O has a band gap of 2.2 eV, allowing for most of the visible light absorption. The conduction band edge of Cu_2O is 0.7 V higher than H_2 generation potential from water, making it a suitable photocathode candidate.[80] The theoretical solar to hydrogen conversion efficiency was calculated to be 18%, corresponding to a photocurrent density of 14.7 mA/cm^2 under AM 1.5.[4] However, Cu_2O is unstable in aqueous solution and the photocorrosion leads to photocurrent decay quickly. As a result, protection layers were always used as a strategy to improve the photocurrent density and stability. A photocurrent density of -7.6 mA/cm^2 and a stability of 33% after a 20 minute test was reported using Cu_2O thin film as a photocathode protected by ZnO and Al_2O_3 multiple layers.[4] Compared with thin film, NWs showed significant enhancement in photocurrents due to enhanced light absorption and decreased recombination.[76, 81, 82] Cu_2O NWs synthesized by an electrochemical anodization method were employed as photocathodes using 10-20 nm NiO_X as protection layer.[83] The electrodes showed a current density up to -4.98 mA/cm^2 and the photocurrent remained 72% after 20 minutes test. When 20 nm carbon layer were used as the protection layer on Cu_2O NWs, the NW photocathodes produced a photocurrent density of 3.98 mA/cm^2 and the photocurrent remained 80.7% after 20 minutes test.[84]

2.1.3.3 Application in solar cells

A semiconductor that can absorb solar radiation in visible and near infrared region is reported to be a good solar absorber.[85] Among the various semiconducting metal oxides, CuO is attractive as

a selective soar absorber because of its high light absorbance efficiency and low thermal emittance.[86, 87] The theoretical power conversion efficiency (PCE) of CuO is around 30% considering only radiative recombination.[29] However, CuO based solar cells have rarely been reported to have a high PCE in experiments. CuO nanocrystals have been used as the light absorber, showing an efficiency of 0.004%.[88] Core/shell CuO/C_{60} heterjuctions were reported to have an efficiency of 0.02%.[89] To improve the cell efficiency, single crystalline CuO NWs synthesized by thermal oxidation of Cu foils are covered by n-type ZnO to form a p-n junction, showing a PCE of 0.1%.[27] CuO nanorods based dye-sensitized solar cells were reported to achieve a PCE of 0.29%. A higher efficiency of 0.41% was reported for p-type CuO/n-Si structure solar cells.[90] The highest reported PCE of CuO solar cell devices is 0.84% , with a fill factor of 35.2%, V_{oc} of 0.494 V and I_{sc} of 4.8 mA/cm^2.[91] There were some other reported CuO solar cell structures, which are listed in the **Table 2.2**.

Cu_2O is another attractive alternative solar absorber material, which shows a high absorption coefficient with a light wavelength shorter than 480 nm.[92] The material fabrication cost is low, making it competitive in solar panel markets. The theoretical PCE was reported as 20% considering only radiative recombinations.[93] Cu_2O film is a native p-type semiconductor and an n-type Cu_2O is not achievable because n-type dopants are significantly self-compensated by the native ion defects, or single charged copper vacancies.[94] Thus, the research of Cu_2O solar cells was focused on heterjunction devices. A high turn-on voltage was measured from an FTO/Cu_2O heterjuntions; however, no PCE was obtained from it.[95] Cu_2O/TiO_2 heterjunctions fabricated by depositing Cu_2O on TiO_2 nanotubes using an ECD method, measuring a PCE of 0.01%.[96] ZnO NWs filled with Cu_2O NPs synthesized by aqueous solution methods exhibited an average PCE of 0.02-0.03%.[1] ZnO NWs covered with Cu_2O thin films were fabricated with an electrochemical

Table 2.2. A summary of reported Cu_2O and CuO based solar cell structure and efficiency.

p-type	n-type	η	ff	Voc (V)	Isc	Reference
Cu_2O	ITO and ZnO	2%	50%	0.595	6.78	Ref. [28]
Cu_2O	Al: ZnO	1.52%	53%	0.41	6.94	Ref. [97]
Cu_2O	ZnO NWs	0.1%	29%	0.13	2.54	Ref. [98]
Cu_2O	ZnO NRs	0.56%	41.5%	0.514	2.64	Ref. [93]
Cu_2O	ZnO	0.053%				Ref. [99]
Cu_2O	a-ZnSnO	2.65%	65.0%	0.553	7.37	Ref. [100]
Cu_2O	Al:ZnO/Ga_2O_3	5.38%	67%	0.80	9.99	Ref. [101]
Cu_2O	MgF_2/AZO/ $Al_{0.025}$-$Ga_{0.975}$–	6.1%	66%	0.84	10.95	Ref. [102]
Cu_2O	Al:ZnO/ZnO	3.83%	55%	0.69	10.1	Ref. [103]
Cu_2O	ZnO	0.24%	27%	0.24	1.96	Ref. [104]
Cu_2O	Cu_2O	1.06%	42%	0.621	4.07	Ref. [105]
Cu_2O	ZnO	1.28%	35%	0.42	2.2	Ref.[106]
Cu_2O	ZnO	1.43%	59.6%	0.535	4.47	Ref. [107]
Cu_2O	TiO2	0.01%		0.1	0.33	Ref. [108]
Cu_2O	Mg: ZnO	0.71%	42%	0.575	3	Ref. [109]
Cu_2O	ZnO	0.1%	0.88%	0.29	8.2	Ref. [110]
CuO	Sn: ZnO	0.232%	63%	0.48	0.326	Ref. [111]
CuO	ZnO	0.1%		0.37	0.264	Ref. [27]
CuO	ZnPc2	0.191%	32%	0.251	2.35	Ref. [112]
CuO	TiO2/Dye	0.29%	17%	0.45	0.564	Ref. [113]
CuO	n-Si	0.84%	35.2%	0.494	4.8	Ref. [91]

*η: Energy conversion efficiency, ff: fill factor, Voc: open circuit voltage, Isc: short circuit current. a-ZnSnO: amorphous Zinc tin oxide, ZnPc: Zinc phthalocyanines.

deposition (ECD) method, displaying a PCE of 0.13%.[114] A ZnO/Cu_2O film heterojunction prepared using LiOH by ECD gave a PCE of 1.43%.[107] Mg doped ZnO films grown by metal-

organic chemical vapor deposition (MOCVD) were chosen to form a heterojunction with ECD Cu_2O film, obtaining a high PCE of 0.71%.[115] To improve the Cu_2O solar cell performance, a few strategies were employed, i.e. increase the Cu_2O film quality, decrease the damage of n-type film deposition, and increase the carrier concentration of n-type material by introducing dopants. High quality Cu_2O film synthesized by thermal oxidation at a high temperature >1100 ^oC with 0.27 Torr O_2 partial pressure was coated by transparent ITO and ZnO to form Cu_2O / transparent conductive oxides heterojuntions, obtaining a PCE of 2.01%.[30] Pulse layer deposition was used to deposit low damage Al doped ZnO on high quality thermal oxidized Cu_2O film to form a heterojunction. This solar cell structure showed a PCE of 3.83%.[103] The highest reported PCE of Cu_2O solar cells is 6.1% using multiple n-type metal oxide layers.[102] Other Cu_2O solar cell structures are listed in **Table 2.2**.

2.2 Atomic layer deposition

Atomic layer deposition, which is originally known as atomic layer epitaxy,[116] is a technique to conformally deposit thin film on two dimensional [117] or three dimensional (3D) materials with atomic precision. The self-limiting nature can controllably grow thin film in atomic scale. The chemicals sequentially go to the reaction chamber and react with the reactants. Unreacted reactants and byproducts are constantly pumped out during the purge cycle. A diagram of ALD processes in one cycle is shown in **Figure 2.1**.[118] Therefore, the thickness of ALD films can be precisely controlled at angstrom or monolayer level, making it an alternative thin film growth technique in nanoelectronics fabrication.

The self-limiting surface reactions make the reaction self-controllable. As a result, ALD grown films are extremely conformal, uniform in thickness, pin-hole free, independent of substrates geometry, and extendable to very large substrates.[119, 120] In recent decades, ALD has

been widely applied both in industry for microelectronics production and in research to increase the control over materials growth.

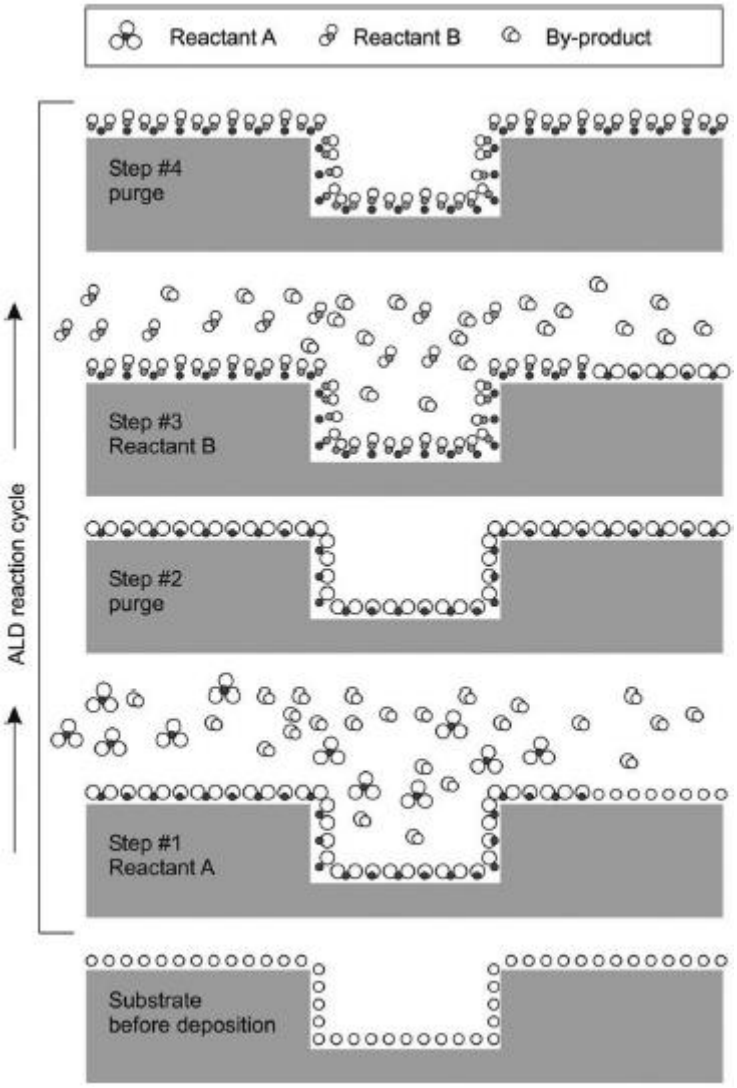

Figure 2.1. A diagram of ALD processes in one cycle. **Step 1**: pulse of reactant A to the reactor to be adsorbed on the substrate surface. **Step 2**: Ar gas purge to remove unreacted precursor A and byproducts. **Step 3**: Pulse of the reactant B, which reacts with the surface adsorbed reactant A. **Step 4**: Ar gas purge of to remove the unreacted reactant B and by products.[118] Copyright Wiley-VCH, 2012.

2.2.1 ZnO ALD

The application of ZnO in low dimensional microelectronics leads to a remarkable rise of research interests of ALD ZnO. The development in number of ZnO publications involving ALD or ALE has been quickly growing in the past 30 years.[121] The study of ZnO ALD is increasing, indicating that application of ALD ZnO in device fabrication is also increasing.

The first ZnO ALD process was reported in 1985 using zinc acetate (ZnAc) and water as precursors.[122] However, the ZnAc precursor required a relatively high temperature to react with water. The lowest temperature reported was 280 ^{o}C. In 1994, diethylzinc (DEZ) and dimethylzinc (DMZ) and water were developed as precursors.[123] The deposition temperature can be lowered below 200 ^{o}C using DEZ or DMZ. Inside the "ALD growth window" of 100-170 ^{o}C, which means the growth rate is stable in a certain temperature range, ZnO shows a growth rate of 1.8 Å per cycle.[124] DMZ is similar to DEZ so that DMZ can be used in the same deposition temperature range. The growth rate in the "growth window" was reported to be a little higher, compared with the growth rate using DEZ. What's more, the resultant film orientation was also reported to be different using DMZ or DEZ. Otherwise, the film quality is equal no matter which kind of Zn precursor is used.[125]

Several other oxygen precursors other than water, i.e. O_2, O_3, and N_2O, have been used as the alternatives in ZnO depositions. They can be used to deposit ZnO in a similar growth rate as water, but require higher deposition temperatures. Water and oxygen were used to create plasma to grow ZnO films with a higher degree of atomic stoichiometry at a low deposition temperature because of the high reactivity of oxygen plasma. [120]

High quality crystalline ZnO with hexagonal wurtzite structure is usually obtained from ALD deposition. However, the preferred crystalline growth orientations can be controlled by deposition temperatures. Below 70 ^{o}C, ZnO film exhibits a strong X-ray diffraction peak, indicating a preferred <002> growth direction.[126] The <100> orientation becomes more and more prominent in temperature range of 70-200 ^{o}C.[127] Above 220 ^{o}C, the preferred growth orientation switches back to <002> again.[128] Some other deposition parameters also have influence on the dominant growth orientations, for example, precursor chemicals,[129] and precursor pulse time.[130]

The stoichiometry and electronic properties strongly depend on deposition temperature, using DEZ and water as precursors. Rutherford backscattering spectrometry (RBS) was used to evaluate Zn/O ratio in the ZnO films deposited at different temperatures.[124] Zn/O ratio calculated using RBS spectra varies from 0.93 to 1.01 with increasing the temperature from 100 ^{o}C to 200 ^{o}C. XPS spectra was also employed to calculate the Zn/O ratio by considering surface carbon and hydrogen atoms. It also showed that Zn/O ratio increased with increasing the deposition temperature.[124] Furthermore, electron concentration of ZnO films deposited at different temperatures ware also examined, showing that electron concentration increases with increasing the deposition temperature, i.e. 4×10^{16} at 100 ^{o}C, 1×10^{20} at 240 ^{o}C.[124]

2.2.2 Application of ALD ZnO thin films

The self-limiting reactive nature of the ALD technique makes ALD ZnO films with low roughness, pinhole free, and highly stoichiometic. These advantages of the ALD ZnO films attracted a wide range of applications, including thin film transistors (TFTs), solar applications, and light-emitting diodes (LEDs).

Thin film transistors (TFTs). TFTs are mostly used in liquid crystal displays, requiring the thin film material to have a high degree of transparency, a low carrier concentration, and a high carrier mobility.[121] ZnO is transparent and the ALD technique can enable the ZnO film deposition in a large area with high uniformity at a relatively low temperature. However, ZnO films deposited at low temperatures satisfy the requirement for low carrier concentration but not for the high carrier mobility. To obtain a high saturation carrier mobility of the transistor, nitrogen dopants were used to synthesize ZnO TFTs with a high performance.[131]

Solar cell applications. ALD ZnO was found to be an alternative of CdS as a buffer layer in $CuInGaSe_2$ (CIGS) solar cells because the ALD technique provides the possibility to deposit uniform ZnO film with high resistivity in a large area scale.[132] The low deposition temperature of ALD ZnO has made it suitable for use as protection layers, electron sensitivity layers, and photoanodes in organic solar cells,[133] and dye-sensitized solar cells (DSSCs). In organic solar cells, ALD ZnO was used as a protection layer to quench electron-hole recombination at surface defects.[133] In DSSCs, it also was used as a photoanode and a blocking layer to reduce the electron-hole recombination and increase the electron conductivity.[134]

Light-emitting diodes (LEDs). ALD ZnO is mainly used in heterojunction LED devices due to lack of reliable p-type doping ZnO. Thus, most of the reported ALD ZnO based LED devices used GaN as the p-type semiconductor.[135] ALD enables the controllability of doping N atoms into ZnO in atomic layer to get a high dopant concentration, which decreases the electron injection from n-type ZnO to p-type GaN resulting in a dominant UV light emission from ZnO.[135] Al-doped ZnO has been used as a current spreading layer in InGaN/GaN blue light LEDs because the current crowding of GaN based LEDs caused non-uniform distribution of light.[136] Al doped ZnO was also used as a buffer layer in organic LEDs for effective carrier injection and transport.[137]

Chapter 3 Controllable CuO nanowires growth using a thermal oxidation method

3.1 Introduction

CuO NW nucleation and growth was widely researched because of the promising applications in solar cell, phoelectrochemical cell, and gas sensing and oxidation.[99, 113, 138-141] Important contributions have been made in understanding the mechanism of spontaneous CuO NW formation in air in the past years. Fast grain boundary diffusion of Cu ions was considered to be the basic mechanism to understand CuO NW growth on thermal oxidized copper foil.[7, 142-144] CuO NW formation was reported to occur within a 400 to 700 ^{o}C temperature window.[62, 63, 66, 139, 143] More than 700 ^{o}C, fast lattice diffusion dominated the Cu cations diffusion and released the driving force for forming NWs.[33, 142, 145] However, no direct evidence showed the Cu ions diffusion through the grain boundaries of copper oxide layers to drive NW growth.

In this chapter, we are going to systematically study the CuO NW array growth through thermal oxidation methods to show the direct evidence that the single crystalline CuO NWs' growth is driven by the fast diffusion of Cu ions through the grain boundaries of the copper oxides films. By controlling the growth mechanism, we grow single crystalline CuO NW arrays with a high aspect ratio and density.

3.2 Experiments

127 μm Copper foils were purchased from VWR International® with a purity of 99.9%. The foils were cut into 1cm × 1cm pieces and surface native oxide was removed by placing the pieces in 1M HCl solution for 0.5 hour. The etched foils were rinsed in de-ionized water and dried using compressed air flow. The foils were then immediately put in an alumina combustion boat and

inserted into a tube furnace maintained at 500 ^{o}C for 20 minutes to 70 minutes with a 10 minutes step in air. Samples were cooled in the furnace to room temperature.

To introduce concentrated stress into the Cu foils, we used a rolling machine to roll the Cu foils from 127 μm into 26 μm using a rolling machine. Then, the rolled Cu was cut into 1 cm × 0.5 cm^2 pieces. Surface native oxides were removed by 1 M HCl solution for 0.5 hour, followed by a de-ionized water cleaning and compressed air drying. The cleaned foils were oxidized at 500 ^{o}C, 600 ^{o}C, and 700 ^{o}C for 1 hour, 5 hours, and 10 hours in the air, respectively. Samples were cooled in the furnace to room temperature.

SEM images were taken using a JEOL-7001LVF. Statistical data on NW density, length and oxide layer thickness below NWs was obtained from SEM images using Image-J software. X-ray diffraction (XRD) was performed on a Rigaku Geigerflex D-MAX/A diffractometer. Raman spectra of the samples were obtained using a Renishaw® in Via Raman Microscope with a spot size < 1 μm^2. The objective of the microscope was 50x with an N.A. of 0.75. The wavelength of the laser was 514 nm.

3.3 Results

3.3.1 Microstructure characterization by SEM and XRD

SEM images of CuO NWs were obtained by oxidizing 127 μm thick Cu foils at 500 ^{o}C (**Figure 3.1.** The NWs' density and length changes when we increase the oxidation time. To quantitatively characterize the relationship between CuO NWs density and length vs. the oxidation time, we statistically calculated the NW density and measure the length of the NWs using Image-J software, as seen in **Figure 3.2**. The NWs density is around 2.1×10^8/cm^2 with the oxidation time less than 40 minutes. The NWs density starts to decrease with an oxidation time longer than 40 minutes.

The length of the NWs increases first, reaches the maximum $2.8 \pm 1.5 \mu m$ with an oxidation time of 40 minutes and decreases for a longer oxidation time.

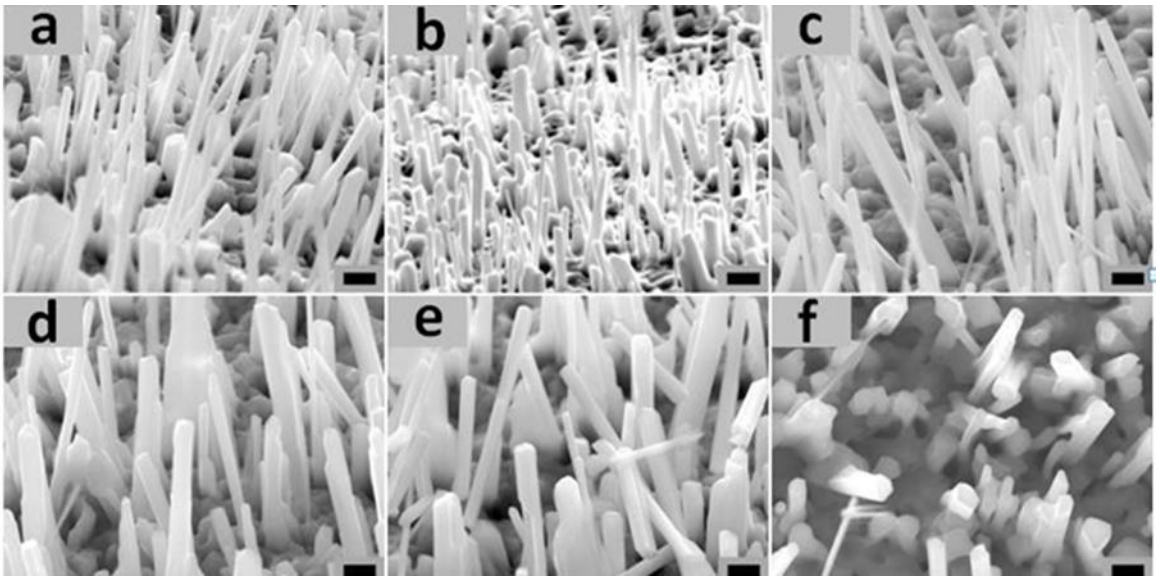

Figure 3.1. SEM images of 127 μm Cu foils annealed at 500 ^{o}C for **a)** 20 minutes, **b)** 30 minutes, **c)** 40 minutes, **d)** 50 minutes, **e)** 60 minutes, **f)** 70 minutes in air. The scale bar is 500 nm.

To increase the length of the nanowires, we introduced surface stresses on the starting Cu foil by rolling them using a rolling machine. Stresses are known to increase diffusion of the ionic species and to lead to CuO NW growth. To introduce concentrated stress into Cu foils, we roll the Cu foils from 127 μm to 26 μm. The SEM images of the rolled copper foils oxidized at 500 ^{o}C, 600 ^{o}C, 700 ^{o}C for 1 hour, 5 hours, and 10 hours are shown in **Figure 3.3**. The average CuO NW density, length and the total oxide thickness below NWs were listed in **Table 3.1**. We notice that most of the NWs show a length longer than 10 μm and the NWs with a maximum length of 30.9 μm are obtained at 600 ^{o}C for 10 hours. The NW diameter is around 230 nm. According to the statistical data in Table 2.1, the NW density is around $1.0 \times 10^{8}/cm^{2}$ and shows no obvious changes with increasing the oxidation time. However, the NW length decreases with a long oxidation time

at 500 °C. At 600 °C, both NW density and length increase with an increase of oxidation time and reach the maximum value of $1.7\times10^8/cm^2$ and 30.9 μm. When the oxidation temperature reaches 700 °C, the NW length slightly increases with oxidation time. However, the NW density is $0.7\times10^8/cm^2$ at 700 °C for 1 hour, increases to $1.3\times10^8/cm^2$ for 5 hours, and significantly drops to $0.3\times10^8/cm^2$ for 10 hours. Therefore, optimized conditions for long and dense CuO NWs synthesis is oxidation of rolled 26 μm thick Cu foils at 600 °C for 10 hours. The highest average aspect ratio obtained in our experiment is 134.

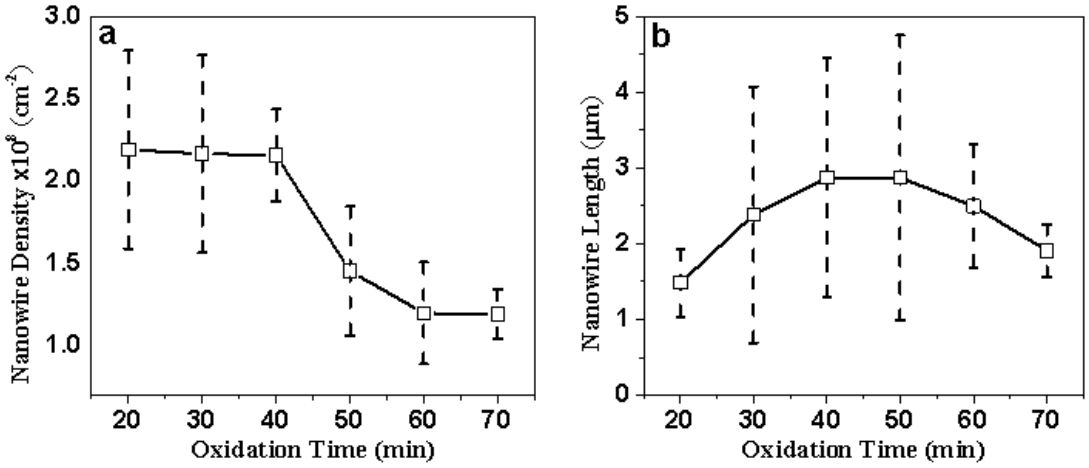

Figure 3.2. The statistical **a)** CuO NW density vs. oxidation time, and **b)** CuO NW length vs. the oxidation time at 500 °C in air.

Cu phase signals of the oxidized Cu foils under different conditions are characterized by XRD, which are shown in **Figure 3.4**.**Figure 3.4a** shows the a full spectrum of XRD to show Cu phase transformation for 1 hour, 5 hours, and 10 hours at 500 °C, 600 °C, and 700 °C, respectively. The strongest diffraction peaks for CuO and Cu_2O shown in **Figure 3.4a** are $(\bar{1}11)$ and (200) of CuO, and (111) are Cu_2O.

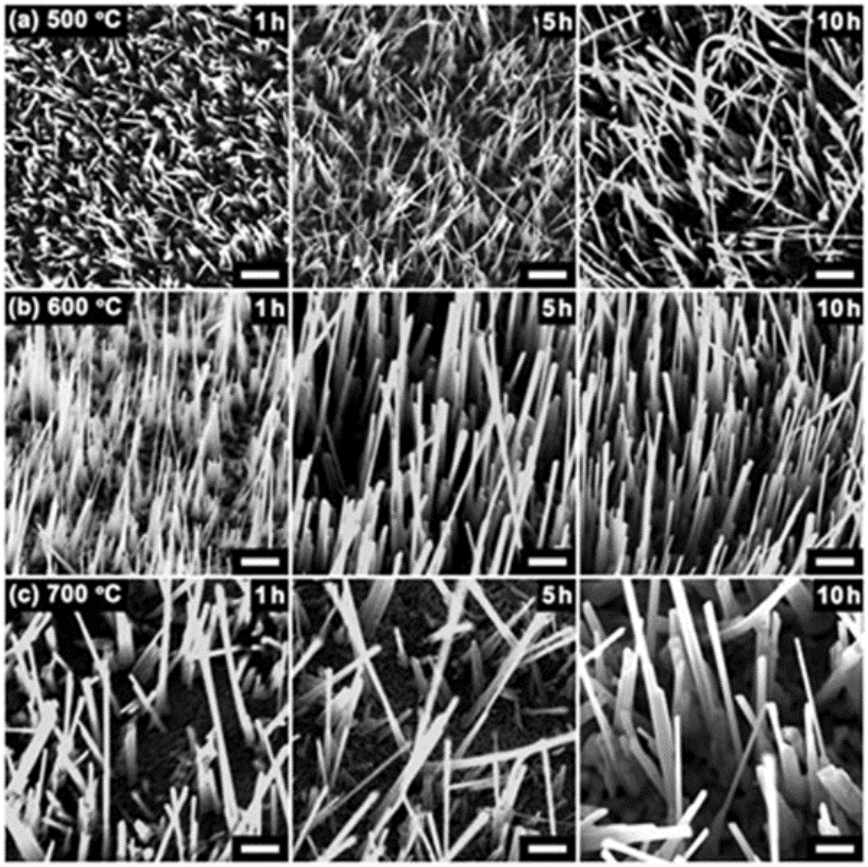

Figure 3.3. The SEM images of CuO NWs by oxidizing 26 μm Cu foil in air at 500 °C, 600 °C and 700 °C for 1, 5, and 10 hours, respectively. Scale bar is 1 μm.

Table 3.1. The CuO NW length, density and combined oxide thickness below NWs.[146]

Temperature (°C)	Time (hours)	NW length (μm)	NW Density x10^8 (μm^{-2})	Combined oxide thickness (μm)	Copper present?
500	1	16.3	1.0	14.0	Yes
	5	13.7	1.1	27.9	Yes
	10	8.4	1.0	34.6	Yes
600	1	2.8	1.2	22.0	Yes
	5	15.3	1.4	36.4	No
	10	30.9	1.7	25.6	No
700	1	10.2	0.7	32.1	No
	5	10.8	1.3	31.8	No
	10	13.9	0.3	35.2	No

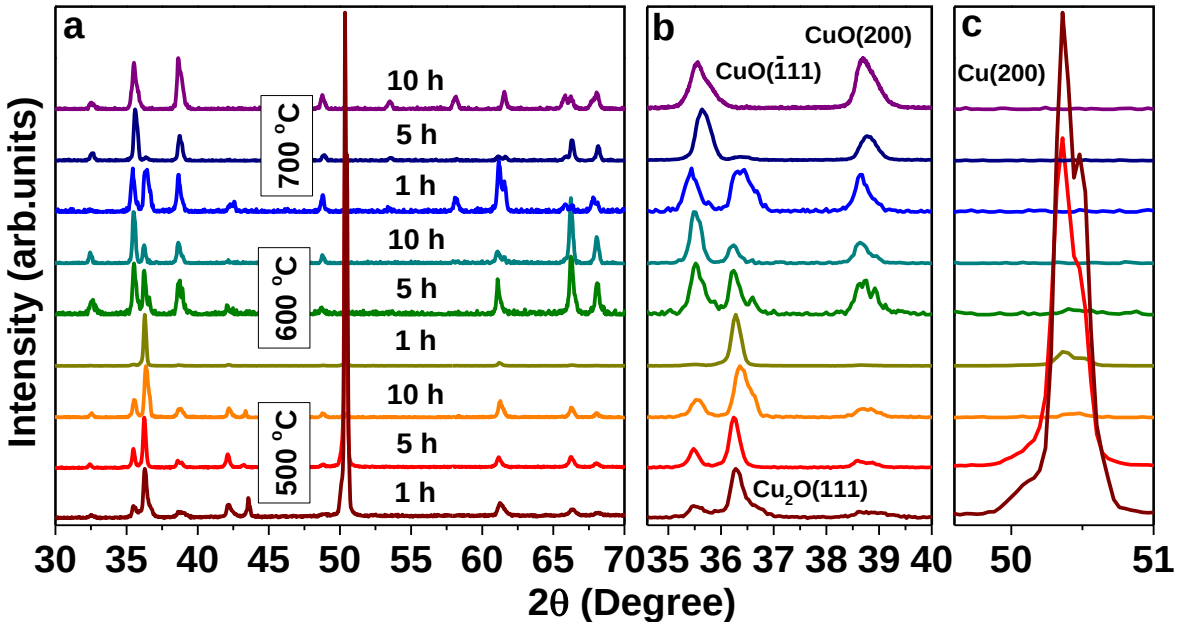

Figure 3.4. XRD patterns of **a)** Cu foils oxidized at 500-700 ℃ for 1-10 hours. Magnified peaks in the range of **b)** 2θ = 35-40 degrees and **c)** 2θ = 49.5-51.0 degrees to show CuO ($\bar{1}11$),(200), Cu_2O (111) and Cu (200).

Figure 3.4b displays the enlarged region of the main diffraction peaks of CuO and Cu_2O. Initially, strong Cu_2O phase is seen at 500 ^oC for 1 hour. A weaker CuO peak is seen as well and comes from the CuO NWs. This CuO phase diffraction peak intensity increases with the oxidation time. CuO NWs length summarized in **Table 3.1** decreases with increasing the oxidation time, indicating that CuO film thickness increases because the NW density has no obvious change. Over the course of increasing temperature and time, CuO peaks start to become stronger. In fact, the XRD data for 700 ^oC at 10 hours shows no Cu_2O and the presence of CuO only.

Figure 3.4c shows the enlarged region where the metallic Cu peak is expected. Metallic Cu peaks are only observed at 500 ^oC for 1, 5 and 10 hour samples and at 600 ^oC for 1 hour sample.

At 600 ^{o}C for 5 and 10 hours and at 700 ^{o}C for 1, 5, and 10 hours, no Cu signal is recorded. This confirms that all metallic Cu is consumed for these samples during oxidation.[146]

The above results demonstrate that we can synthesize CuO NW with an average length ranging from 1 μm to 31 μm and a diameter around 230 nm. The maximum NW length reaches 51 μm. Thus, a tunable aspect ratio from 4 to 134 is available by simply controlling the thermal oxidation time and temperature. The maximum aspect ratio was calculated to be 222. It has been reported that chemical potential difference among Cu, Cu_2O, and CuO forces Cu ions to move from bottom oxides to the surface to grow CuO NWs.[34] Meanwhile, the grain boundaries of the oxides provide a fast diffusion path for Cu ion to quickly reach the surface to drive NW to grow. However, XRD and SEM cannot provide direct evidence to show whether mechanism dominates the NW growth or both contribute equally.

3.3.2 Phases characterization by Raman Microscopy

To study the CuO NW growth mechanism during thermal oxidation, we employed Raman microscopy to characterize the phases of copper oxides obtained under different conditions. A Raman microscope image of a representative cross-section is shown in **Figure 3.5a**. We chose three ~ 1 μm diameter size points across the cross-sections: point 1 on the NWs, point 2 below the NWs' root, and point 3 at the bottom edge of the oxides' film.

The Raman spectra is collected at point on the NWs in **Figure 3.5b**. Two peaks, which belong to A_g mode and B_g mode of CuO,[47, 147] are observed at 298 cm^{-1} and 340 cm^{-1}. No Cu_2O signal is detected, indicating that the NWs are pure CuO. **Figure 3.5c** displays the Raman spectra collected at point 2. Both CuO (A_g) and Cu_2O ($2E_u$ mode at 218 cm^{-1})[47, 148] peaks are observed at 500 ^{o}C for 1 hour, 5 hours, and 10 hours and at 600 ^{o}C for 1 hour. Both the CuO and the Cu_2O

peaks are broad, but the CuO A_g peak shifts to a lower wave number (284 cm-1). It was reported that stress and non-stoichiometry contribute to the peak broadening and shift.[149] The samples oxidized at 600 ^oC for 5 hours and 10 hours, and 700 ^oC for 1 hour, 5 hours, and 10 hours, only show CuO peaks without any observed shift. These peaks are narrow, showing a wave number of 298 cm^{-1}, indicating that the CuO phase is stoichiometric.

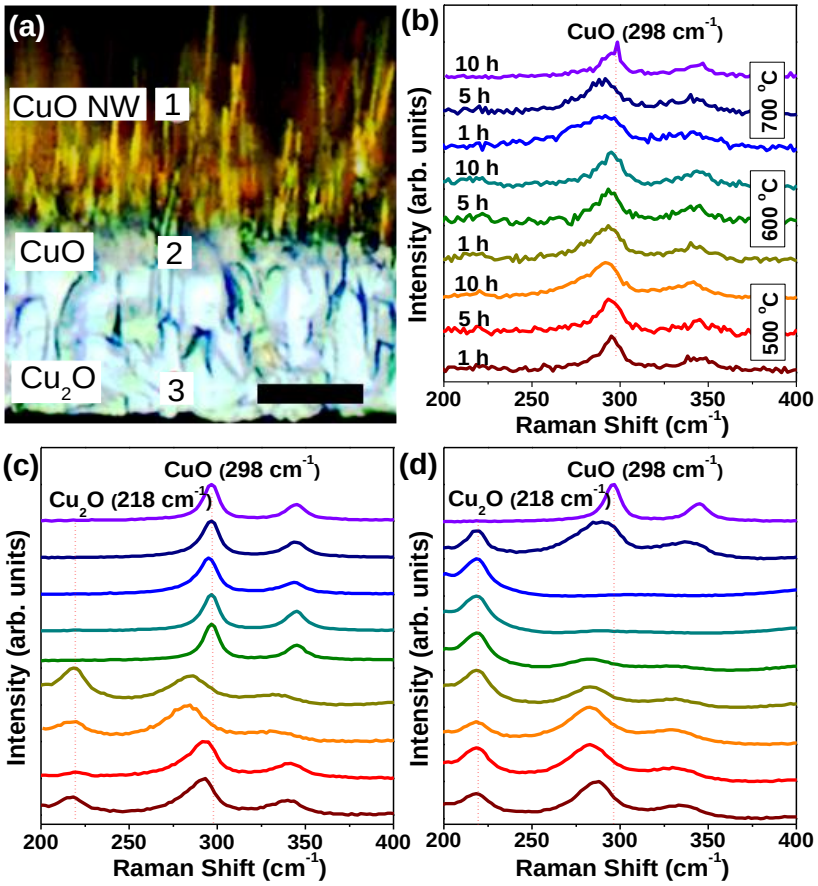

Figure 3.5. a) Representative cross-section of a CuO NW sample under the Raman microscope showing the three spots (1, 2 and 3) from where spectra was acquired in **b)**, **c)**, and **d)**, respectively. The scale bar in **a)** is 10 μm.

At point 3, we see both the CuO and the Cu_2O peaks. The CuO peaks emerge at 500 ^oC 1, 5, and 10 hours, and 600 ^oC 1 and 5 hour samples. They disappear at 600 ^oC for 10 hours and 700

^{o}C for 1 hour samples. They then re-emerge at 700 ^{o}C for 5 and 10 hour samples.[150] Initially, the CuO peak shifts to the lower wave number and disappears at 600 ^{o}C for 10 hours. A broad CuO peak shows up again at 700 ^{o}C for 5 hours and becomes a sharp narrow peak at 298 cm^{-1}at 700 ^{o}C for 10 hours.

The above data demonstrate that CuO NWs can be grown by oxidizing pure copper foils in air. Stress which are introduced to the copper foils by rolling the foils from 127 μm to 26 μm contributes to the dense and long CuO NWs growth with an average aspect ratio of 134. Raman spectra show the non-stoichiometric CuO phase when the samples have remaining Cu inside, indicating that bottom metallic Cu plays an important role in affecting the ions diffusion, and further influencing the NWs growth. To investigate the relationship between the ions diffusion and the CuO NWs growth mechanism, further analysis is provided in the discussion section below.

3.4 Discussion

The chemical potential gradient generated between Cu foil and CuO drives the Cu ions to diffuse from Cu to CuO when Cu foils get oxidized. Compared with diffusion through lattice, diffusion through grain boundaries was reported to be much easier and faster at low temperatures.[151] The fast outward diffusion of Cu ions through grain boundaries contributes to the nucleation and growth of CuO NWs. If the Cu ions mostly diffuse through the grain boundaries during the CuO NW growth, the non-stoichiometric CuO phase should predictably be observed at the grain boundaries.

To show the evidence of a transient phase at the grain boundaries, we did Raman line scan mapping on the cross-section of oxide layers below CuO NWs, which is shown in **Figure 3.6**. The sample I chose in **Figure 3.6** is 500 ^{o}C for 10 hours' oxidation because XRD shows that copper is

left in the foil and the samples show a strong Cu_2O diffraction peak, making this sample very easy to capture the transient $Cu_{1-x}O$ phase at the grain boundaries.

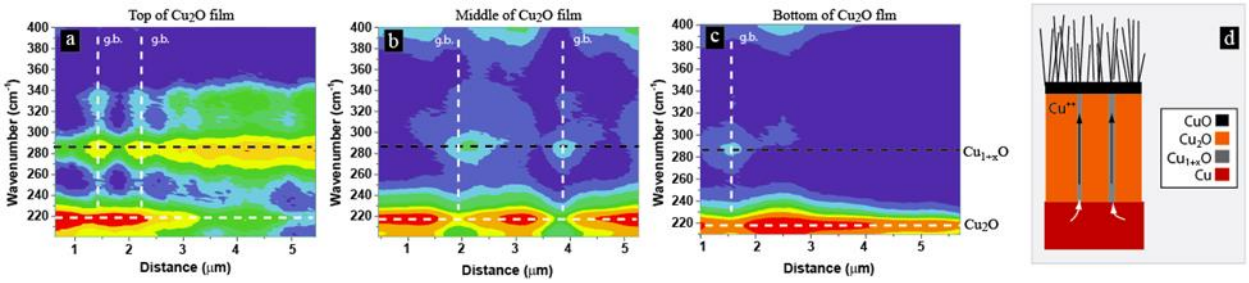

Figure 3.6. Raman contour maps through the Cu_2O film for the 500 ºC 10 hour sample corresponding to **a)** the top of the Cu_2O film, **b)** the middle of Cu_2O film and **c)** the bottom of Cu_2O film. "g.b." = Grain Boundary. Note: Colour coded intensities are normalized on the log scale to highlight the weaker $Cu_{1+x}O$ signals. **d)** Schematic of cross section and phases observed.

The line scan mapping is on the cross-section of the sample at the top, middle, and bottom of the bottom oxide layers. The x-axis represents the scan distance and the y-axis represents the Raman shift. At the top of the oxide layer (**Figure 3.6a**), both Cu_2O and $Cu_{1-x}O$ phases display high Raman intensity. It can be clearly observed that in instances where the laser traverses between two Cu_2O grains (a drop in Cu_2O intensity is shown as vertical, dotted lines), the $Cu_{1-x}O$ signal becomes stronger. The Raman peak centered at 218 cm^{-1} is Cu_2O. At the top of the oxide layer, the $Cu_{1-x}O$ phase is dominant because rich adsorbed O diffuse into the oxidized the Cu_2O into CuO. However, the Raman peak centering at 284 cm^{-1} is not stoichiometric CuO, which was reported to be related to an non-stoichiometric CuO with Cu lean ($Cu_{1+x}O$).[152] This indicates that Cu ions diffused into the root of NWs to make the NWs grow longer. In **Figure 3.6b**, the Cu_2O phase and the transient $Cu_{1-x}O$ phase cannot simultaneously exist. $Cu_{1-x}O$ phase only shows a strong Raman

intensity when the Cu_2O phase signal is weak or absent. When a strong Cu_2O phase signal is observed, no transient $Cu_{1-x}O$ phase exhibits. At the bottom of the oxide layer (**Figure 3.6c**), we also observed a similar phenomenon. The results demonstrates that $Cu_{1-x}O$ phase appears at in the grain boundaries of Cu_2O films.

The off-stoichiometric $Cu_{1-x}O$ phase was found in the grain boundaries of Cu_2O film, providing strong evidence that Cu ions flow through grain boundaries. Compared with the diffusion through lattice, the grain boundary diffusion is dominant at a temperature lower than 800 ^oC.[63] When temperature is higher than 800 ^oC, lattice diffusion becomes dominant, and homogenous nucleation happens at the interface of CuO/air. As a result, no NWs growth was observed by oxidizing Cu foils. When grain boundaries dominate the outward diffusion of Cu ions, the ions reach the surface at the grain boundaries.[34, 67] Because of the high energy at the grain boundary, CuO nanocrystals start to nucleate. The nanocrystals grow into NWs because of the continuous quick outward diffusion of Cu ions through grain boundaries. A CuO NW growth diagram is shown in **Figure 3.6d**.

To investigate the Cu ions diffusion mechanism when there is no Cu remaining in the sample, we did Raman line mapping parallel and vertical to the cross-section of a completely oxidized Cu foil, respectively, shown in **Figure 3.7**.In this case, we clearly see a gap produced in the center of the foil due to the unit cell volume difference between Cu and Cu_2O. On both sides of the gap, the oxide layers consist of a 5 μm thick Cu_2O and a 16 μm thick CuO on the top side, and a 4 μm thick Cu_2O and a 16 μm thick CuO on the bottom side, respectively. Inside the CuO or Cu_2O layers, no transient phase was observed in **Figure 3.7**. Therefore, when Cu foils are fully oxidized, fast grain boundary diffusion was not observed. It was reported that both lattice and grain boundary diffusion play an important role in oxidizing Cu foils during the oxidation process at 600 ^oC and 700 ^oC.[151]

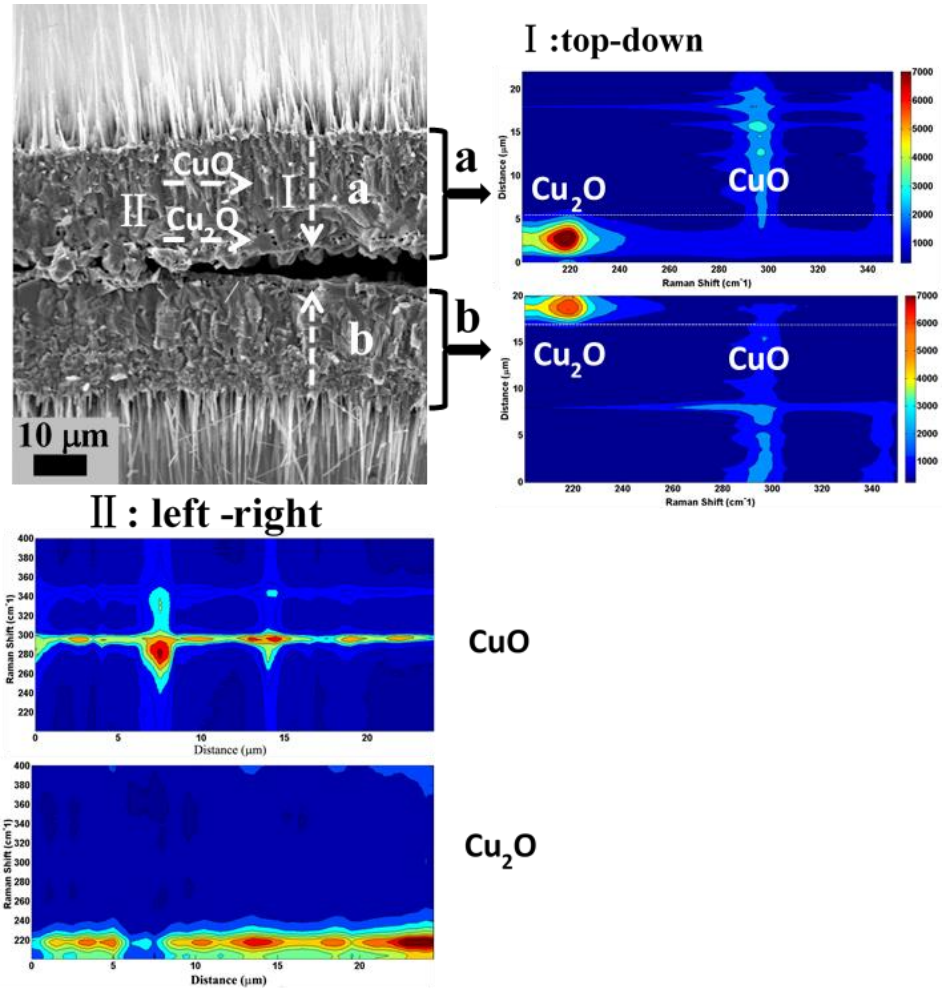

Figure 3.7. The SEM image showed complete cross-section of 600 ºC 5 hour sample with no copper left after oxidation. The CuO NWs and copper oxide under layer are symmetric on both sides. Two different line scans were made on the cross sections: **Part** Ⅰ: bottom-up line scan and **Part** Ⅱ: parallel line scan. Raman line scan from the root of NW to the edge of the oxides layer (Bottom-up line scan) showed that a thick CuO layer formed below CuO NWs and then a pure Cu_2O layer existed below CuO (**part I**). In order to confirm the CuO and Cu_2O are pure, parallel line scans indicated that both CuO and Cu_2O are pure without impurity phases existing in the grain boundaries (**part** Ⅱ).

The chemical potential between Cu_2O and CuO forces Cu ions to diffuse out, which explains that the maximum length of CuO NWs are obtained at 600 ºC for 10 hours and the length and density decrease when increasing the oxidation time at 700 ºC.

3.5 Conclusions

In this chapter, we studied CuO NWs' growth on both 127 μm and rolled 26 μm thick pure Cu foils using a thermal oxidation method in the air to understand the mechanism of the spontaneous growth of CuO NWs. The maximum CuO NWs density obtained by oxidizing 127 μm Cu foil is 2.2×10^8 /cm^2 at 500 ^{o}C for 20 minutes. The density decreases with increasing the oxidation time. The NWs length is around 1-2 μm.

To increase the NW length (longer than 10 μm), we introduced stress into the foils by rolling 127 μm foils into 26 μm ones. We systematically study the CuO NWs growth on these rolled thin foils at 500 ^{o}C, 600 ^{o}C, and 700 ^{o}C for 1 hour, 5 hours, and 10 hours, respectively. We found that most of the CuO NWs are longer than 10 μm with a density of more than 1×10^8 /cm^2. The maximum density and the longest NWs with an average length of 31 μm and an aspect ratio of 134 were obtained at 600 ^{o}C for 10 hours.

The 26 μm thick Cu foils can be fully oxidized at 600 ^{o}C for 5 hours with no detected Cu left. At 700 ^{o}C for 10 hours, the oxidized foils completely transformed into CuO with 13 μm long NWs on surface. The average diameter of the NWs is 230 nm.

We showed direct evidence of Cu ions outward diffusion through grain boundaries of the oxide films to drive nanocrystals to nucleate and then grow into NWs. The off-stoichiometric $Cu_{1-x}O$ phase appears in the Cu_2O film when Cu is remaining in the oxidized foils because of the fast diffusion of Cu ions through the grain boundaries. When all Cu is oxidized at 600 and 700 ^{o}C, the chemical potential between Cu_2O and CuO still force Cu ions move to the surface by grain boundaries to increase the length of the NWs. However, the transient phase was not observed in the grain boundaries any more. The possible reason is that the diffusion speed is significantly

slowed down when there is no Cu in in the foils. At 700 ^{o}C, the NWs density dramatically decreases with an increase in oxidation time, demonstrating that lattice diffusion affects the growth of CuO NWs.

Chapter 4 Reduction of CuO NWs and the phase transformation kinetics

4.1 Introduction

Many synthesis strategies for obtaining Cu_2O NWs have been attempted. Randomly distributed single crystal Cu_2O NWs have been synthesized by a hydrothermal method at 180 ^oC and an aqueous solution method at 95 ^oC.[153, 154] Linear sweep voltammetry has been used to reduce copper duplex oxides using 6 M KOH + 1 M LiOH.[155] Porous nanotemplate-based electrochemical techniques have been shown to yield high density Cu_2O NWs ~ 200 nm in diameter, but limited in length to 4 μm, due to diffusion limited electrolyte transport in narrow nanopores.[156] However, synthesis of vertical Cu_2O NW arrays is still under study.

There have been reports of reducing thermal oxidized CuO NWs to Cu_2O NWs. For example, discrete Cu_2O nanoparticles on the NW surface formed under high vacuum (~2×10^{-6} torr), annealing at 450 ^oC.[157] Alternately, a thin carbon coating layer was used to completely reduce CuO NW to Cu_2O segments inside a transmission electron microscope column.[158] N_2/H_2 mixed plasma was also used to reduce CuO NWs.[159] Porous polycrystalline NWs were observed after the reduction processes. The ratio of Cu_2O/CuO can be adjusted by the ratio of N_2/H_2. However, CuO NWs were only partially reduced, forming small Cu_2O nanoparticles on CuO NWs. Under CO atmosphere, CuO NW was reduced to Cu_2O and then to Cu.[160] Until now, Cu_2O NWs array with a high crystalline quality and high aspect ratio has not been reported yet. The phase transformation kinetics in CuO NWs during the reduction reactions is still unclear.

In this chapter, we slow the phase transformation kinetic processes by systematically lowering the reduction temperature and controlling the total number of CO molecules adsorbed on

the surface of CuO NWs. The phase transformation processes can be controlled to simultaneously grow amorphous can conformal Cu_2O layer on either CuO NWs or CuO/Cu_2O NWs. We applied Kolmogorov–Johnson–Mehl–Avrami (KJMA) equation to fit the phase transformation kinetics, demonstrating that desirable CuO NWs, Cu_2O NWs, or CuO/Cu_2O NWs can be easily synthesized by tuning the surface diffusion and surface reactions.

4.2 Experiments

Pure CuO foils with NWs on the surface were used as starting samples,[161] synthesis details of which are described in **Chapter 3**. These samples do not contain any residual Cu or Cu_2O phases. To ensure the carbothermal reduction of the CuO foil, the samples were held inside a graphite cylinder opened at both ends. This cylinder was then put inside a furnace. The furnace was pumped to 1 Torr pressure using an Edwards RV12 mechanical pump. The furnace temperature was then raised and the sample was reduced at three temperatures, namely 300 ^oC, 350 ^oC, or 400 ^oC at various times. The specific temperature-time conditions are shown in **Table 4.1**.

Table 4.1. Temperature-time conditions for the samples used to study the carbothermal reduction of CuO to Cu_2O.

Temperature (^oC)	Time (minutes)								
300	30	60	120	180	240	300			
350	45	60	75	90	105	120	180	300	
400	20	30	40	50	60	120	180	300	600

The reduced samples were broken into small pieces and mounted at the edge of a sample holder for micro Raman spectroscopy of the cross-sections. A Renishaw InVia Raman Microscope was used for all Raman measurements. The laser wavelength used was 514 nm. A 50 X microscope objective with a numerical aperture (N.A.) of 0.75 was used. The laser spot size was ~1 μm^2. The

laser spot was made to focus on the NWs along the cross section of the samples, effectively yielding an ensemble average fraction of phases present in the NWs. The laser was also moved down to the bottom oxides layer to investigate the phase transformation process during the reduction, focusing on three different positions: at the top, in the middle, and at the bottom of the oxide layer.

SEM images on cross-section and single NW were taken using JEOL 7001LVF at 15 KVs. TEM, high resolution transmission electron microscopy (HR-TEM), and scanning transmission electron microscopy (STEM) images of NWs were obtained by JEOL 2100 F with a voltage at 200 KVs. Fast Fourier transformation (FFT) and corresponding crystal structure analysis were conducted using a Gatan® image analysis software. X-ray photoelectron spectroscopy (XPS) was conducted using the PHI 5000 VersaProbe II from Physical Electronics Inc., using Al Kα X-ray source with beam energy 1486.6 eV.

To provide more information of the surface morphology and quantitative analysis on the samples after reduction, we employed Scanning transmission electron microscopy (STEM) and line scan energy dispersive X-ray spectroscopy (EDX) across the NWs reduced at 300 ºC for 30 minutes in diameter direction. The concentration of Cu/O ratio collected through EDX is corrected by the equation: $\frac{C_{Cu}}{C_O} = k_{CuO}\frac{I_{Cu}}{I_O}$ without considering absorption.[162, 163] The EDX spectrum corrections are provided in **appendix I**.

4.3. Results

4.3.1 Phase transformation of CuO NWs

In last chapter, we reported that rolled 26 μm pure copper foils can be completely oxidized into CuO with vertical CuO NWs on top of the surface. These NWs have an average length of 13 μm

and an average diameter of 230 nm. To obtain tunable morphologies and phases of the CuO NWs, we reduce CuO NWs in mild CO ambient self-produced by a graphite cylinder holder during the heat-treatment.

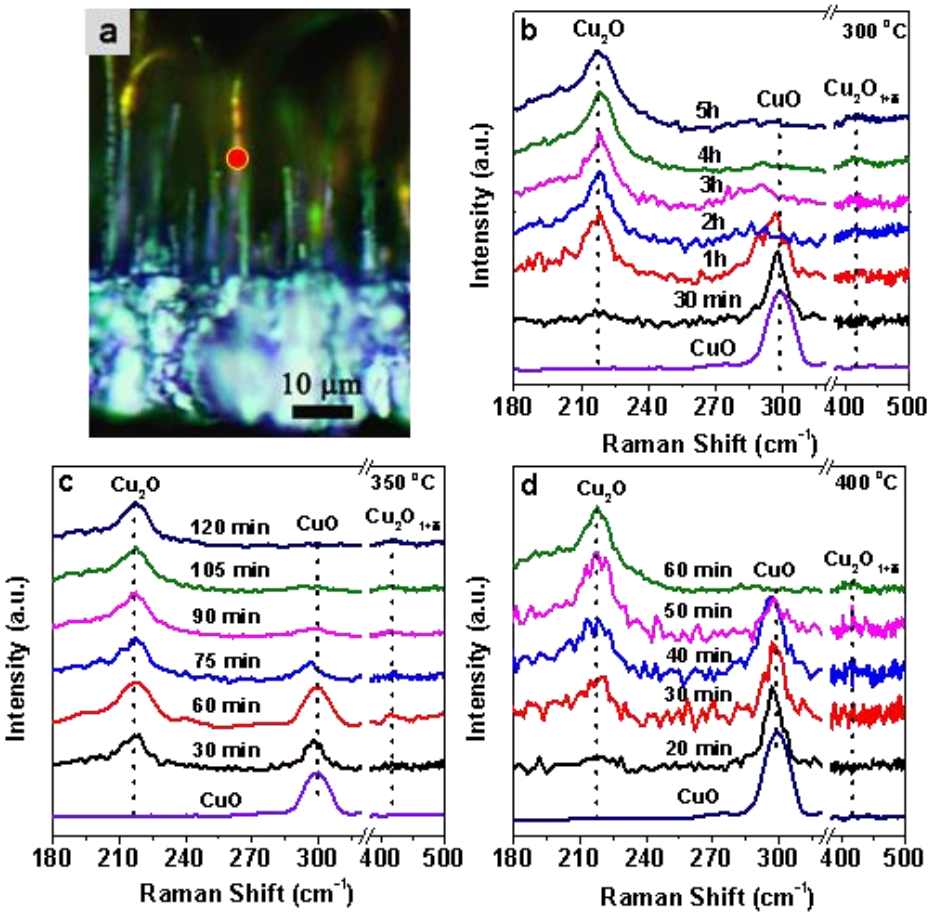

Figure 4.1. a) Cross-section of the NW sample under Raman microscope. The spot marks the place where the laser is focused. Raman spectra of the CuO NWs reduced at **b)** 300 ^{o}C, **c)** 350 ^{o}C, and **d)** 400 ^{o}C.

The oxidation state of the copper oxide NWs is studied by focusing the Raman laser on the NWs in cross-section. This is shown schematically in **Figure 4.1a** where the cross-section with

NWs can easily be resolved under the Raman microscope. The resultant spectra collected is an ensemble average and is representative of the state of transformation of the NWs.

The effect of CuO NW reduction on the Raman spectra is shown in **Figure 4.1b** at 300 ^{o}C for times ranging from 20 minutes to 5 hours, **Figure 4.1c** at 350 ^{o}C for times ranging from 30 minutes to 2 hours and in **Figure 4.1d** at 400 ^{o}C for times ranging from 20 minutes to 1 hour. Here, we monitor the peaks at 218 cm^{-1} and 298 cm^{-1} belonging to the $2E_u$ mode of Cu_2O and the A_g mode of CuO, respectively.[150] Additionally, a sub-stoichiometric $Cu_2O_{1+\delta}$ phase also appears at 418 cm^{-1} during various times of reduction.[164]

4.3.2 Microstructure of the reduced CuO NWs

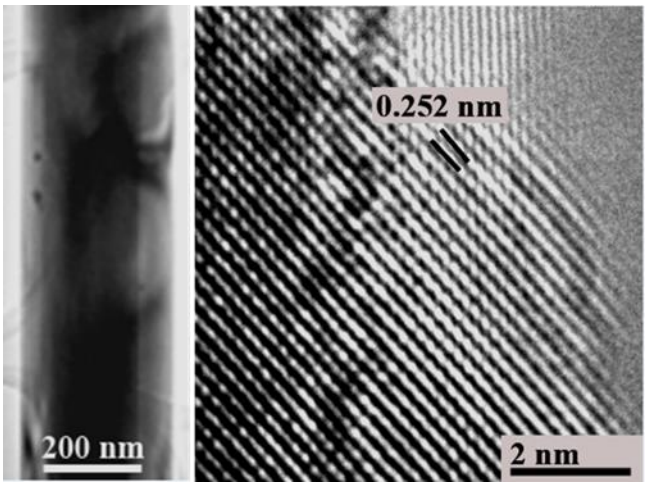

Figure 4.2. Left, pristine CuO NW**, right,** HRTEM of CuO NW surface with a lattice distance of 0.252 nm, corresponding to ($\bar{1}11$).

For all temperatures tested, it is found that the Cu_2O $2E_u$ Raman peak intensity increases with increasing reduction time. Correspondingly, the CuO A_g Raman peak intensity decreases. Thus, a clear CuO → Cu_2O phase transition occurs at all tested temperatures. However, the rates of transformation are significantly longer for the 300 ^{o}C sample as compared to the 350 ^{o}C or 400 ^{o}C sample. For example, at 300 ^{o}C the CuO signal is still visible after 5 hours reduction (**Figure**

4.1b). However, at 350 ^{o}C the CuO peak disappears after 2 hours (**Figure 4.1c**) while at 400 ^{o}C CuO peak disappears after just 1 hour (**Figure 4.1d**). Thus, the Raman data shows that the phase transformation of CuO to Cu_2O can be visibly slowed down by a low temperature carbothermal reduction process. Therefore, we choose to systematically characterize the NWs reduced at 300 ^{o}C to study the phase transformation kinetics in a CuO NW. The morphology evolution of the Cu_2O NWs at 400 ^{o}C is shown in **appendix Ⅱ**.

To study the CuO NW phase transformation mechanism, we systematically characterized the partially reduced CuO NWs at 300 ^{o}C. To show the surface morphology evolution with the phase transformation, TEM and HRTEM images a CuO NW are shown in **Figure 4.2**, indicating that CuO NW are smooth with no particles, cracks, and curvatures. The NW diameter is around 300 nm with a smooth surface terminated by $(\bar{1}11)$ plane.[34]

To obtain structural information of the transformed NWs, SEM was conducted on the 300 ^{o}C samples carbothermally reduced for various times from 30 minutes to 5 hours. This is shown in a series of images in **Figure 4.3**. After 30 minutes of carbothermal reduction, the NW surfaces appear roughened while the diameter of the NWs does not show obvious change. The NW becomes curved as the reduction time extends past 1 hour. Thereafter, the NW roughness progressively increases and cracks appear on the NW surface. The development of cracks and a curved shape are related to the tensile stress in the Cu_2O released during phase transformation. Here we note that the unit cell volumes of CuO and Cu_2O are 81.16Å^3 and 77.83 Å^3, respectively.[34] The release of stress results in the NWs being curved and cracked. All reduced NWs show an average length ~20 μm.

According to **Figure 4.1a** and **Figure 4.3**, an obvious morphology evolution is observed with reduction reactions proceeding. To investigate the relationship between the phase transformation and the surface morphology of the reduced NWs, we conducted TEM and HRTEM characterizations on the sample reduced at 300 ^{o}C for 30 minutes.

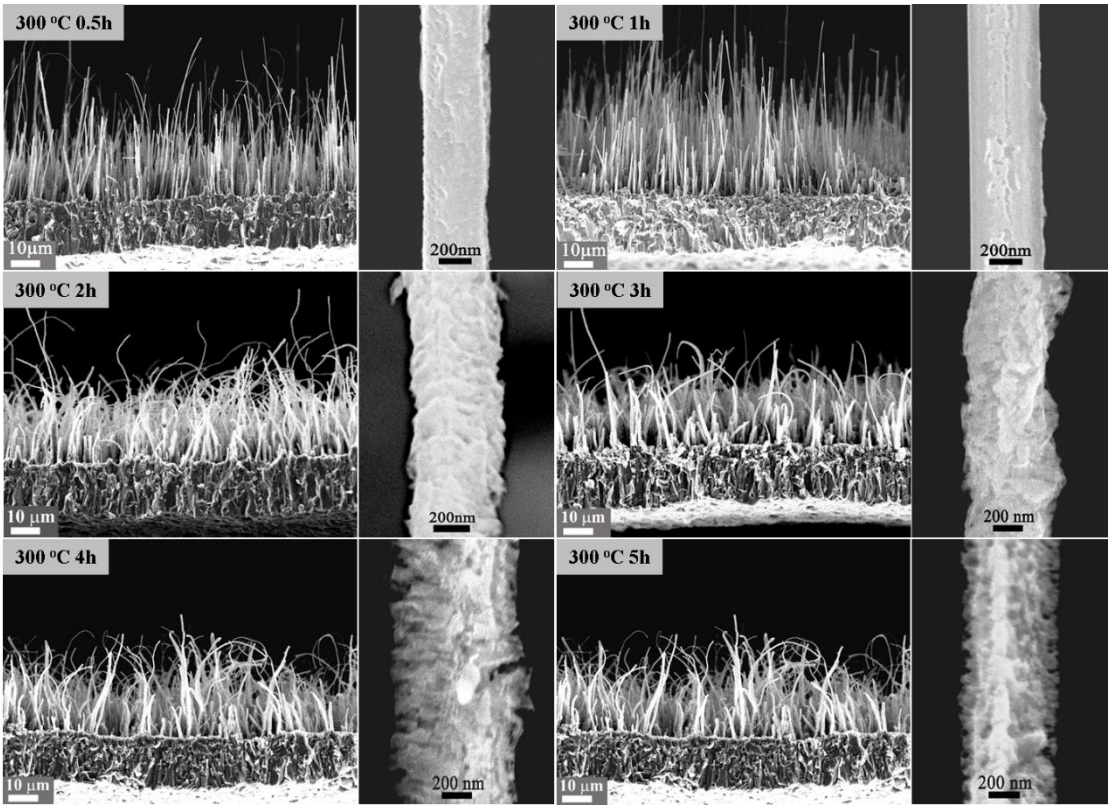

Figure 4.3. SEM images of cross-sections and NWs obtained under different reduction times at 300 ^{o}C. The wires start as straight and vertical. However, after 1 hour reduction, the NW surface is roughened. The wires visibly bend and shrink after 2 hours of reduction.

Figure 4.4a is a TEM image of the reduced NW, showing the emergence of a roughened surface. An enlarged HR-TEM image of the rough area is shown in **Figure 4.4b**, indicating that the surface layer is amorphous with a thickness that varies from 9 to 12 nm at various points on the surface. The amorphous region may not fully disordered but can retain some lattice order,

which comes from its crystalline parent during the reduction.[165, 166] Below the amorphous layer, a crystal with a lattice parameter of 0.252 nm is indicative of the CuO ($\bar{1}11$) plane.[167] Thus, for the NW considered in this image, the primary material remains CuO while the surface consists of a 9-12 nm thick amorphous layer.

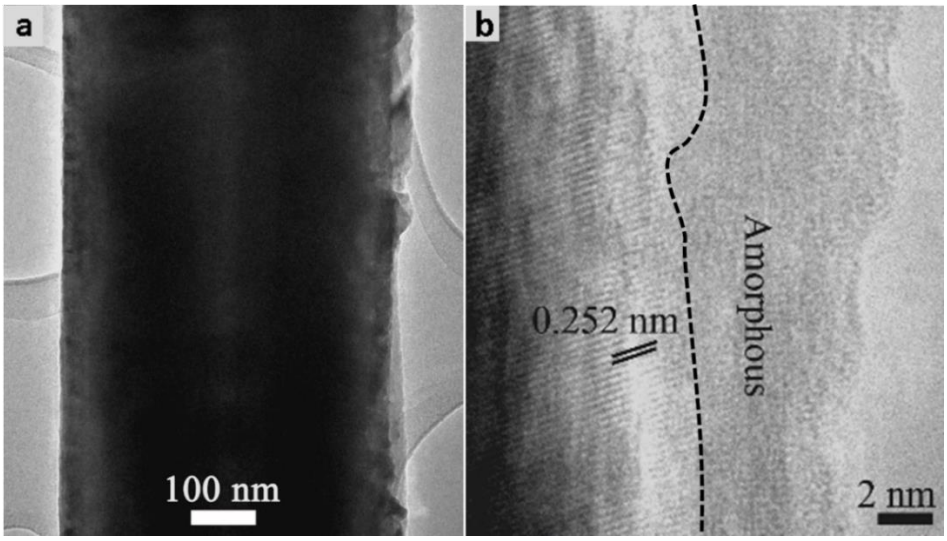

Figure 4.4. CuO NW reduced at 300 ºC for 30 minutes: **a)** TEM image shows the appearance of protrusions at the edges**. b)** HR-TEM image shows the presence of an amorphous layer which is 9-12 nm thick.

To quantitatively characterize the stoichiometry of the amorphous layer and the material below it, we conducted an EDX line scan under the dark STEM mode across the NW reduced for 30 minutes in the diameter direction. The STEM image and the line scan EDX are shown in **Figure 4.5a** and **b**, respectively. The edge of the NW in the STEM image shows a different contrast with the center crystalline part, the layer appears to conformally coat on the NW. A line scan EDX across the NW in the diameter direction (red line under STEM mode is employed to quantitatively examine the stoichiometry of the reduced NWs. The stoichiometry of the NW provides important

information to illustrate the phase transformation mechanism in a NW. The resulting Cu/O ratio vs. scanning distance is plotted in **Figure 4.5b**.

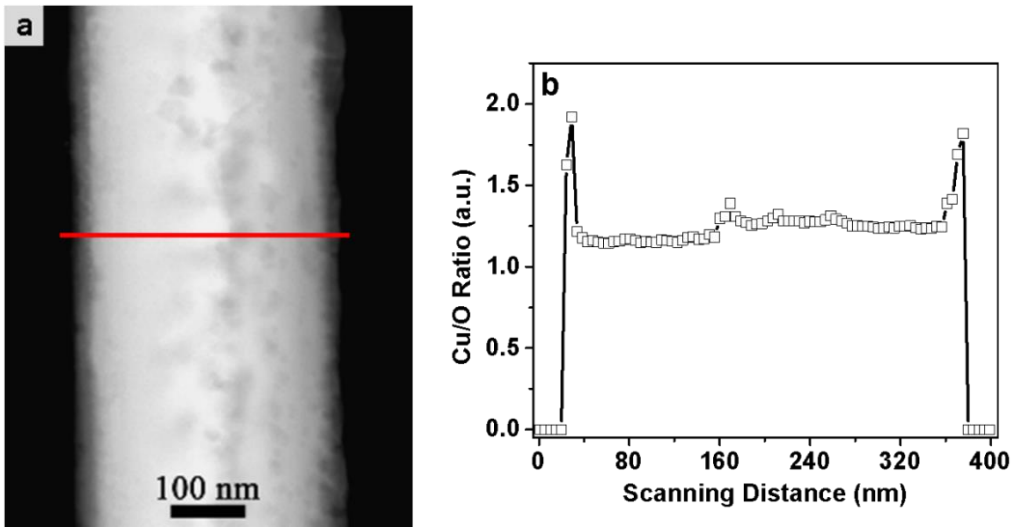

Figure 4.5. a) STEM image of the CuO NW reduced at 300 ^{o}C, 30 minutes. Notice the edge contrast is different than the center of the wire indicating a different phase along the surface of the NW. **b)** Line scan EDX of the NW parallel to the diameter direction shown as red line in **(a)**.

EDX data shows that Cu/O ratio is 1.7-1.8 at both edges of the NW and the ratio decreases to 1.1-1.2 in the core part of the NW. Here, we note that the signal and stoichiometry observed is dependent on the region of the NW scanned.[168] Thus, at the edges where the electron beam has to pass through the amorphous oxide only, the ratio of Cu/O is 1.8. However at the center of the NW, assuming that the amorphous layer is conformally coating the NW, the electron beam has to pass twice through the amorphous layer and the core of the NW. Thus, the Cu/O may be higher than for a pure CuO wire and may explain the 1.1-1.2 ratio in the center. In any event, these results suggest that the surface amorphous layer is O-lean with respect to CuO or, O-rich with respect to Cu_2O.

Based on the analysis of EDX, the amorphous non stoichiometric Cu_2O layer is found conformally coating the NW surface. We increased the reduction time 1 hour. The TEM image of the NW is shown in **Figure 4.6a**.Compared the NWs shown in **Figure 4.6a** (300 ^oC for 30 minutes),

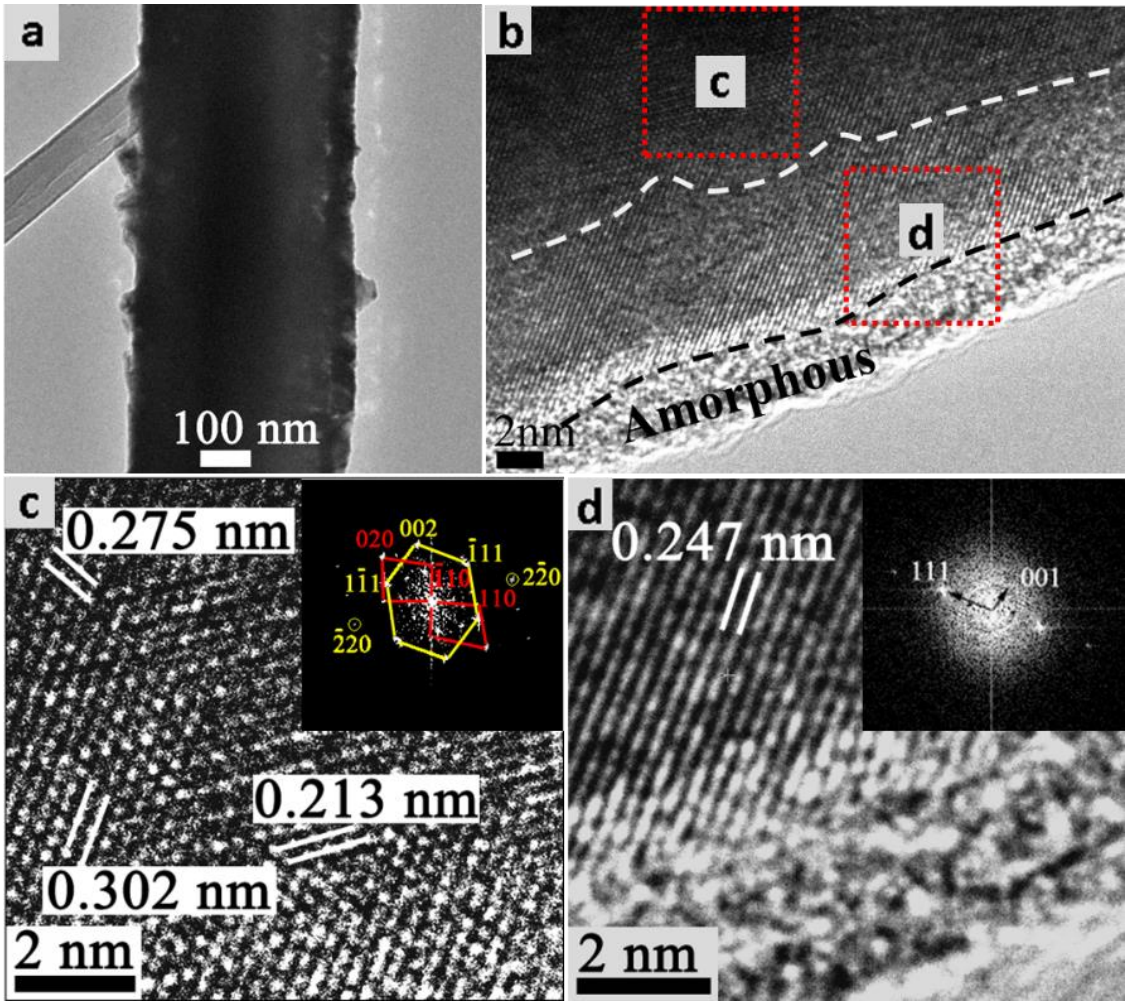

Figure 4.6. CuO NW is reduced at 300 ^oC for 1 hour: **a)** TEM image, **b)** HRTEM image, **c)** enlarged area of top red marked region in '**b**', with the corresponding FFT on the right, **d)** enlarged area of bottom red marked region in '**b**', with the corresponding FFT on the right.

the surface of the NW reduced for 1 hour grows small nodules. The HRTEM image in **Figure 4.6b** displays the lattice fringes of the NW surface, showing three different layers. The interfaces are

labeled with a white line and a black line, respectively. An amorphous layer with a thickness of 2-3 nm is still visible in **Figure 4.6b**, indicating that longer reduction time makes the amorphous crystallize. Under the amorphous layer, there are two different crystalline layers. In order to characterize the phases and crystal growth directions in the crystal layers, enlarged areas of the inner region ('c') and close to surface ('d') of the NW, marked by red boxes in **Figure 4.6b**, are shown in **Figure 4.6c** and **4.6d**, respectively.

HR-TEM image of the inner region marked 'c' is shown in **Figure 4.6c**, and the corresponding FFT on the right inset shows the presence of both CuO and Cu_2O diffraction patterns. The lattice distances of 0.275 nm, 0.213 nm, and 0.302 nm belong to (110) of CuO, (002) and (110) planes of Cu_2O, respectively. The FFT indicates that both CuO and Cu_2O belong to the [110] zone axis. It is reported that $\{\bar{1}10\}$ of CuO is parallel to the {111} of Cu_2O showing preferential epitaxial growth.[157]

The lattice fringe below the amorphous layer in **Figure 4.6d** shows a distance of 0.247 nm, corresponding to the (111) plane of Cu_2O shown in FFT.[169] Thus, for the 300 ^oC, 1 hour sample, the region contiguous to the inner side of the amorphous layer is transformed to crystalline Cu_2O.

The observed data from **Figures 4.6 b**, **c** and **d** are important. According to these HRTEM images, after 300 ^oC, 1 hour the CuO NW consists of a CuO core, a Cu_2O shell and a covering amorphous $Cu_{1.8}O$ layer shell with a thickness of 2-3 nm. The Cu:O ratio varies as 1, 2 and 1.8, respectively for the three layers. This is a key piece of evidence to show that the amorphous layer is driven by CO controlled surface reactions because the surface reactions cause the NW metastable, resulting in Cu_2O crystallization starts from the CuO/Cu_2O interface.

To further confirm that the CuO NW is only reduced to Cu_2O instead of Cu, even though the amorphous Cu_2O starts to crystalize, we performed XPS on the surface of the CuO foil before reduction and after reduction for 1 hour at 300 ^oC, respectively. A full survey scan spectra, and fine scan spectrum of C 1s, O 1s and Cu 2p are shown in **Figure 4.7a**. The deconvoluted C 1s, O 1s and Cu $2p_{3/2}$ peak positions are listed in **Table 4.2**.

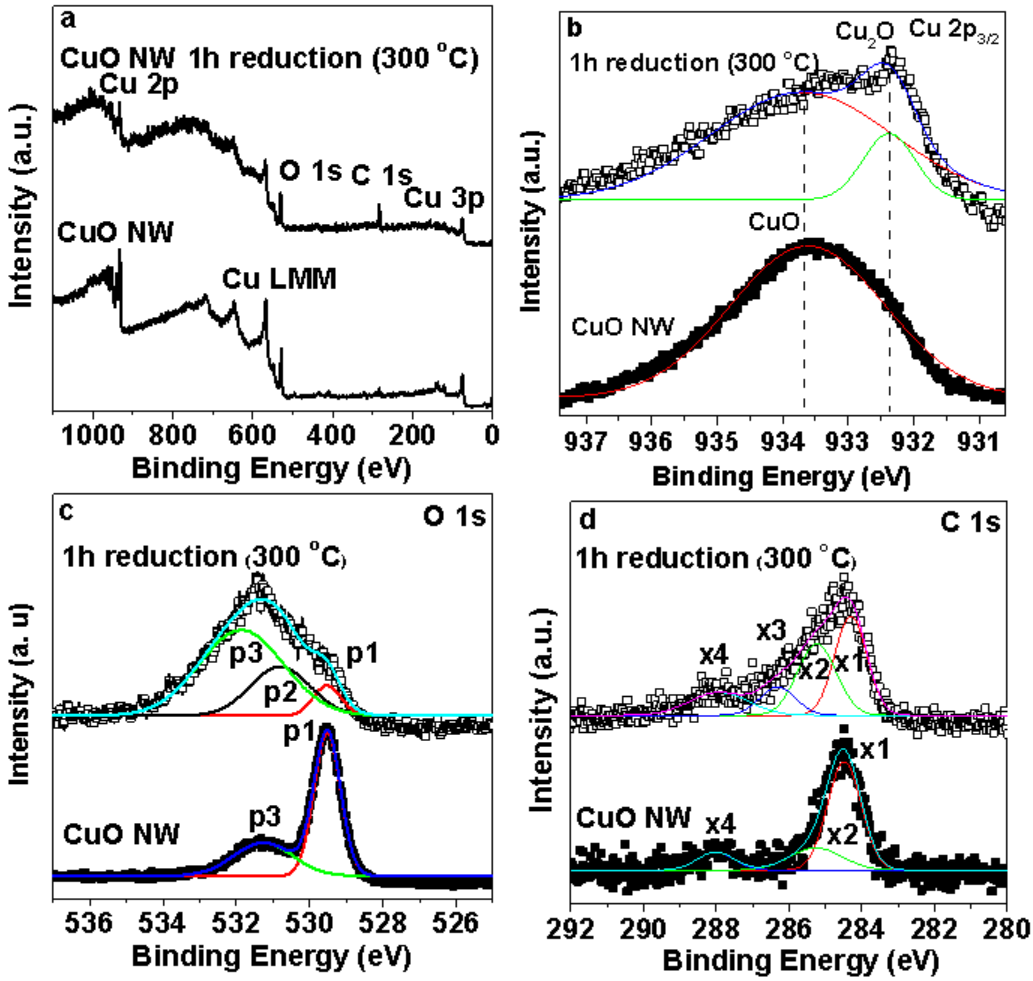

Figure 4.7. XPS collected on CuO NW and 1 hour reduced CuO NW: **a)** a full spectrum survey XPS scan, **b)** Cu 2p peak, **c)** O 1s peak, which is fitted by 3 peaks, **d)** C 1s, peak which is fitted from four peaks.

Figure 4.7a shows the full survey spectrum of the CuO foil and the reduced CuO foil from 0 to 1100 eV. Except Cu, O and C elements, no impurity is observed. A fine scan of Cu $2p_{3/2}$ is shown in **Figure 4.7b**. The Cu $2p_{3/2}$ peak of CuO NW is at a binding energy of 933.7 eV.[27] This corresponds to the Cu^{2+} valence state of the Cu-O bond as is to be expected from the pure CuO NWs. On the other hand, the 300 ^{o}C 1 hour sample shows a broadened Cu $2p_{3/2}$ peak. This can be deconvoluted into two peaks, one at 933.7 eV and the other 932.4 eV. While, the peak at 933.7 eV is assigned to CuO, the peak at 932.4 eV corresponds to Cu_2O.[170, 171]

The O 1s peak in **Figure 4.7b** is asymmetrical and can be fitted from three symmetrical Gaussian peaks, p1, p2, and p3. The p1 peak at 529.5 eV is attributed to the Cu-O bond of CuO, which is consistent with the reported data.[172] The reduced CuO NW shows a p2 peak at 530.8 eV, which belongs to Cu-O bond in Cu_2O.[170] The p3 peaks at 531.3 eV on CuO and 531.8 eV on reduced CuO NW originate from surface absorbed oxygen of CuO,[173, 174] and surface absorbed oxygen of Cu_2O,[171] respectively.

The C 1s signals from both samples were collected for comparison and are shown in **Figure 4.7d**. The asymmetrical peaks are fitted from four symmetrical Gaussian peaks, x1, x2, x3, and x4. The deconvoluted peaks at 284.3 eV (x1), 285.2 eV(x2), and 288.0 eV (x4) are respectively attributed to C-sp^2, C-sp^3, and O-C-O chemical bonding.[175, 176] There is one more deconvoluted C 1s peak from reduced CuO NW at 286.3 eV (x3), corresponding to the C-O bond, which is due to the adsorbed CO on the NW surface during the reaction.[169, 175, 176] The C-O bond could represent a transition state of the CO molecules as it converts to CO_2. The presence of the C-O bond proves that the carbothermal reduction mechanism of CuO is operative on the surface of these NWs.

XPS surface analysis demonstrates that the surface is Cu_2O. No Cu signal is detected. Therefore, we can conclude that reduction of CuO can be controlled to pass through amorphous Cu_2O and then crystallize into crystalline Cu_2O. The amorphous phase crystalize starts from CuO/Cu_2O interface and the crystallization is homogeneous because thermal energy provided is isotropic. As a result, we observed these layer structures in experiments.

The amorphous phase is unstable according to thermodynamic theory. To study how quickly the amorphous phase fully crystallizes, we did TEM and HRTEM on the NWs reduced at 300 ^oC for 2 hours, and 3 hours, respectively. The TEM and HRTEM images are displayed in **Figure 4.8**.

Table 4.2. Deconvolution of XPS peaks of CuO NW and the 1 hour reduced CuO NW.

Element	Peak Position (eV)				
Cu $2p_{3/2}$	CuO NW	933.7			
	Reduced CuO NW	933.7	932.4		
O 1s	CuO NW	592.5 (p1)		531.3 (p3)	
	Reduced CuO NW	592.5 (p1)	530.8 (p2)	531.8 (p3)	
C 1s	CuO NW	284.3 (x1)	285.2 (x2)		288.0 (x4)
	Reduced CuO NW	284.3 (x1)	285.2 (x2)	286.3 (x3)	288.0 (x4)

Figure 4.8a shows TEM and HRTEM images of CuO NW reduced at 300 ^oC for 2 hours. The NW surface becomes very rough, with visible shrinkages and cracks. The HRTEM image in **Figure 4.8b** shows that part of the surface area is still amorphous. As an aid to the eye, the crystal and amorphous interface is marked with a black dashed line in **Figure 4.8b**. While the amorphous region is still around 2-3 nm thick, we find that its presence is not conformal anymore. The amorphous regions are now present as islands over a largely crystalline Cu_2O surface. An enlarged

image of the red marked region in **Figure 4.8b** is shown in **Figure 4.8c**. The lattice distance is measured to be 0.247 nm which is indexed as the (111) plane of Cu_2O and is well matched with the FFT in the inset.

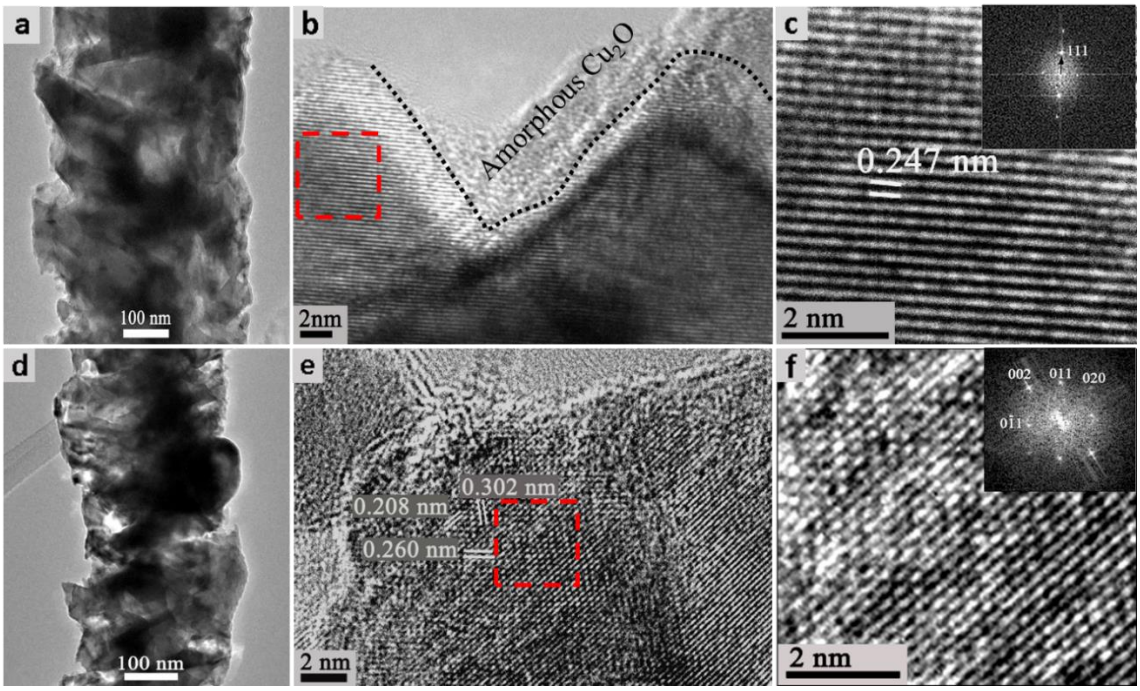

Figure 4.8. a) TEM image of CuO NW reduced at 300 ^{o}C for 2 hours, **b)** surface HRTEM image, **c)** enlarged view of red marked region of c, with the corresponding FFT in the up right corner, **d)** TEM image CuO NW is reduced at 300 ^{o}C for 3 hours, **e)** surface HRTEM image, **f)** enlarged area of red marked view of e with the corresponding FFT in the up right corner.

Finally, **Figure 4.8d** shows the NW sample carbothermally reduced at 300 ^{o}C for 3 hours. The image shows stark contrast differences between fully cracked regions and crystals which have agglomerated as a result of the phase transformation. The HRTEM image in **Figure 4.8e** demonstrates that the NW surface has fully crystallized into Cu_2O. No evidence of a surface amorphous layer can now be observed. An enlarged HRTEM image is shown in **Figure 4.8f**. The

lattice fringe distances of 0.208 nm, 0.260 nm, and 0.302 nm are attributed to the (002), (011) and $(0\bar{1}1)$ planes of Cu_2O in the [100] zone axis, respectively.

We investigated the phase transformation kinetic process, indicating that surface reactions amorphize the CuO NW surface to generate Cu_2O. The amorphous phase crystallizes for a longer reduction time. Then, we took temperature into account to see how temperature affects the CuO NW reduction. **Figure 4.9** shows a series of reduced NWs at 300 ^oC, 350 ^oC, 400 ^oC and 450 ^oC for 1 hour. Pure CuO has a very smooth surface without any particles or cracks. At 300 ^oC for 1 hour, the CuO NW surface becomes rough, forming some small features. At 350 ^oC for 1 hour,

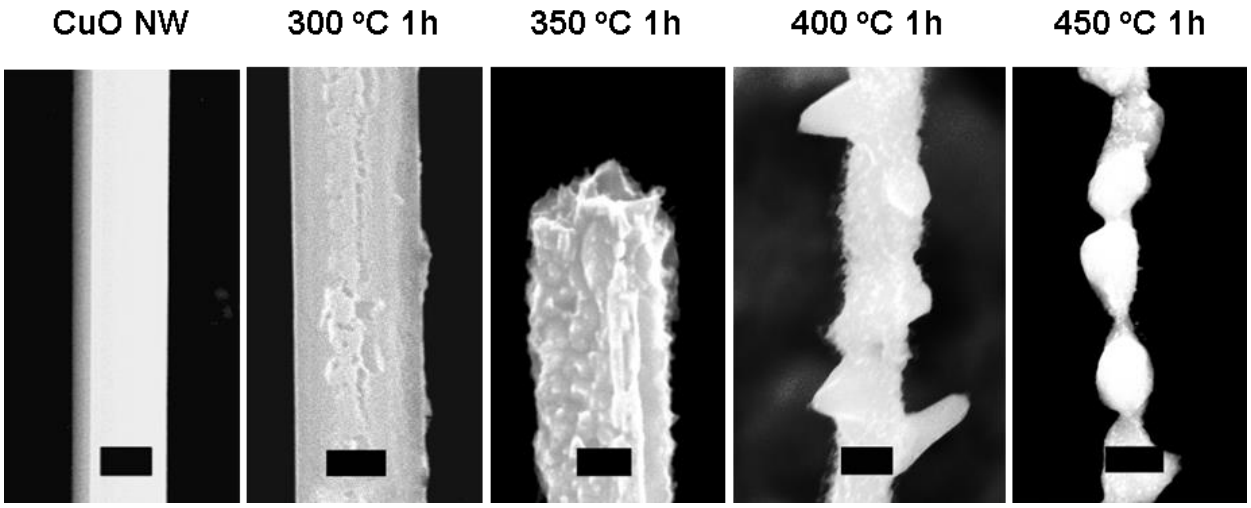

Figure 4.9. The SEM images of CuO NW and the CuO NW reduced at 300 ^oC, 350 ^oC, 400 ^oC and 450 ^oC for 1 hour. The scale bar is 200 nm.

small nodules homogeneously form on the NW surface. These small nodules grow bigger with a length around 200 nm (from NW surface to the tip of the nodules) at 400 ^oC for 1 hour. When temperature is increased to 450 ^oC, the NW grows into a chain of beads which are connected by narrow necks. A temperature higher than 450 ^oC for CuO NW reduction can break the NWs into particles, leaving no NWs on the surface of the reduced samples. Even though the NW is reduced

at 450 ^{o}C with a reduction time longer than 1 hour, no NWs are observed after reduction. As the Raman spectra in **Figure 4.2d** display, the CuO NWs are fully reduced to Cu_2O NWs for 1 hour at 400 ^{o}C. The morphology changes in **Figure 4.9** indicate that temperature significantly affects the morphology variation when the NWs are completely reduced.

4.4 Discussion

We designed experiments to study phase transformation kinetics in CuO NW to show that the phase transformation kinetics can be controlled to obtain metastable phase during phase transformation process from one stable phase to another stable phase. As a result, this controllability over phase transformation in a NW provides promising possibility for engineering a NW with tunable core and shells. By using the similar strategy, the morphology of a NW can also be modulated by varying the thermal kinetic and dynamic parameters. The mechanisms for growing these NWs with a complex structure are discussed in this section.

4.4.1 Thermodynamics of the CuO → Cu_2O carbothermal reduction

At 300 ^{o}C, we used a weak carbothermal environment in low vacuum to controllably reduce CuO NWs. The carbothermal reduction environment consists of gaseous CO which, when adsorbed on the surface of CuO NWs, causes the reduction of the CuO to Cu_2O. However, the slowing of the reduction process leads to the formation of a series of intriguing nanostructures whose surfaces show the presence of a 9-12 nm amorphous $Cu_{1.8}O$ phase before it transforms to crystalline Cu_2O with increasing reduction time. In this section, we determine thermodynamic and kinetic aspects of this phase transformation. It has been reported that during CuO reduction in CO environment, the reaction starts with CuO and ends with Cu, with an intermediate phase of Cu_2O.[177] The sequential reduction reactions are given as:

$$2CuO+CO \rightarrow Cu_2O+CO_2 \qquad (4.1)$$

ΔG_1=-48.8 kJ/mol (0.51 eV) @ 300 ^oC and -42.2 kJ/mol (0.44 eV) @ 400 ^oC

Followed by,

$$Cu_2O+CO \rightarrow Cu+CO_2 \qquad (4.2)$$

ΔG_2=-9.7 kJ/mol (0.10 eV) @ 300 ^oC and -8.7 kJ/mol (0.09 eV) @ 400 ^oC

Here, ΔG represents the Gibbs free energy change of each of the reactions, which is calculated using the *NIST* thermodynamic database.[178] One can see that within the temperature range (300 ^oC – 400 ^oC) of our experiments, the more negative ΔG for reaction 4.1 provides a thermodynamically higher driving force than reaction 4.2. Thus, in the reduction sequence of CuO → Cu_2O → Cu, reaction 4.2 is the slower rate determining step and under aggressive reduction conditions, Cu is indeed the final product.[160, 177, 179]

However, in our experiments the limited amount of CO created by the sub atmospheric (1 Torr) reduction, which as a result controls the surface reaction rate on the NW. During the CO generation process, there are also two possible reactions.[180]

$$C + 1/2O_2 \rightarrow CO \qquad (4.3)$$

ΔG_3 = -96.9 KJ/mol @ 300 ^oC, and -115.4 kJ/mol @ 400 ^oC

$$C + O_2 \rightarrow CO_2 \qquad (4.4)$$

ΔG_4 = -107.7 KJ/mol @ 300 ^oC, and -128.6 kJ/mol @ 400 ^oC.

ΔG represents the Gibbs free energy change of each of the reactions, which is calculated using the NIST thermodynamic database.[178]

These two reactions generally happen when graphite (C) is annealed with enough O.

Here, the equilibrium constant for reaction 4.3 is given as

$$k_{CO} = \frac{P_{CO}}{p_{O_2}^{1/2}} = RTln(-\Delta G_3) \qquad (4.5)$$

Similarly, for reaction 4, the equilibrium constant is given as

$$k_{CO_2} = \frac{p_{CO_2}}{p_{O_2}} = RTln(-\Delta G_4) \qquad (4.6)$$

Taking the ratio of the two equilibrium constants k_{CO} in (4.5) and in k_{CO_2}(4.6) one finds that

$$\frac{p_{CO}}{p_{CO_2}} = p_{O_2}^{-1/2} \frac{\ln(-\Delta G_3)}{\ln(-\Delta G_4)} \qquad (4.7)$$

Based on the above equation (4.7), therefore, at a given temperature, when the O pressure is low, CO prefers to form.[181] In our experiments, the graphite holder reacts with O to form a limited amount of CO. At the same time, the furnace is pumped to 1 torr continuously with a mechanical pump. This creates a rare concentration of CO and leads to the reaction limited transformation of CuO to Cu_2O.

Low temperature (300 ^oC) also significantly slows the rate for reaction 4.2 to the point where only reaction 4.1 appears to occur within the time frame of our experiments. Indeed, Cu_2O phase becomes the final product without any Cu formation, which is proved by the XPS results in **Figure 4.8**. Therefore, both limited CO and the low temperature only make the reaction 4.1 possible avoiding reaction 4.2 to generate Cu.

4.4.2 Kinetics of the CuO NW → Cu_2O NW transformation

To quantitatively study the kinetics of this transformation, we analyze the Raman data in **Figure 4.1** by integrating the Raman $2E_u$ peak of Cu_2O and Ag peak of CuO to calculate the CuO molar reduction rate. The same Raman absorption cross-section of CuO and Cu_2O makes this calculation possible.[182] The reduction rate of CuO NW is plotted in **Figure 4.10a** using the Raman data collected in **Figure 4.1**. At 400 °C, the CuO NW is completely reduced to Cu_2O within 1 hour. At 350 °C, it takes 2 hours to obtain full reduction. When the temperature is decreased to 300 °C, after 5 hours, only 82.3% of the CuO is reduced.

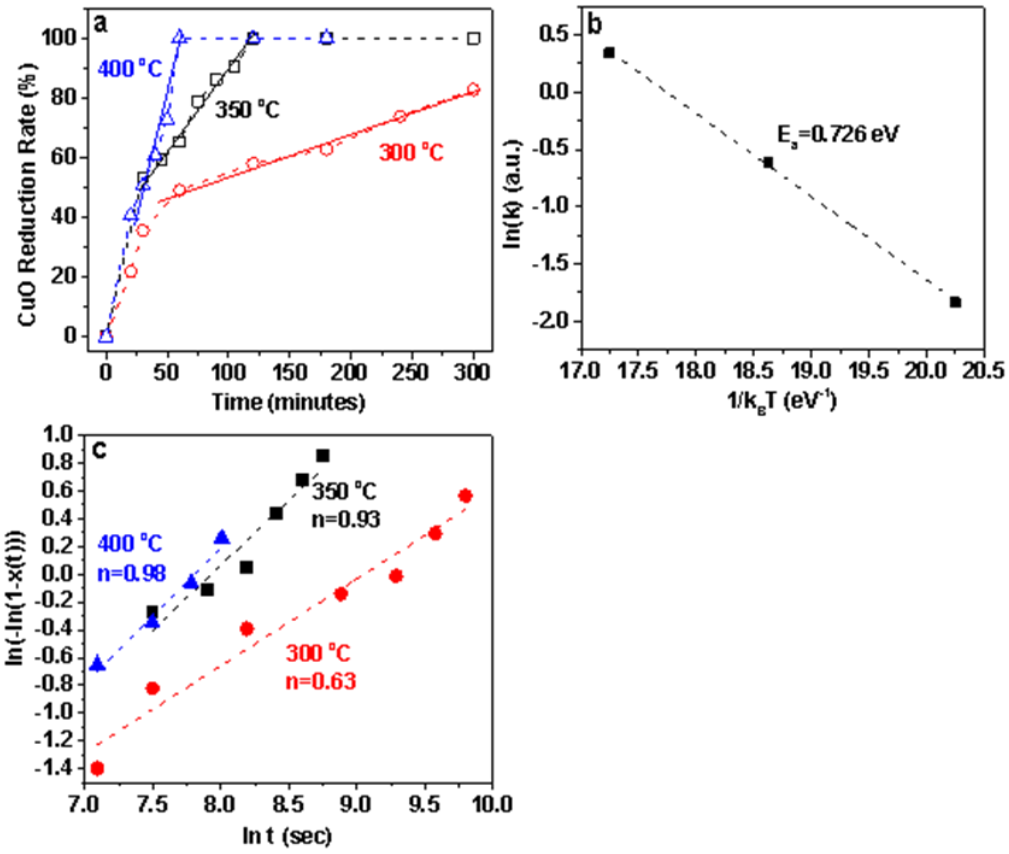

Figure 4.10. a) CuO NW reduction rate vs. reduction time, **b)** ln(k) vs. $1/k_BT$, **c)** KJMA equation fitting of the phase transformation kinetics.

The reduction reaction given by reaction 1 above shows a linear relationship between reduction rate and time at all temperatures (i.e, 300 ^{o}C, 350 ^{o}C, and 400 ^{o}C). Further, the linear regimes in reaction rates occur between 30 minutes to 5 hours, 45 minutes to 2 hours, and 20 minutes to 1 hour for the three temperatures, respectively. The linear relationship indicates that the surface reaction follows a zeroth order of reaction kinetics because the number of adsorbed CO controls the reaction rate, no matter how many O atoms diffuse to the surface.[183] This is in line with the thermodynamics of limited CO reduction conditions as explained in the previous section.

The above results imply that under limited CO supply, the out-diffusion of O should build up on the surface. Indeed, EDX line scan provides evidence that the surface amorphous layer is O rich with respect to Cu_2O i.e., as $Cu_{1.8}O$. Because of the linear zeroth order reaction kinetics, the kinetic relationship can be expressed as d[CuO]/dt=-k, where [CuO] is the CuO molar concentration, the negative sign is for the reduction and k is the reduction reaction rate constant.

According to the Arrhenius equation, $k \propto e^{-\frac{E_a}{k_B T}}$, where k_B is Boltzmann constant and E_a is the CuO to Cu_2O reduction activation energy in CO ambient. E_a is determined to be 0.73 eV by linearly fitting *ln(k)* as a function of $1/k_BT$ in **Figure 3.10b**. This activation energy is 44% lower than the activation energy of 1.10 eV needed to reduce polycrystalline CuO thin films to Cu_2O in vacuum.[184] This could be due to the high surface energy of single crystalline CuO NW and the fact it has no grain boundaries to move during the phase transition. The presence of CO could alter this value as well as it is a significantly stronger reductant than vacuum.

Finally, to understand the solid-state phase transformation mechanism in CuO NWs, we analyzed the kinetics by the KJMA equation[183, 185, 186] given as:

$$\ln(-\ln(1-x(t))) = lnk_A + n \times \ln(t - t_0), \qquad (4.8)$$

Where, *x(t)* represents the reduction rate of CuO at time *t* and is described by Cu_2O phase fraction in CuO NW, k_A is the Avrami rate constant and *n* is the Avrami exponent which is indicative of the phase growth mode. Also, t_0 is the incubation time for phase transition, which is set to 0 because no induction time has been observed in our experiments and other published work.[36, 177, 179, 187] We note that the CO reaction rate constant *k* obtained earlier is different than the Avrami rate constant k_A. Whereas *k* represents the rate constant of the chemical reaction 1, k_A represents the rate at which the solid phase CuO transforms to Cu_2O. Solid-state processes of germinating nuclei followed by growth govern Avrami rates.

Table 4.3. Avrami exponent (n) and Avrami rate constant (k_A) are extracted from linear fitting of the experiment data with Avrami equation.

T (^{o}C)	n	k_A
300	0.63	7.23×10^{-3}
350	0.93	6.65×10^{-5}
400	0.98	4.95×10^{-4}

In **Figure 4.10c**, *ln(-ln(1-x(t)))* linearly depends on *ln(t)* regardless of the annealing temperature. The *n* and k_A extracted from linear fitting are listed in **Table 4.3**. We obtain *n* at 350 ^{o}C and 400 ^{o}C are 0.93 and 0.98, respectively. The *n* value is close to 1 indicating that temperatures $\geq$ 350 ^{o}C, the phase transformation is controlled by diffusion in a cylindrical geometry.[188] Generally speaking, k_A increases with increasing temperature. The k_A at 300 ^{o}C is two orders higher than k_A at 350 ^{o}C and one order higher than k_A at 400 ^{o}C, respectively, indicating that the phase transformation from CuO to Cu_2O do not pass through direct pathway.

On the other hand, the *n* value at 300 ^{o}C is only 0.63 which is close to 0.5, indicating a possible diffusion controlled phase transformation but one, which is controlled by planar diffusion

geometry.[188] This result provides another evidence that the surface reduction reaction is controlled by the limited number of CO. The out-diffusing flux of O reaches the surface in sufficient quantity but has to diffuse on the NW surface to find a site which has a co-adsorbed CO molecule for the reduction reaction to occur. Therefore, the O flux and the slow surface reaction creates an O-rich (w.r.t. Cu_2O), $Cu_{1.8}O$ phase which is detected by the STEM-EDX in **Figure 4.5b**.

4.4.3 Surface amorphization mechanism

We now explain the presence of the amorphous $Cu_{1.8}O$ layer. We propose that the appearance of the transient amorphous $Cu_{1.8}O$ phase is due to Ostwald-Lussac's law. According to this law, the pathway to a final, stable, crystalline phase may pass through a series of less stable and intermediate phases.[189] The relationship is schematically shown in **Figure 4.11** for crystalline CuO → amorphous $Cu_{1.8}O$ → crystalline Cu_2O. The intermediate phase can be kinetically stabilized under two conditions: 1) by having large energetic barriers for the formation of the most stable phase (pathway 1) and, 2) by having small energetic barriers to the formation of the intermediate phase (pathway 2a and 2b). The phase stabilization then is a kinetic effect due to the differential rates of the transformation processes between starting, intermediate and final phases.

For the case of the copper-oxide system, the free energy of formation (ΔG_f), i.e., the absolute value on the Y-axis in **Figure 4.11**, for CuO and Cu_2O is given to be -4.6 kJ/mol and -40.5 kJ/mol at 300 ^oC, respectively.[178] If amorphous $Cu_{1.8}O$ phase forms before crystalline Cu_2O phase appears, the rate of formation of the amorphous phase should be much higher than the rate of formation for the crystalline phase, implying that the energy barrier for crystalline CuO → amorphous $Cu_{1.8}O$ is low (pathway 2a in **Figure 4.11**), while the crystalline CuO → crystalline Cu_2O is high (pathway 1 in **Figure 4.11**).

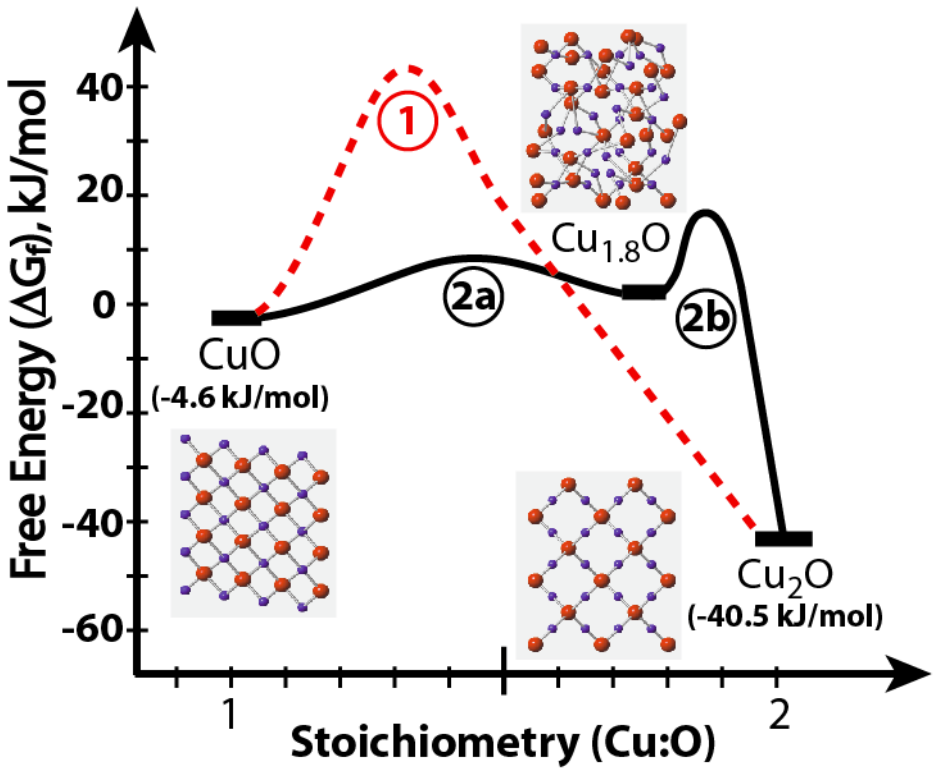

Figure 4.11. Free energy landscape of the copper oxides as a function of their stoichiometry. According to Ostwald-Lussac's law, the transition from crystalline CuO NW to crystalline Cu_2O NW passes through the amorphous $Cu_{1.8}O$ phase (**pathway 2a** and **2b**), even though the amorphous phase may have a higher free energy of formation than CuO. The activation energy of the amorphization process may be negligbly small (**pathway 2a**) as compared to the Cu_2O formation (**pathway 1**). However given enough time, the $Cu_{1.8}O$ eventually crystallized to Cu_2O (**pathway 2b**).

In CuO NW reduction experiments, the reaction 1 happens on the surface of single crystalline CuO NWs and the reduction rate is controlled by the concentration of adsorbed CO molecules. The reduction reaction rate can be controlled by the reduction temperatures. Lattice O is taken away by reacting with CO and pumping out as CO_2, resulting in collapse of monoclinic crystal structure of CuO. The formation of disordered Cu_2O phase from the disordered CuO phase

requires much less energy than the energy needed for a crystalline Cu_2O phase. Thus, this transient amorphous appears and is observed before it finally transforms to a stable crystalline Cu_2O phase. The phenomena provide strong evidence that Ostwald-Lussac's law exists and the predicted transient phase can be observed during the phase transformation in a NW.

At 400 ^oC, the reduction rate becomes much quicker than at 300 ^oC. The formation of nodules on the Cu_2O NWs is obtained by fully reducing CuO NWs. Continuous reduction of these Cu_2O NWs can only causes a periodicity and morphology change of the nodules without losing the NW shape. Although the Cu_2O NWs do not get further reduction, the bottom CuO film is reduced for longer reduction time, indicating that the O diffusion from bottom CuO to Cu_2O NWs significantly affect the NWs' morphology evolution.

4.5. Conclusions

In this chapter, we have systematically studied the phase transformation kinetics in CuO NWs in a reduction CO ambient produced by graphite holder during the heat treatment. The reduction reactions are localized on the surface of CuO NWs are dominated by CO because of the limited numbers of CO produced during the reduction, which is proved by the linear relationship between CuO reduction rate vs. reduction time.

The moderate reduction reactions controlled by CO slow the phase transformation kinetics down, making the transient amorphous Cu_2O phase a long lived stable phase on surface of CuO NWs after 30 minutes reduction at 300 ^oC. The amorphous phase crystallizes and remains an amorphous layer about 2-3 nm thick on CuO/Cu_2O core/shell NWs' surface after 1 hour reduction. For even longer reduction time to 3 hours, the amorphous phase completely transformed to crystalline Cu_2O.

Due to the surface phases evolution from crystalline CuO to amorphous Cu_2O and then to crystalline Cu_2O, the morphology the reduced NWs also changes with reduction. The reduced NWs keep the vertical NW shape when conformal amorphous Cu_2O grows on the surface of CuO NWs. Once the amorphous phase is no more a continuous film or fully crystallizes, the NWs lose their vertical shape and become curved. Meanwhile, cracks and shrinkages are observed on the reduced NWs.

The kinetics of the phase transformation is analyzed within the framework of the KJMA equation. A surface diffusion mechanism is found to regulate the phase transformation process, where the O has to find a favorable site with limited CO co-adsorbed, for the reduction to occur. The CuO NW phase transformation activation energy is extracted from the experiments with a value of 0.73 eV.

The amorphous phase is found to be defective, which is characterized by EDX line mapping, showing an O rich $Cu_{1.8}O$ phase. The observation of the amorphous phase during phase transformation can be explained by Ostwald-Lussac's law which states that the pathway to a final, stable, crystalline phase may pass through a series of less stable, intermediate phases.

The techniques to simultaneously grow amorphous coating layer on surface of vertical NWs provide a new method to synthesize controllably CuO/Cu_2O core/shell NW arrays with desirable structures for photovoltaic applications. Structures like the one presented in this chapter can form the basis of novel energy harvesting and storage devices and may be useful for catalytic reactions as well.[164]

Chapter 5 Optoelectronic properties of ZnO coated CuO NWs

5.1 Introduction

The importance of ZnO surface in controlling semiconducting properties has been studied for a long time.[190] Especially, when nanostructured ZnO have been widely used, high surface/volume ratios cause the surface defects to play an important role in controlling properties.[191] Surface defects dramatically affect the conductance when the surface to volume ratio is high. The adsorption and desorption of gas molecules can control the conductivity of ZnO, which is used to make gas sensors because adsorbed molecules accept electrons from ZnO to deplete the surface causing a reduction of conductivity.[191] A desorption of molecules donate electrons to the ZnO surface leading to an increase in the conductivity. Therefore, surface defect study is of great meaning to synthesize sensitive sensors by using these low cost CuO and ZnO.

In this chapter, we employ surface engineering strategies to synthesize optoelectronic materials with different performances by modifying the surface defect density. Single crystalline CuO NWs with a low surface defect density synthesized by a thermal oxidation method were deposited with 1 nm, and 10 nm ZnO, respectively. 1 nm ZnO was found to have a surface defects density three times higher than 10 nm ZnO. As a result, the photocurrent decay time of CuO NW-1 nm ZnO is 4 times longer than the CuO NW-10 nm ZnO and two times longer than CuO NWs. Similar results were reported, indicating that an increase of surface defect density of ZnO nanorods greatly improved the catalytic performance of methylene blue.[192] What is more, the carrier conductive mechanism is also affected by the surface defects.

To get better understanding of the CuO NWs synthesized by thermal oxidation for various optoelectronic applications, the photocurrent decay processes of CuO NWs modified by thin ALD

ZnO films are investigated. The photocurrent decay time can be controlled by the density of O vacancies.

5.2 Experiments

CuO film was made by thermal oxidizing high purity Cu foils at 500 ^{o}C for 1 hour under 1 torr pumped by a mechanical pump (Edwards RV12). The Cu foils were etched in 1 mol/L HCl to remove the native oxides, cleaned with deionized water clean, and dried by the air flow. CuO NWs were thermally grown on high purity Cu foils at 500 ^{o}C for 30 minutes in air. These wires grow to a height of 1-2 μm with an average diameter of 230 nm and a density of 2.1×10^{8} NWs cm^{-2}.[161, 193] ALD ZnO was carried out at 150 ^{o}C using DEZ and H_2O as precursors. The growth rate was measured to be 0.17 nm/cycle.[194] Using 5 cycles of ALD, ~ 1 nm of ZnO was deposited on CuO NWs. Using 63 cycles of ALD, ~ 10 nm of ZnO was deposited on CuO NW. CuO NWs are high quality single crystalline with few surface defects. The surface defect density can be significantly changed by depositing ZnO with different thicknesses. All the ZnO deposited by ALD used Zn terminated surfaces.

For photoconductivity measurements, silver paste (Circuit Writer, CAIG Labs) was applied on to CuO NW film to define circular side electrodes, creating a channel ~ 2 mm long. The side electrode architecture allows one to test the vertically standing CuO NWs present in the channel between the electrodes.[7, 195, 196] Transmission electron microscopy and high resolution transmission electron microscopy (HRTEM) images are taken by JEOL 2100F with an operating voltage at 200 KV. TEM samples are made by dropping NW ethanol solution to 300 mesh carbon type-B copper grids. Fast Fourier Transform (FFT) of HRTEM images and additional measurements are conducted by Gatan software. The surface morphology of CuO foils was characterized by FE-SEM (JEOL-7001LVF) operated at 15 kV. The epitaxy growth of CuO and

ZnO crystal structure is made by crystal maker software. A JANIS probe station (ST500-1-2CX) connected to a Keithley 2400 was used to measure photoresponse from 80 K to 320 K with a temperature step of 40 K, respectively. The steady state, room temperature photoluminescence (PL) measurements of the samples are collected using He-Cd laser (λ = 325 nm) as excitation source with 1 nm resolution. An Edmund Optics® (MI150) lamp is used for sample illumination. Spectral light intensity is shown in **appendix Ⅲ**. The lamp only provides light in visible light range from 450 nm to 750 nm to avoid UV-light excitation. The overall light intensity is measured to be 5.7 mW/cm^2. The spectral intensity is negligible below 450 nm (2.76 eV). X-ray photoelectron spectroscopy (XPS) was conducted using the PHI 5000 VersaProbe II from Physical Electronics Inc., using Al Kα X-ray source with beam energy 1486.6 eV. Angular XPS was done by mounting samples on a 4 point holder with an angle profile from 15º to 75º in a step of 15º.

5.3. Results

We systematically studied the conductivity of ALD ZnO films with a thickness profile and found that surface defects dominate the conductivity with a film thickness below 12.6 nm and bulk conduction becomes dominant with a film thickness thicker than 12.6 nm. The surface conductivity of ZnO films are shown in **appendix Ⅳ**. The thinner the film, the denser the surface defects. 5.4 nm ZnO has a surface defect density 2.6 times higher than the surface defect density on 20 nm ZnO films. Once the film thickness reaches 20 nm or thicker, more electrons contributed to the conductivity through the thin film other than the surface defects. As a result, the conductivity significantly increases when increasing the thickness.

To understand how these surface defects affect the electron excitation and recombination, we deposited the thin ZnO films to single crystalline CuO NWs to study the photocurrent

recombination mechanism by modulating the NW surface with different densities of surface defects. The ALD ZnO film thicknesses are controlled below 10 nm because the surface defects dominate the properties of the thin films in this thickness scale. This study will shine light on the novel optoelectronic devices by controlling the electrons excitation and recombination processes.

5.3.1 Microstructure of CuO-ZnO nanocomposites

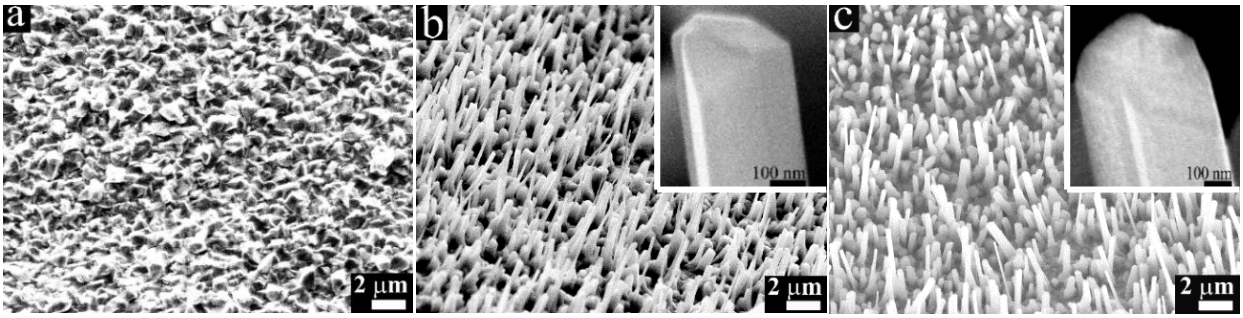

Figure 5.1. SEM images of **a)** CuO film, **b)** CuO NWs with an enlarged NW morphology on the right corner, **c)** CuO NWs – 10 nm ZnO with an enlarged NW morphology on the right corner.

Figure 5.1a shows the surface of CuO film prepared by oxidizing pure Cu foils at 500 ^{o}C for 1 hour under 1 torr. There is no growth of CuO NWs on the CuO thin film's surface. **Figure 5.1b** shows the top surface SEM image of CuO NWs synthesized by oxidizing Cu foils at 500 ^{o}C for 30 minutes in air. The density and length are 2.18×10^{8} /cm^{2} and 1-2 μm long, respectively. The CuO NW morphology is displayed on the upper right copper. To modify the CuO NW surface, we deposited 1 nm and 10 nm ZnO on CuO NWs, respectiviely. The surface SEM image the 10 nm ZnO coated CuO NWs is shown in **Figure 5.1c** and the NW SEM image is shown on the upper right corner. NW surface is conformally coated with ZnO.

The cross-section SEM images of CuO film and CuO NWs are shown in **Figure 5.2**. The CuO film thickness is around 540 nm growing on 3.1 μm thick Cu_2O film (**Figure 5.2a**). The CuO NW sample shows 1-2 μm long CuO NWs on 540 nm CuO thin film. Below the CuO film, the

Cu_2O film displays a thickness of 5.4 μm (**Figure 5.2b**). The CuO NWs grown on the surface of the CuO film in **Figure 5.2b** is only dthe ifference between the CuO film samples and the CuO NWs samples.

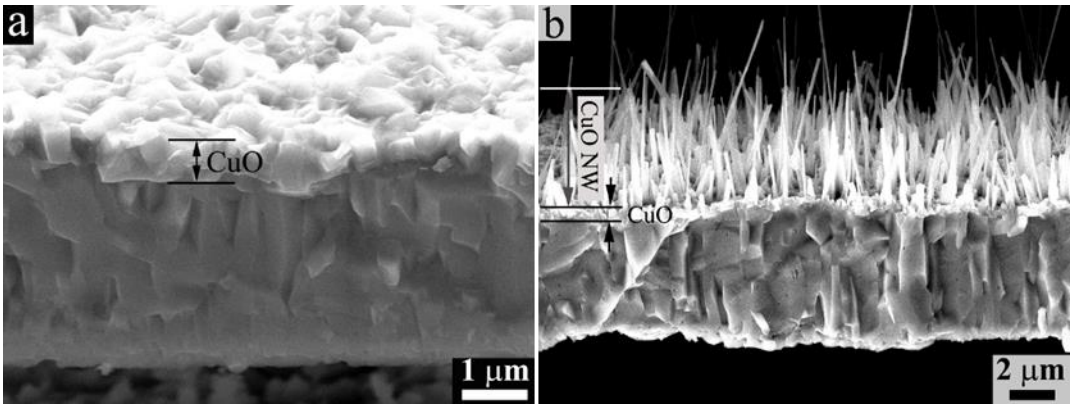

Figure 5.2. a) Cross-section images of a CuO film, **b)** CuO NWs on CuO film. Both CuO films show a thickness of 540 nm.

Figure *5.3.*5.3**a** and **b** show the TEM and HRTEM images of the CuO NW, respectively. The CuO NW is single crystalline with smooth surfaces. The exposed planes on the CuO NWs are $\{\bar{1}11\}$ family of planes of the monoclinic phase. An inter-planar distance of 0.252 nm as obtained from the Fast Fourier Transform (FFT) electron diffraction pattern of the HRTEM image, is in line with literature values.[65]

In **Figure *5.3.*5.3c** and **d**, the CuO NW–1 nm ZnO shows a nanocrystalline, roughened surface. Contrary to how ALD films are expected to deposit, a nucleation and growth mechanism could be active for ZnO deposition over CuO NWs. This results in an 'incubation' period for the ALD film, before continuous layer-by-layer growth occurs.[197-199] The ZnO forms nanocrystalline nuclei on the surface of CuO NWs as is evidenced by the contrast differences in the TEM image in **Figure *5.3.*5.3c** and also our previous data.[200] The HRTEM image of CuO NW–1 nm ZnO is

shown in **Figure *5.3*.5.3d**. The nanocrystalline conical facets are characteristic of the ZnO {10$\bar{1}$1} surfaces.[201, 202] The exposed plane is verified to be (10$\bar{1}$1). The interplanar distance is 0.247 nm. Thus, an epitaxy is established between the CuO NWs and the ALD ZnO as CuO ($\bar{1}$11) || ZnO (10$\bar{1}$1) in **Figure 5.3g**.[203, 204]

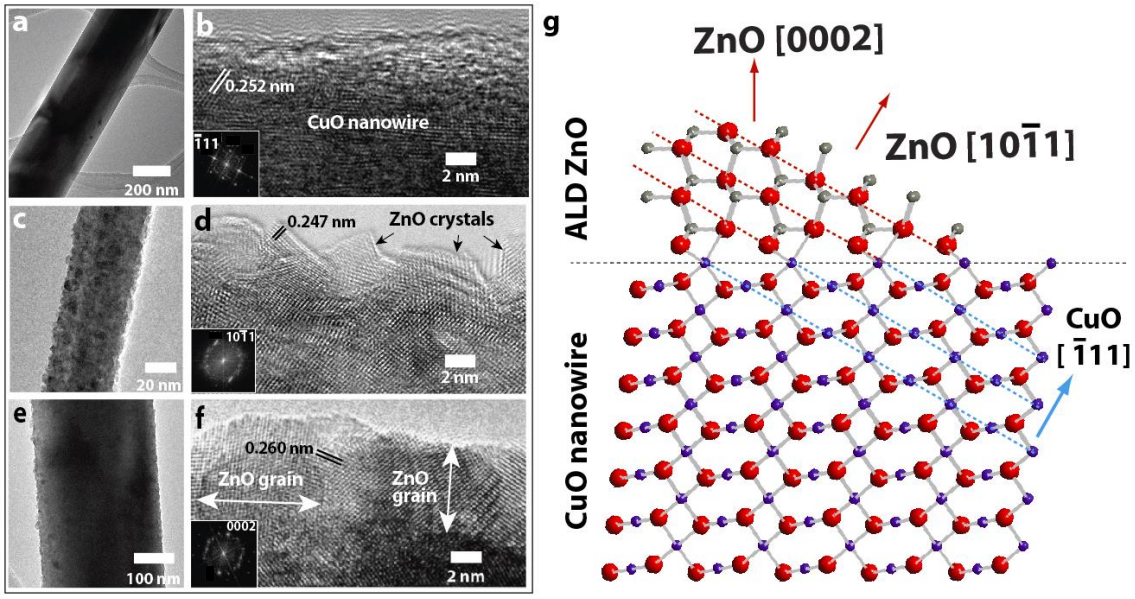

Figure 5.3. a) TEM image of CuO NW and **b)** HRTEM image of CuO NW with fast Fourier transform (FFT electron diffraction(ED) of the image in inset. **c)** TEM image of CuO NW - 1 nm ZnO. **d)** HRTEM image of CuO NW – 1 nm ZnO showing well-facetted, ZnO nanocrystals (FFT ED in inset). **e)** TEM of CuO NW - 10 nm ZnO on the surface. **f)** HRTEM image showing merged ZnO crystals (FFT ED in inset). Note: Different TEM magnifications in a,c and e are used to elucidate surface features on the NWs. **g)** The epitaxy between the CuO NW and the ZnO is schematically shown above.

Facets observed in **Figure 5.3d** can be compared with the above schematic to understand the spatial orientation of the ZnO nanocrystals on the surface of CuO NW. We note that the ZnO{10$\bar{1}$1} is polar[202] and unstable[201] with a highly activated photocatalytic surface.[205]

In **Figure *5.3.*5.3e** and **f**, the TEM and HRTEM images for CuO NW – 10 nm ZnO are shown. The ZnO is smoother as it continues to deposit on the CuO NW. The ZnO is oriented along the [0002] direction with an inter-planar distance of 0.260 nm (see FFT in **Figure *5.3.*f**). The ZnO {0002} is a polar surface.

To show the surface difference, XPS were conducted on CuO NWs, CuO NWs-1 nm ZnO, and CuO NWs-10 nm ZnO samples. Survey spectrum for the three samples are shown in **Figure 5.4a**. CuO NWs only displays Cu, O and C elements without showing any impurities. CuO NWs-1nm ZnO presents Cu, Zn, O, C elements, indicating that both ZnO and CuO are detected. CuO NWs-10 nm ZnO can only detect Zn, O and C elements because ZnO thickness is thicker than the XPS detection depth of 10 nm.

O 1s peaks for the three samples are shown in **Figure 5.4b**. O 1s peak is deconvoluted into two peaks at 529.5 eV and 531.3 eV, which are attributed to Cu-O bond of CuO and oxygen vacancy of CuO, respectively.[172-174] The O 1s peak of CuO NWs-1 nm ZnO can also be deconvoluted into two peaks 529.5 eV (Cu-O bond) 531.6 eV (O vacancy of ZnO),[206] respectively. Two deconvoluted peaks from CuO NWs-10 nm ZnO at 529.9 eV and 531.4 are attributed to Zn-O bond of Zn and O vacancies, respectively. To quantitatively characterize the surface defects of modified CuO NWs, we calculated the ratio of V_O''/Zn-O or V_O''/Cu-O using XPS integrated peak intensity from O 1s deconvoluted peaks, which are 0.6 for CuO NWs, 1.6 for CuO NWs-1 nm ZnO, and 0.9 for CuO NWs-10 nm ZnO. Apparently, ZnO coated CuO NWs show a much higher density of O vacancies. Especially for CuO NWs-1nm ZnO samples, a 2.5 times higher density oxygen vacancies is obtained, compared with CuO NWs.

5.3.2 Optical Characterization

Figure *5.5.* **5.5** shows PL spectrum of CuO NW (bottom), CuO NW - 1 nm ZnO (middle) and CuO NW - 10 nm ZnO (top). A full description of PL has been described elsewhere.[200] Here, we concentrate on features relevant to the photoresponse behavior. For CuO NW, a broad emission peak from 400 to 700 nm, belonging to the intra band transitions in CuO, is seen.[207] After ZnO deposition, both 1 nm and 10 nm ZnO show a near band emission [208] at 381 nm corresponding to the band gap of ZnO (3.25 eV). Broad defect related peaks appear in the green to red range.[42, 43, 209]

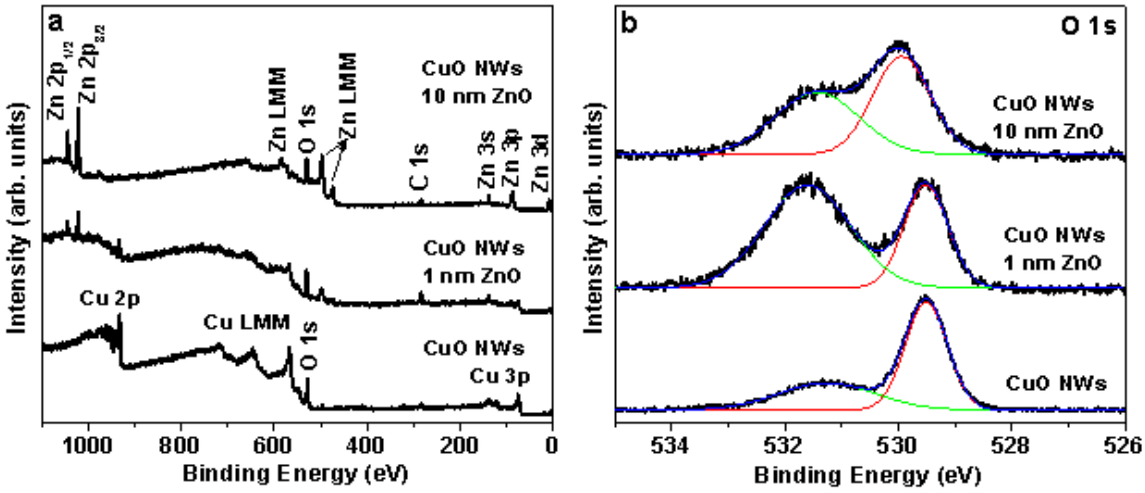

Figure 5.4. XPS of CuO NWs, CuO NWs-1 nm ZnO, and CuO NWs-10 nm ZnO: **a)** survey spectrum, **b)** O1s.

For the CuO NW - 1 nm ZnO, the green defect band is centered at 509 nm (2.43 eV). The green defect band is attributed to Zn vacancies (V_{Zn}) or O antisite (O_{Zn}) defects.[209] The intensity ratio of near band to defects emission (I_{NBE}/I_{defect}) is 0.25. Based on Shalish et al., we conclude that the 1 nm ZnO has a high concentration of surface defects.[210]

For the CuO NW - 10 nm ZnO, the defect band stretches from green to red suggesting bulk defects are introduced due to increasing thickness of ZnO. The bulk defects are related to singly and doubly charged oxygen vacancies.[209] A stronger NBE is observed since the film is thicker. An I_{NBE}/I_{defect} = 0.78 indicates the reduced role of the surface of ZnO.[210]

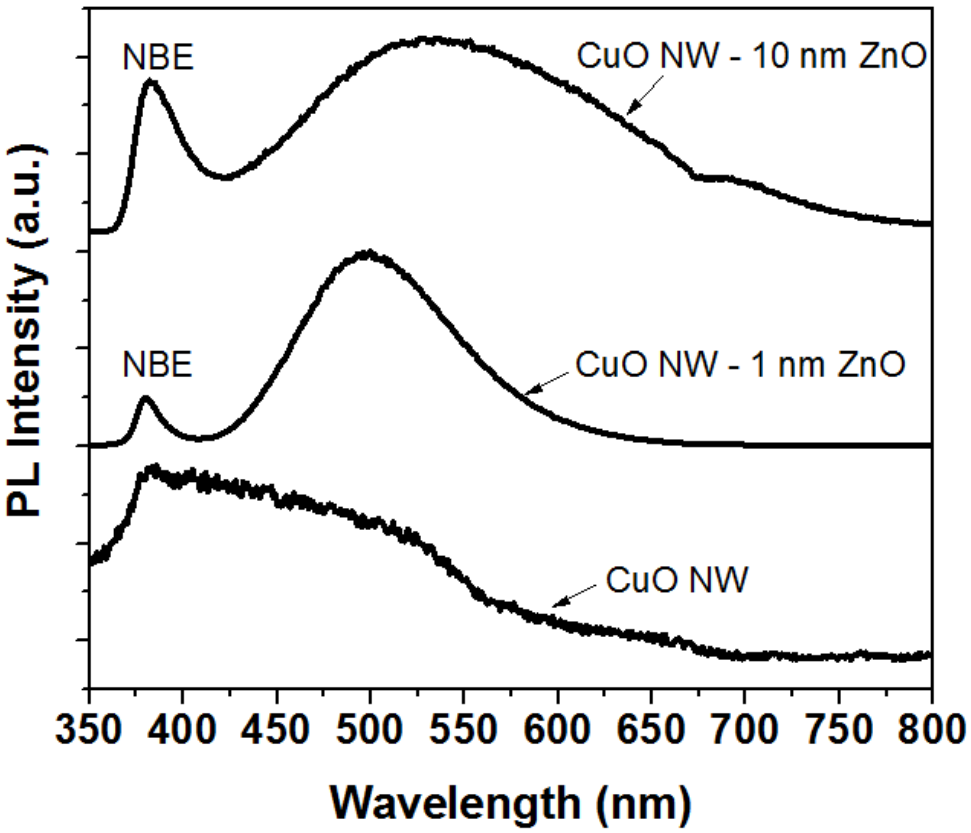

Figure 5.5. Photoluminescence (PL) data of CuO NW (bottom), CuO NW – 1 nm ZnO (middle) and CuO NW – 10 nm ZnO (top).

5.3.3 Photoconductivity Measurements

In **Figure *5.6.* .6a**, the photoresponse for CuO film, CuO NW, CuO NW – 1 nm ZnO and CuO NW – 10 nm ZnO at 80 K, $2x10^{-5}$ Torr is shown. The photoconductivity is measured at 0.1 V and light 'ON' and 'OFF' responses, each 30 seconds long. Since we compare and contrast time

constants for the photocurrent decay for the samples, we plot normalized the currents, offset for clarity. In these experiments, we aimed to study the effect of surface defect density on the photocurrent decay process to provide a new method to fabricate optoelectronic devices by engineering surface structure with controlling surfaces defect densities.

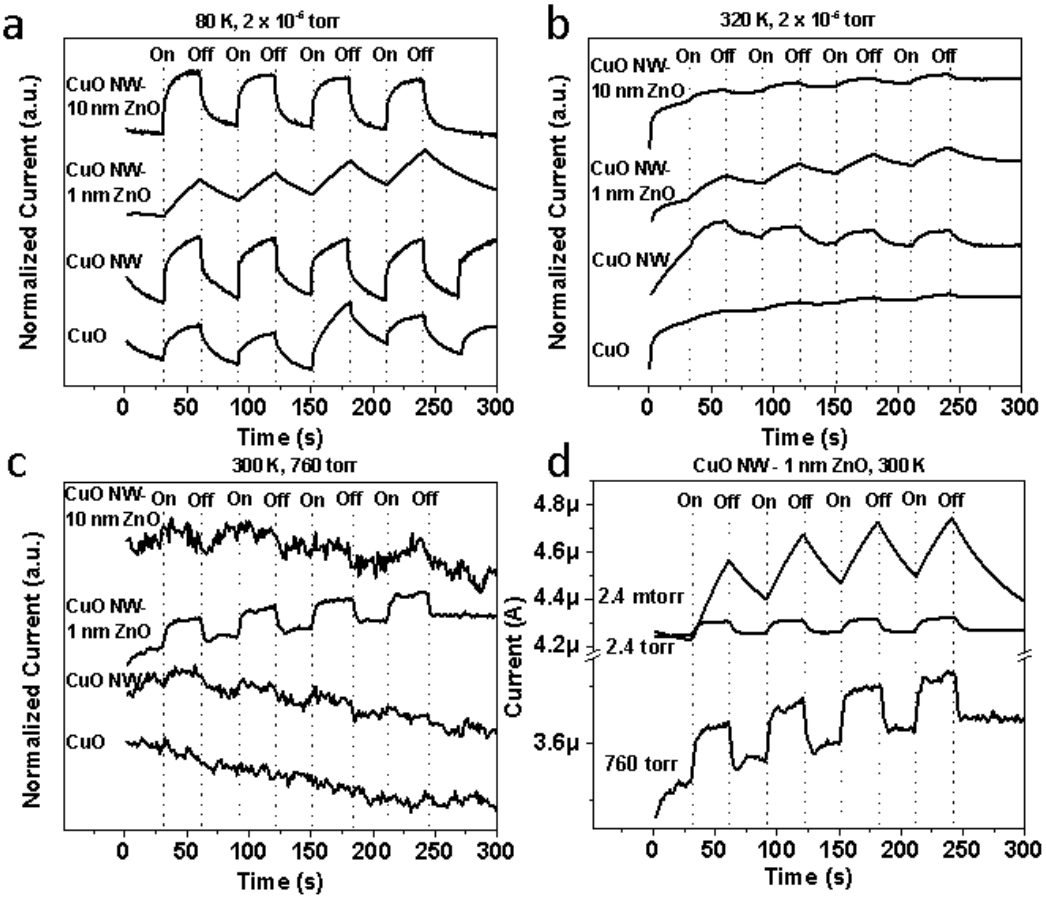

Figure 5.6. a) Photoresponse at 80 K, $2x10^{-5}$ Torr and **b)** at 320 K, $2x10^{-5}$ torr for CuO, CuO NW, CuO NW – 1 nm ZnO and CuO NW – 10 nm ZnO. **c)** The photoresponse at 300 K, 760 torr shows measurable photoresponse from the CuO NW – 1 nm ZnO only. **d)** Photocurrent response of the CuO NW – 1 nm ZnO as a function of three different pressures at 300 K.

A CuO thin film sample shows a slow photocurrent decay after illumination. In contrast, the CuO NW shows an initial drop in photocurrent, with a time constant 0.63 seconds, followed

by a slow decay curve.[211] This quick photocurrent drop is attributed to the fast carrier recombination across the band gap of CuO followed by a slower surface trap related decay process. For the slow decay process, an exponential decay curve, $I = I_o \exp(-\frac{t}{\tau})$ is used to fit the data. Here I_o and τ represent dark current and decay time constants, respectively.[212, 213] We find a single exponential function to satisfactorily fit all data indicating a single recombination mechanism may be prevalent in the devices. For CuO thin film, CuO NW, CuO NW – 1 nm ZnO and CuO NW – 10 nm ZnO, τ varies as10.3 ± 1.45, 15.8 ± 3.0, 42.1 ± 8.5 and 4.8 ± 0.7 seconds, respectively. Thus, the CuO NW – 1 nm ZnO has the longest decay time. For comparison, the only difference between the CuO film sample and the CuO NW samples is that the CuO NW sample has dense CuO NWs growing on the CuO thin film so that the decay process difference in **Figure 5.6a** is coming from the CuO NWs. The decay difference between CuO NW and CuO NW – ZnO should be from the as-deposited ZnO. Thus, these differences shown in the decay process indicate that a modification of the surface of CuO NWs by depositing ZnO nanoparticles and thin films significantly changes the photocurrent decay processes as we see in **Figure 5.6a**.

The effect of raising temperature can be seen in **Figure *5.6.*** 5**.6b**. Here, the photoresponse in terms of normalized current (offset for clarity) is shown at 320 K, 2×10^{-5} Torr. The τ is given as 5.0 ± 0.9, 9.7 ± 1.3, 18.7 ± 2.82, 4.5 ± 0.6 seconds for CuO film, CuO NW, CuO NW–1 nm ZnO and CuO NW–10 nm ZnO, respectively. Even though the higher temperature reduces τ, CuO NW–1 nm ZnO still shows the longest decay times, twice higher than the τ of CuO NW. The shape of the decay curve does not have obvious changes, compared with it at 80 K.

In **Figure *5.6.*** 5**.6c**, the effect of raising pressure to 760 Torr on the photocurrent decay can be readily observed. The normalized current (offset for clarity) is shown for samples tested at

300 K, 760 Torr (ambient). The only significant photoresponse comes from the CuO NW – 1 nm ZnO. In contrast, τ is much shorter, ~ 2.7 ± 1.1 seconds.

In **Figure 5.6d**, we show variation of measured current in CuO NW – 1 nm ZnO as a function of pressure. Two points need be noted. First, the dark, baseline current increases with decreasing pressure, reminiscent of an *n*-type behavior even though CuO is known to be *p*-type. Second, τ increases with decreasing pressure (2.7 ± 1.1 seconds at 760 Torr, 5.1 ± 0.9 seconds at 2.4 Torr, 22.4 ± 2.1 seconds at 2.4 x 10^{-3} Torr).

Temperature based photocurrent-time measurements on CuO NW – 1nm ZnO are shown in **Figure 5.7a** from 80 K to 360 K with a step of 40 K. The shape of the decay curve does not have conspicuous changes with an increase of the measurement temperature. The time constants extracted by one exponential fitting are also plotted with respective to the temperature in **Figure 5.7b**. Below 120 K, the time constants stay round 48.9 s. After 120 K, the time constant linearly decreases with temperature. The results indicate that the trapped holes inside of CuO NWs cannot be excited by thermal energy with a temperature below 120K. The thermal energy starts to release the trapped holes to valance band, contributing to the recombination after 120 K.

In **Figure 5.7c**, we plot τ vs. $1/k_BT$. The graph shows the temperature effects on the relaxation process of CuO NW – 1 nm ZnO nanocomposites. The relationship can be depicted by the Arrhenius law given by: $\tau = \tau_0 e^{E_a/k_BT}$.[214] The E_a is determined to be 13.3 meV, indicating that a temperature higher than 154 K can thermally excite the holes, contributing to the conduction. With increasing the temperature, thermal excitation become more and more prominent. When temperature is up to 360K, thermal excitation dominates the holes exciations, leading to unvisible

light response. Thus, thermal excitation dominate the excitation of the trapped holes so that the excitation and recombination processes compensate each other.

5.4. Discussion

Conductivity in ultra-thin film, especially with a thickness below 12.6 nm, is significantly affected by the surface defects. The surface defect density decreases with the surface to volume ratio, leading to a decrease of the conductivity (**appendix Ⅳ**). However, when the film thickness goes higher than 20.0 nm, surface effects on the conductivity becomes negligible.

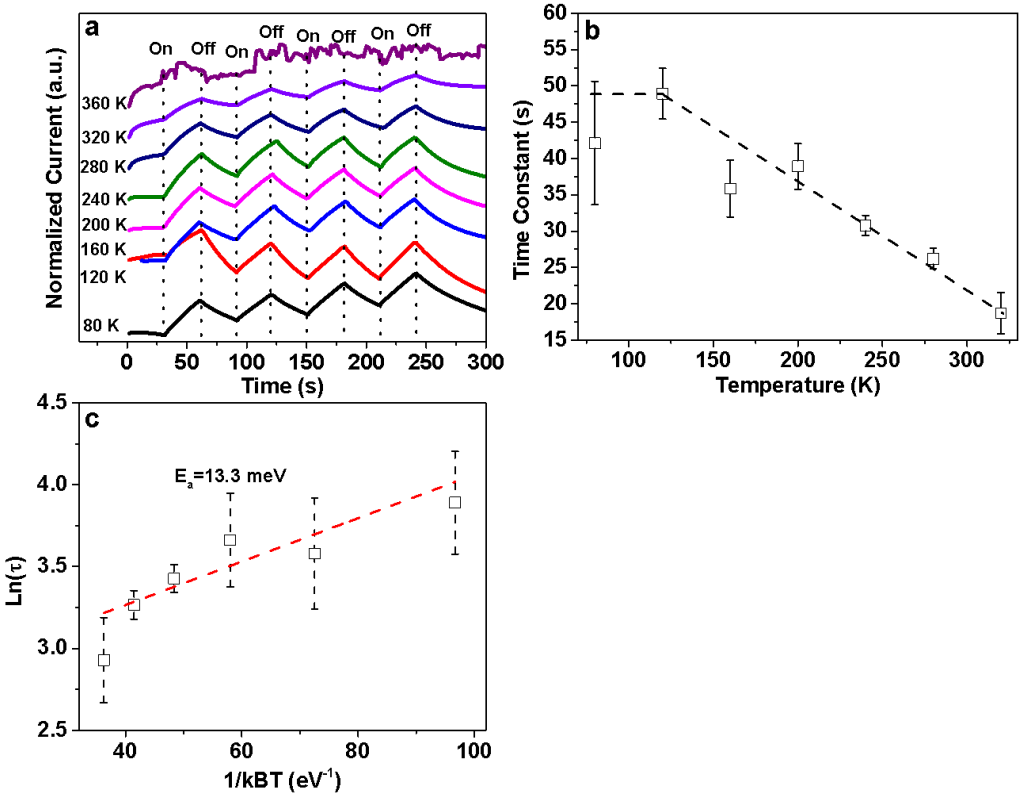

Figure 5.7. CuO NW – 1 nm ZnO, **a)** temperature dependent photoresponse, **b)** time constant vs. temperature, **c)** Ln(τ) vs. $1/k_BT$.

To understand the effect of surface defects on the electron excitation and photocurrent decay processes is to shine light on designing optoelectronic devices with desired properties by controlling surface defects. We coated single crystalline CuO NWs with 1 nm and 10 nm ZnO, respectively. Because of the differences of the surface defect densities (**Figure 5.4** and **Figure 5.5**), the photocurrent decay behaviors are completely changed.

The relaxation difference between CuO film and CuO NW is attributed to the single crystalline CuO NW because the high quality crystalline phase has no grain boundaries and few defects. As a result, a quick relaxation with a time constant of 0.63 s is observed on CuO NW samples after illumination as we see in **Figure 5.6a**. Once 1 nm ZnO nanoparticles are deposited to the surface of CuO NW, a high density of surface defects contribute to the hole traps leading to a very slow relaxation process.

The photoresponse of CuO NW – 1 nm ZnO is also very different from CuO NW with 10 nm ZnO. This suggests that the presence of surface defects and its interaction with O_2 determines the photocurrent decay characteristics of CuO NW – 1 nm ZnO. These defects are known to be optically active and are detected in the PL spectra at 509 nm i.e., 2.43 eV below the conduction band edge.[215] Under low pressures with little O_2 adsorbed on the surface, the traps are vacant and are considered deep states with slow carrier trapping dynamics (**Figure *5.8.*5.8a**).

Upon white light excitation, excitons are produced in *p*-type CuO NW. By virtue of the band alignment between CuO and ZnO, the electrons travel into the ZnO nanocrystals and are trapped in the deep levels at the surface. The strong electron trapping leads to photocurrent generation as the holes in the *p*-type CuO NW are now free to move. However, the kinetics of

electron trapping and release is slow, given the deep level of the traps in the ZnO. Thus, slow rise/decay currents are observed.

At ambient pressure (760 Torr), O_2 is readily available to interact with ZnO traps. Under dark conditions, adsorbed O_2 on ZnO extracts electrons from the conduction band, depleting the ZnO surface.[216] In the present case, since ZnO is only 1 nm thick, a fraction of the electrons are withdrawn from the CuO NW surface.[217] Thus, underneath a ZnO nanocrystal, *p*-type CuO NW energy bands bend upwards in accumulation (**Figure *5.8.*5.8b**). Electrostatic interactions of substrates with nanocrystals have been reported.[218] Here, we suggest the converse, i.e., the charged state of ZnO nanocrystals affects the local carrier concentration in the underlying CuO NW.

It is important to note that since the nanocrystallites of ZnO are individual disconnected islands,[200] accumulation regions in the CuO NW are also disconnected and represent electrostatically 'frozen' holes on the CuO NW surface (**Figure *5.8.*5.8d**). Adsorption of O_2 is known to occur on CuO NW as well[217] but our recent data[219] shows that the trap density on the CuO NW is quite low ($1.5x10^{10}$ cm^{-2}). Hence, compared to the CuO NW under the ZnO nanocrystal, the exposed CuO NW regions have negligible accumulated charge. Therefore, the localized electrical field builds potential gradient between ZnO nanocrystals, which force the electrons move through the CuO NWs' surface. The higher the O partial pressure, the less of the electrons participate in the migration and the lower the current.

Upon white light excitation (**Figure *5.8.*5.8c**), O_2 photodesorbs and the released electrons are excited to the conduction band of ZnO. The electrons produced within the ZnO as a result of sub bandgap excitation come from O_2 desorbing from highly defective ZnO surfaces.[220, 221] These electrons rapidly recombine with accumulated holes at the CuO NW interface and reduce the band

bending. Depending on the number of O_2 desorbed, flat band conditions may prevail at the interface. Photocurrent generation will subsequently proceed in the mechanism described in **Figure *5.8.*5.8a**. The established epitaxy is key in making this process fast. When light is shut off, O_2 rapidly adsorbs again on the highly defective ZnO surface and 'freezes' accumulated holes in the CuO NW. Thus, the photoresponse in the CuO NW – 1 nm ZnO at 760 Torr is the shortest.

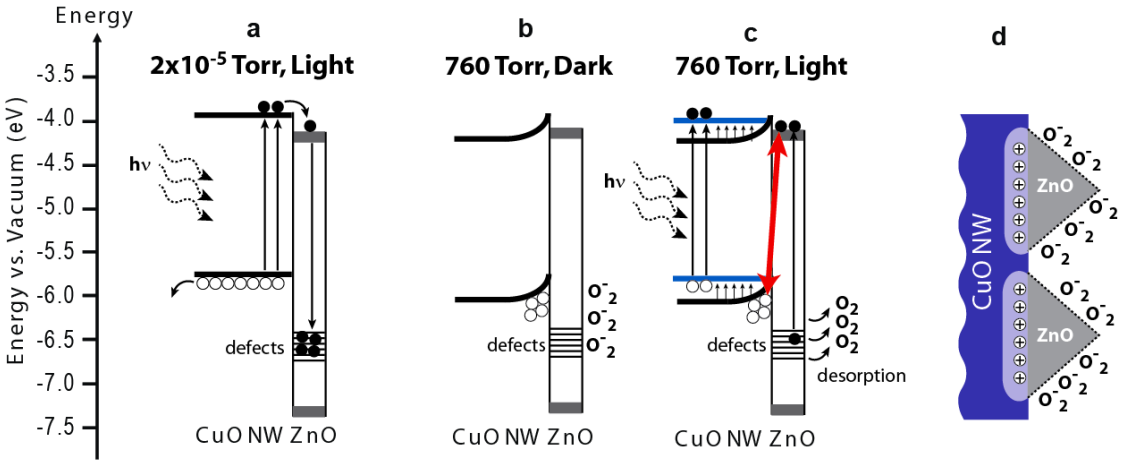

Figure 5.8. a) Band diagram of CuO NW – 1 nm ZnO at $2x10^{-5}$ Torr and under light excitation. The defects are empty in dark and trap photoexcited electrons under illumination allowing holes to freely conduct. **b)** Band diagram of CuO NW – 1 nm ZnO at 760 Torr and under dark. The accumulation layer in the CuO NW is due to the adsorbed O_2. **c)** Under light excitation, O_2 photodesorbs, leaving the electrons to be excited to the conduction band of the ZnO. These electrons recombine with accumulated holes in the CuO NW (red arrow) and bands flatten (blue). **d)** Schematic of the CuO NW – 1 nm ZnO surface showing accumulated holes under the ZnO nanocrystals.

5.5. Conclusions

In this chapter, we studied the relationship between surface defects and the conductivity of ALD ZnO films. We found that surface conduction dominate the conductivity with a ZnO film thickness

below 12.6 nm because of the high density of surface defects. The bulk conduction begun to dominate the conductivity with a film thickness thicker than 20 nm. The thinner the film, the denser the surface defects. Thus, we can conclude that ALD ZnO films with a thickness less than 12.6 nm can be employed to modify the surface states of single crystalline CuO NWs to study the effect of surface defects on the photoexcitation and recombination behaviors.

An engineering of the single crystalline CuO NWs by these highly defective ALD ZnO films (less than 10 nm) provide indications that modified NWs shows different surface chemistry, which, as a result, changes the photocurrent decay processes. First, CuO NW – 1 nm ZnO should act as an 'apparent' *n*-type oxide i.e., as pressure decreases, the dark current should increase. This is because at low pressures, O_2 should desorb releasing accumulated holes at the CuO / ZnO interface to the bulk CuO NW, increasing conductivity. It is indicated that CuO NW – 1 nm ZnO has promising applications for O_2 sensors. Second, τ for CuO NW – 1 nm ZnO increases with a decrease in O_2 partial pressure. In other words, as O_2 adsorbs, deep surface traps in the ZnO slowly trap holes produced during the photoexcitation process and lead to a slow photocurrent decay at low pressures. Third, thermal energy linearly affects the time decay constants with a temperature higher than 120 K. Holes can be released from hole trap levels by thermal energy, contributing to the recombination process by showing a decrease in the decay time constant with an increase of temperature.

Therefore, the CuO NW – 1 nm ZnO is sensitive to O_2 pressure and slows down the light excitation and relaxation processes by exposing the active ZnO $\{10\bar{1}1\}$ surface. Defect mediated spontaneous adsorption/desorption of O_2 on ZnO surfaces is well-known.[222] Recent reports on the ZnO $\{10\bar{1}1\}$ surface properties further corroborates the fact that a highly defective ZnO $\{10\bar{1}1\}$ planes may have unique charge trapping characteristics.[205] These surfaces can be used to induce

specific photocatalytic reactions.[41] These results shows clear indications that modification of surface structures of NWs can obtain some unique performance for functional material design.

Chapter 6 ZnO coated CuO nanowires for CO_2 photoreduction

6.1 Introduction

Wide bandgap semiconductors, such as ZnO and titania (TiO_2) are the popular photocatalysts for CO_2 photoreduction due to their favorable band edges. A disadvantage of using these semiconductors is the requirement of high energy input, i.e., ultraviolet light.[108] Conversion yields of less than 250 μmol/g-cat/hr are routinely obtained.[223-225] Modifications on traditional semiconductors are the current trends to enhance CO_2 photoreduction performance, such as doping/depositing metals,[6, 226-229] making mesoporous matrix,[230-236] developing high aspect ratio nanostructures[6, 237-239] and incorporating photosensitive enzymes or dyes.[225, 240] Until now, the maximum conversion yield due to these efforts is reported to be 1.3 mmol/g-cat/hr (in terms of CH_4 formation)[6]. However, the above processes either use expensive metals with stability issues,[241] or have scalability or capacity limits which hinder future adoption in a wide range of applications.

In this chapter, we report for the first time a facile development of ZnO-CuO composite nanowires that demonstrate the yield of CO_2 photoreduction to CO reaching 1.9 mmol/g-cat/hr. From an application perspective, while direct conversion to a hydrocarbon fuel such as methane may be preferred, reducing CO_2 to syngas (CO and H_2) is also desirable, as the chemical industry is well set up to produce a range of downstream products from syngas.[242]

Single crystalline, high density (10^8 cm^{-2}) CuO nanowires were made by thermal oxidation of high purity Cu foils[65] and the ZnO was deposited by ALD (see **Methods** for details).[243] Several unique aspects of this work are: (1) the new composite material does not use expensive, noble metal catalyst nanoparticles; (2) the raw materials are abundant, and CuO with a bandgap of 1.53

eV is better matched to the solar spectrum than pristine ZnO or TiO_2; (3) interfacing CuO; a *p*-type semiconductor with ZnO; an *n*-type semiconductor, leads to suitable alignment of the band edges which favor electron-hole separation; and (4) the processes for making the material are highly scalable.

6.2. Experiments

Materials Synthesis. 127 μm thick copper foils were purchased from VWR International® with a purity of 99.9%. The foils were cut into 1 cm × 1 cm pieces and surface native oxide was removed by placing the pieces in 1M HCl solution for 30 min. The foils were then immediately put into a tube furnace maintained at 500 ℃ for 30 min at ambient pressure after de-ionized (DI) water cleaning and compressed air drying. Dense CuO nanowires were grown on the surface of the foil. ALD was used to deposit different thicknesses of ZnO on CuO nanowires at 150 ℃ with a background pressure of 50 mTorr. DEZ with a purity of 99.9% (SAFC Hitech®) and DI water were used as precursors, using a precursor pulse time of 1.5 s and 1.0 s, respectively. The growth rate of ZnO is around 0.17 nm/cycle. Mass determination of CuO nanowires was done by thermogravimetric analysis, as shown below.

Mass Calculation. Mass determination is critical to estimating photocatalyst yields. We determine photocatalyst active mass by conducting thermogravimetric (TGA) measurements. This approach is more sensitive to mass gain during oxidation of metals and, as will be shown below, does not depend on the variability of the nanowire density, diameter or length. Our results show that even after accounting for statistical variations of measured parameters (using error propagation) and under assumptions that are highly conservative, record photocatalytic yields are obtained.

The CuO nanowire + CuO film mass is distributed on two surfaces of the oxidized Cu foils (top and bottom), whereas, only the top surface of the Cu foil was exposed to the CO_2 + H_2O mixture. Assuming the CuO thickness and therefore mass, is proportional to the Cu_2O underlying thickness[142, 244], we obtain a CuO mass of at most, $(40.17 \times 10^{-6}) \times 4.83 / (4.83 + 2.81) = 25.40 \times 10^{-6}$ gm. Based on this mass, we claim with 95% confidence, that the catalyst yield is *at least* 1.9 mmol /g-cat/hr or higher. The mass calculation details are provided in **appendix Ⅴ.**

Materials Characterization and CO_2 Photoreduction Analysis. The morphology of nanowires were examined using FE-SEM (JEOL-7001LVF) operated at 15 kV. The inner structure of the nanowires was analyzed by TEM (JEM-2100F, JEOL) at 200 kV. The FFT patterns were generated from the high resolution TEM images using Digital Micrograph GMS 1.4 (Gatan, Inc.). The optical property of the CuO nanowires was measured by UV-VIS-NIR spectroscopy from which the bandgap of the nanowires was estimated by Tauc plot (**appendix Ⅵ**). The morphology and rms surface roughness of the pure CuO and ALD coated ZnO-CuO nanowires were analyzed by AFM (Dimension 3000, Digital Instruments) using a light tapping mode. An 8 nm radius, Si tip (MikroMasch®, HQ:NSC35) was used in tapping mode to obtain AFM height images on multiple facets of CuO nanowires. Z-height statistics is a reliable method to probe the surface morphology during N&G growth[198] and therefore we focus on the RMS roughness in **Figure 6.3**. The steady state photoluminescence measurements of these nanowires were carried out by using a He-Cd laser (λ = 325 nm) as the excitation source with 1 nm resolution.

Transient absorption spectrum (TAS). Time-resolved pump-probe absorption experiments were carried out using Helios, a femtosecond transient absorption spectrometer from Ultrafast Systems. The spectrometer is coupled to a femtosecond laser system consisting Solstice, a one

box ultrafast amplifier (Spectra-Physics) built of Spitfire Pro XP, a Ti:sapphire regenerative amplifier with a pulse stretcher and compressor, Mai-Tai, a femtosecond oscillator as seeding source and Empower, a diode-pumped solid state pulsed green laser as the pump source. The amplifier produces pulses centered at 800 nm with energy of ~3.5 mJ, ~90 fs duration and 1 kHz repetition rate. Ninety percent of the output beam was used to generate a pump beam in Topas-C, an optical parametric amplifier equipped with Berek extension (Light Conversion Ltd, Lithuania). The remaining 10% was used to produce probe pulses in the Helios spectrometer. A white light continuum probe in the visible [245] region was generated by a 3 mm thickness Sapphire plate. A complementary metal–oxide–semiconductor (CMOS) linear sensor with 1024 pixels was used as a detector in the VIS range. To provide an isotropic excitation of the sample and avoid pump-probe polarization effects, the pump beam was depolarized. The excitation was set to 325 nm with beam energy of 2 μJ and spot size of 1 mm diameter, corresponding to intensity between 4×10^{14} photons/cm^2 per pulse. During measurements the liquid sample was kept in 2 mm quartz cuvette and was vigorously stirred using a magnetic stirrer.

CO_2 photoreduction analysis. The photoreduction analysis system used in this experiment has been reported in the papers.[6, 235] Briefly, compressed CO_2 was used as the carbon source, which passed through a water bubbler to generate a mixture of CO_2 and water vapor. The gaseous mixture was then fed into a continuous flow reactor where the nanowires were loaded. The nanowires were activated by a Xe lamp (Oriel 66021, Newport Co.) operated at 400 W with an accumulated intensity of 300 mW/cm^2 in the wavelength from 250 to 950 nm. The light spectrum is shown in **appendix Ⅶ**. The light spectrum was measured by a spectroradiometer (ILT-900R, Polytec GmbH) and the light intensity in the effective range (250 to 810 nm) was measured as 196.8 mW/cm^2.The concentrations of effluent gases as a function of irradiation time were recorded automatically by

gas chromatography (GC) through an automated gas valve, equipped with a PLOT capillary column (Supelco Car-boxen-1010) and a thermal conductivity detector. To understand the detailed CO_2 photoreduction mechanisms in the system, various blank and control experiments were also carried out.

The ZnO-CuO nanowires with different ZnO thicknesses (ALD cycles) were subjected to CO_2 photoreduction. Analysis details are described above and the recent publications.[6, 235] CO was found to be the major product based on the two electron photoreduction reaction ($CO_2 + 2H^+ + 2e^- \rightarrow CO + H_2O$, Eq. 6.1).[6, 246] This reaction requires the simultaneous photooxidation of H_2O and production of protons given as ($H_2O + 2h^+ \rightarrow ½\ O_2 + 2H^+$, Eq. 6.2).

6.3 Results

6.3.1 Carbon dioxide photoreduction using ALD ZnO coated CuO nanowires

From **Figure 6.1a**, the ZnO-CuO nanowires demonstrated extremely high CO_2 conversion performance. The maximum CO yield achieved was 1.9 mmol/g-cat/hr for the 8 ALD ZnO cycles deposited on CuO nanowires. The mass of the exposed CuO nanowires was used to estimate the net conversion yields. Details about the mass determination using thermogravimetric analysis are provided in supplementary information in experiment part. To the best of our knowledge, this value is the highest CO yield reported in the literature of CO_2 photoreduction.[6, 223, 238, 247] The quantum yield at this condition was calculated based on the equation:

$$\emptyset_{CO}(\%) = \frac{2mol\ of\ CO\ yield}{moles\ of\ photon\ absorbed\ by\ catalyst} \times 100,$$

Where the $\emptyset_{CO}$ represents the quantum yield of CO, and the moles of absorbed photons can be calculated by photon energy used to reduce CO_2 using the equation: $E_{photon} = \frac{hc}{\lambda}$. The average photon energy thus can be estimated by averaging the photon energy from 250 to 810 nm. The

integrated light intensity used in this experiment is 196.8 mW/cm^2. The effective sample area is 1 cm^2. Average photon energy is 4.17×10^{-19} J. The yield of CO is 1900 μmol/g/hr. The effective mass calculated in the experiment is 0.02573 mg. Based on these data, the quantum yield is calculated to be 0.0035%, which is low but not unusual for CO_2 photoreduction reactions.[248] After 5h of irradiation, the CO yield started to decline, which may be attributed to the deterioration of the photocatalytic activity owing to diminishment of the adsorption power of the catalyst and the saturation of adsorption sites on the catalyst surface with intermediate products.[6, 228, 249] A time dependency on the CO yield was also observed. This behavior can be attributed to the adsorption/reaction/desorption of gases on the surface of the catalyst. Assuming Langmuir adsorption based kinetics, an exponential saturation curve was used to model this behavior, i.e., CO Yield = $A[1 - \exp(-t/\theta)]$, where A is constant, t is time, and θ is the kinetic parameter that quantifies the rate of CO yield. It was found that θ varied as 80, 36, 42 and 240 minutes for 5, 8, 18 and 35 ALD cycles of ZnO, respectively. As in the case of CO yield, the fastest reaction rate (smallest θ) was found for the 8 ALD cycle ZnO sample. The CuO nanowires with 0 and 63 ALD cycles of ZnO showed negligible CO yields and were not considered for fitting.

Further, we report on control experiments (**Figure 6.1a**) as well. The first control experiment was performed using pristine CuO nanowires. No CO_2 photoreduction was observed. Utilizing bare ZnO layer (thickness = 1.4 nm) deposited on an indium tin oxide substrate did not yield any CO either. Theoretically, ZnO is a good photocatalyst for CO_2 photoreduction. However, the ZnO layer may not be activated and generate electron-hole pairs if the thickness is below the effective absorption depth. Finally, CO_2 was replaced with N_2 gas to rule out the possibility of surface carbon contamination. No carbon based products were detected indicating that these

nanowires have negligible adventitious carbon. Thus, any CO detected from the following CO_2 photoreduction analyses would come from CO_2 gas.

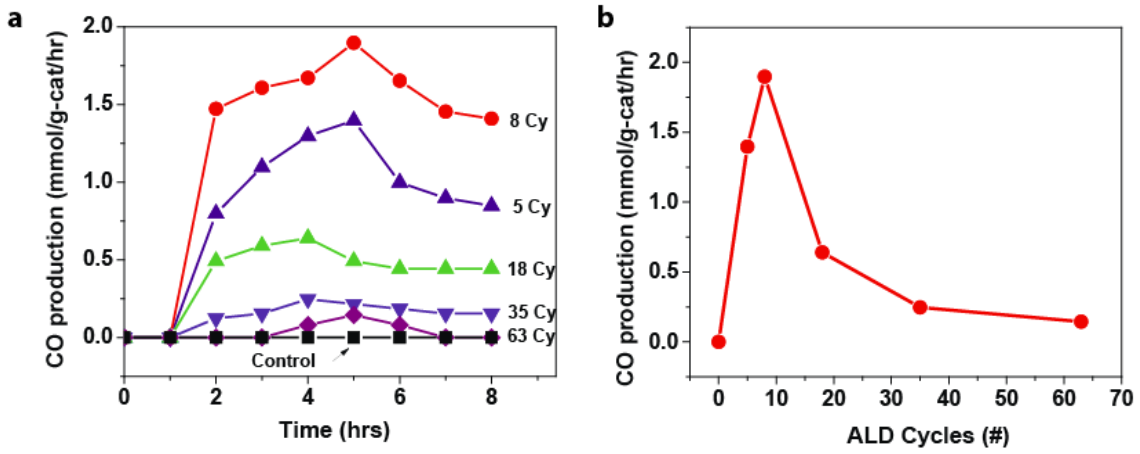

Figure 6.1. CO_2 photoreduction results. **a)** CO yields of ZnO-CuO nanowires with different ZnO ALD cycles as a function of irradiation time. Results of control experiments were included as black squares. **b)** Maximum CO yield as a function of ZnO ALD cycles.

From the above discussion, it is clear that neither pure CuO nanowires nor an ultra-thin ZnO layer by itself was responsible for CO_2 photoreduction. However, a combination of ZnO on CuO nanowires led to effective CO production. Based on reactions given by *Eqs. 6.1* and *6.2*, this implies that *both* ZnO and CuO surfaces determine the photoreduction yield of CO_2.

The number of ALD cycles of ZnO plays an important role in CO_2 photoreduction process (**Figure 6.1b**). While the ALD deposition rate on Si is found to be 0.17 nm/cycle (through ellipsometry),[194] in this paper the metric of ZnO thickness will be conveyed through the number of cycles deposited. The CO yield first increases with increasing ALD ZnO cycles with the optimal thickness at 8 ALD cycles. Beyond the optimal condition, the ZnO-CuO nanowires demonstrate

lower CO yields. These results indicate that ZnO thickness also is critical in determining catalyst yield.

6.3.2 Interface and structural analysis using electron microscopy

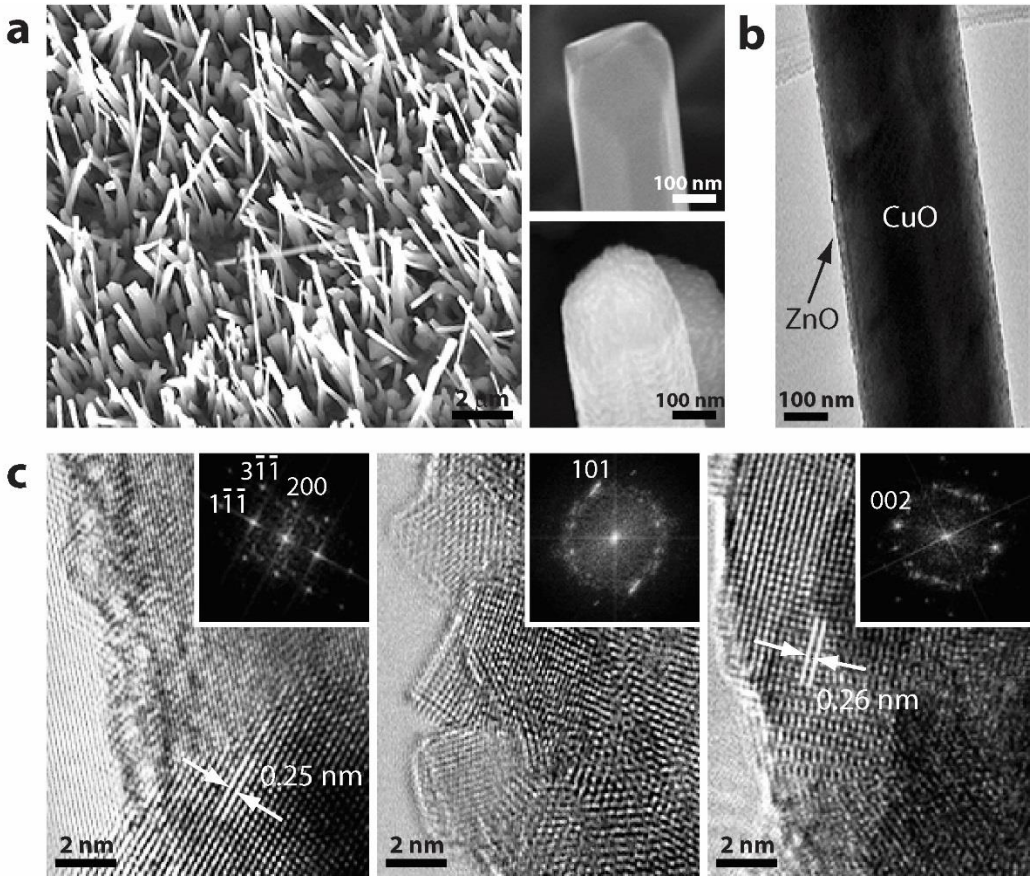

Figure 6.2. Characterization of representative CuO and ZnO coated CuO nanowires. **a)** FE-SEM image of ZnO-CuO nanowire arrays with magnified pristine CuO nanowire (upper right) and 63 cycles of ALD ZnO coated CuO nanowire (lower right). **b)** TEM image of 63 cycles of ALD ZnO coated single CuO nanowire. **c)** HRTEM and corresponding FFT images of pure single crystalline CuO (left), 5 cycles of ALD ZnO coated (middle), and 63 cycles of ALD ZnO coated CuO nanowire surface.

Detailed structural and morphological analyses were performed on the ZnO-CuO nanowires. Representative pristine CuO and ZnO-CuO nanowires are characterized by SEM and TEM (**Figure 6.2**). High density CuO nanowire arrays are observed in **Figure 6.2a**. The average diameter and length of the nanowires are about 230 nm and 1.2 μm, respectively, which can be tuned by changing temperature, time, and oxygen concentration.[161] The surface of the pristine CuO nanowire is faceted and fairly smooth (upper right, **Figure 6.2a**), indicating that these nanowires have high crystallinity based on earlier studies.[65, 144] In comparison, after 63 cycles of ALD deposition of ZnO, the surface of CuO nanowires became rough with ZnO grains (lower right, **Figure 6.2a**). A representative TEM image of a 63 cycle ALD ZnO on a CuO nanowire is shown in **Figure 6.2b**. A continuous and crystalline ZnO film is observed on the CuO nanowire surface.

To investigate the surface structure of the nanowires with and without ZnO, a high resolution HR TEM analysis of the three samples, i.e., pristine CuO, 5 cycle- and 63 cycle-ALD ZnO coated CuO nanowires, was performed. HRTEM images are shown in **Figure 6.2c** with corresponding FFT patterns. It is apparent that the pristine CuO nanowire mainly consists of $(\bar{1}11)$ plane (inter-planar spacing = 0.252 nm), which was reported by other groups as well[65]. For 5 cycle ZnO (middle), discrete and well-defined crystals of ZnO are seen on the surface of the CuO NWs. This is surprising since ALD is known for being a conformal, layer-by-layer deposition process. However, under substrate inhibited growth conditions (such as pristine single crystal surfaces with little or no surface defects), a nucleation and growth (N&G) mechanism may be well active, which results in an 'incubation' period for the ALD film, before continuous layer-by-layer growth occurs.[40, 41, 42] As indicated in its corresponding FFT pattern, the major ZnO plane is (101) with the lattice distance of 0.248 nm, matching closely with the CuO $(\bar{1}11)$ plane. This indicates that the initial growth of ZnO is determined by the crystallography of underlying CuO nanowires

following the epitaxial relationship, CuO($\bar{1}$11) || ZnO (101).[203, 250] It is to be noted that the ZnO (101) plane is a non-polar, low symmetry plane.[251-253]

After 63 cycles of ALD ZnO deposition (**Figure 6.2c**, right), the primary ZnO plane changed from (101) to (002) plane with a smoother surface. The possible pathway for this structural and crystallographic transformation can be understood by considering an N&G mechanism for ALD ZnO thin films. While the epitaxial matching between CuO and ZnO determines initial nucleation of the discrete pyramidal-like nanocrystals with ZnO (101) exposed surface, continuous growth leads to the merging of these surfaces and the formation of a crystalline ZnO film with *c*-axis orientation. It is to be noted that the (002) plane is polar in nature (either O- or Zn-terminated).[251]

6.3.3 Morphological evolution of ZnO films on CuO nanowire surface

Next, atomic force microscopy (AFM) analysis of the ZnO-CuO composite nanowires during the initial ZnO ALD cycles was carried out. As from **Figure 6.3a**, the root mean square (RMS) surface roughness of the nanowires increases initially till 8 ALD cycles. Past 8 cycles, the roughness starts to decrease. This behavior suggests an N&G mechanism for thin film growth. During the nucleation phase, discrete islands contribute to surface roughness. Once the islands impinge neighboring nuclei, islands merge to form a conformal film, as expected of an ALD mechanism. The size of the ZnO islands is determined by the ALD deposition cycles where, 8 ALD cycles corresponds to a thickness of 1.4 nm. The RMS roughness trend observed in **Figure 6.3a** matches the CO_2 photoreduction data in **Figure 6.3b**. The striking resemblance between CO_2 photoreduction response with ALD ZnO cycle numbers and the surface roughness variation of ALD ZnO, reiterates the fact that surface morphology plays a critical role in determining high CO_2 photoreduction yields.

The morphology of the nanowires facets with changing ALD ZnO cycles (0, 5, 8, 11 and 21 cycles) are shown in **Figure 6.3c-g**. The surface textures of these nanowires are visible from the AFM images. For instance, a very smooth surface is observed for pristine CuO nanowires in **Figure 6.3c**. But for ZnO-CuO nanowires, in particular for 5 and 8 cycles, textured surfaces due to the presence of ZnO islands can be identified. The results are consistent with our FESEM and TEM analyses shown in **Figure 6.2**.

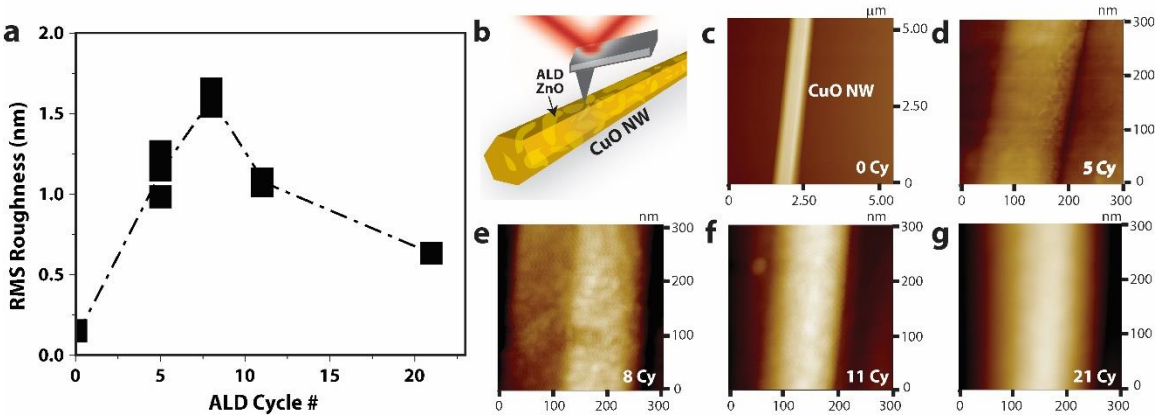

Figure 6.3. Surace roughness characterization by AFM. **a)** RMS roughness as a function of ALD ZnO cycles. **b)** Schematic of AFM measurements on ZnO islands on CuO nanowires. **c-g)** A series of AFM images show the surface roughness on single CuO nanowire as the number of ALD ZnO cycles increase from 0 to 21 cycles. Scan size and height are adjusted to best capture the texture of the growing film on a single facet of the wire. Roughness was measured locally and at multiple locations of equal area on the surface of the CuO nanowires. Copyright 2015 American Chemistry Society.

6.3.4 Photoluminescence and defect studies

To understand the CO_2 photoreduction pathways, PL measurements of the CuO and ZnO-CuO NWs were conducted at room temperature. **Figure 6.4** displays normalized PL emission

spectra of a representative CuO nanowire and CuO nanowires with 5 and 63 cycles ALD ZnO recorded by 325 nm He-Cd laser excitation. It is to be noted that while the 5 cycle sample has discrete ZnO nanocrystals on CuO nanowires surface, the 63 cycle sample has a continuous ZnO film.

The CuO nanowire sample shows a broad emission peak from 400 nm – 700 nm. This data is similar to the recent reports on PL of CuO nanowires. For example, Jin et al.[254] reported relatively sharp PL peaks centered around 350, 510 and 760 nm and attribute them to excitons and deep level defects. Othonos et al.,[207] however showed a broad PL spectra of CuO nanowires much closer to the one observed in our work and assign the peaks to the recombination of intra valence band electrons with simultaneous contributions from mid-gap defect states.

The ZnO-CuO nanowires exhibit PL spectra typical of previous reported ZnO with a relatively sharp UV band and a broad visible emission band. The PL spectra are fitted by Voigt functions. The UV emission is attributed to the excitonic recombination (near band emission, NBE = 381 nm) and the broad visible emission is ascribed to recombination related to structural and surface defects, such as oxygen vacancies with different charged states, zinc vacancies, and zinc interstitials.[42, 43, 209]

For the 5 cycle ALD sample – where discrete nanocrystals of ZnO are observed on CuO nanowire surface, the defect-related green emission dominates the PL response. The ratio of intensity of NBE to defect peaks, I_{NBE}/I_{defect} was found to be 0.25 indicating surface defects determine much of the electronic and optical properties.[210] Further, two peaks can be deconvoluted from the defect band emission. This emission can be related to an acceptor like vacancy of zinc (V_{Zn}, 2.53 eV) and antisite oxygen (O_{Zn}, 2.33 eV), respectively.[255] We also note that the green

emission has been linked to Cu^{2+} impurities (2.86 eV) and in our case likely to occur, given the proximity to the CuO surface.[256] However, our PL data does not suggest any Cu^{2+} related peaks.

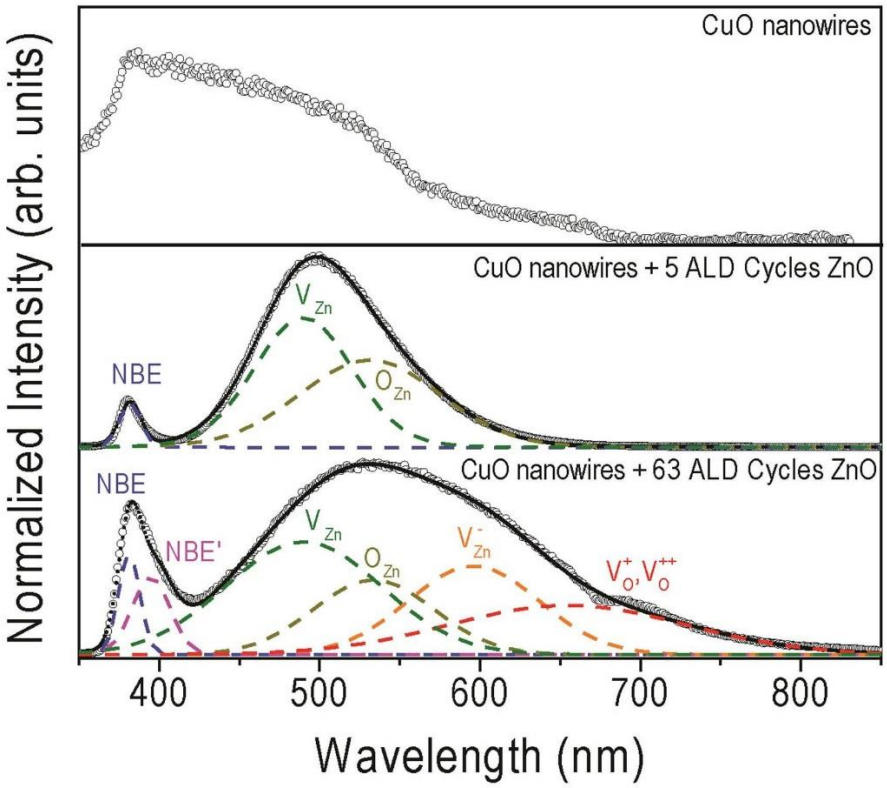

Figure 6.4. Room temperature photoluminescence of CuO nanowires and ALD ZnO coated CuO nanowires. CuO nanowires show a broad emission between 400 nm – 700 nm related to valence intraband transitions. For 5 ALD cycles ZnO on CuO nanowires, an NBE at 381 nm is seen while a strong defect related emission is observed. This has been deconvoluted to belong to V_{Zn} and O_{Zn} defects – both residing close to the valence band (VB) edge. For 63 cycles ZnO, a stronger NBE and NBE' (395 nm) is observed. The defect related emission consists of 4 distinct peaks associated with defects lying close to the valence band (V_{Zn}, O_{Zn}) and conduction band [257] edges (V_{Zn}^{-}, V_O^{+}, VO^{++}).

For the 63 cycle ALD ZnO, INBE/Idefect was 0.78 indicating reduced impact of the surface states as compared to the 5 cycle ALD ZnO. The crystallinity of the film is better developed and defects, while present, have a lower PL intensity.[210] The NBE band can be deconvoluted into two separate UV emission peaks – NBE and NBE'. While NBE belongs to single crystalline ZnO, NBE' (395 nm) is due to internal stresses in the film.[258] These stresses can be formed due to the coalescence of the nanocrystals as these impinge on one another. The NBE peak detected in our work is much sharper and hence, indicates better crystalline quality, than those reported for ALD ZnO ultrathin films (~3.5 nm) on single crystalline Si.[259] This is possibly due to better epitaxial matching of the ZnO (101) deposited in this work with the underlying CuO($\bar{1}11$) nanowires. Comparing the defect band of the 63 cycle with the 5 cycle ALD sample, two additional defect related peaks are observed. These correspond to donor-like, monovalent vacancies of zinc (V_{Zn}^{-}) and single and double ionized oxygen vacancies (V_O^{+} and V_O^{++}), respectively.[209] The fractions of the resolved PL bands for both samples are listed in supplementary information, **Table 6.1**.

Table 6.1. Position, FWHM and Area % of resolved bands from the photoluminescence for the 5 cycle and 63 cycle ZnO ALD samples.

sample	5 cycle ZnO			63 cycle ZnO					
Peak	NBE	V_{Zn}	O_{Zn}	NBE	NBE'	V_{Zn}	O_{Zn}	V_{Zn}^{-}	V_O^{+},V_O^{++}
Position (nm)	381	489	531	381	394	489	533	596	654
Position (eV)	3.25	2.53	2.33	3.25	3.2	2.53	2.33	2.08	1.89
FWHM	16	72.9	103.5	16.2	28.3	114.6	88.6	96.3	174.6
Area (%)	3.6	49.2	47.2	3.9	5.4	31.9	16.4	21.1	21.3

6.4. Discussion

6.4.1 Transient absorption spectroscopy of CuO and CuO–ZnO nanowires

Figure 6.5a shows the representative transient absorption (TA) spectra of CuO nanowires taken at various delay times after excitation at 325 nm. It is known that trapping of photoexcited electrons in the conduction band occurs on time scales of 100-200 fs[260] which is close to the temporal resolution of the spectrometer and this process cannot be sufficiently resolved. The early TA spectra (0.7 ps) contain characteristic negative bands at ~490 nm and 610 nm, similar to the bands present in the PL spectra of CuO nanowires (**Figure 6.4**). When the scaled 0.7 ps TA spectrum is subtracted from the 12 ps TA spectrum, an elevated positive transient signal spanning the entire spectral range is obtained, indicating the presence of photoexcited, shallowly trapped electrons in the conduction band. Theoretically, absorption of such "free" electrons is proportional to the square of absorbing wavelength and such simulative fit is also provided (dashed line)[261].

Upon assumption that bleaching of absorption bands is practically constant within the range of spectrometer time window, the dynamic properties of recombination of weakly trapped electrons with holes may be obtained from direct fitting of kinetic traces probed at wavelengths in which TA of these electrons occurs. **Figure 6.5b-d** show representative TA dynamics of the CuO and ZnO-CuO nanowires with different ALD cycles (8 and 63 cycles). The fitting was done according to second order decay.[262]

To model the electron-hole recombination dynamics, the average number of electron-hole pairs $\langle x \rangle$ present in semiconductor at time t can be described by following general equation:[262]

$$\langle x \rangle(t) = \sum_{n=1}^{\infty}(2\exp(-\langle x \rangle_0)(-1)n\sum_{j=1}^{\infty}\frac{\langle x \rangle_{0}{}^{i}}{(n+i)!}\prod_{j=1}^{n}(n-i-j))\exp(-n^2kt) \qquad \text{Eq. 6.3}$$

Where $\langle x \rangle_0$ is an average number of pairs at time t = 0, n – number of particles per unit volume.

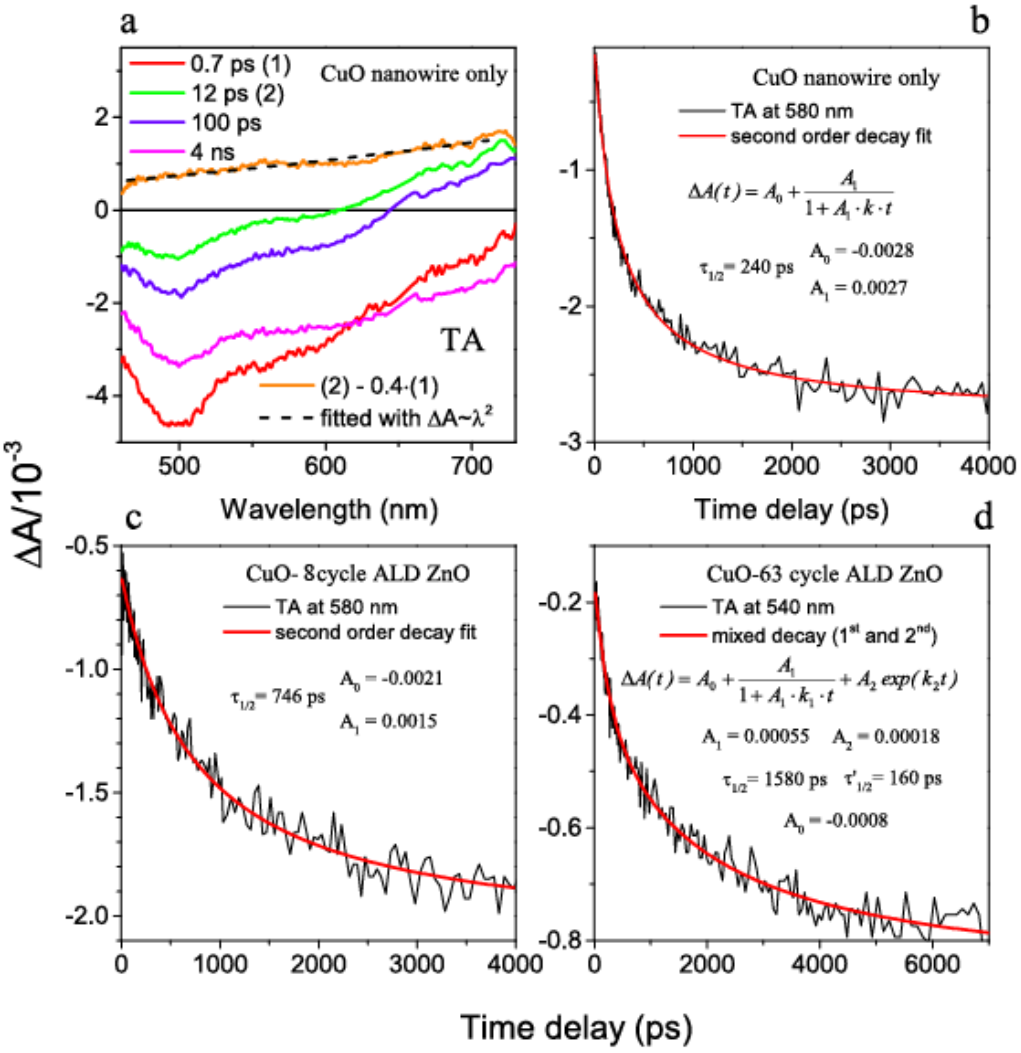

Figure 6.5. Transient absorption results of CuO and ALD ZnO coated CuO nanowires. **a)** representative transient absorption spectra of CuO nanowires taken at various delay times after excitation at 325 nm. The orange line corresponds to predicted spectrum of transient absorption of shallowly trapped electrons promoted to conduction band after laser photoexcitation. The spectrum was fitted with theoretical function with parameters provided in the figure; **b-d)** demonstrative kinetic traces extracted from transient absorption datasets of the each sample accompanied by fits. The dynamic parts of kinetic traces are associated with recombination of the e-h pair and can be successfully (except d) fitted with a second order decay.

If $\langle x \rangle_0$ is small, *Eq. 3*simplifies to first order decay:

$$\langle x \rangle(t) = \langle x \rangle_0 \exp(-\mathrm{k}t) \qquad \text{Eq. 6.4}$$

If If $\langle x \rangle_0$ is large, *Eq. 3*simplifies to second order decay:

$$\langle x \rangle(t) = \frac{\langle x \rangle_0}{1+\langle x \rangle_0 kt} \qquad \text{Eq. 6.5}$$

Because $\langle x \rangle$ is proportional to ΔA (number of holes equal to number of electrons, eand each electron give the same contriubution to ΔA at a specific wavelength):

$$\Delta\mathrm{A}(t) = \Delta\mathrm{A}_0 \exp(-\mathrm{k}t) \qquad \text{Eq. 6.6}$$

and

$$\Delta\mathrm{A}(t) = \frac{\Delta\mathrm{A}_0}{1+\Delta\mathrm{A}_0 kt} \qquad \text{Eq. 6.7}$$

It is very possible that the TA data of the semiconductor will exhibit multiple decays depending on density of photogenerated electron-hole pairs.

Longer recombination lifetimes ($\tau_{1/2}$) of weakly trapped electrons in CuO-ZnO nanowires are obtained. Specifically, compared to $\tau_{1/2}$ = 240 ps of CuO nanowires, $\tau_{1/2}$ = 746 ps and $\tau_{1/2}$ = 1580 ps are obtained for 8 ALD cycle ZnO and 63 ALD cycle ZnO samples, respectively. TA data therefore shows that electrons enjoy at least 3x higher lifetimes on ZnO coated CuO nanowires in line with recent published results.[250]

6.4.2 Mechanism of CO_2 photoreduction in ALD ZnO coated CuO nanowires

Taken together, the combined results obtained in this work suggest that the ultra-high CO_2 photoreduction performance observed in ALD ZnO coated CuO nanowires result from three

primary sources. First, the choice of material is important. The deposition of ZnO on CuO allows favorable band alignment of the CuO and ZnO conduction and valence band edges (**Figure 6.6a**). The bandgap of CuO (1.53 eV) is well suited for visible light absorption and the band alignment provides suitable electron transfer from the CuO to ZnO and hole transfer from ZnO to CuO. Further, the CuO ($\bar{1}11$) plane allows epitaxial growth of the ZnO (101) and creates a defect free interface between the two disparate materials.

Second and more importantly, the surface morphology proves to be critical in enhancing the yields even further. TA data indicates that both 8 cycle ($\tau_{1/2}$ = 746 ps) and 63 cycle ($\tau_{1/2}$ = 1580 ps) ALD ZnO samples exhibit higher electron lifetimes as compared to pristine CuO nanowires ($\tau_{1/2}$ = 240 ps). This confirms the favorable transfer of electrons from CuO and its extended lifetime in ZnO. However, the TA data by itself fails to explain the thickness dependency of CO_2 yield, since according to the $\tau_{1/2}$ values, thicker ZnO films should generate higher CO yields. This inconsistency can be explained by considering the discrete island-like morphology of the 8 cycle ALD ZnO samples.

Since the $CO_2 \rightarrow CO$ is a 2 electron process requiring the presence of both electrons and H^+, we propose that exposure of both ZnO (for *Eq. 1*) and CuO (for *Eq. 2*) surfaces to the gas ambient is important (**Figure 6.6b**). This is achieved by ALD of ZnO on pristine CuO nanowires for deposition less than 8 cycles. We surmise then that reaction *Eqs. 6.1* and *6.2* occur around the perimeter of the ZnO nanocrystals—triple phase boundaries, where a rich source of *both* electrons and H^+ are available. Past 8 ALD cycles, the nanocrystals merge forming grain boundaries (**Figure 6.3a**) and this significantly reduces the photoreduction performance (**Figure 6.1b**), not because of

low electron lifetimes in ZnO, but because H_2O is unable to be protonated on an exposed CuO nanowire surface.

Third and finally, surface defects play the most important (and perhaps, the least understood) role in the development of new materials for high yield CO_2 photoreduction. A schematic diagram is drawn in appendix I to show CO_2 adsorption and reaction at the interface of the island grown ZnO NPs on CuO NWs. The triple phases interface (ZnO, CuO and CO_2) is modeled as the active reaction volume allowing for both h^+ (o) based oxidation of H_2O and e^- (•) based reduction of the CO_2. Therefore, the two-step reactions happen to reduce CO_2 to CO.

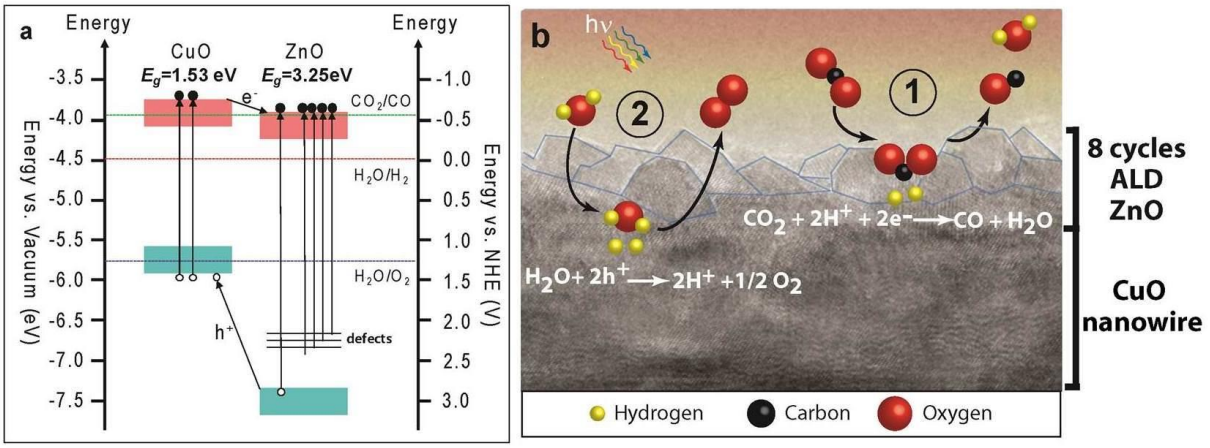

Figure 6.6. Band diagram and schematic of the CO_2 photoreduction process in ZnO-CuO nanowires. **a)** Band alignment of CuO nanowires coated with ALD ZnO and their energy levels with respect to the vacuum (left Y-axis) and normal hydrogen electrode (NHE) (right Y-axis). **b)** Schematic of the reactions Eq. 1 and Eq. 2 (see main text) needed to occur simultaneously on ZnO and CuO, respectively for CO_2 photoreduction.

Geometric modeling of the N&G phenomena yields a curve (**appendix Ⅷ**) similar to **Figure 6.1b** for nuclei densities of 1.4×10^{13} cm^{-2} and the maximum perimeter value fitted for 8 cycles—just before nuclei coalescence occurs. When compared to typical cation areal densities in metal

oxides[198] (~10^{15} atoms cm^{-2}), this nuclei represents clusters that consists of a few hundred ZnO molecular units only and thus highlights the effect of extremely high surface to volume ratio nanocrystals on catalytic activity. Indeed PL data shows that such nanocrystals have a high concentration of surface defects arising from interstitials and vacancies. Low quantum yields are therefore not surprising, given such high density of surface defects. Regardless, the ZnO surfaces lead to defect mediated activated adsorption, reaction and desorption of molecules and are reflected in the combined kinetics of the CO yield (derived from **Fig6.1a**) that shows the 8 cycle ALD ZnO sample with the fastest mean time to saturation of $\theta \sim 36$ minutes.

Structurally, the (101) plane of ZnO is a charge neutral surface consisting of both Zn^{2+} or O^{2-} ions. This plane has 2 unterminated bonds associated for each tetragonally coordinated ion (Zn^{2+} or O^{2-}). On the other hand, the (002) plane is charged (either positive or negative depending on Zn^{2+} or O^{2-} surface termination, respectively) and consists of 1 unterminated bond per ion. Recent theoretical investigation[263] suggests that chemisorption of CO_2 is thermodynamically favored on charge neutral surfaces (like the (101) plane) and the presence of a high density of unterminated bonds may in fact lead to an efficient and large concentration of an activated, intermediate carbonate-ion adsorbed complex, before bond cleavage and desorption of CO occurs. Thus, surface defects contribute to the enhancement of CO_2 photoreduction performance in the ZnO-CuO nanowire system.

6.5 Conclusions

In this chapter, a CO_2 photoconversion yield of at least 1.9 mmol/g-cat/hr is reported for ALD ZnO coated CuO nanowire catalysts. This value is the highest reported CO_2 photoconversion yield, to date. The processes involved in the manufacturing of the photocatalysts are highly efficient, manufacturing scalable and obviate the use of expensive and noble metal catalysts. The CuO

nanowire growth using thermal oxidation of Cu foils is spontaneous and leads to a dense (10^8 nanowires cm^{-2}), high surface area photocatalyst nanostructure. ALD of ZnO on the CuO nanowires can be well controlled at the atomic level, leading to formation of distinct and highly activated ZnO nanocrystals. The choice of materials, resultant nanostructure and surface defects have been synergistically combined with scalable processes to rationally design photocatalysts. This approach should open opportunities targeting other gas phase remediation processes of immediate and immense importance.

Chapter 7 Flexible CuO nanowires solar cells

7.1. Introduction

Over the past decades, silicon solar cells have contributed more than 70% of the world solar energy market.[44] However, the processes to purify the silicon to a solar grade make the solar power expensive.[264] Therefore, semiconductor materials with a lower cost and a lower purity tolerance should significantly reduce the cost of solar cells. Vertical silicon NW arrays have been reported, both theoretically and experimentally, less sensitive to impurities compared with planar silicon solar cells.[32, 265] Vertical single NW solar cells was reported to show a short current density of 180 mA/cm^2 with an energy conversion efficiency of 40%.[266] The external quantum efficiency (EQE) of vertical standing NWs is reported to be seven times higher than the EQE of the NWs that are lying down.[267] Therefore, standing semiconductor NW arrays would be promising to produce low cost commercial solar cells.

Light absorption of NWs is different from the absorption of bulk materials because light interaction and scattering in the periodical NW arrays significantly enhance light absorption, leading to a lesser amount of materials to be used in NW devices for light absorbers.[268] NW synthesis methods can be simplified by using low cost materials with low energy consumption.[269] What's more, flexible transparent polymer substrates could also reduce the material costs and apply the solar cell modules to wide range of applications.[44]

However, high quality crystalline NWs used for photovoltaic devices are usually grown on brittle crystal substrates. To use these NWs in transparent substrates such as polydimethylsiloxane (PDMS) and polymethylmethacrylate (PMMA) is a good choice for making less expensive solar cells.[270-273] However, PMMA was reported to cause the vertical NWs' tips bundling and crashing,

damaging the NWs' vertical alignment.[274] PDMS mechanical properties can be easily controlled by adjusting the ratio of the PDMS base and the curving agent. It is also inert, nonflammable and optically transparent down to 300 nm[271] and has a low surface energy of 22 mJ/m^2.[275] To get better controllability of the polymer substrates, PDMS is a better choice.

In this chapter, we synthesized high density single crystalline CuO NWs with a maximum average length of 50-60 μm using thermal oxidation method. The synthesis process is simple and has a low thermal energy cost. The CuO NWs show a band gap of 1.2 eV, which covers the whole visible light range. The theoretical solar cell energy conversion efficiency of CuO was reported to be around 30% considering only radiative recombination.[29] However, the highest reported energy conversion efficiency of CuO base solar cells is 0.64%,[276] which is far lower than the theoretical value. To increase the solar cell efficiency and material cost, we used the synthesized long vertical single crystalline CuO NWs as light absorbers to increase light absorption. ALD ZnO was coated on top of the NWs as an n-type semiconductor to form a simple heterojunction. We measured the photovoltaic performance of simple heterojunction to understand the reason for causing the low energy conversion efficiency.

7.2. Experiments

CuO NWs with a density of $1.7\times10^8/cm^2$ and a maximum average length of 50-60 μm are synthesized by thermal oxidation of 99.9% pure Cu foils purchased from VWR International® at 600 ^oC for 10 hours. The synthesis details are provided in **chapter 3**. PDMS base and curving agent (Sylgard 184, Dow Corning) are mixed in 10:1 w/w ratio. The mixed PDMS is put into a vacuum oven (THEL CO.) to remove the bubbles for half an hour. Then, using spin-coating machine for 30s at 1500 rpm, we spin-coat the PDMS to glass slides which are cleaned in ethanol and de-ionized water. The thickness of the spin-coating layer is around 65 μm. The thickness is

measured under an optical microscope. A cross-section of the PDMS film is shown in **Figure 7.1a**.We inversely put the CuO NW foils on the surface of the PDMS substrates to make the NWs immerse into the PDMS by the foils' gravity. After this step, we put the PDMS substrates with CuO NW foils into a vacuum oven and set the temperature at 150 ^{o}C for 45 minutes to solidify the PDMS. The vertical aligned CuO NWs are left in the PDMS layer after removing the surface CuO foils. We deposit 10 nm Cr and 20 nm Au onto PDMS layer as rear electrodes. Then, we peel the PDMS layers from glass substrates using a doctor blade method and etch the extra-PDMS to expose NWs in the front side of the PDMS using reactive-ion etching (RIE). The etching rate is roughly 1μm/min with etching gas SF6 (15 sccm), RF power of 200 W and inductive coupled plasma (ICP) power 1000 W.

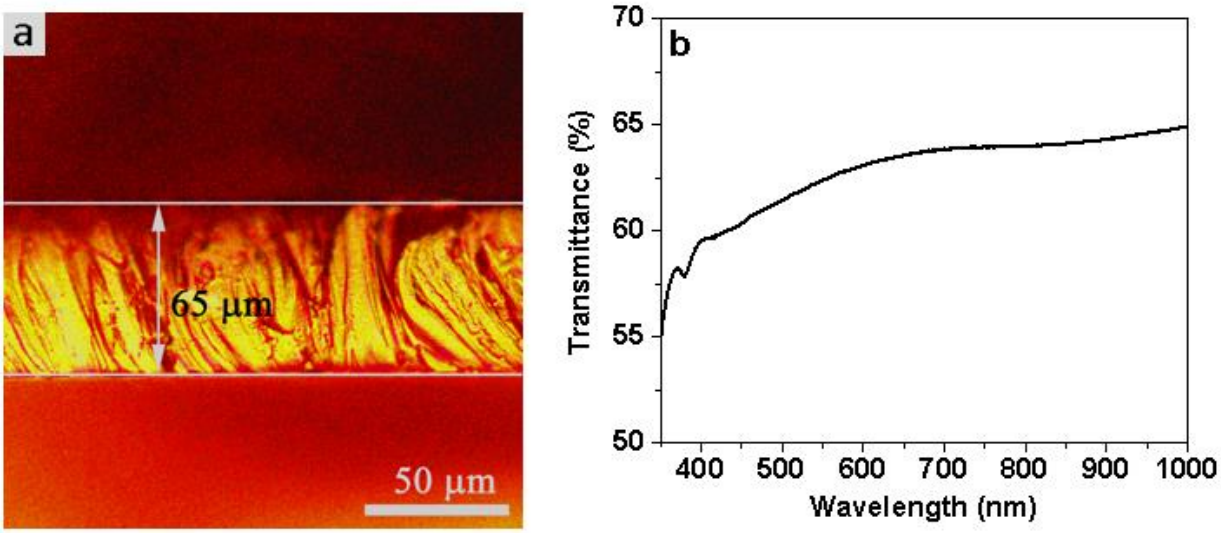

Figure 7.1. a) Optical microscope image of the PDMS film cross-section. The thickness of spin-coating film is around 65 μm. **b)** Transmittance of the 1 nm Cr + 10 nm Au, showing a transmittance more than 60% with a wavelength longer than 450 nm.

After etching processes, we divided the samples into two groups. For the first group of samples, 1 nm Cr and 10 nm Au are thermally deposited on etching side as front electrodes to test

the conductivity of CuO. For the second group of samples, we deposited 40 nm ALD ZnO film directly onto the etched PDMS side and 1nm Cr and 10 nm Au are thermally deposited on the ZnO to work as front electrodes. The front Cr+Au electrodes are 60% transparent in the range from 450nm to 1000 nm. The transmittance of the same thickness of Cr and Au deposited on glass slides is shown in **Figure 7.1b**. A schematic diagram of the CuO NWs-ZnO heterojunctions synthesis processes is shown in **Figure 7.2**.

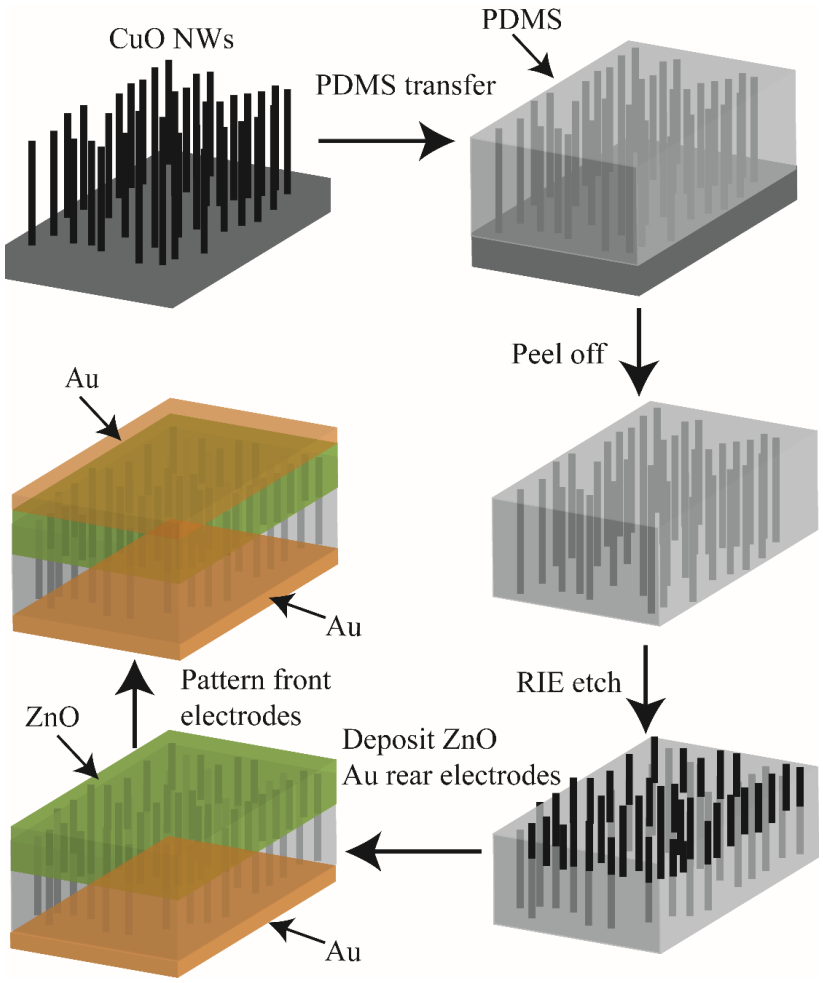

Figure 7.2. A schematic diagram of CuO NWs transfer and solar cell preparation processes.

The surface morphology of PDMS substrates embedded with NWs before and after ALD ZnO deposition was characterized by FE-SEM (JEOL-7001LVF) operated at 15 kV.

Transmittance is measured by SHIMADZU UV-1800. Optical microscope is used to image the PDMS and CuO NWs embedded PDMS. JANIS probe station (ST500-1-2CX) connected to a Keithley 2400 was used to measure the dark and light I-V curve of CuO NWs and CuO NWs heterojunctions at 298 K in air. The light intensity vs. wavelength is shown in **appendix Ⅲ**.

7.3. Results

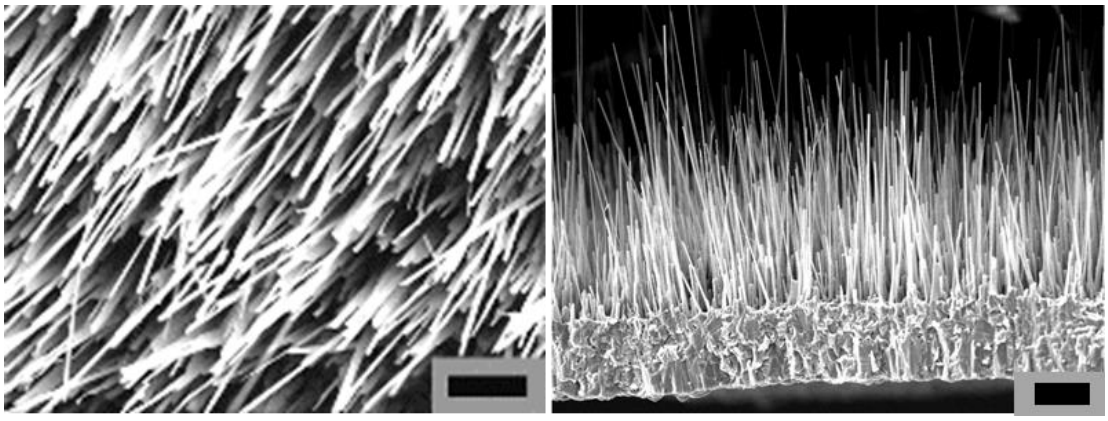

Figure 7.3. Left, top surface of CuO NW with a density of $1.7\times10^8/cm^2$ obtained by thermal oxidation Cu foils in air at 600 ^oC for 10 hours. **Right**, cross-section of CuO NW with a length of 50 mm. The scale bars are 2 μm (**left**) and 10 μm, respectively.

Figure 7.3 shows the densest and longest NWs we synthesized by thermal oxidation of pure Cu foils at 600 ^oC for 10 hours. The top-down SEM image is shown in Figure **7.3 left**. The density of the NWs is around $1.7\times10^8/cm^2$, which is statistically calculated by SEM images. **Figure 7.3 right** exhibits both the cross-section of CuO NWs and the bottom oxides. The NW length is measured by ImageJ software, showing a maximum length round 50-60 μm.

TEM and HRTEM images of the CuO NW is displayed in **Figure 4.2**. The NW surface is smooth with a diameter around 230 nm. The HRTEM image indicates that CuO is a high quality single crystalline without visible surface defects. The NW surface is terminated by $(\bar{1}11)$ planes

with plane distance of 0.252 nm. The surface roughness is less than 1 nm, demonstrating that these CuO NWs could be good candidates for solar cells because the low density of surface defects can lead to a low surface recombination rate. Our previous work calculated the surface defects density by I-V measurements of single NWs devices, giving a defects density of 1.5 $\times 10^{10}$ cm^{-3}.[167] The low surface defect density can lead to a low surface recombination rate.

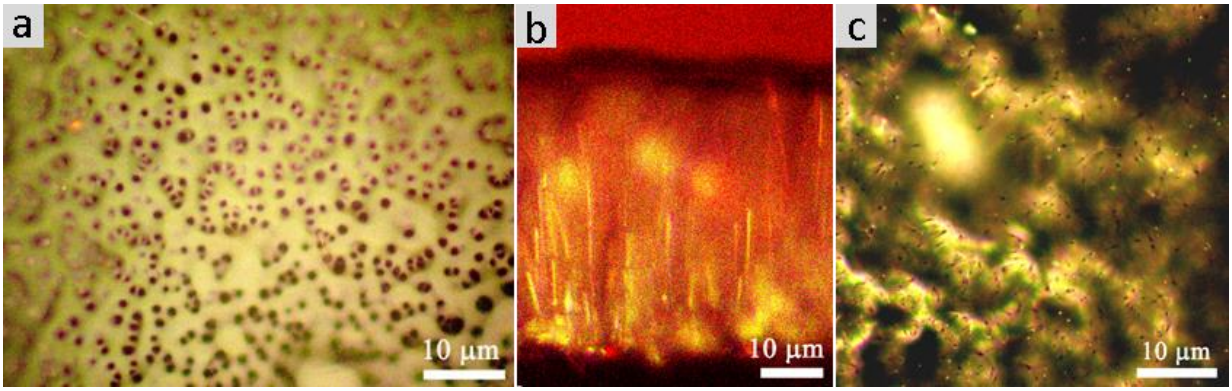

Figure 7.4. Optical microscope images of **a)** PDMS with embedded CuO NWs, **b)** the cross-section of the PDMS with CuO NWs, **c)** PDMS with embedded CuO NWs after RIE etching to expose CuO NWs.

After we peeled the PDMS with embedded CuO NWs from glass substrates, the PDMS films were taken to an optical microscope to look at the NWs. The black points in **Figure 7.4a** are CuO NWs tips. These points disperse very well without bundling with each other and no crashed NWs are observed. To confirm that the CuO NWs are successfully transferred to the PDMS substrates, we took a cross-section image of the sample, which is shown in **Figure 7.4b**. The CuO NWs stand vertically without showing any bundled and crashed NWs. To remove the extra-PDMS from the substrates to expose the CuO NWs for ZnO deposition and electrode patterning, we used RIE to etch 8-10 μm PDMS away**. Figure 7.4c** shows the exposed CuO NWs after 8 minutes

etching. The NW tips in **Figure 7.4c** can be clearly observed through optical microscope, showing exposed sharp NW tips.

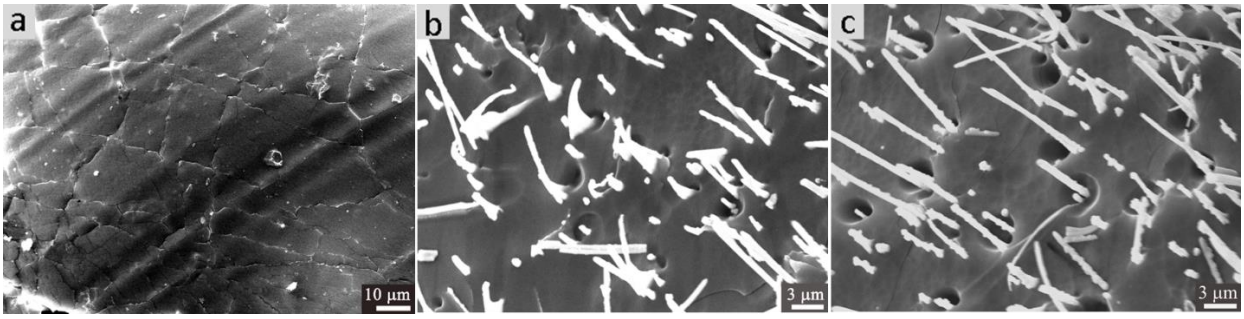

Figure 7.5. SEM images of **a)** PDMS surface with CuO NWs embedded, **b)** PDMS after etching for 8 minutes to expose CuO NWs, **c)** 42 nm ALD ZnO deposited on the exposed CuO NWs.

The PDMS surface is flat with some stretch textures (**Figure 7.5a**). When the PDMS is etched away by SF6 plasma, the embedded CuO NWs are exposed, which are shown in **Figure 7.5b**. Then, to make heterojunctions using these vertical CuO NWs, we deposit 42 nm ZnO on CuO NWs (**Figure 7.5c**). The ZnO fully covers the CuO and works as an n-type semiconductor to collect electrons. We still see the CuO NWs because the ZnO film thickness is too thin.

Current voltage relation is measured on the vertical CuO NWs embedded into PDMS substrates with the NW tips exposed on both sides under dark and visible light. The J-V curve is shown in **Figure 7.6a**. A photocurrent is observed. At 1 V, the photocurrent density with a value of 5.6 mA/cm^2 is 9.8 times higher than dark current density. The J-V curve is nonlinear, indicating the Au electrodes and CuO form Schottky contacts.

Due to the excellent light absorption performance of vertical CuO NW arrays, we deposit 40 nm ALD ZnO on to CuO NWs to form a heterojunction solar cell structure. Au electrodes are patterned on both sides. The front electrons have an Au thickness of 10 nm, showing 60%

transparency (**Figure 7.1b**). The CuO NWs-ZnO heterojunctions are measured under dark and visible light. The J-V curve is shown in **Figure 7.6b**. Front electrodes are 1 nm Cr and 10 nm Au deposited by thermal evaporation. After visible light illumination, the heterojunctions display light response. An open voltage of -0.4 V is obtained. However, the short current density is very low with a value of 10.4 μA/cm^2, resulting in no calculated efficiency from the CuO NWs heterojunctions.

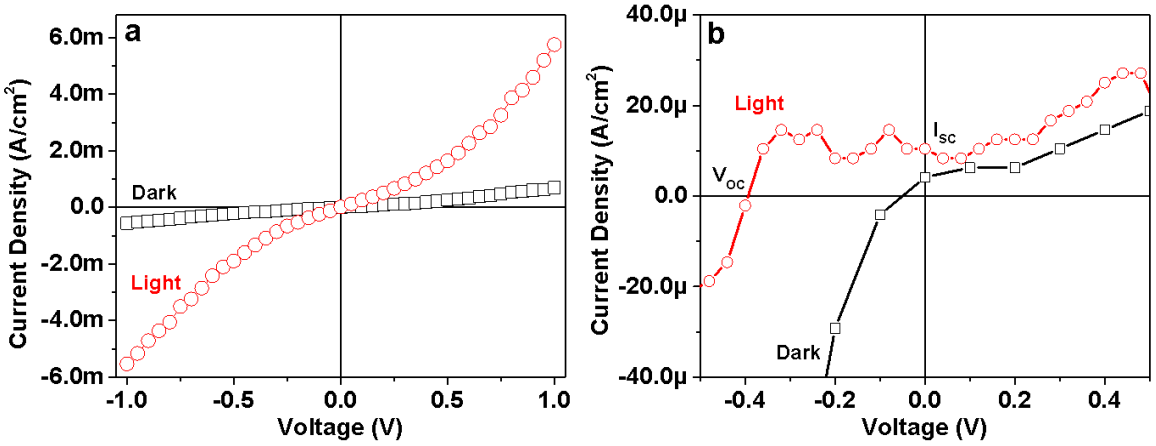

Figure 7.6. J-V characteristic measured under visible light for **a)** vertical CuO NWs, **b)** CuO NWs-ZnO solar cells.

7.4. Discussion

Vertical NWs has much higher light absorption rate than corresponding to thickness of thin films.[32] CuO has a high light absorption coefficient, showing excellent light absorption in solar spectrum range 200 – 800 nm.[85] According to the relationship between the absorption coefficient (a) and light absorption thickness (t): $I = I_0 exp^{-\alpha t}$, we calculated light absorption length in CuO films using AM1.5 light intensity data from NREL database,[277] which is plotted in **Figure 7.7**. The

calculated results indicates that 95% of light is absorbed with a 30 μm thick CuO film. Thus, 50 μm long CuO NW arrays also can absorb at least 95% of light.

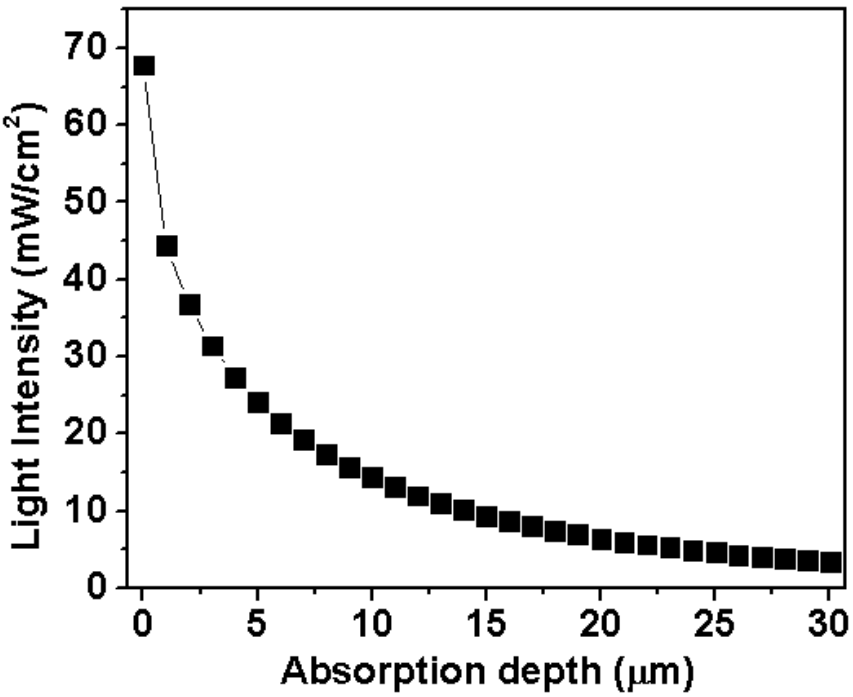

Figure 7.7. The calculated light intensity decay with increase the CuO film thickness.

Single crystalline CuO NWs synthesized by thermal oxidation has a hole mobility of 2-5 cm^2/V·s (μ),[278] and a carrier lifetime of 0.24 ns (τ_h).[41] According to the relationship between holes gth (L_h) and holes lifetime (τ_h): $L_h = (\mu k_B T \tau_h)^{1/2}$,[279] the holes diffusion length is calculated to be 135.6 nm – 339.1 nm, which is larger than the CuO NWs' radius of 115 nm. Due to the large hole diffusion length and high light absorption rate, the light response the vertical CuO NWs is pretty high, showing a current density of 5.6 mA/cm^2, 9.8 times higher than dark current density.

The CuO NWs-ZnO heterojunctions exhibit a very low short current density of 10.4 μA/cm^2, which might be attributed to the small contact area between CuO NW tips and ZnO films leading to an ultra-low electrons collection efficiency. What's more, the hole concentration of CuO

without doping is around $6.51 \times 10^{18}/cm^3$ at room temperature,[54, 55] which may also contributed to the low short current density. The exposed CuO NW tips after SF_6 ions bombarding roughen the surfaces, introducing high density surface defects, which might also contribute to the high interface recombination rate. The open circuit voltage of 0.4 V is similar to the reported CuO based solar cells.[27]

7.5 Conclusions

We successfully created a protocol to transfer CuO NWs to PDMS substrates without breaking and crashing the NW tips. The embedded NWs are exposed from the PDMS substrates by RIE. The vertical NWs show an excellent light absorption. At 1 V, the light current density is 5.6 mA/cm^2, 9.8 times higher than the dark current density.

ALD ZnO is deposited on the CuO NWs to form heterojunctions. The V_{OC} is 0.4 V, which is similar to the reported value of CuO solar cells. However, the I_{SC} is only 10.4 $\mu A/cm^2$, resulting in no calculated efficiency. The small contact areas between CuO NWs and ZnO and the high recombination rate at the interface of CuO NWs and ZnO might contribute to the low performance of the CuO NWs-ZnO heterojunctions. The ZnO film thickness is too thin to efficiently collect electrons.

Chapter 8 Conclusions and future work

This research aims to study CuO, Cu_2O, and ZnO, which are low cost metal oxides abundant in the earth, for the purpose of designing novel function nanostructures for efficient energy harvesting. To combat the cost of synthesizing materials, we employed a thermal oxidation method to oxidize pure commercial Cu foils, thereby synthesizing dense and long single crystalline CuO NWs. Phase transformation is one of strategies to obtain controllability over diverse NW structures. Therefore, we systematically studied the phase transformation kinetics and dynamics of single crystalline CuO NWs and synthesized a series of CuO/Cu_2O core/shell NWs with different CuO/Cu_2O molar ratios. The phase transformation can also cause changes to the surface of NWs, including surface areas and surface defects. As a result, these surface changes lead to a significant effect on the properties of the NWs, such as optoelectronic properties, photoelectrochemical properties, and solar cell performance.

8.1 Conclusions

1. Using Raman spectrum mapping we found direct evidence to show Cu ions quickly diffusing through the grain boundaries of Cu_2O and CuO grain to drive the growth of single crystalline CuO NWs. A transient CuO phase ($Cu_{1+x}O$) was found in the grain boundaries of Cu_2O and CuO crystals because the fast grain boundary diffusion evacuates the Cu ions driven by the chemical potential gradient of Cu, contributing to the $Cu_{1+x}O$ phase formation. We controlled the diffusion processes and synthesized CuO NWs with a length of ~50 μm long CuO NWs and a density of $1.7 \times 10^8/cm^2$ at 600 ^oC for 10 hours. At 700 ^oC for 10 hours, the whole Cu foils with a thickness of 26 μm were completely oxidized into CuO with dense and long CuO NW on the surfaces.

2. Oswald Lussac law predicted that phase transformation from one stable phase to another stable phases passes a series of unstable amorphous phases. However, the amorphous phase is hardly stabilized so that it is difficult to observe the stable amorphous phase during phase transformation, especially in a NW. We designed experiments to slow down the phase transformation kinetics to stablize the amorphous phase on the surface of CuO NWs.

CuO NWs was reduced at 300 ^{o}C with limited numbers of adsorbed CO molecules under 1 torr vacuum. The phase transformation of CuO NWs starts from surface by forming 9-12 nm thick amorphous Cu_2O and then the amorphous phase crystalizes into crystal Cu_2O. The conformal amorphous Cu_2O layer releases stress generated during CuO reduction and prevents the reduced NWs from bending and curving. EDX analysis shows that the amorphous phase is Cu^{+} rich Cu_2O with a Cu/O ratio of 1.8 due to the surface reactions. The KJMA equation was used to model the phase transformation kinetics, indicating that surface diffusion dominates the phase transformation which confirms that surface adsorbed CO predominates the phase transformation kinetics and the temperatures control the O diffusion rate. By controlling the phase transformation rate, we obtained a series of CuO/Cu_2O core/shell NWs with different surface morphologies and a length more than 20 μm.

At 400 ^{o}C for 1 hour, the high temperature completely reduced the CuO NWs into Cu_2O NWs with periodical nodules forming on the surface of NWs. For longer reduction time (> 1 hour), curved Cu_2O NWs still exist, even though the reduction time is as long as 10 hours. However, the morphology and periodicity of the nodules change with different reduction times. The growth of periodical nodules is attributed to Rayleigh instability.

When CuO NWs are fully reduced to Cu_2O NWs, the CuO film below NWs starts to be reduced. After 5 hours reduction, the under layer CuO film is also fully reduced to Cu_2O. The reduction reaction is not dominated by the inward diffusion of CO but by the outward diffusion of O. This chemical potential gradient contributes to the quick film reduction. Appearance of CuO NWs is another factor dramatically increasing the film reduction rate.

3. To show the importance of surface defects in application for optoelectronics, we modulated the single crystal CuO NWs with different thicknesses of ZnO deposited by ALD. In our experiments, we found that the conductivity of the ZnO film with a thickness below 12.6 nm is dominated by surface defects. With a decrease of the film thickness, the surface defects' density increases several times. Therefore, we investigated photocurrent decay processes of CuO NWs, CuO NWs-1 nm ZnO, and CuO NWs-10 nm ZnO by illuminating visible light. CuO NWs can observe band-to-band recombination processes. However, CuO NWs-1nm ZnO and CuO NWs-10 nm ZnO cannot see the band-to-band recombination behavior because of the dense surface defects. Compared with CuO NWs-10 nm ZnO, CuO NWs-1 nm ZnO shows three times higher surface defects so that the photocurrent decay time constant of CuO NWs-1 nm ZnO is three times higher than the time constant of CuO NWs-10 nm ZnO at room temperature. The thermal activation energy of CuO NWs-1 nm ZnO is as low as 30 meV. What's more, 1 nm ZnO on surface of CuO NWs grow as discontinuous NPs. These NPs form localized electronic fields and drive the electrons diffuse to the surface of CuO NWs, changing the conductivity of CuO NWs from p-type to n-type.

4. We applied CuO NWs as photocatalysts for CO_2 photoreduction due to the high density surface defects of CuO NWs-1 nm ZnO. The highest CO yield with a value of 1.9 mmol/g-cat/hr was obtained on the CuO NWs-1 nm ZnO samples until this work was published. There are several reasons for showing such a high CO yield for CO_2 photoreduction. First, the high density of surface

defects increase the numbers of CO_2 reduction. Secondly, the ZnO NPs terminate the surface with (101) planes, which were reported to be charge-neutral planes with low surface energy, making the CO_2 molecular favorable to be adsorbed. Thirdly, the exposed CuO surfaces of the CuO NW between ZnO NPs contribute holes to react with H_2O molecules to generate H^+. These H^+ and electrons on ZnO NPs together complete CO_2 reduction. Finally, the CuO NWs show a narrow band gap of 1.53 eV, which covers the whole range of the light spectrum active for CO_2 reduction from 250 nm to 810 nm.

8.2 Future work

8.2.1. Plasmonic enhanced photocatalytic performance of CO_2

Surface plasmon polarization was recognized on the surface of metals because of the resonant interaction between the surface charge oscillation and the electromagnetic field of the incident light.[280] Because of the interaction, subwavelength metal nanoparticles can concentrate the light to increase light absorption and transfer light energy to the coating semiconductor thin films.[281] The harvested light energy can be transferred into two ways from the metal to the coupling semiconductor materials: direct electron transfer (DET)[257, 282] and plasmon-induced resonant energy transfer (PIRET)[283].

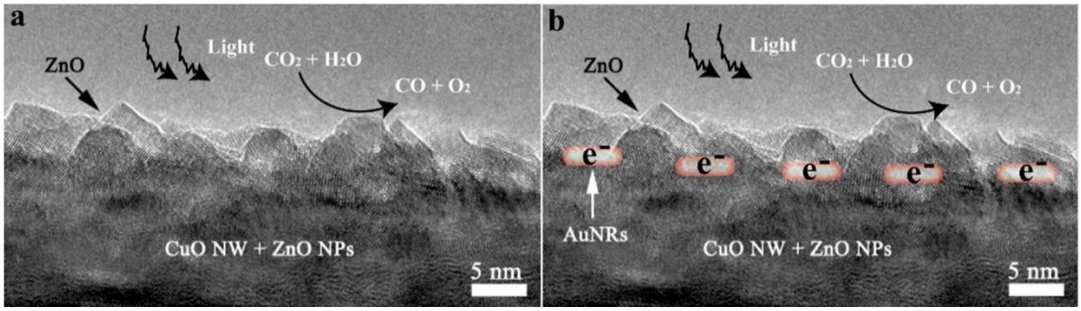

Figure 8.1. a) A nanocomposite consisted of CuO NWs and ZnO NPs for CO_2 photoreduction, **b)** AuNRs decorated CuO NWs-ZnO NPs nanocomposites for CO_2 photoreduction.

In our experiments, we found that single crystalline CuO NWs decorated with dispersed ZnO NPs show a high CO yield with a value of 1.9 mmol/g-cat/hr. To further increase the CO_2 reduction efficiency, AuNRs can be attached to the surface of CuO NWs, and 1 nm ZnO NPs will be deposited to the surface of CuO NWs-AuNRs nanocomposites. The hot electrons excited by surface plasmon of AuNRs transfers to ZnO NPs to increase CO_2 reduction rate. A diagram of these nanocomposites are shown in **Figure 8.1**. The nanostructure in **Figure 7.1a** is the one we used in our experiments. The new structure in **Figure 8.1b** can be used for plasmonic enhanced photocatalytic performance of CO_2 reduction.

8.2.2. CuO/Cu_2O core/shell NWs and Cu_2O NWs for solar cell applications

Cu_2O shows direct band gap of 2.0 eV and has a theoretical PCE of 20%.[93] However, the highest reported PCE of Cu_2O thin film solar cells is 6.1%.[102] The highest reported hole mobility for Cu_2O polycrystalline films is 256 $cm^2/V{\cdot}S$.[284] The minority diffusion length is reported to be 10-100 nm.[285] Thus, a thick Cu_2O film used for light absorber can cause a dramatic loss of the charge collection because of the recombination. To overtake short minority diffusion length caused recombination problem, crystalline Cu_2O NWs can be good candidates for solar cell applications.

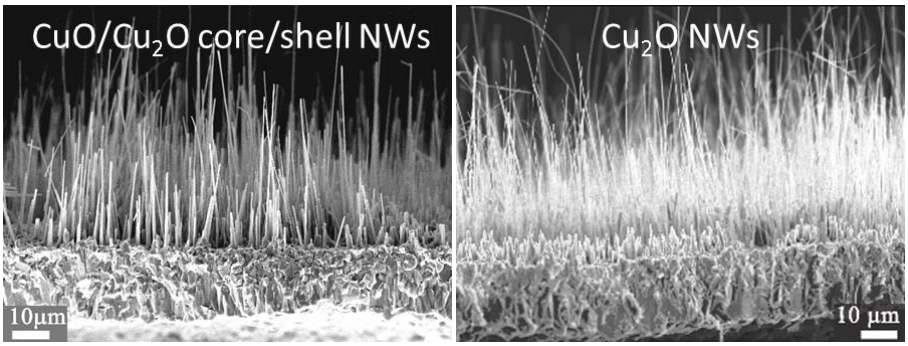

Figure 8.2. Cross-section SEM images of CuO/Cu_2O core/shell NWs and Cu_2O NWs with a length up to 50 μm.

In our experiments, we have synthesized CuO/Cu_2O core/shell NWs and Cu_2O NWs with a maximum length of 50 μm (**Figure 8.2**). These long NWs can be extracted by PDMS for fabricating flexible solar cells using the protocol developed in this research.

References

1. Yuhas, B. D.; Yang, P. D., Nanowire-Based All-Oxide Solar Cells. *Journal of the American Chemical Society* **2009,** 131, (10), 3756-3761.
2. Lee, J.; Orilall, M. C.; Warren, S. C.; Kamperman, M.; Disalvo, F. J.; Wiesner, U., Direct access to thermally stable and highly crystalline mesoporous transition-metal oxides with uniform pores. *Nature Materials* **2008,** 7, (3), 222-228.
3. Law, M.; Greene, L. E.; Johnson, J. C.; Saykally, R.; Yang, P. D., Nanowire dye-sensitized solar cells. *Nature Materials* **2005,** 4, (6), 455-459.
4. Paracchino, A.; Laporte, V.; Sivula, K.; Gratzel, M.; Thimsen, E., Highly active oxide photocathode for photoelectrochemical water reduction. *Nature Materials* **2011,** 10, (6), 456-461.
5. Fortunato, E.; Barquinha, P.; Martins, R., Oxide Semiconductor Thin-Film Transistors: A Review of Recent Advances. *Advanced Materials* **2012,** 24, (22), 2945-2986.
6. Wang, W. N.; An, W. J.; Ramalingam, B.; Mukherjee, S.; Niedzwiedzki, D. M.; Gangopadhyay, S.; Biswas, P., Size and Structure Matter: Enhanced CO_2 Photoreduction Efficiency by Size-Resolved Ultrafine Pt Nanoparticles on TiO_2 Single Crystals. *Journal of the American Chemical Society* **2012,** 134, (27), 11276-11281.
7. Zhong, M. L.; Zeng, D. C.; Liu, Z. W.; Yu, H. Y.; Zhong, X. C.; Qiu, W. Q., Synthesis, growth mechanism and gas-sensing properties of large-scale CuO nanowires. *Acta Materialia* **2010,** 58, (18), 5926-5932.
8. Kim, S. S.; Na, H. G.; Choi, S.-W.; Kwak, D. S.; Kim, H. W., Novel growth of CuO-functionalized, branched SnO2nanowires and their application to H2S sensors. *Journal of Physics D: Applied Physics* **2012,** 45, (20), 205301.
9. Alivisatos, A. P., Semiconductor clusters, nanocrystals, and quantum dots. *Science* **1996,** 271, (5251), 933-937.
10. Alda, J.; Rico-Garc á, J. M.; L ópez-Alonso, J. M.; Boreman, G., Optical antennas for nano-photonic applications. *Nanotechnology* **2005,** 16, (5), S230-S234.
11. Cui, Y.; Wei, Q. Q.; Park, H. K.; Lieber, C. M., Nanowire nanosensors for highly sensitive and selective detection of biological and chemical species. *Science* **2001,** 293, (5533), 1289-1292.
12. Huang, Y.; Duan, X. F.; Cui, Y.; Lauhon, L. J.; Kim, K. H.; Lieber, C. M., Logic gates and computation from assembled nanowire building blocks. *Science* **2001,** 294, (5545), 1313-1317.
13. Andzane, J.; Petkov, N.; Livshits, A. I.; Boland, J. J.; Holmes, J. D.; Erts, D., Two-terminal nanoelectromechanical devices based on germanium nanowires. *Nano Letters* **2009,** 9, (5), 1824-1829.
14. Wang, X. D.; Summers, C. J.; Wang, Z. L., Large-scale hexagonal-patterned growth of aligned ZnO nanorods for nano-optoelectronics and nanosensor arrays. *Nano Letters* **2004,** 4, (3), 423-426.
15. Wang, Z. L.; Song, J. H., Piezoelectric nanogenerators based on zinc oxide nanowire arrays. *Science* **2006,** 312, (5771), 242-246.
16. Rao, P. M.; Zheng, X. L., Rapid catalyst-free flame synthesis of dense, aligned alpha-Fe_2O_3 Nanoflake and CuO Nanoneedle Arrays. *Nano Letters* **2009,** 9, (8), 3001-3006.
17. Liu, S. M.; Gan, L. M.; Liu, L. H.; Zhang, W. D.; Zeng, H. C., Synthesis of single-crystalline TiO2 nanotubes. *Chemistry of Materials* **2002,** 14, (3), 1391-1397.
18. Kumar, M. A.; Jung, S.; Ji, T., Protein biosensors based on polymer nanowires, carbon nanotubes and zinc oxide nanorods. *Sensors* **2011,** 11, (5), 5087-5111.
19. Devan, R. S.; Gao, S. Y.; Ho, W. D.; Lin, J. H.; Ma, Y. R.; Patil, P. S.; Liou, Y., Electrochromic properties of large-area and high-density arrays of transparent one-dimensional beta-Ta_2O_5 nanorods on indium-tin-oxide thin-films. *Applied Physics Letters* **2011,** 98, (13), 133117.
20. Zhu, K.; Neale, N. R.; Miedaner, A.; Frank, A. J., Enhanced charge-collection efficiencies and light scattering in dye-sensitized solar cells using oriented TiO_2 nanotubes arrays. *Nano Letters* **2007,** 7, (1), 69-74.

21. He, Y. B.; Li, G. R.; Wang, Z. L.; Su, C. Y.; Tong, Y. X., Single-crystal ZnO nanorod/amorphous and nanoporous metal oxide shell composites: Controllable electrochemical synthesis and enhanced supercapacitor performances. *Energy & Environmental Science* **2011,** 4, (4), 1288-1292.
22. Kim, J.; Yun, J. H.; Kim, C. H.; Park, Y. C.; Woo, J. Y.; Park, J.; Lee, J. H.; Yi, J.; Han, C. S., ZnO nanowire-embedded Schottky diode for effective UV detection by the barrier reduction effect. *Nanotechnology* **2010,** 21, (11), 115205.
23. Nguyen, P.; Ng, H. T.; Yamada, T.; Smith, M. K.; Li, J.; Han, J.; Meyyappan, M., Direct integration of metal oxide nanowire in vertical field-effect transistor. *Nano Letters* **2004,** 4, (4), 651-657.
24. Casadei, A.; Pecora, E. F.; Trevino, J.; Forestiere, C.; Ruffer, D.; Russo-Averchi, E.; Matteini, F.; Tutuncuoglu, G.; Heiss, M.; Fontcuberta i Morral, A.; Dal Negro, L., Photonic-plasmonic coupling of GaAs single nanowires to optical nanoantennas. *Nano Lett* **2014,** 14, (5), 2271-2278.
25. Kim, T. W.; Ha, H.-W.; Paek, M.-J.; Hyun, S.-H.; Choy, J.-H.; Hwang, S.-J., Unique phase transformation behavior and visible light photocatalytic activity of titanium oxide hybridized with copper oxide. *Journal of Materials Chemistry* **2010,** 20, (16), 3238-3245.
26. Olsen, L. C.; Bohara, R. C.; Urie, M. W., Explanation for low-efficiency Cu_2O Schottky-barrier solar-cells. *Applied Physics Letters* **1979,** 34, (1), 47-49.
27. Wang, P.; Zhao, X. H.; Li, B. J., ZnO-coated CuO nanowire arrays: fabrications, optoelectronic properties, and photovoltaic applications. *Optics Express* **2011,** 19, (12), 11271-11279.
28. Mittiga, A.; Salza, E.; Sarto, F.; Tucci, M.; Vasanthi, R., Heterojunction solar cell with 2% efficiency based on a Cu_2O substrate. *Applied Physics Letters* **2006,** 88, (16), 163502.
29. Bu, I. Y. Y., Novel all solution processed heterojunction using p-type cupric oxide and n-type zinc oxide nanowires for solar cell applications. *Ceramics International* **2013,** 39, (7), 8073-8078.
30. Mittiga, A.; Salza, E.; Sarto, F.; Tucci, M.; Vasanthi, R., Heterojunction solar cell with 2% efficiency based on a Cu_2O substrate. *Applied Physics Letters* **2006,** 88, (16).
31. Garnett, E. C.; Brongersma, M. L.; Cui, Y.; McGehee, M. D., Nanowire solar cells. *Annual Review of Materials Research* **2011,** 41, (1), 269-295.
32. Kayes, B. M.; Atwater, H. A.; Lewis, N. S., Comparison of the device physics principles of planar and radial p-n junction nanorod solar cells. *Journal of Applied Physics* **2005,** 97, (11), 114302.
33. Xu, C. H.; Woo, C. H.; Shi, S. Q., Formation of CuO nanowires on Cu foil. *Chemical Physics Letters* **2004,** 399, (1-3), 62-66.
34. Yuan, L.; Wang, Y. Q.; Mema, R.; Zhou, G. W., Driving force and growth mechanism for spontaneous oxide nanowire formation during the thermal oxidation of metals. *Acta Materialia* **2011,** 59, (6), 2491-2500.
35. Liao, L.; Yan, B.; Hao, Y. F.; Xing, G. Z.; Liu, J. P.; Zhao, B. C.; Shen, Z. X.; Wu, T.; Wang, L.; Thong, J. T. L.; Li, C. M.; Huang, W.; Yu, T., P-type electrical, photoconductive, and anomalous ferromagnetic properties of Cu2O nanowires. *Applied Physics Letters* **2009,** 94, (11), 113106.
36. Wang, R. C.; Lin, H. Y., Efficient surface enhanced Raman scattering from Cu_2O porous nanowires transformed from CuO nanowires by plasma treatments. *Materials Chemistry and Physics* **2012,** 136, (2-3), 661-665.
37. Meyer, B. K.; Alves, H.; Hofmann, D. M.; Kriegseis, W.; Forster, D.; Bertram, F.; Christen, J.; Hoffmann, A.; Strassburg, M.; Dworzak, M.; Haboeck, U.; Rodina, A. V., Bound exciton and donor-acceptor pair recombinations in ZnO. *Physica Status Solidi B-Basic Solid State Physics* **2004,** 241, (2), 231-260.
38. Beek, W. J. E.; Wienk, M. M.; Janssen, R. A. J., Efficient hybrid solar cells from zinc oxide nanoparticles and a conjugated polymer. *Advanced Materials* **2004,** 16, (12), 1009-1013.
39. Wei, Y. F.; Ke, L.; Kong, J. H.; Liu, H.; Jiao, Z. H.; Lu, X. H.; Du, H. J.; Sun, X. W., Enhanced photoelectrochemical water-splitting effect with a bent ZnO nanorod photoanode decorated with Ag nanoparticles. *Nanotechnology* **2012,** 23, (23), 235401.
40. Wang, C. J.; Ranasingha, O.; Natesakhawat, S.; Ohodnicki, P. R.; Andio, M.; Lewis, J. P.; Matranga, C., Visible light plasmonic heating of Au-ZnO for the catalytic reduction of CO_2. *Nanoscale* **2013,** 5, (15), 6968-6974.

41. Wang, W. N.; Wu, F.; Myung, Y.; Niedzwiedzki, D. M.; Im, H. S.; Park, J.; Banerjee, P.; Biswas, P., Surface engineered CuO nanowires with ZnO islands for CO_2 photoreduction. *ACS Applied Materials & Interfaces* **2015,** 7, (10), 5685-5692.
42. Panigrahy, B.; Aslam, M.; Misra, D. S.; Ghosh, M.; Bahadur, D., Defect-related emissions and magnetization properties of ZnO nanorods. *Advanced Functional Materials* **2010,** 20, (7), 1161-1165.
43. Djurisic, A. B.; Leung, Y. H., Optical properties of ZnO nanostructures. *Small* **2006,** 2, (8-9), 944-961.
44. Kempa, T. J.; Day, R. W.; Kim, S. K.; Park, H. G.; Lieber, C. M., Semiconductor nanowires: a platform for exploring limits and concepts for nano-enabled solar cells. *Energy & Environmental Science* **2013,** 6, (3), 719-733.
45. Martin, L.; Martinez, H.; Poinot, D.; Pecquenard, B.; Le Cras, F., Comprehensive X-ray photoelectron spectroscopy study of the conversion reaction mechanism of CuO in lithiated thin film electrodes. *Journal of Physical Chemistry C* **2013,** 117, (9), 4421-4430.
46. Chen, H. M.; Chen, C. K.; Liu, R. S.; Zhang, L.; Zhang, J. J.; Wilkinson, D. P., Nano-architecture and material designs for water splitting photoelectrodes. *Chemical Society Reviews* **2012,** 41, (17), 5654-5671.
47. Meyer, B. K.; Polity, A.; Reppin, D.; Becker, M.; Hering, P.; Klar, P. J.; Sander, T.; Reindl, C.; Benz, J.; Eickhoff, M.; Heiliger, C.; Heinemann, M.; Blasing, J.; Krost, A.; Shokovets, S.; Muller, C.; Ronning, C., Binary copper oxide semiconductors: from materials towards devices. *Physica Status Solidi B-Basic Solid State Physics* **2012,** 249, (8), 1487-1509.
48. Bourne, L. C.; Yu, P. Y.; Zettl, A.; Cohen, M. L., High-pressure electrical-conductivity measurements in the copper oxides. *Physical Review B* **1989,** 40, (16), 10973-10976.
49. Wu, D. X.; Zhang, Q. M.; Tao, M., LSDA+U study of cupric oxide: Electronic structure and native point defects. *Physical Review B* **2006,** 73, (23), 235206.
50. Hu, J.; Li, D. D.; Lu, J. G.; Wu, R. Q., Effects on electronic properties of molecule adsorption on CuO surfaces and nanowires. *Journal of Physical Chemistry C* **2010,** 114, (40), 17120-17126.
51. Luo, L. B.; Wang, X. H.; Xie, C.; Li, Z. J.; Lu, R.; Yang, X. B.; Lu, J., One-dimensional CuO nanowire: synthesis, electrical, and optoelectronic devices application. *Nanoscale Research Letters* **2014,** 9, 1-8.
52. Ito, T.; Yamaguchi, H.; Okabe, K.; Masumi, T., Single-crystal growth and characterization of Cu2O and CuO. *Journal of Materials Science* **1998,** 33, (14), 3555-3566.
53. Soon, A.; Todorova, M.; Delley, B.; Stampfl, C., Thermodynamic stability and structure of copper oxide surfaces: A first-principles investigation. *Physical Review B* **2007,** 76, (12), 125420.
54. Musa, A. O.; Akomolafe, T.; Carter, M. J., Production of cuprous oxide, a solar cell material, by thermal oxidation and a study of its physical and electrical properties. *Solar Energy Materials and Solar Cells* **1998,** 51, (3-4), 305-316.
55. Huang, Q.; Wang, L.; Bi, X. F., On the dependence of hole concentration and its mobility on crystallization degree in p-type cuprous oxide film. *Journal of Physics D-Applied Physics* **2013,** 46, (50).
56. Wang, W.; Liu, Z.; Liu, Y.; Xu, C.; Zheng, C.; Wang, G., A simple wet-chemical synthesis and characterization of CuO nanorods. *Applied Physics a-Materials Science & Processing* **2003,** 76, (3), 417-420.
57. Wang, Y. I.; Suh, J. Y.; Lee, Y. S.; Shim, J. H.; Fleury, E.; Cho, Y. W.; Koh, S. U., Direct measurement of hydrogen diffusivity through Pd-coated Ni-based amorphous metallic membranes. *Journal of Membrane Science* **2013,** 436, 195-201.
58. Lu, C. H.; Qi, L. M.; Yang, J. H.; Zhang, D. Y.; Wu, N. Z.; Ma, J. M., Simple template-free solution route for the controlled synthesis of $Cu(OH)_2$ and CuO nanostructures. *Journal of Physical Chemistry B* **2004,** 108, (46), 17825-17831.
59. Ethiraj, A. S.; Kang, D. J., Synthesis and characterization of CuO nanowires by a simple wet chemical method. *Nanoscale Research Letters* **2012,** 7.
60. Wang, W. Z.; Wang, G. H.; Wang, X. S.; Zhan, Y. J.; Liu, Y. K.; Zheng, C. L., Synthesis and characterization of Cu_2O nanowires by a novel reduction route. *Advanced Materials* **2002,** 14, (1), 67-69.

61. Hacialioglu, S.; Meng, F.; Jin, S., Facile and mild solution synthesis of Cu_2O nanowires and nanotubes driven by screw dislocations. *Chemical Communications* **2012,** 48, (8), 1174-1176.
62. Kumar, A.; Srivastava, A. K.; Tiwari, P.; Nandedkar, R. V., The effect of growth parameters on the aspect ratio and number density of CuO nanorods. *Journal of Physics: Condensed Matter* **2004,** 16, (47), 8531-8543.
63. Kaur, M.; Muthe, K. P.; Despande, S. K.; Choudhury, S.; Singh, J. B.; Verma, N.; Gupta, S. K.; Yakhmi, J. V., Growth and branching of CuO nanowires by thermal oxidation of copper. *Journal of Crystal Growth* **2006,** 289, (2), 670-675.
64. Pfefferkorn, V. G., den Oxydationsvorgang von Metallen. *Naturwiss* **1953,** 40, 2.
65. Jiang, X. C.; Herricks, T.; Xia, Y. N., CuO nanowires can be synthesized by heating copper substrates in air. *Nano Letters* **2002,** 2, (12), 1333-1338.
66. Chen, J. T.; Zhang, F.; Wang, J.; Zhang, G. A.; Miao, B. B.; Fan, X. Y.; Yan, D.; Yan, P. X., CuO nanowires synthesized by thermal oxidation route. *Journal of Alloys and Compounds* **2008,** 454, (1-2), 268-273.
67. Goncalves, A. M. B.; Campos, L. C.; Ferlauto, A. S.; Lacerda, R. G., On the growth and electrical characterization of CuO nanowires by thermal oxidation. *Journal of Applied Physics* **2009,** 106, (3), 034303.
68. Zhang, Q. B.; Zhang, K. L.; Xu, D. G.; Yang, G. C.; Huang, H.; Nie, F. D.; Liu, C. M.; Yang, S. H., CuO nanostructures: Synthesis, characterization, growth mechanisms, fundamental properties, and applications. *Progress in Materials Science* **2014,** 60, 208-337.
69. Kumar, A.; Srivastava, A. K.; Tiwari, P.; Nandedkar, R. V., The effect of growth parameters on the aspect ratio and number density of CuO nanorods. *Journal of Physics-Condensed Matter* **2004,** 16, (47), 8531-8543.
70. Li, X. Z.; Zhang, J.; Yuan, Y. W.; Liao, L. M.; Pan, C. X., Effect of electric field on CuO nanoneedle growth during thermal and its growth mechanism. *Journal of Applied Physics* **2010,** 108, (2).
71. Liu, J.; Jin, J.; Deng, Z.; Huang, S. Z.; Hu, Z. Y.; Wang, L.; Wang, C.; Chen, L. H.; Li, Y.; Van Tendeloo, G.; Su, B. L., Tailoring CuO nanostructures for enhanced photocatalytic property. *Journal of Colloid and Interface Science* **2012,** 384, 1-9.
72. Farbod, M.; Ghaffari, N. M.; Kazeminezhad, I., Effect of growth parameters on photocatalytic properties of CuO nanowires fabricated by direct oxidation. *Materials Letters* **2012,** 81, 258-260.
73. Kuo, C. H.; Chen, C. H.; Huang, M. H., Seed-mediated synthesis of monodispersed Cu_2O nanocubes with five different size ranges from 40 to 420 nm. *Advanced Functional Materials* **2007,** 17, (18), 3773-3780.
74. Yu, Y.; Zhang, L. Y.; Wang, J.; Yang, Z.; Long, M. C.; Hu, N. T.; Zhang, Y. F., Preparation of hollow porous Cu_2O microspheres and photocatalytic activity under visible light irradiation. *Nanoscale Research Letters* **2012,** 7.
75. Pan, Y. L.; Deng, S. Z.; Polavarapu, L.; Gao, N. Y.; Yuan, P. Y.; Sow, C. H.; Xu, Q. H., Plasmon-enhanced photocatalytic properties of Cu_2O nanowire-Au nanoparticle assemblies. *Langmuir* **2012,** 28, (33), 12304-12310.
76. Sunkara, S.; Vendra, V. K.; Kim, J. H.; Druffel, T.; Sunkara, M. K., Scalable synthesis and photoelectrochemical properties of copper oxide nanowire arrays and films. *Catalysis Today* **2013,** 199, 27-35.
77. Choi, H. J.; Kang, M., Hydrogen production from methanol/water decomposition in a liquid photosystem using the anatase structure of Cu loaded TiO_2. *International Journal of Hydrogen Energy* **2007,** 32, (16), 3841-3848.
78. Tang, H. W.; Matin, M. A.; Wang, H. L.; Sudhakar, S.; Chen, L.; Al-Jassim, M. M.; Yan, Y. F., Enhancing the stability of CuO thin-film photoelectrodes by Ti alloying. *Journal of Electronic Materials* **2012,** 41, (11), 3062-3067.
79. Han, J. F.; Zong, X.; Zhou, X.; Li, C., Cu_2O/CuO photocathode with improved stability for photoelectrochemical water reduction. *Rsc Advances* **2015,** 5, (14), 10790-10794.
80. de Jongh, P. E.; Vanmaekelbergh, D.; Kelly, J. J., Cu_2O: a catalyst for the photochemical decomposition of water? *Chemical Communications* **1999**, (12), 1069-1070.

81. Lewis, N. S., Toward cost-effective solar energy use. *Science* **2007,** 315, (5813), 798-801.
82. Chen, L.; Shet, S.; Tang, H. W.; Wang, H. L.; Deutsch, T.; Yan, Y. F.; Turner, J.; Al-Jassim, M., Electrochemical deposition of copper oxide nanowires for photoelectrochemical applications. *Journal of Materials Chemistry* **2010,** 20, (33), 6962-6967.
83. Lin, C. Y.; Lai, Y. H.; Mersch, D.; Reisner, E., Cu_2O vertical bar NiOx nanocomposite as an inexpensive photocathode in photoelectrochemical water splitting. *Chemical Science* **2012,** 3, (12), 3482-3487.
84. Zhang, Z. H.; Dua, R.; Zhang, L. B.; Zhu, H. B.; Zhang, H. N.; Wang, P., Carbon-layer-protected cuprous oxide nanowire arrays for efficient water reduction. *Acs Nano* **2013,** 7, (2), 1709-1717.
85. Shabu, R.; Raj, A. M. E.; Sanjeeviraja, C.; Ravidhas, C., Assessment of CuO thin films for its suitablity as window absorbing layer in solar cell fabrications. *Materials Research Bulletin* **2015,** 68, 1-8.
86. Maruyama, T., Copper oxide thin films prepared by chemical vapor deposition from copper dipivaloylmethanate. *Solar Energy Materials and Solar Cells* **1998,** 56, (1), 85-92.
87. Chen, A. P.; Yang, G.; Long, H.; Li, F.; Li, Y. H.; Lu, P. X., Nonlinear optical properties of laser deposited CuO thin films. *Thin Solid Films* **2009,** 517, (15), 4277-4280.
88. Lim, Y. F.; Choi, J. J.; Hanrath, T., Facile synthesis of colloidal CuO nanocrystals for light-harvesting applications. *Journal of Nanomaterials* **2012**.
89. Bao, Q. L.; Li, C. M.; Liao, L.; Yang, H. B.; Wang, W.; Ke, C.; Song, Q. L.; Bao, H. F.; Yu, T.; Loh, K. P.; Guo, J., Electrical transport and photovoltaic effects of core-shell CuO/C-60 nanowire heterostructure. *Nanotechnology* **2009,** 20, (6).
90. Gao, F.; Liu, X. J.; Zhang, J. S.; Song, M. Z.; Li, N., Photovoltaic properties of the p-CuO/n-Si heterojunction prepared through reactive magnetron sputtering. *Journal of Applied Physics* **2012,** 111, (8).
91. Masudy-Panah, S.; Dalapati, G. K.; Radhakrishnan, K.; Kumar, A.; Tan, H. R., Reduction of Cu-rich interfacial layer and improvement of bulk CuO property through two-step sputtering for p-CuO/n-Si heterojunction solar cell. *Journal of Applied Physics* **2014,** 116, (7), 074501.
92. Akkari, F. C.; Kanzari, M., Optical, structural, and electrical properties of Cu_2O thin films. *Physica Status Solidi a-Applications and Materials Science* **2010,** 207, (7), 1647-1651.
93. Chen, J. W.; Perng, D. C.; Fang, J. F., Nano-structured Cu_2O solar cells fabricated on sparse ZnO nanorods. *Solar Energy Materials and Solar Cells* **2011,** 95, (8), 2471-2477.
94. Tsur, Y.; Riess, I., Self-compensation in semiconductors. *Physical Review B* **1999,** 60, (11), 8138-8146.
95. Hsu, F. Y.; Liu, S. J.; Lu, Y. I.; Chen, L. Y.; Fang, H. W., Fabrication and Characterization of Oxide Heterojunctions Prepared by Electrodepositing Cuprous Oxide on Conductive Glasses. *Japanese Journal of Applied Physics* **2009,** 48, (3), 035501.
96. Li, D. D.; Chien, C. J.; Deora, S.; Chang, P. C.; Moulin, E.; Lu, J. G., Prototype of a scalable core-shell Cu_2O/TiO_2 solar cell. *Chemical Physics Letters* **2011,** 501, (4-6), 446-450.
97. Minami, T.; Miyata, T.; Ihara, K.; Minamino, Y.; Tsukada, S., Effect of ZnO film deposition methods on the photovoltaic properties of ZnO-Cu_2O heterojunction devices. *Thin Solid Films* **2006,** 494, (1-2), 47-52.
98. Hsueh, T. J.; Hsu, C. L.; Changa, S. J.; Guo, P. W.; Hsieh, J. H.; Chen, I. C., Cu_2O/n-ZnO nanowire solar cells on ZnO : Ga/glass templates. *Scripta Materialia* **2007,** 57, (1), 53-56.
99. Benjamin D. Yuhas, P. Y., Nanowire-based all-oxide solar cells. *J. Am. Chem. Soc.* **2009,** 131, 6.
100. Lee, Y. S.; Heo, J.; Siah, S. C.; Mailoa, J. P.; Brandt, R. E.; Kim, S. B.; Gordon, R. G.; Buonassisi, T., Ultrathin amorphous zinc-tin-oxide buffer layer for enhancing heterojunction interface quality in metal-oxide solar cells. *Energy & Environmental Science* **2013,** 6, (7), 2112-2118.
101. Minami, T.; Nishi, Y.; Miyata, T., High-efficiency Cu_2O-based heterojunction solar cells babricated using a Ga_2O_3 thin film as n-type layer. *Applied Physics Express* **2013,** 6, (4), 044101.
102. Minami, T.; Nishi, Y.; Miyata, T., Heterojunction solar cell with 6% efficiency based on an n-type aluminum-gallium-xide thin film and p-type sodium-doped Cu_2O sheet. *Applied Physics Express* **2015,** 8, (2), 022301.

103. Minami, T.; Nishi, Y.; Miyata, T.; Nomoto, J., High-efficiency oxide solar cells with ZnO/Cu_2O heterojunction fabricated on thermally oxidized Cu_2O sheets. *Applied Physics Express* **2011,** 4, (6), 062301.
104. Wei, H.; Gong, H.; Wang, Y.; Hu, X.; Chen, L.; Xu, H.; Liu, P.; Cao, B., Three kinds of Cu_2O/ZnO heterostructure solar cells fabricated with electrochemical deposition and their structure-related photovoltaic properties. *CrystEngComm* **2011,** 13, (20), 6065-6070.
105. McShane, C. M.; Choi, K.-S., Junction studies on electrochemically fabricated p–n Cu_2O homojunction solar cells for efficiency enhancement. *Physical Chemistry Chemical Physics* **2012,** 14, (17), 6112-6118.
106. Izaki, M.; Shinagawa, T.; Mizuno, K. T.; Ida, Y.; Inaba, M.; Tasaka, A., Electrochemically constructed p-Cu2O/n-ZnO heterojunction diode for photovoltaic device. *Journal of Physics D-Applied Physics* **2007,** 40, (11), 3326-3329.
107. Fujimoto, K.; Oku, T.; Akiyama, T., Fabrication and characterization of ZnO/Cu_2O Solar Cells prepared by electrodeposition. *Applied Physics Express* **2013,** 6, (8), 086503.
108. Li, D.; Chien, C.-J.; Deora, S.; Chang, P.-C.; Moulin, E.; Lu, J. G., Prototype of a scalable core–shell Cu_2O/TiO_2 solar cell. *Chemical Physics Letters* **2011,** 501, (4-6), 446-450.
109. Duan, Z.; Du Pasquier, A.; Lu, Y.; Xu, Y.; Garfunkel, E., Effects of Mg composition on open circuit voltage of Cu_2O–$MgxZn_{1-x}O$ heterojunction solar cells. *Solar Energy Materials and Solar Cells* **2012,** 96, 292-297.
110. Cui, J. B.; Gibson, U. J., A Simple Two-Step Electrodeposition of Cu_2O/ZnO Nanopillar Solar Cells. *Journal of Physical Chemistry C* **2010,** 114, (14), 6408-6412.
111. Omayio, E. O., Karimi, P. M., Njoroge, W. K., Mugwanga, F. K., Current-voltage characteristics of p-CuO/n-ZnO:Sn Solar cell. *Int. J. Thin Film Sci. Tec.* **2013,** 2, 4.
112. Langmar, O.; Ganivet, C. R.; Lennert, A.; Costa, R. D.; de la Torre, G.; Torres, T.; Guldi, D. M., Combining electron-accepting phthalocyanines and nanorod-like CuO electrodes for p-type dye-Sensitized Solar Cells. *Angewandte Chemie-International Edition* **2015,** 54, (26), 7688-7692.
113. Anandan, S.; Wen, X.; Yang, S., Room temperature growth of CuO nanorod arrays on copper and their application as a cathode in dye-sensitized solar cells. *Materials Chemistry and Physics* **2005,** 93, (1), 35-40.
114. Wei, H. M.; Gong, H. B.; Wang, Y. Z.; Hu, X. L.; Chen, L.; Xu, H. Y.; Liu, P.; Cao, B. Q., Three kinds of Cu_2O/ZnO heterostructure solar cells fabricated with electrochemical deposition and their structure-related photovoltaic properties. *Crystengcomm* **2011,** 13, (20), 6065-6070.
115. Duan, Z. Q.; Du Pasquier, A.; Lu, Y. C.; Xu, Y.; Garfunkel, E., Effects of Mg composition on open circuit voltage of Cu_2O-$MgxZn_{1-x}O$ heterojunction solar cells. *Solar Energy Materials and Solar Cells* **2012,** 96, (1), 292-297.
116. Herrera, J. E.; Kwak, J. H.; Hu, J. Z.; Wang, Y.; Peden, C. H. F., Synthesis of nanodispersed oxides of vanadium, titanium, molybdenum, and tungsten on mesoporous silica using atomic layer deposition. *Topics in Catalysis* **2006,** 39, (3-4), 245-255.
117. Annamalai, S.; Parmar, M. K.; Ling, Y.; Balachandar, S., Nonlinear Rayleigh-Taylor instability of a cylindrical interface in explosion flows. *Journal of Fluids Engineering-Transactions of the Asme* **2014,** 136, (6).
118. Marichy, C.; Bechelany, M.; Pinna, N., Atomic layer deposition of nanostructured materials for energy and environmental applications. *Advanced Materials* **2012,** 24, (8), 1017-1032.
119. Puurunen, R. L., Surface chemistry of atomic layer deposition: A case study for the trimethylaluminum/water process. *Journal of Applied Physics* **2005,** 97, (12), 121301.
120. George, S. M., Atomic Layer Deposition: An Overview. *Chemical Reviews* **2010,** 110, (1), 111-131.
121. Tynell, T.; Karppinen, M., Atomic layer deposition of ZnO: a review. *Semiconductor Science and Technology* **2014,** 29, (4), 043001.
122. Tammenmaa, M.; Koskinen, T.; Hiltunen, L.; Niinisto, L.; Leskela, M., Zinc chalcogenide thin-films grown by the atomic layer epitaxy technique using zinc acetate as source material. *Thin Solid Films* **1985,** 124, (2), 125-128.

123. Wang, S.; Petzold, V.; Tripkovic, V.; Kleis, J.; Howalt, J. G.; Skulason, E.; Fernandez, E. M.; Hvolbaek, B.; Jones, G.; Toftelund, A.; Falsig, H.; Bjorketun, M.; Studt, F.; Abild-Pedersen, F.; Rossmeisl, J.; Norskov, J. K.; Bligaard, T., Universal transition state scaling relations for (de)hydrogenation over transition metals. *Physical Chemistry Chemical Physics* **2011,** 13, (46), 20760-20765.
124. Guziewicz, E.; Godlewski, M.; Wachnicki, L.; Krajewski, T. A.; Luka, G.; Gieraltowska, S.; Jakiela, R.; Stonert, A.; Lisowski, W.; Krawczyk, M.; Sobczak, J. W.; Jablonski, A., ALD grown zinc oxide with controllable electrical properties. *Semiconductor Science and Technology* **2012,** 27, (7), 074011.
125. Tanskanen, J. T.; Bakke, J. R.; Pakkanen, T. A.; Bent, S. F., Influence of organozinc ligand design on growth and material properties of ZnS and ZnO deposited by atomic layer deposition. *Journal of Vacuum Science & Technology A* **2011,** 29, (3), 031507.
126. Malm, J.; Sahramo, E.; Perala, J.; Sajavaara, T.; Karppinen, M., Low-temperature atomic layer deposition of ZnO thin films: Control of crystallinity and orientation. *Thin Solid Films* **2011,** 519, (16), 5319-5322.
127. Yuan, N. Y.; Wang, S. Y.; Tan, C. B.; Wang, X. Q.; Chen, G. G.; Ding, J. N., The influence of deposition temperature on growth mode, optical and mechanical properties of ZnO films prepared by the ALD method. *Journal of Crystal Growth* **2013,** 366, 43-46.
128. Pung, S. Y.; Choy, K. L.; Hou, X.; Shan, C. X., Preferential growth of ZnO thin films by the atomic layer deposition technique. *Nanotechnology* **2008,** 19, (43).
129. Park, S. H. K.; Lee, Y. E., Controlling preferred orientation of ZnO thin films by atomic layer deposition. *Journal of Materials Science* **2004,** 39, (6), 2195-2197.
130. Wojcik, A.; Godlewski, M.; Guziewicz, E.; Minikayev, R.; Paszkowicz, W., Controlling of preferential growth mode of ZnO thin films grown by atomic layer deposition. *Journal of Crystal Growth* **2008,** 310, (2), 284-289.
131. Lim, S. J.; Kwon, S. J.; Kim, H.; Park, J. S., High performance thin film transistor with low temperature atomic layer deposition nitrogen-doped ZnO. *Applied Physics Letters* **2007,** 91, (18).
132. Chaisitsak, S.; Yamada, A.; Konagai, M.; Saito, K., Improvement in performances of ZnO : B/i-ZnO/Cu(InGa)Se-2 solar cells by surface treatments for Cu(InGa)Se_2. *Japanese Journal of Applied Physics Part 1-Regular Papers Short Notes & Review Papers* **2000,** 39, (4A), 1660-1664.
133. Lim, D. C.; Kim, K. D.; Park, S. Y.; Hong, E. M.; Seo, H. O.; Lim, J. H.; Lee, K. H.; Jeong, Y.; Song, C.; Lee, E.; Kim, Y. D.; Cho, S., Towards fabrication of high-performing organic photovoltaics: new donor-polymer, atomic layer deposited thin buffer layer and plasmonic effects. *Energy & Environmental Science* **2012,** 5, (12), 9803-9807.
134. Williams, V. O.; Jeong, N. C.; Prasittichai, C.; Farha, O. K.; Pellin, M. J.; Hupp, J. T., Fast Transporting ZnO-TiO_2 coaxial photoanodes for dye-sensitized solar cells based on ALD-modified SiO_2 aerogel frameworks. *Acs Nano* **2012,** 6, (7), 6185-6196.
135. Chien, J. F.; Liao, H. Y.; Yu, S. F.; Lin, R. M.; Shiojiri, M.; Shyue, J. J.; Chen, M. J., Ultraviolet electroluminescence from nitrogen-doped ZnO-based heterojuntion light-emitting diodes prepared by remote plasma in situ atomic layer-doping technique. *ACS Applied Materials & Interfaces* **2013,** 5, (2), 227-232.
136. Kong, B. H.; Cho, H. K.; Kim, M. Y.; Choi, R. J.; Kim, B. K., InGaN/GaN blue light emitting diodes using Al-doped ZnO grown by atomic layer deposition as a current spreading layer. *Journal of Crystal Growth* **2011,** 326, (1), 147-151.
137. Choi, Y. J.; Gong, S. C.; Park, C. S.; Lee, H. S.; Jang, J. G.; Chang, H. J.; Yeom, G. Y.; Park, H. H., Improved performance of organic light-emitting diodes fabricated on Al-doped ZnO anodes incorporating a homogeneous Al-doped ZnO buffer layer grown by atomic layer deposition. *ACS Applied Materials & Interfaces* **2013,** 5, (9), 3650-3655.
138. MacDonald, A. H., Copper oxides get charged up. *Nature* **2001,** 414, 409-410.
139. Feng, Y.; Zheng, X., Plasma-Enhanced Catalytic CuO Nanowires for CO Oxidation. *Nano Letters* **2010,** 10, (11), 4762-4766.

140. Mashock, M.; Yu, K.; Cui, S.; Mao, S.; Lu, G.; Chen, J., Modulating Gas Sensing Properties of CuO Nanowires through Creation of Discrete Nanosized p–n Junctions on Their Surfaces. *ACS Applied Materials & Interfaces* **2012,** 4, (8), 4192-4199.
141. Zhang, Z.; Wang, P., Highly stable copper oxide composite as an effective photocathode for water splitting via a facile electrochemical synthesis strategy. *Journal of Materials Chemistry* **2012,** 22, (6), 2456-2464.
142. Yuan, L.; Wang, Y.; Mema, R.; Zhou, G., Driving force and growth mechanism for spontaneous oxide nanowire formation during the thermal oxidation of metals. *Acta Materialia* **2011,** 59, (6), 2491-2500.
143. Gonçalves, A. M. B.; Campos, L. C.; Ferlauto, A. S.; Lacerda, R. G., On the growth and electrical characterization of CuO nanowires by thermal oxidation. *Journal of Applied Physics* **2009,** 106, (3), 034303.
144. Hansen, B. J.; Chan, H.-l.; Lu, J.; Lu, G.; Chen, J., Short-circuit diffusion growth of long bi-crystal CuO nanowires. *Chemical Physics Letters* **2011,** 504, (1-3), 41-45.
145. Vanithakumari, S. C.; Shinde, S. L.; Nanda, K. K., Controlled synthesis of CuO nanostructures on Cu foil, rod and grid. *Materials Science and Engineering: B* **2011,** 176, (8), 669-678.
146. Wu, F., Myung, Y., Banerjee, P., Unravelling transient phases during thermal oxidation of copper for dense CuO nanowire growth. *CystEngComm* **2014,** DOI: 10.1039/C4CE00275J.
147. Debbichi, L.; de Lucas, M. C. M.; Pierson, J. F.; Kruger, P., Vibrational Properties of CuO and Cu4O3 from first-principles calculations, and Raman and infrared spectroscopy. *Journal of Physical Chemistry C* **2012,** 116, (18), 10232-10237.
148. H. Solache-Carranco, G. J.-D., M. Galvan-Arellano, J. Martinez-Juarez, G. Romero-Paredes, R. Pena-Sierra, Raman scattering and photoluminescence studies on Cu_2O. *2008 5th International Conference on Electrical Engineering, Computing Science and Automatic Control (CCE2008)* **2008**, 4.
149. Gouadec, G.; Colomban, P., Raman Spectroscopy of nanomaterials: How spectra relate to disorder, particle size and mechanical properties. *Progress in Crystal Growth and Characterization of Materials* **2007,** 53, (1), 1-56.
150. Wu, F.; Myung, Y.; Banerjee, P., Unravelling transient phases during thermal oxidation of copper for dense CuO nanowire growth. *Crystengcomm* **2014,** 16, (16), 3264-3267.
151. Zhu, Y. F.; Mimura, K.; Lim, J. W.; Isshiki, M.; Jiang, Q., Brief review of oxidation kinetics of copper at 350 degrees C to 1050 degrees C. *Metallurgical and Materials Transactions a-Physical Metallurgy and Materials Science* **2006,** 37A, (4), 1231-1237.
152. Du, Y. L.; Zhang, M. S.; Chen, Q.; Yin, Z., Investigation of size-driven phase transition in bismuth titanate nanocrystals by Raman spectroscopy. *Applied Physics a-Materials Science & Processing* **2003,** 76, (7), 1099-1103.
153. Tan, Y. W.; Xue, X. Y.; Peng, Q.; Zhao, H.; Wang, T. H.; Li, Y. D., Controllable fabrication and electrical performance of single crystalline Cu2O nanowires with high aspect ratios. *Nano Letters* **2007,** 7, (12), 3723-3728.
154. Hacialioglu, S.; Meng, F.; Jin, S., Facile and mild solution synthesis of Cu_2O nanowires and nanotubes driven by screw dislocations. *Chemical Communications* **2012,** 48, (8), 1174-1176.
155. Nakayama. S.; Kaji, T. S., M.; Notoya, T.; Osakai, T., Which Is Easier to Reduce, Cu_2O or CuO? *J. Electrochem. Soc.* **2007,** 154, 7.
156. Ko, E.; Choi, J.; Okamoto, K.; Tak, Y.; Lee, J., Cu_2O nanowires in an alumina template: Electrochemical conditions for the synthesis and photoluminescence characteristics. *Chemphyschem* **2006,** 7, (7), 1505-1509.
157. Wang, C.; Wang, Y. Q.; Liu, X. H.; Diao, F. Y.; Yuan, L.; Zhou, G. W., Novel hybrid nanocomposites of polyhedral Cu_2O nanoparticles-CuO nanowires with enhanced photoactivity. *Physical Chemistry Chemical Physics* **2014,** 16, (33), 17487-17492.
158. Yuan, L.; Van der Geest, A. G.; Zhu, W. H.; Yin, Q. Y.; Li, L.; Kolmogorov, A. N.; Zhou, G. W., Reduction of CuO nanowires confined by a nano test tube. *Rsc Advances* **2014,** 4, (57), 30259-30266.
159. Wang, R.-C.; Lin, H.-Y., Efficient surface enhanced Raman scattering from Cu_2O porous nanowires transformed from CuO nanowires by plasma treatments. *Materials Chemistry and Physics* **2012,** 136, (2-3), 661-665.

160. Feng, Y. Z.; Zheng, X. L., Plasma-Enhanced Catalytic CuO Nanowires for CO Oxidation. *Nano Letters* **2010,** 10, (11), 4762-4766.
161. Wu, F.; Myung, Y.; Banerjee, P., Unravelling transient phases during thermal oxidation of copper for dense CuO nanowire growth. *CrystEngComm* **2014,** 16, 3264-3267.
162. Love, J. N., W. A. P.; Armigliato, A., Modern Developments and Applications in Microbeam Analysis *Springer* **1998**, 392.
163. Nacucchi, M. A., M.; Altamura, D.; Pfister, V.; Re, M.; Signore, M. A.; Vittori Antisari, M., Quantitative EDS analysis in transmission electron microscopy using unconventional reference materials *IOP Conf. Series: Materials Science and Engineering* **2010,** 7, 12.
164. Wu, F.; Myung, Y.; Banerjee, P., Rayleigh Instability Driven Nodular Cu_2O Nanowires via Carbothermal Reduction of CuO Nanowires. *Crystal Growth & Design* **2015,** 15, (4), 1588-1595.
165. Lu, X. J.; Hu, Q. Y.; Yang, W. G.; Bai, L. G.; Sheng, H.; Wang, L.; Huang, F. Q.; Wen, J. G.; Miller, D. J.; Zhao, Y. S., Pressure-induced amorphization in single-crystal Ta_2O_5 nanowires: a kinetic mechanism and improved electrical conductivity. *Journal of the American Chemical Society* **2013,** 135, (37), 13947-13953.
166. Sharma, S. M.; Sikka, S. K., Pressure induced amorphization of materials. *Progress in Materials Science* **1996,** 40, (1), 1-77.
167. Wu, J. N.; Yin, B.; Wu, F.; Myung, Y.; Banerjee, P., Charge transport in single CuO nanowires. *Applied Physics Letters* **2014,** 105, (18), 183506.
168. Perez, I.; Robertson, E.; Banerjee, P.; Henn-Lecordier, L.; Son, S. J.; Lee, S. B.; Rubloff, G. W., TEM-based metrology for HfO_2 layers and nanotubes formed in anodic aluminum oxide nanopore structures. *Small* **2008,** 4, (8), 1223-1232.
169. Dubale, A. A.; Su, W. N.; Tamirat, A. G.; Pan, C. J.; Aragaw, B. A.; Chen, H. M.; Chen, C. H.; Hwang, B. J., The synergetic effect of graphene on Cu_2O nanowire arrays as a highly efficient hydrogen evolution photocathode in water splitting. *Journal of Materials Chemistry A* **2014,** 2, (43), 18383-18397.
170. Tahir, D.; Tougaard, S., Electronic and optical properties of Cu, CuO and Cu_2O studied by electron spectroscopy. *Journal of Physics-Condensed Matter* **2012,** 24, (17).
171. Ji, R.; Sun, W. D.; Chu, Y., One-step hydrothermal synthesis of Ag/Cu_2O heterogeneous nanostructures over Cu foil and their SERS applications. *Rsc Advances* **2014,** 4, (12), 6055-6059.
172. Liu, P. S.; Li, Z. G.; Cai, W. P.; Fang, M.; Luo, X. D., Fabrication of cuprous oxide nanoparticles by laser ablation in PVP aqueous solution. *Rsc Advances* **2011,** 1, (5), 847-851.
173. Han, W. K.; Choi, J. W.; Hwang, G. H.; Hong, S. J.; Lee, J. S.; Kang, S. G., Fabrication of Cu nano particles by direct electrochemical reduction from CuO nano particles. *Applied Surface Science* **2006,** 252, (8), 2832-2838.
174. Dubal, D. P.; Gund, G. S.; Holze, R.; Jadhav, H. S.; Lokhande, C. D.; Park, C. J., Surfactant-assisted morphological tuning of hierarchical CuO thin films for electrochemical supercapacitors. *Dalton Transactions* **2013,** 42, (18), 6459-6467.
175. Marcondes, A. R.; Ueda, M.; Kostov, K. G.; Beloto, A. F.; Leite, N. F.; Gomes, G. F.; Lepienski, C. M., Improvements of ultra-high molecular weight polyethylene mechanical properties by nitrogen plasma immersion ion implantation. *Brazilian Journal of Physics* **2004,** 34, (4B), 1667-1672.
176. Park, O. K.; Choi, Y. M.; Hwang, J. Y.; Yang, C. M.; Kim, T. W.; You, N. H.; Koo, H. Y.; Lee, J. H.; Ku, B. C.; Goh, M., Defect healing of reduced graphene oxide via intramolecular cross-dehydrogenative coupling. *Nanotechnology* **2013,** 24, (18), 185604.
177. Wang, X. Q.; Hanson, J. C.; Frenkel, A. I.; Kim, J. Y.; Rodriguez, J. A., Time-resolved studies for the mechanism of reduction of copper oxides with carbon monoxide: Complex behavior of lattice oxygen and the formation of suboxides. *Journal of Physical Chemistry B* **2004,** 108, (36), 13667-13673.
178. **NIST Thermodynamic Database.** **http://webbook.nist.gov/chemistry/form-ser.html**.
179. Kim, J. Y.; Rodriguez, J. A.; Hanson, J. C.; Frenkel, A. I.; Lee, P. L., Reduction of CuO and Cu_2O with H-2 : H embedding and kinetic effects in the formation of suboxides. *Journal of the American Chemical Society* **2003,** 125, (35), 10684-10692.

180. Sundararaman, R.; Narang, P.; Jermyn, A. S.; Goddard, W. A., 3rd; Atwater, H. A., Theoretical predictions for hot-carrier generation from surface plasmon decay. *Nat Commun* **2014,** 5, 5788.
181. Arthur, J. R., Reactions between Carbon and Oxygen. *Transactions of the Faraday Society* **1951,** 47, (2), 164-178.
182. Valentinuzzi, M. C.; Sanchez, H. J.; Abraham, J.; Perez, C., Comparative analysis of the resonant Raman cross sections of pure samples and oxides. *X-Ray Spectrometry* **2008,** 37, (5), 555-560.
183. Xie, J. L.; Quo, C. X.; Li, C. M., Interface functionalization with polymer self-assembly to boost photovoltage of Cu2O/ZnO nanowires solar cells. *International Journal of Hydrogen Energy* **2014,** 39, (28), 16227-16233.
184. Li, J.; Vizkelethy, G.; Revesz, P.; Mayer, J. W.; Tu, K. N., Oxidation and Reduction of Copper-Oxide Thin-Films. *Journal of Applied Physics* **1991,** 69, (2), 1020-1029.
185. Choi, H. W.; Kim, Y. H.; Rim, Y. H.; Yang, Y. S., Crystallization kinetics of lithium niobate glass: determination of the Johnson-Mehl-Avrami-Kolmogorov parameters. *Physical Chemistry Chemical Physics* **2013,** 15, (24), 9940-9946.
186. Gutzow, I. S., Schmelzer, J. W. P., *The Vitreous State: Thermodynamics, Structure, Rheology, and Crystallization, Second Edition, Berlin, New York, Springer*. **2013**.
187. Nakayama, S.; Kaji, T.; Shibata, M.; Notoya, T.; Osakai, T., Which is easier to reduce, Cu_2O or CuO? *Journal of the Electrochemical Society* **2007,** 154, (1), C1-C6.
188. Papon, p. L., J. Meeijer, P. H. E., *The physics of phase transitions concepts and applications, Springer-Verlag, Berlin, New York* **2006**.
189. De Yoreo, J. J.; Vekilov, P. G., Principles of crystal nucleation and growth. *Biomineralization* **2003,** 54, 57-93.
190. Collins, R. J.; Thomas, D. G., Photoconduction and surface effects with zinc oxide crystals. *Physical Review* **1958,** 112, (2), 388-395.
191. Schmidt-Mende, L.; MacManus-Driscoll, J. L., ZnO - nanostructures, defects, and devices. *Materials Today* **2007,** 10, (5), 40-48.
192. Zhang, X. Y.; Qin, J. Q.; Xue, Y. N.; Yu, P. F.; Zhang, B.; Wang, L. M.; Liu, R. P., Effect of aspect ratio and surface defects on the photocatalytic activity of ZnO nanorods. *Scientific Reports* **2014,** 4.
193. Wu, F.; Myung, Y.; Banerjee, P., Rayleigh instability driven nodular Cu_2O nanowires via carbothermal reduction of CuO nanowires. *Crystal Growth & Design* **2014,** 15, (4), 1588-1595.
194. Wu, F.; Tian, L.; Kanjolia, R.; Singamaneni, S.; Banerjee, P., Plasmonic metal-to-semiconductor switching in Au nanorod-ZnO nanocomposite films. *ACS Applied Materials & Interfaces* **2013,** 5, (16), 7693-7.
195. Wang, J. X.; Sun, X. W.; Yang, Y.; Kyaw, K. K. A.; Huang, X. Y.; Yin, J. Z.; Wei, J.; Demir, H. V., Free-standing ZnO-CuO composite nanowire array films and their gas sensing properties. *Nanotechnology* **2011,** 22, (32).
196. Hsueh, H. T.; Hsueh, T. J.; Chang, S. J.; Hung, F. Y.; Tsai, T. Y.; Weng, W. Y.; Hsu, C. L.; Dai, B. T., CuO nanowire-based humidity sensors prepared on glass substrate. *Sensors and Actuators B-Chemical* **2011,** 156, (2), 906-911.
197. Puurunen, R. L.; Vandervorst, W., Island growth as a growth mode in atomic layer deposition: aphenomenological model. *Journal of Applied Physics* **2004,** 96, (12), 7686-7695.
198. Alam, M. A.; Green, M. L., Mathematical description of atomic layer deposition and its application to the nucleation and growth of HfO_2 gate dielectric layers. *Journal of Applied Physics* **2003,** 94, (5), 3403-3413.
199. Satta, A.; Schuhmacher, J.; Whelan, C. M.; Vandervorst, W.; Brongersma, S. H.; Beyer, G. P.; Maex, K.; Vantomme, A.; Viitanen, M. M.; Brongersma, H. H.; Besling, W. F. A., Growth mechanism and continuity of atomic layer deposited TiN films on thermal SiO_2. *Journal of Applied Physics* **2002,** 92, (12), 7641-7646.
200. Wang, W.-N.; Wu, F.; Myung, Y.; Niedzwiedzki, D. M.; Im, H. S.; Park, J.; Banerjee, P.; Biswas, P., Surface engineered CuO nanowires with ZnO islands for CO_2 photoreduction *ACS Applied Materials & Interfaces* **2015**.

201. Chang, J.; Ahmed, R.; Wang, H.; Liu, H.; Lo, R.; Wang, P.; Waclawikt, E. R., ZnO nanocones with high-index {10(1)over-bar1} facets for enhanced energy conversion efficiency of dye-sensitized solar cells. *Journal of Physical Chemistry C* **2013,** 117, (27), 13836-13844.
202. Song, T.; Choung, J. W.; Park, J.-G.; Il Park, W.; Rogers, J. A.; Paik, U., Surface polarity and shape-controlled synthesis of ZnO nanostructures on GaN thin films based on catalyst-free metalorganic vapor phase epitaxy. *Advanced Materials* **2008,** 20, (23), 4464-4469.
203. Ohyama, M.; Kozuka, H.; Yoko, T., Sol-gel preparation of ZnO films with extremely preferred orientation along (002) plane from zinc acetate solution. *Thin Solid Films* **1997,** 306, (1), 78-85.
204. Bian, Z.; Tachikawa, T.; Zhang, P.; Fujitsuka, M.; Majima, T., A Nanocomposite superstructure of metal oxides with effective charge transfer interfaces. *Nat. Commun.* **2013,** 5, 3038.
205. Tan, S. T.; Umar, A. A.; Balouch, A.; Yahaya, M.; Yap, C. C.; Salleh, M. M.; Oyama, M., ZnO nanocubes with (101) basal plane photocatalyst prepared via a low-frequency ultrasonic assisted hydrolysis process. *Ultrasonics Sonochemistry* **2014,** 21, (2), 754-760.
206. Tang, Y. W.; Zhou, H.; Zhang, K.; Ding, J.; Fan, T. X.; Zhang, D., Visible-light-active ZnO via oxygen vacancy manipulation for efficient formaldehyde photodegradation. *Chemical Engineering Journal* **2015,** 262, 260-267.
207. Othonos, A.; Zervos, M., Ultrafast hole carrier relaxation dynamics in p-type CuO nanowires. *Nanoscale Research Letters* **2011,** 6, 1-5.
208. Kelzenberg, M. D.; Boettcher, S. W.; Petykiewicz, J. A.; Turner-Evans, D. B.; Putnam, M. C.; Warren, E. L.; Spurgeon, J. M.; Briggs, R. M.; Lewis, N. S.; Atwater, H. A., Enhanced absorption and carrier collection in Si wire arrays for photovoltaic applications. *Nature Materials* **2010,** 9, (3), 239-244.
209. Zhu, Y. W.; Sow, C. H.; Yu, T.; Zhao, Q.; Li, P. H.; Shen, Z. X.; Yu, D. P.; Thong, J. T. L., Co-synthesis of ZnO-CuO nanostructures by directly heating brass in air. *Advanced Functional Materials* **2006,** 16, (18), 2415-2422.
210. Shalish, I.; Temkin, H.; Narayanamurti, V., Size-dependent surface luminescence in ZnO nanowires. *Physical Review B* **2004,** 69, (24).
211. Hansen, B. J.; Kouklin, N.; Lu, G.; Lin, I. K.; Chen, J.; Zhang, X., Transport, analyte detection, and opto-electronic response of p-Type CuO nanowires. *Journal of Physical Chemistry C* **2010,** 114, (6), 2440-2447.
212. C. Eiche, D. M., M. Schneider, D. Sinerius, J. Weese, K. W. Benz, J. Honerkamp, Analysis of photoinduced current transient spectroscopy (PICTS) data by a regularization method. *J. Phys.: Condens. Matter* 4, 10.
213. El Akkad, F.; Ashour, H., Photoinduced current transient spectroscopy technique applied to the study of point defects in polycrystalline CdS thin films. *Journal of Applied Physics* **2009,** 105, (9), 093113.
214. Belardini, A.; Dominici, L.; Larciprete, M. C.; Michelotti, F.; Rousseau, A.; Ratsimihety, A., Enhanced stability of the second order optical properties of high-T-g fluorinated electro-optic copolymer. *Applied Physics Letters* **2006,** 89, (23), 231110.
215. Li, Q. H.; Gao, T.; Wang, Y. G.; Wang, T. H., Adsorption and desorption of oxygen probed from ZnO nanowire films by photocurrent measurements. *Applied Physics Letters* **2005,** 86, (12), 123117.
216. Melnick, D. A., Zinc oxide photoconduction, an oxygen adsorption process. *Journal of Chemical Physics* **1957,** 26, (5), 1136-1146.
217. Wang, C.; Fu, X. Q.; Xue, X. Y.; Wang, Y. G.; Wang, T. H., Surface accumulation conduction controlled sensing characteristic of p-type CuO nanorods induced by oxygen adsorption. *Nanotechnology* **2007,** 18, (14), 145506.
218. Ben-Porat, C. H.; Cherniavskaya, O.; Brus, L.; Cho, K. S.; Murray, C. B., Electric fields on oxidized silicon surfaces: static polarization of PbSe nanocrystals. *Journal of Physical Chemistry A* **2004,** 108, (39), 7814-7819.
219. Wu, J.; Yin, B.; Wu, F.; Myung, Y.; Banerjee, P., Charge transport in single CuO nanowires. *Applied Physics Letters* **2014,** 105, (18), 183506.

220. Moazzami, K.; Murphy, T. E.; Phillips, J. D.; Cheung, M. C. K.; Cartwright, A. N., Sub-bandgap photoconductivity in ZnO epilayers and extraction of trap density spectra. *Semiconductor Science and Technology* **2006,** 21, (6), 717-723.
221. Baruah, S.; Sinha, S. S.; Ghosh, B.; Pal, S. K.; Raychaudhuri, A. K.; Dutta, J., Photoreactivity of ZnO nanoparticles in visible light: Effect of surface states on electron transfer reaction. *Journal of Applied Physics* **2009,** 105, (7).
222. Gopel, W., REACTIONS OF OXYGEN WITH ZNO-1010-SURFACES. *Journal of Vacuum Science & Technology* **1978,** 15, (4), 1298-1310.
223. Usubharatana, P.; McMartin, D.; Veawab, A.; Tontiwachwuthikul, P., Photocatalytic process for CO_2 emission reduction from industrial flue gas streams. *Industrial & Engineering Chemistry Research* **2006,** 45, (8), 2558-2568.
224. Indrakanti, V. P.; Kubicki, J. D.; Schobert, H. H., Photoinduced activation of CO_2 on Ti-based heterogeneous catalysts: Current state, chemical physics-based insights and outlook. *Energy & Environmental Science* **2009,** 2, (7), 745-758.
225. Woolerton, T. W.; Sheard, S.; Reisner, E.; Pierce, E.; Ragsdale, S. W.; Armstrong, F. A., Efficient and clean photoreduction of CO_2 to CO by enzyme-modified TiO_2 nanoparticles using visible Light. *Journal of the American Chemical Society* **2010,** 132, (7), 2132-2133.
226. Kohno, Y.; Hayashi, H.; Takenaka, S.; Tanaka, T.; Funabiki, T.; Yoshida, S., Photo-enhanced reduction of carbon dioxide with hydrogen over Rh/TiO_2. *Journal of Photochemistry and Photobiology a-Chemistry* **1999,** 126, (1-3), 117-123.
227. Tseng, I. H.; Chang, W. C.; Wu, J. C. S., Photoreduction of CO_2 using sol-gel derived titania and titania-supported copper catalysts. *Applied Catalysis B-Environmental* **2002,** 37, (1), 37-48.
228. Sasirekha, N.; Basha, S. J. S.; Shanthi, K., Photocatalytic performance of Ru doped anatase mounted on silica for reduction of carbon dioxide. *Applied Catalysis B-Environmental* **2006,** 62, (1-2), 169-180.
229. Koci, K.; Mateju, K.; Obalova, L.; Krejcikova, S.; Lacny, Z.; Placha, D.; Capek, L.; Hospodkova, A.; Solcova, O., Effect of silver doping on the TiO_2 for photocatalytic reduction of CO_2. *Applied Catalysis B-Environmental* **2010,** 96, (3-4), 239-244.
230. Anpo, M.; Yamashita, H.; Ikeue, K.; Fujii, Y.; Ichihashi, Y.; Zhang, S. G.; Park, D. R.; Ehara, S.; Park, S. E.; Chang, J. S.; Yoo, J. W., Photocatalytic reduction of CO_2 with H_2O on titanium oxides anchored within zeolites. *Advances in Chemical Conversions for Mitigating Carbon Dioxide* **1998,** 114, 177-182.
231. Ikeue, K.; Yamashita, H.; Anpo, M.; Takewaki, T., Photocatalytic reduction of CO_2 with H_2O on Ti-beta zeolite photocatalysts: Effect of the hydrophobic and hydrophilic properties. *Journal of Physical Chemistry B* **2001,** 105, (35), 8350-8355.
232. Lin, W. Y.; Han, H. X.; Frei, H., CO_2 splitting by H_2O to CO and O_2 under UV light in TiMCM-41 silicate sieve. *Journal of Physical Chemistry B* **2004,** 108, (47), 18269-18273.
233. Yang, H. C.; Lin, H. Y.; Chien, Y. S.; Wu, J. C. S.; Wu, H. H., Mesoporous TiO_2/SBA-15, and Cu/TiO_2/SBA-15 Composite Photocatalysts for Photoreduction of CO_2 to Methanol. *Catalysis Letters* **2009,** 131, (3-4), 381-387.
234. Shunliu, D.; Yin, Z.; Brozena, A. H.; Mayes, M. L.; Banerjee, P.; Wen-An, C.; Rubloff, G. W.; Schatz, G. C.; YuHuang, W., Confined propagation of covalent chemical reactions on single-walled carbon nanotubes. *Nature Communications* **2011,** 2, 382 (6 pp.)-382 (6 pp.).
235. Wang, W. N.; Park, J.; Biswas, P., Rapid synthesis of nanostructured Cu-TiO_2-SiO_2 composites for CO_2 photoreduction by evaporation driven self-assembly. *Catalysis Science & Technology* **2011,** 1, (4), 593-600.
236. Liu, L. J.; Zhao, C. Y.; Zhao, H. L.; Pitts, D.; Li, Y., Porous microspheres of MgO-patched TiO_2 for CO_2 photoreduction with H_2O vapor: temperature-dependent activity and stability. *Chemical Communications* **2013,** 49, (35), 3664-3666.
237. Yu, K. P.; Yu, W. Y.; Ku, M. C.; Liou, Y. C.; Chien, S. H., Pt/titania-nanotube: A potential catalyst for CO_2 adsorption and hydrogenation. *Applied Catalysis B-Environmental* **2008,** 84, (1-2), 112-118.

238. Varghese, O. K.; Paulose, M.; LaTempa, T. J.; Grimes, C. A., High-rate solar photocatalytic conversion of CO_2 and water vapor to hydrocarbon fuels. *Nano Letters* **2009,** 9, (2), 731-737.
239. Feng, X. J.; Sloppy, J. D.; LaTemp, T. J.; Paulose, M.; Komarneni, S.; Bao, N. Z.; Grimes, C. A., Synthesis and deposition of ultrafine Pt nanoparticles within high aspect ratio TiO_2 nanotube arrays: application to the photocatalytic reduction of carbon dioxide. *Journal of Materials Chemistry* **2011,** 21, (35), 13429-13433.
240. Zhou, H.; Guo, J. J.; Li, P.; Fan, T. X.; Zhang, D.; Ye, J. H., Leaf-architectured 3D hierarchical artificial photosynthetic system of perovskite titanates towards CO_2 photoreduction into hydrocarbon fuels. *Scientific Reports* **2013,** 3, 1667.
241. Satoh, N.; Hasegawa, H.; Tsujii, K.; Kimura, K., Photoinduced coagulation of Au nanocolloids. *Journal of Physical Chemistry* **1994,** 98, (8), 2143-2147.
242. Song, C. S., Global challenges and strategies for control, conversion and utilization of CO_2 for sustainable development involving energy, catalysis, adsorption and chemical processing. *Catalysis Today* **2006,** 115, (1-4), 2-32.
243. Banerjee, P.; Lee, W.-J.; Bae, K.-R.; Lee, S. B.; Rubloff, G. W., Structural, electrical, and optical properties of atomic layer deposition Al-doped ZnO films. *Journal of Applied Physics* **2010,** 108, (4), 043504.
244. Mema, R.; Yuan, L.; Du, Q.; Wang, Y.; Zhou, G., Effect of surface stresses on CuO nanowire growth in the thermal oxidation of copper. *Chemical Physics Letters* **2011,** 512, (1-3), 87-91.
245. Viswanadham, N.; Sharma, S. M.; Taneja, M., Inspection allocation in manufacturing systems using stochastic search techniques. *Ieee Transactions on Systems Man and Cybernetics Part a-Systems and Humans* **1996,** 26, (2), 222-230.
246. Inoue, T.; Fujishima, A.; Konishi, S.; Honda, K., Photoelectrocatalytic reduction of carbon dioxide in aquesous suspensions of semiconductor powders. *Nature* **1979,** 277, 637.
247. Roy, S. C.; Varghese, O. K.; Paulose, M.; Grimes, C. A., Toward solar fuels: photocatalytic conversion of carbon dioxide to hydrocarbons. *ACS Nano* **2010,** 4, (3), 1259-1278.
248. Tahir, M.; Amin, N. S., Photocatalytic CO_2 reduction and kinetic study over In/TiO_2 nanoparticles supported microchannel monolith photoreactor. *Applied Catalysis a-General* **2013,** 467, 483-496.
249. Linsebigler, A. L.; Lu, G. Q.; Yates, J. T., Photocatalysis on TiO_2 Surfaces - Principles, Mechanisms, and Selected Results. *Chemical Reviews* **1995,** 95, (3), 735-758.
250. Bian, Z.; Tachikawa, T.; Zhang, P.; Fujitsuka, M.; Majima, T., A nanocomposite superstructure of metal oxides with effective charge transfer interfaces. *Nature Communications* **2013,** 5, 3038.
251. Woll, C., The chemistry and physics of zinc oxide surfaces. *Progress in Surface Science* **2007,** 82, (2-3), 55-120.
252. Zhao, J. H.; Han, E. J.; Liu, T. M.; Zeng, W., First-principles study on electronic properties of low-index ZnO surfaces. *Asian Journal of Chemistry* **2012,** 24, (7), 2903-2908.
253. Vayssieres, L., Growth of arrayed nanorods and nanowires of ZnO from aqueous solutions. *Advanced Materials* **2003,** 15, (5), 464-466.
254. Jin, C.; Kim, H.; Hong, C.; Kim, H. W.; Lee, C., Preparation and photoluminescence properties of silica-coated CuO nanowires. *Applied Physics a-Materials Science & Processing* **2010,** 100, (1), 151-157.
255. Lin, Y. J.; Tsai, C. L.; Lu, Y. M.; Liu, C. J., Optical and electrical properties of undoped ZnO films. *Journal of Applied Physics* **2006,** 99, (9).
256. Dingle, R., Luminescent transitions associated with divalent copper impurities and the green emission from semiconducting zinc oxide. *Physical Review Letters* **1969,** 23, (11), 579-81.
257. Wu, K.; Chen, J.; McBride, J. R.; Lian, T., CHARGE TRANSFER Efficient hot-electron transfer by a plasmon-induced interfacial charge-transfer transition. *Science* **2015,** 349, (6248), 632-635.
258. Ye, J. D.; Gu, S. L.; Zhu, S. M.; Chen, T.; Liu, W.; Qin, F.; Hu, L. Q.; Zhang, R.; Shi, Y.; Zheng, Y. D., Raman and photoluminescence of ZnO films deposited on Si(111) using low-pressure metalorganic chemical vapor deposition. *Journal of Vacuum Science & Technology A* **2003,** 21, (4), 979-982.

259. Chang, Y.-M.; Jian, S.-R.; Lee, H.-Y.; Lin, C.-M.; Juang, J.-Y., Enhanced visible photoluminescence from ultrathin ZnO films grown on si-nanowires by atomic layer deposition. *Nanotechnology* **2010,** 21, (38), 385705.
260. Tamaki, Y.; Furube, A.; Murai, M.; Hara, K.; Katoh, R.; Tachiya, M., Dynamics of efficient electron-hole separation in TiO_2 nanoparticles revealed by femtosecond transient absorption spectroscopy under the weak-excitation condition. *Physical Chemistry Chemical Physics* **2007,** 9, (12), 1453-1460.
261. Pankove, J. I., *Optical Processes in Semiconductors*. Dover Publication, Inc.: New York, 1975.
262. Rothenberger, G.; Moser, J.; Gratzel, M.; Serpone, N.; Sharma, D. K., Charge carrier trapping and recombination dynamics in small semiconductor particles. *Journal of the American Chemical Society* **1985,** 107, (26), 8054-8059.
263. Tang, Q. L.; Luo, Q. H., Adsorption of CO_2 at ZnO: A surface structure effect from DFT+U calculations. *Journal of Physical Chemistry C* **2013,** 117, (44), 22954-22966.
264. Mauk, M. G., Silicon solar cells: physical metallurgy principles. *Jom-Journal of the Minerals Metals & Materials Society* **2003,** 55, (5), 38-42.
265. Garnett, E. C.; Yang, P. D., Silicon nanowire radial p-n junction solar cells. *Journal of the American Chemical Society* **2008,** 130, (29), 9224-9225.
266. Krogstrup, P.; Jorgensen, H. I.; Heiss, M.; Demichel, O.; Holm, J. V.; Aagesen, M.; Nygard, J.; Morral, A. F. I., Single-nanowire solar cells beyond the Shockley-Queisser limit. *Nature Photonics* **2013,** 7, (4), 306-310.
267. Kempa, T. J.; Cahoon, J. F.; Kim, S. K.; Day, R. W.; Bell, D. C.; Park, H. G.; Lieber, C. M., Coaxial multishell nanowires with high-quality electronic interfaces and tunable optical cavities for ultrathin photovoltaics. *Proceedings of the National Academy of Sciences of the United States of America* **2012,** 109, (5), 1407-1412.
268. Polman, A.; Atwater, H. A., Photonic design principles for ultrahigh-efficiency photovoltaics. *Nature Materials* **2012,** 11, (3), 174-177.
269. Green, M. A., Third generation photovoltaics: ultra-high conversion efficiency at low cost. *Progress in Photovoltaics* **2001,** 9, (2), 123-135.
270. Garra, J.; Long, T.; Currie, J.; Schneider, T.; White, R.; Paranjape, M., Dry etching of polydimethylsiloxane for microfluidic systems. *Journal of Vacuum Science & Technology a-Vacuum Surfaces and Films* **2002,** 20, (3), 975-982.
271. Hwang, S. J.; Oh, D. J.; Jung, P. G.; Lee, S. M.; Go, J. S.; Kim, J. H.; Hwang, K. Y.; Ko, J. S., Dry etching of polydimethylsiloxane using microwave plasma. *Journal of Micromechanics and Microengineering* **2009,** 19, (9).
272. Wu, S. T.; Huang, K.; Shi, E. Z.; Xu, W. J.; Fang, Y.; Yang, Y. B.; Cao, A. Y., Soluble polymer-based, blown bubble assembly of single- and double-layer nanowires with shape control. *Acs Nano* **2014,** 8, (4), 3522-3530.
273. Lee, C. H.; Kim, D. R.; Zheng, X. L., Fabrication of nanowire electronics on nonconventional substrates by water-assisted transfer printing method. *Nano Letters* **2011,** 11, (8), 3435-3439.
274. Shiu, S. C.; Hung, S. C.; Chao, J. J.; Lin, C. F., Massive transfer of vertically aligned Si nanowire array onto alien substrates and their characteristics. *Applied Surface Science* **2009,** 255, (20), 8566-8570.
275. She, H. Q.; Malotky, D.; Chaudhury, M. K., Estimation of adhesion hysteresis at polymer/oxide interfaces using rolling contact mechanics. *Langmuir* **1998,** 14, (11), 3090-3100.
276. Jayathilaka, C.; Kapaklis, V.; Siripala, W.; Jayanetti, S., Improved efficiency of electrodeposited p-CuO/n-Cu2O heterojunction solar cell. *Applied Physics Express* **2015,** 8, (6).
277. *AM1.5 light intensity database-NREL*. http://rredc.nrel.gov/solar/spectra/am1.5/.
278. Liao, L.; Zhang, Z.; Yan, B.; Zheng, Z.; Bao, Q. L.; Wu, T.; Li, C. M.; Shen, Z. X.; Zhang, J. X.; Gong, H.; Li, J. C.; Yu, T., Multifunctional CuO nanowire devices: p-type field effect transistors and CO gas sensors. *Nanotechnology* **2009,** 20, (8).
279. Allen, J. E.; Hemesath, E. R.; Perea, D. E.; Lensch-Falk, J. L.; Li, Z. Y.; Yin, F.; Gass, M. H.; Wang, P.; Bleloch, A. L.; Palmer, R. E.; Lauhon, L. J., High-resolution detection of Au catalyst atoms in Si nanowires. *Nature Nanotechnology* **2008,** 3, (3), 168-173.

280. Barnes, W. L.; Dereux, A.; Ebbesen, T. W., Surface plasmon subwavelength optics. *Nature* **2003,** 424, (6950), 824-830.
281. Li, J. T.; Cushing, S. K.; Zheng, P.; Meng, F. K.; Chu, D.; Wu, N. Q., Plasmon-induced photonic and energy-transfer enhancement of solar water splitting by a hematite nanorod array. *Nature Communications* **2013,** 4.
282. Tian, Y.; Tatsuma, T., Mechanisms and applications of plasmon-induced charge separation at TiO_2 films loaded with gold nanoparticles. *Journal of the American Chemical Society* **2005,** 127, (20), 7632-7637.
283. Cushing, S. K.; Li, J. T.; Meng, F. K.; Senty, T. R.; Suri, S.; Zhi, M. J.; Li, M.; Bristow, A. D.; Wu, N. Q., Photocatalytic activity enhanced by plasmonic resonant energy transfer from metal to semiconductor. *Journal of the American Chemical Society* **2012,** 134, (36), 15033-15041.
284. Li, B. S.; Akimoto, K.; Shen, A., Growth of Cu_2O thin films with high hole mobility by introducing a low-temperature buffer layer. *Journal of Crystal Growth* **2009,** 311, (4), 1102-1105.
285. de Jongh, P. E.; Vanmaekelbergh, D.; Kelly, J. J., Cu2O: Electrodeposition and characterization. *Chemistry of Materials* **1999,** 11, (12), 3512-3517.
286. *http://physics.nist.gov/PhysRefData/XrayMassCoef/tab3.html* **X-Ray Mass Attenuation Coefficients**.
287. Shen, J. P.; Qiao, Z. Q.; Zhang, K. L.; Wang, J.; Li, R.; Xu, H. M.; Yang, G. C.; Nie, F. D., Effects of nano-Ag on the combustion process of Al-CuO metastable intermolecular composite. *Applied Thermal Engineering* **2014,** 62, (2), 732-737.
288. Hansen, B. J.; Kouklin, N.; Lu, G. H.; Lin, I. K.; Chen, J. H.; Zhang, X., Transport, analyte detection, and opto-electronic response of p-Type CuO nanowires. *Journal of Physical Chemistry C* **2010,** 114, (6), 2440-2447.
289. Liu, L. F.; Lee, W.; Scholz, R.; Pippel, E.; Gosele, U., Tailor-made inorganic nanopeapods: Structural design of linear noble metal nanoparticle chains. *Angewandte Chemie-International Edition* **2008,** 47, (37), 7004-7008.
290. Toimil Molares, M. E.; Balogh, A. G.; Cornelius, T. W.; Neumann, R.; Trautmann, C., Fragmentation of nanowires driven by Rayleigh instability. *Applied Physics Letters* **2004,** 85, (22), 5337.
291. Rauber, M.; Muench, F.; Toimil-Molares, M. E.; Ensinger, W., Thermal stability of electrodeposited platinum nanowires and morphological transformations at elevated temperatures. *Nanotechnology* **2012,** 23, (47), 475710.
292. Huang, X. H.; Zhan, Z. Y.; Wang, X.; Zhang, Z.; Xing, G. Z.; Guo, D. L.; Leusink, D. P.; Zheng, L. X.; Wu, T., Rayleigh-instability-driven simultaneous morphological and compositional transformation from Co nanowires to CoO octahedra. *Applied Physics Letters* **2010,** 97, (20), 203112.
293. Qin, Y.; Yang, Y.; Scholz, R.; Pippel, E.; Lu, X. L.; Knez, M., Unexpected oxidation behavior of Cu nanoparticles embedded in porous alumina films produced by molecular layer deposition. *Nano Letters* **2011,** 11, (6), 2503-2509.
294. Fan, P.-W.; Chen, W.-L.; Lee, T.-H.; Chiu, Y.-J.; Chen, J.-T., Rayleigh-instability-driven morphology transformation by thermally annealing electrospun polymer fibers on substrates. *Macromolecules* **2012,** 45, (14), 5816-5822.
295. Ragone, D. V., *Thermodynamics of materials*. Wiley: New York, 1995.
296. Nichols, F. A., Mullins, W. W., Surface- (interface-) and volume-diffusion contributions to morphological changes driven by capillarity. *Transactions of the Metallurgical Society of AIME* **1965,** 233, 9.
297. Balluffi, R. W.; Allen, S. M.; Carter, W. C.; Kemper, R. A., *Kinetics of materials*. J. Wiley & Sons: Hoboken, N.J., 2005; p xxvi, 645 p.
298. Panat, R.; Hsia, K. J.; Cahill, D. G., Evolution of surface waviness in thin films via volume and surface diffusion. *Journal of Applied Physics* **2005,** 97, (1), 013521.
299. Soon, A.; Todorova, M.; Delley, B.; Stampfl, C., Thermodynamic stability and structure of copper oxide surfaces: A first-principles investigation. *Physical Review B* **2007,** 75, (12), 129902.

300. Wang, L. C.; de Tacconi, N. R.; Chenthamarakshan, C. R.; Rajeshwar, K.; Tao, M., Electrodeposited copper oxide films: Effect of bath pH on grain orientation and orientation-dependent interfacial behavior. *Thin Solid Films* **2007,** 515, (5), 3090-3095.
301. Liu, X. M.; Zhou, Y. C., Electrochemical deposition and characterization of Cu_2O nanowires. *Applied Physics a-Materials Science & Processing* **2005,** 81, (4), 685-689.
302. Siegfried, M. J.; Choi, K. S., Electrochemical crystallization of cuprous oxide with systematic shape evolution. *Advanced Materials* **2004,** 16, (19), 1743-1746.
303. Jing, L. Q.; Xu, Z. L.; Sun, X. J.; Shang, J.; Cai, W. M., The surface properties and photocatalytic activities of ZnO ultrafine particles. *Applied Surface Science* **2001,** 180, (3-4), 308-314.
304. Wu, F.; Myung, Y.; Banerjee, P., Unravelling transient phases during thermal oxidation of copper for dense CuO nanowire growth. *CrystEngComm* **2014,** 3264-3267.

Appendix I TEM line scan correction

However, the X-ray absorption is significant because the absorption distance is changing as the beam penetrates across the CuO NW diameter. This equation can be modified as the following form:

$$\frac{C_{Cu}}{C_O} = k_{CuO}\frac{I_{Cu}}{I_O} \times \left[\frac{\left(\frac{\mu}{\rho}\right)_{Cu}}{\left(\frac{\mu}{\rho}\right)_O}\right] \times \{\frac{1-exp-[\left(\frac{\mu}{\rho}\right)_{Cu} cosec(\alpha)(\rho t)]}{1-exp-[\left(\frac{\mu}{\rho}\right)_O cosec(\alpha)(\rho t)]}\} \quad \text{(a1.1)}$$

Where,

- C_{Cu} and C_O are the weight fractions of the Cu and O contained in the sample,
- $k_{CuO}$is Cliff-Lorimer factor,
- I_{Cu} and I_O are the measured characteristic X-ray intensities,
- $\left(\frac{\mu}{\rho}\right)_{Cu}$ and $\left(\frac{\mu}{\rho}\right)_O$ are the mass absorption coefficient of Cu and O in the sample, which can be respectively depicted as:

  $$\left(\frac{\mu}{\rho}\right)_{Cu} = C_{Cu} \times \left(\frac{\mu}{\rho}\right)_{Cu}^{Cu} + C_O \times \left(\frac{\mu}{\rho}\right)_{Cu}^{O} \quad \text{(a1.2)}$$

  $$\left(\frac{\mu}{\rho}\right)_{O} = C_{Cu} \times \left(\frac{\mu}{\rho}\right)_{O}^{Cu} + C_O \times \left(\frac{\mu}{\rho}\right)_{O}^{O} \quad \text{(a1.3)}$$

  $\left(\frac{\mu}{\rho}\right)_{Cu}^{Cu}$, $\left(\frac{\mu}{\rho}\right)_{Cu}^{O}$, $\left(\frac{\mu}{\rho}\right)_{O}^{Cu}$, and $\left(\frac{\mu}{\rho}\right)_{O}^{O}$ are 52.55 cm^2/g, 10570 cm^2/g, 11.63 cm^2/g, and 4590 cm^2/g, respectively, which can be found in NIST data base of Mass attenuation coefficient table,[286]
- α is take-off angle, which is 35° in our experiment,
- ρ is the density of the sample at thickness t.

- k_{CuO} is an equipment parameter, which can be determined experimentally using a standard sample. For our microscope, k_{CuO} = 1.12.
- ρ of CuO NW is assumed to be the same as the bulk density of 6.3 g/cm^3,[287]
- The geometry of CuO NW is assumed to be a cylinder shape.

Then, $\frac{C_{Cu}}{C_O}$ can be calculated by running a matlab code using equation (a1.1), (a1.2) and (a1.3).[180]

Appendix Ⅱ The morphology of Cu_2O NWs under thermal reduction

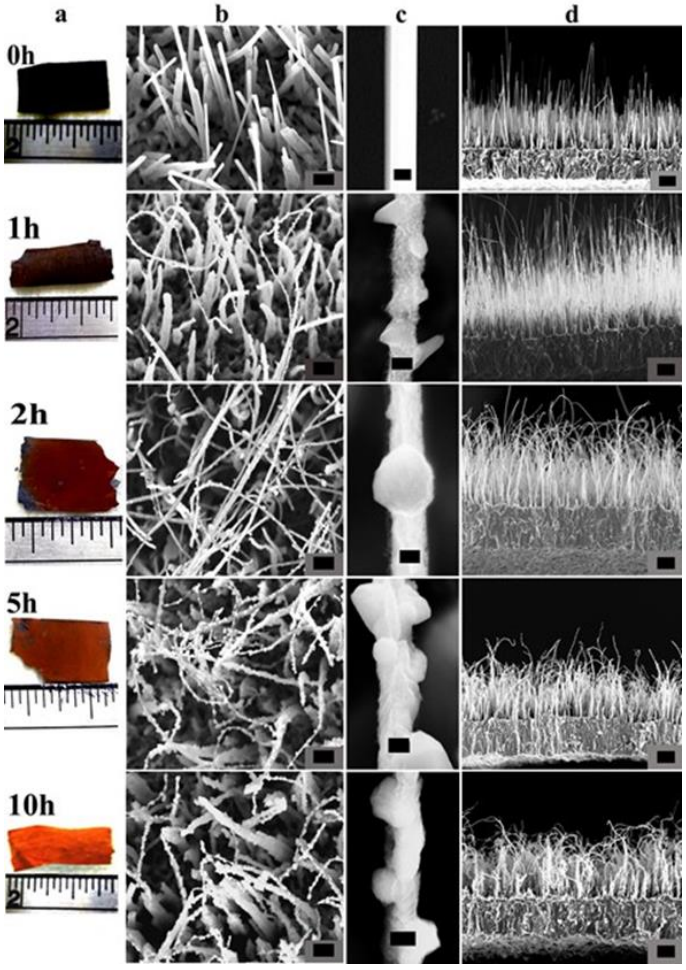

Figure A2.1. Images of Cu_2O obtained after reduction of pure CuO NWs at 400 ^oC for different times. **a)** The first column shows the color change from black of CuO to complete orange color for 10 hours reduction. **b)** The second column shows that all of the samples have dense nodular NWs on the surface after reduction. **c)** The third column shows the NW morphology evolution with reduction time. **d)** The fourth column shows the cross-section of the sample with lengths larger than 20 μm. The scale bars are 1 μm for the top-down, 200 nm for the NW zoomed image and 10 μm for cross-section, respectively.

At 400 ^{o}C, the CuO NWs are completely reduced to Cu_2O NWs for 1hour. To further study the reduction mechanism of CuO in this self-produced CO ambient, the CuO NW are continuously reduced for longer times. **Figure A2.1** shows a matrix of images to highlight the phase transformation of CuO to Cu_2O. Rows represent the CuO NW foils reduction conditions at 400 ^{o}C for 0, 1, 2, 5, and 10 hours**. Column a** shows that the samples' color changes from black of CuO to orange of Cu_2O after the reduction for 10 hours. **Column b** shows the SEM images of density, NW morphology variations with increasing the reduction time. A close-up view of the NWs is shown in **column c**. The smooth and facade CuO NWs grow periodical nodules on the surface when the NW completely transformed into Cu_2O and these periodical nodules grow bigger for a longer reduction time. The corresponding cross-section SEM images are shown in **column d**. Initially, CuO NWs are vertical with an average length of 13.9 μm as we reported in last chapter. After the CuO NWs are fully reduced, the NWs become curved and show an average length larger than 20 μm.

Figure 4.1c shows that CuO NWs can be fully reduced to Cu_2O at 400 for 1 hour. **Figure A2.2** shows that this fully reduced CuO NWs form periodical nodules on surface. To investigate nodules growth mechanism and the Cu_2O NW morphology evolution at 400 ^{o}C, we reduced the CuO NWs for a longer reduction time (longer than 1hour).

In order to confirm the phase of the reduced NWs, TEM and HRTEM on the NWs were conducted. The NW shows the nodules as pyramidal structures growing from the surface of the NW in **Figure A2.3a**. In the many NW samples observed with TEM, we found no evidence of dislocations and grain boundaries separating the pyramidal nodules from the NWs or within NWs. We acknowledge that obtaining a direct image of the interface proved to be difficult, given the curvature of the NWs. Then, we did HRTEM on the edge of the NW and nodules.

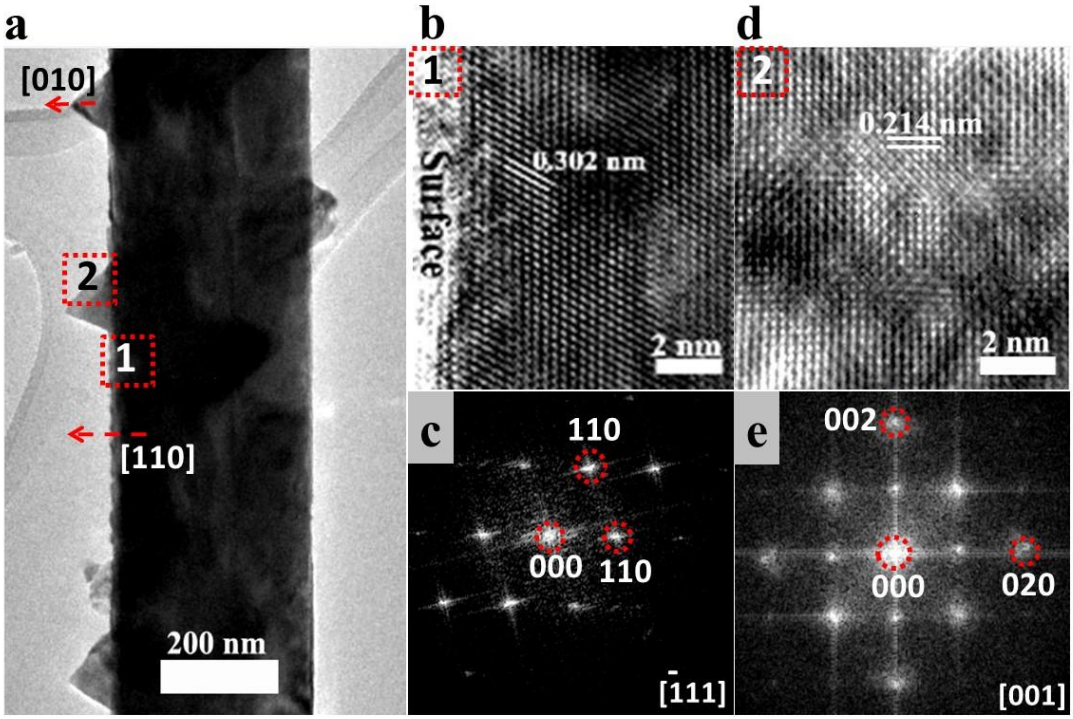

Figure A2.2.a) TEM image of NW by reducing CuO foil at 400 ^{o}C for 1 hour and **b)** the HRTEM image of NW and **c)** the corresponding FFT of NW. **d)** the HRTEM image of the protrusion on the NW and **e)** the corresponding FFT of protrusion. The FFT of NW indicates that the NW is Cu_2O with a beam direction paralleling $[\bar{1}11]$ and the FFT of protrusion indicates that it is Cu_2O with a growth direction of [010] and a beam direction of [001].

Two sets of HRTEM images were obtained next. First, **Figure A2.2b** shows the HRTEM image at spot '1' of the NW previously shown in **Figure A2.2a**. The 400 ^{o}C, 1 hour sample shows pure Cu_2O cubic phase in the NW. There are some dislocations on the NW surface because of the surface reactions. An interplanar distance of 0.302 nm is obtained, which is the same as the {110} set of planes in Cu_2O.[35] The corresponding fast Fourier transform (FFT) of the HRTEM image is also indexed as [110] growth direction in **Figure A2.2c** with a zone axis along the $[\bar{1}11]$. Second, the HRTEM image of the pyramidal protrusion is shown in **Figure A2.2d** and displays an

interplanar distance of 0.214 nm, which is the [200] plane of Cu_2O. The corresponding FFT is shown in **Figure A2.2e** with [001] as zone axis. By comparing the HRTEM images and the corresponding FFTs, the nodules on the NW does not form a new surface but follow the [010] growth direction because the surface reactions cause abnormal crystal growth at surface defect potions. This implies that the NWs undergo a full reduction after only 1 hour of carbothermal annealing at 400 ^oC and the reduction reactions does not break the crystalline structure.

In our experiments, we found that CuO NW can be transformed to Cu_2O layer by layer at 300 ^oC. However, the CuO NW can be quickly converted to pure Cu_2O NWs without showing any Cu at 400 ^oC. HRTEM indicates that the Cu_2O NWs obtained from the reduction has a good crystallinity without observable grain boundaries. On surface, nodules with a size of 200 nm periodically grow on the Cu_2O NW surface. Even though the reduction time was extended to 10 hours and CuO black foils changed to bright orange color, we still saw vertical Cu_2O NWs grow on the surface of the foils. The nodules with a good crystal facets periodically distribute on the NW surface. To study the growth mechanism of these well-grown nodules, we conducted Raman microscopy on the cross-sections of the reduced foils under different reduction conditions at 400 ^oC.

A typical image taken by Raman microscope is schematically to show the process of Raman microscopy analysis on the cross-section of the reduced samples at 400 ^oC in **Figure A2.3a**. The four spots are labeled from 1 to 4 and correspond to the NWs, the root of the NWs, the middle of the oxidized film, and the bottom of the oxidized film, respectively. Due to the sensitivity of Raman spectrum and the large laser spot size of ~ 1 μm, it is sufficient to probe the average phase information of the various regions listed above. In the figures plotted in **Figures A2.3b-e**, we have

included the Raman spectra of starting foil for our experiments to show that the initial cross section consists of pure CuO phase *i.e.*, no chemical potential difference exists prior to reduction.

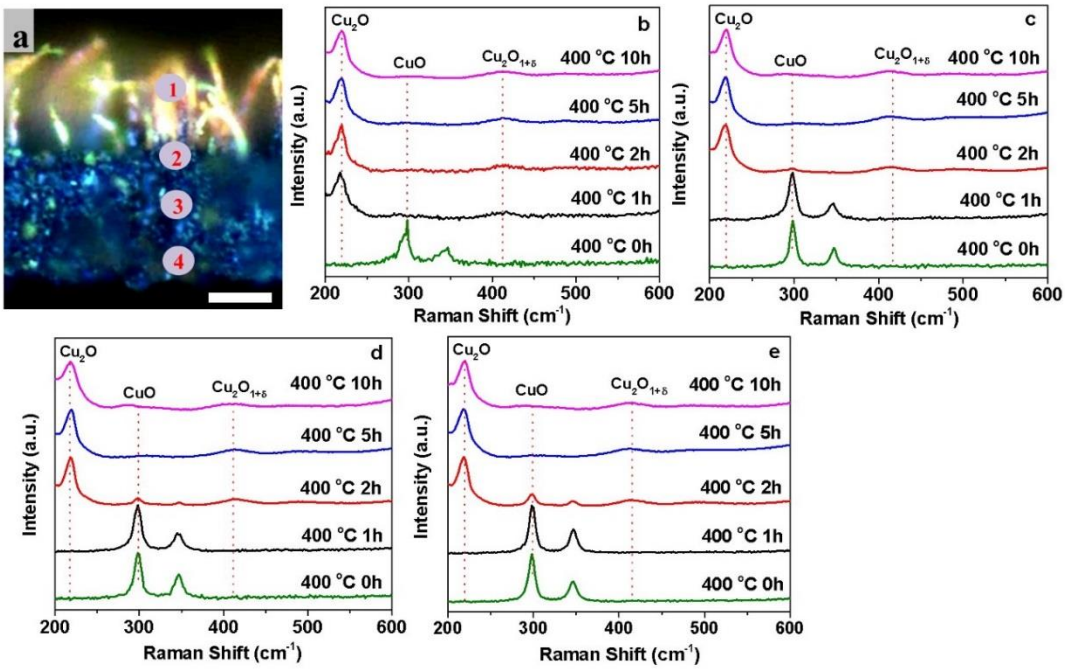

Figure A2.3. Raman spectrum was collected on the cross-sections at different positions: **a)** the optical cross-section of Cu_2O obtained using Raman microscope, the scale bar is 10 μm, **b)** position 1: on Cu_2O NWs, **c)** position 2: at the root of Cu_2O NWs, **d)** position 3: in the middle of the oxide layer, e) position 4: at the bottom of the oxide layer.

Figure A2.3b shows the Raman spectra from spot 1 (the NW region) for the reduced samples. Strong Cu_2O phase is observed with a little $Cu_2O_{1+\delta}$ defective phase with no detected CuO signal which shows the main Raman A_g peak at 298 cm^{-1},[47, 177] indicating that the NWs are indeed pure Cu_2O for reduction time ranging from 1 hour to 10 hours. The generation of defective phases signal comes from the surface reactions, leading to formation of point defects and dislocations, which can be observed by HRTEM in **Figure A2.3b**. **Figure A2.3c** shows the Raman

spectra at the root of the NWs. The sample reduced at 400 ^{o}C for 1 hour shows pure CuO phase and all other samples with longer reduction times show pure Cu_2O phase with a little $Cu_2O_{1+\delta}$ phase. When the laser focuses on the middle of the oxide film, the 400 ^{o}C, 2 hours sample now retains a weak CuO phase signal (**Figure A2.3d**). At this point, the samples reduced for longer reduction times are pure Cu_2O. Finally, the Raman laser probes on the bottom of the oxide layer. The spectrum are plotted and shown in **Figure A2.3e**. The trend is quite similar to **Figure A2.3d** in that both the 400 ^{o}C 1 and 2 hour samples retain the CuO signal, while the samples reduced for 5 hours or more show pure Cu_2O phase with some $Cu_2O_1+_\delta$ defective phase, indicating a complete reduction of the sample.

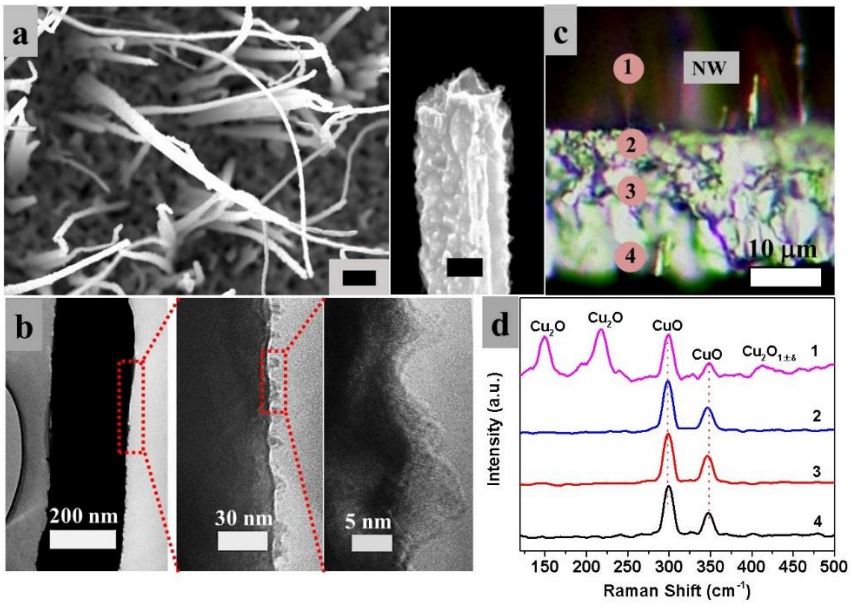

Figure A2.4. **a)** SEM images of NW by reducing CuO NW at 350 ^{o}C for 1 hour, the scale bars are 1 μm and 200 nm, respectively. **b)** TEM image of the NW and the corresponding images of the amplified surface fluctuations. **c)** the cross-section of the sample obtained under Raman microscope and **d)** the corresponding Raman spectrum at different positions across the cross-section.

Based on these results, we can make a few conclusions. First, the reduction of the NWs is rapid at 400 ^{o}C. Second, the transformation front proceeds from NWs and into the underlying oxide film below NWs. Thirdly, the whole foil can be reduced into Cu_2O at 400 ^{o}C for 5 hours. Further, the concurrent presence of $Cu_2O_{1+\delta}$ with Cu_2O indicates that this off-stoichiometric phase is the reaction intermediate during the conversion of CuO to Cu_2O. Finally, the outward diffusion of oxygen plays an important role in the reduction process and could lead to the formation of the intermediate phase, $Cu_2O_{1+\delta}$. However, the relationship between O outward diffusion and the NW morphology evolution is still under study.

In order to study the mechanism for growth of nodules on Cu_2O NWs, we decrease the reduction temperature to 300 ^{o}C. As we see in **Figure 4.4**, the sample reduced at 300 ^{o}C for 1 hour shows a little rough surface with some bumps. HRTEM images indicates that the reduced NW surface is coated with 2-3 nm thick amorphous Cu_2O. Thus, we reduced the CuO NWs sample at 350 ^{o}C for 1 hour.

Figure A2.4 shows the SEM, TEM and Raman data for this sample reduced at 350 ^{o}C for 1 hour. It can be seen from the SEM image (**Figure A2.4a**) that surface roughening of the NWs – otherwise highly smooth and facetted,[288] occurs at 350 ^{o}C. The NWs are curved with small protrusions growing all over the surface. Furthermore, **Figure A2.4b** showed a series of TEM images at increasing magnifications to study the protrusions formed at 350 ^{o}C for 1 hour. Periodic protrusions are seen on the NW surface that have an average periodicity of 5-10 nm and a size of 5-10 nm. We conducted Raman spectroscopy across the cross-section (**Figure A2.4c** and **Figure A2.4d**) from NWs to the edge of the bottom oxides, finding that the reduced NWs contain mixed CuO and Cu_2O phases with a clear $Cu_2O_{1+\delta}$ phase present in the NW only. Additionally, the oxide film below the NW was CuO with no signs of the $Cu_2O_{1+\delta}$ phase, indicating that the NWs only get

partially reduced. Therefore, we can conclude that nodules form because of the fast surface reactions and these nodules grow bigger for longer reduction time.

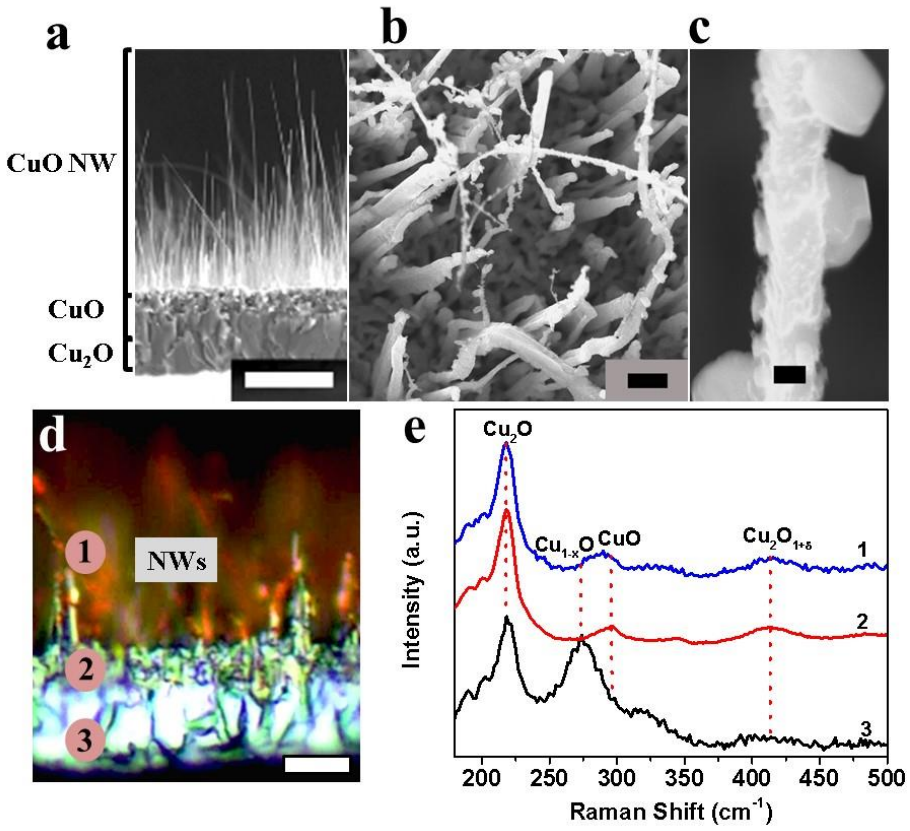

Figure A2.5. a) A sample with Cu_2O-CuO-CuO NW structure obtained at 600 ^oC for 5 hours in previous experiment with a scale bar of 10 μm.[161] **b)** top surface SEM image of the sample a) which is reduced in Ar ambient for 3 hours at 400 ^oC. The scale bar is 1 μm. **c)** SEM image of the NW with a scale bar of 200 nm. **d)** a cross-section of the foil after reduction with a scale bar of 10 μm and **e)** the corresponding Raman spectrum at position 1, 2 and 3.

This set of data shows that the nodule formation is related to the initial surface instability induced by the phase transformation as the NW converts from CuO to Cu_2O and the surface energy

fluctuation. Continued transformation of this NW with quicker surface reaction rates results in the growth of these protrusions to nodules seen at 400 ^{o}C for various times due to the Oswald ripening.

After the CuO NWs are completely reduced to Cu_2O, the formation of these periodical nodules can be attributed to the Rayleigh instability, which often reported for 1D nanostructures of metals, polymers, compound semiconductors and core-shell NWs.[289-294] While there has been only one report on Rayleigh instabilities in NWs which involve phase transformation (Co-CoO phase transformation and fragmentation into CoO nanoparticles),[292] our current work extends the possibilities of synthesis of tunable and hierarchical nanostructures using phase transformation induced Rayleigh instabilities on large array NWs without fragmentation.

To confirm that Rayleigh instability is caused by the surface reactions, creating O chemical potential gradient, which, as a result, leads to the O outward diffusion from the bottom CuO film. If this assumption is true, it means that Cu outward diffusion instead of O can also induce Rayleigh instability to grow periodical nodules on the NWs.

In order to confirm the assumption that Rayleigh instability of Cu_2O NWs is controlled by fast ions diffusion caused the chemical potential gradient, we introduced Cu ions chemical potential gradient to the sample without changing the O chemical potential of the sample. First, we synthesized a NW sample which has a 'duplex' CuO/Cu_2O film structure below the CuO NWs.[161] **Figure A2.5a** shows the cross-section of the synthesized CuO NW sample. The bottom oxides layer consists of Cu_2O columnar grains at the bottom, and a layer of CuO fine crystals on top. The reason we use this sample is to establish a chemical potential gradient of Cu (high at the bottom due to Cu_2O and low on top due to CuO) to allow for Cu diffusion. However, in the previous experiments above, phase pure CuO foils were used with no gradients in the Cu chemical

potential but an oxygen chemical potential gradient created by the surface reduction reactions. If migration of Cu ions are responsible for the phase transformation and the formation of periodical nodules on the reduced NWs' surface, then these foils should exhibit Cu_2O NW formation in a similar temperature regime.

Second, we changed the atmosphere from CO rich to inert Ar when doing heat treatment. It is known that the carbothermal reduction occurs as:

$$2CuO + CO \rightarrow Cu_2O + CO_2 \text{ (reaction 1)}$$

This reaction has a negative free energy change at 400 ^oC (ΔG = -154 kJ/mol), indicating highly favorable thermodynamics.[295] This is borne out by the aggressive reduction of CuO to Cu_2O at 400 ^oC. In an inert Ar atmosphere, however, two possible reactions could take place:

$$2CuO \rightarrow Cu_2O + \tfrac{1}{2}O_2 \text{ (reaction 2)}$$

Reaction 2 assumes that CuO decomposites into Cu_2O and O_2 in inert Ar ambient. Then, O_2 evaporates and flows out with the Ar flow. However, the free energy change is positive for this reaction (ΔG = +70 kJ/mol at 400 ^oC) and therefore, is not feasible under standard conditions of 1 atmosphere and temperature range of interest.[164] On the other hand, Cu ions in diffusion to the NWs is possible from the underlying Cu_2O film passing through the CuO film, given by the reaction:

$$CuO + Cu \rightarrow Cu_2O \text{ (reaction 3)}$$

This reaction has ΔG = -146 kJ/mol at 400 ^oC. Thus, reaction 3 is also feasible provided that a chemical diffusion potential is set up which can readily supply a source of Cu ions. This is the case for the sample chosen.

Figure A2.5b and **Figure A2.5c** shows the SEM images of the NWs annealed at 400 ^{o}C for 3 hours with Ar inertial ambient. Nodules are readily observed in the NW, indicating that the reduction reaction has been operative by controlling the diffusion process of Cu ions. **Figure A2.5d** and **Figure A2.5e** show the cross sectional image from the Raman microscope and the

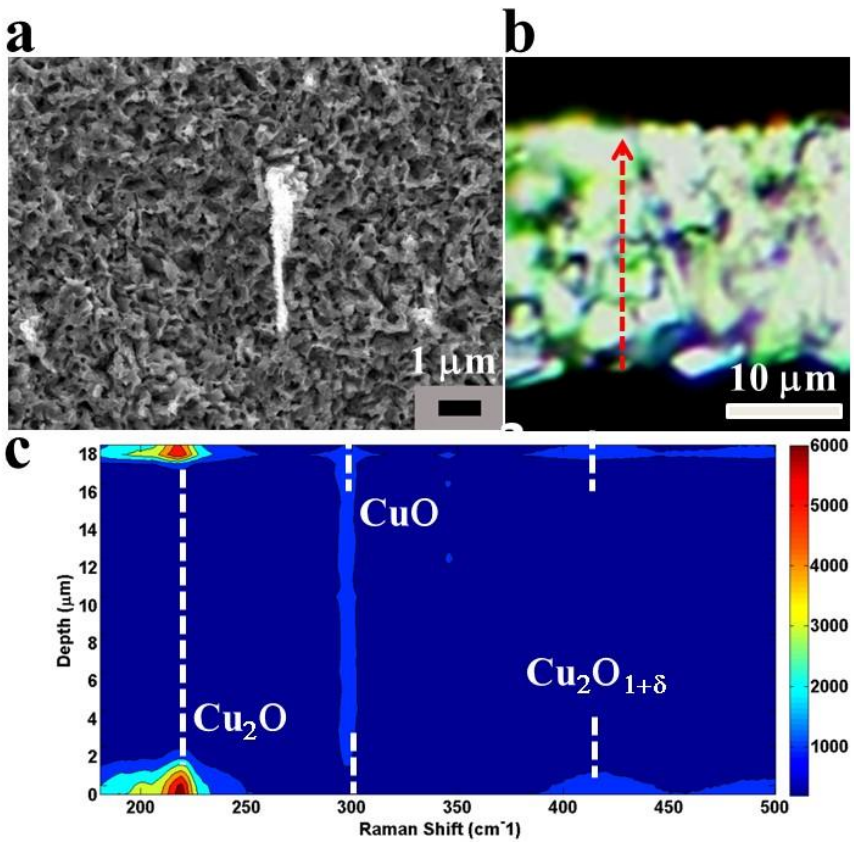

Figure A2.6. a) SEM images of CuO foil with few NWs on the surface and **b)** the cross-section of the CuO foil under Raman microscope is shown on the left side. Laser is set to scan from the bottom to the top of the foil and **c)** the corresponding Raman mapping images.

corresponding spectra at spot 1 - top of the NWs, spot 2 – root of the NWs, and spot 3 – bottom of the Cu_2O columnar film. As expected the NWs have been reduced to Cu_2O (**Figure A2.5e**). However, we also note that a weak CuO peak is observed in the NWs which is not observed in the

NWs reduced by CO (see **Figure A2.3b**). Similarly, the root of the NWs has been converted to Cu_2O as well, but with a weak CuO peak. The bottom of the film shows some Cu_2O converts to $Cu_{1-x}O$, indicating that Cu ions do migrate upwards. Strikingly enough, this effect is shown by the broad $Cu_{1-x}O$ peak[161] shown at 280 cm^{-1}. Overall, the Ar annealing results indicate that CuO → Cu_2O NW transformation can be brought about by Ar annealing or via CO based carbothermal reduction depending on whether Cu ions or O chemical potential gradient works as the reduction controlling mechanism. However, Cu ions gradient is controlled by the Cu/O stoichiometric ratio in Cu_2O and CuO, which is conserved in a sample. As a result, this chemical potential gradient decreases as the diffusion happens, which is the reason we did not obtain a pure Cu_2O NWs as we obtained using CO as reduction scheme.

In these reduction experiments, we found the CuO NW is critical to obtain full reduction of the CuO foils. The role of the NWs can be ascertained by studying the carbothermal reduction of thick CuO films (*i.e.*, with no NWs). Such films are obtained by oxidizing thin Cu foils at temperatures higher than 700 ^oC to make the lattice diffusion as the dominant oxidation mechanism.[33] An SEM image of such a film is shown in **Figure A2.6a**, where a single CuO NW is seen in an area of 28.9 μm^2. The initial cross section (**Figure A2.6b**) consists of a pure monolithic CuO phase with a film thickness approximately 20 μm. When subjected to a 400 ^oC, 10 hour carbothermal anneal; conditions under which CuO NW samples (with 18.3 μm thick underlying oxide film) completely convert to Cu_2O, this sample shows Cu_2O formation only in the first few microns at the top and bottom of the film. Correspondingly, $Cu_2O_{1+\delta}$ phase is also observed with the Cu_2O. The results are shown in **Figure A2.6c** in the form of a contour plot obtained from Raman line scanning the cross section. Here, the X-axis is the Raman shift (cm^{-1}), Y-axis is the depth inside the sample (in μm) and the color represents the intensity of the signal.

This result indicates that the presence of arrays of NWs aids in the carbothermal reduction of CuO to Cu_2O. The increased surface area of interaction between solid-gas and the radius of curvature of the individual NWs could both play a role in enhancing the kinetics of the reduction process. This 'antenna effect' is a unique feature of the NW reduction process.[164]

Rayleigh instability is the propagation of instability for longitudinal perturbations along a cylindrical surface to create a periodicity when the perturbation wavelength (λ) is longer than the cylinder circumference.[296] The driving force for Rayleigh instability is the high surface energy of a nanowire. To form a stable state, the NW which satisfies the Rayleigh instability conditions breaks into sphere particles. Using mass conservation, the shrinkage in the CuO NW radius[297] can be derived as -

$$R_{CuO} = R - \frac{\varepsilon^2(t)}{4R} \qquad \text{(a2.1)}$$

where,

R_{CuO} = average CuO cylinder radius

R = original radius of the cylinder at t = 0 and,

$\varepsilon(t)$ = amplitude of the perturbation.

The characteristic periodicity λ_o, can vary depending on the state of stress, surface and volume diffusion components during perturbation propagation.[296] **Table A2.1** shows the average periodicity of the nodules for the samples reduced at 400 ^oC. The λ_0 is 406 ± 82.8 nm, 336 ± 47.2 nm, 1328 ± 317.6 nm and 670.0 ± 157.1 nm for 1, 2, 5 and 10 hours, respectively.[164] The average starting CuO NW radius is R_o = 110 ± 30 nm in our samples and thus, according to the Rayleigh

instability condition, $\lambda_0 > 2\pi R_o = 680.8 \pm 188.4$ nm. Comparing the periodicity listed in **Table A2.1** with the Rayleigh instability condition, the samples reduced for 1 hour and 2 hours show a much smaller periodicity (λ_o) of the critical Rayleigh instability condition. Therefore, the 1 hour and 2 hours reduced samples should not see nodules production on the Cu_2O NWs.

Table A2.1. Periodicity (in nm) of the nodules for Cu_2O NWs obtained at 400 ^oC 1, 2, 5 and 10 hours. To obtain standard deviation at least 30 nodules were measured per sample.

	400 ^oC - 1 hour	400 ^oC - 2 hours	400 ^oC - 5 hours	400 ^oC - 10 hours
Periodicity (nm)	406±82.8	336±47.2	1328±317.6	670.0±157.1

In order to explain the discrepancy, as we remember for the 1 hour and 2 hours samples, there is thick CuO film remaining below the Cu_2O NWs (**Figure A2.3e**), creating an O chemical potential gradient between the fully converted Cu_2O NWs on top and the underlying CuO film. In contrast, negligible oxygen diffusion occurs for the 5 and 10 hours samples because of the uniformity in composition (i.e., fully converted Cu_2O). As a result, continuous O outwardly diffuse to the surface of Cu_2O NWs to react with CO. Additionally, stress generated during the transformation CuO NW → Cu_2O NW can increase the energy states of the NWs as evidenced by the warpage of NW during the reduction process (**Figure A2.1**). Under conditions of stress, volume diffusion effectively reduces perturbation wavelengths.[298] Therefore, it seems reasonable that λ_o for 1 and 2 hours samples is lower than the criteria for Rayleigh instability to occur. Variability in the starting NW radius and the defective $Cu_2O_{1+\delta}$ phases generation in the NWs may also contribute to additional complications and discrepancy observed in the Rayleigh criteria.

The Cu_2O NWs terminate surface with (110) planes, as shown in **Figures A2.2a-e.** Both the Cu_2O NW surface and the nodules have the same surface planes which are (110) since it is well known that the Cu_2O (110) plane is one of the lowest energy planes.[299] This effect can be explained firstly, by considering the CuO → Cu_2O reduction process. It has been shown through structural studies using X-ray absorption spectroscopy[177] that the CuO reduction under CO lean conditions occurs via formation of oxygen vacancies in the CuO or the presence of excess oxygen in Cu_2O. This initial surface depletion of oxygen creates a chemical potential gradient between the NW surface and the sample and results in the continuous out diffusion of oxygen, initially from the NW and subsequently from the underlying film.[164]

Our results reiterate this aspect of the reduction process by 1), demonstrating that loss of oxygen occurs at the NW/ambient interface in a form of CO_2 and subsequently proceeds into the film for longer reduction times because of the O chemical potential gradient and 2), observing the presence of $Cu_2O_{1+\delta}$ phase whenever the Cu_2O is formed (**Figures A2.3a-e**). Thus, creation of an oxygen chemical gradient (or its lack of) plays a crucial role in determining the kinetics and energetics of the reduction processes and NWs' morphology evolution.

When oxygen concentration in Cu_2O atomic planes with low energy are considered, we find that this density varies from 2.78 nm^{-2} to 5.89 nm^{-2} to 8.83 nm^{-2} for (100), (110) and (111) planes, respectively.[300] Given the arguments in the previous paragraph for CuO reduction, it becomes obvious that planes with the least oxygen atomic densities will be favored during a rapid reduction process (kinetically controlled). Thus, from a pure kinetic consideration, the growth rates of the Cu_2O planes during carbothermal reduction should be given as (100) > (110) > (111).[164]

From an energetics point of view however, a different picture emerges. The stability of Cu_2O surfaces was recently studied using first principle method,[299] wherein the surface energy of the Cu_2O (110) neutral surface under reducing atmosphere is 0.026 eV/Å^2 as compared to the Cu – rich Cu_2O (100) surface (0.098 eV/Å^2). Based on these values, both of the surface energies are low; however, the (110) plane is more favorable. We surmise that initially, the Cu_2O carbothermal reduction process favors both (100) and (110) planes – being the two lowest oxygen density planes as we mentioned in last paragraph. That is a non-equilibrium process is confirmed by reports of electrochemically grown Cu_2O NWs where (100) and (110) oriented planes have been reported under large over-potentials *i.e.*, non-equilibrium conditions.[301] However, under extended periods of reduction (eg., 400 ^oC 1 hour and more), the (100) plane grows the fastest and disappears in favor of the energetically stable (110) plane as proved by the HRTEM in **Figure A2.2** by showing (110) termination planes on both NWs' and nodules' surfaces. This is further borne out by the characteristic pyramidal protrusions in the [100] growth directions in **Figure A2.2a**.[302]

We combine the Rayleigh instability and phase transformation of CuO to Cu_2O NWs together to develop a picture for the results observed in this paper, which is shown in **Figure A2.7a-d**. First, the CO reducing environment reacts with the CuO on the surface of NWs to produce Cu_2O. As a result, an oxygen chemical potential is built up between CuO and Cu_2O. The high surface area of the NWs accelerates the kinetics and therefore quickly reduces the CuO NWs completely into Cu_2O NWs. At the same time, The defective $Cu_2O_{1+\delta}$ phase forms accompanied with phase transformation which is observed using Raman (**Figure A2.3a-e**) and indicates the extra oxygen stays inside of free space in the of the oxygen lattice because of the limited surface reaction rates.[177]

Surface stress generation occurs when crystalline Cu_2O grow on the surface of single crystalline CuO NW core. The stress energy produced during this phase transformation process

forces abnormal growth of small nodules on the surface of the reduced NWs, as we observed in **Figure A2.4**. Once the CuO NW is fully reduced to Cu_2O, continuous heat treatment induces Rayleigh instability to grow periodical protrusions on Cu_2O NW surface. These protrusions are the starting points for Rayleigh instability to propagate.

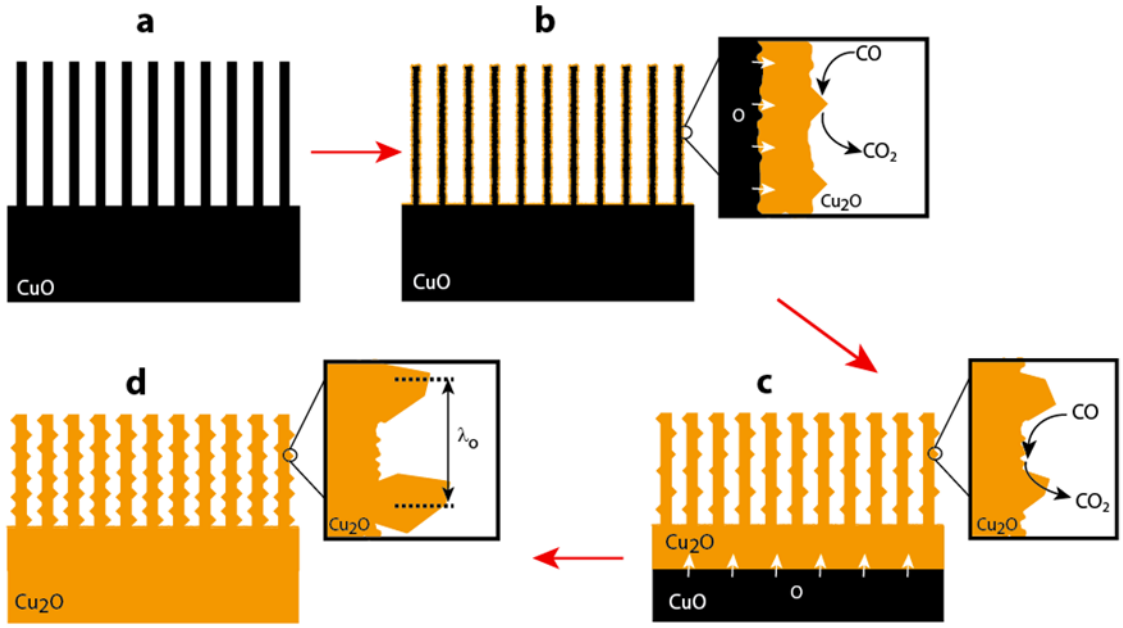

Figure A2.7. Schematic of proposed mechanism for transformation of CuO NWs to Cu_2O NWs under carbothermal reduction conditions. **a)** Starting foil, **b)** incipient stage of the transformation process, **c)** full conversion of the NWs and partial conversion of the underlying oxide film and, **d)** complete conversion of the CuO NWs and underlying oxide film.

When only oxygen out diffusion is considered in the NWs with periodic protrusions consisting of an outer Cu_2O shell layer of thickness τ over an inner CuO NW, we obtain using Cu ion conservation, the following relationship for NW radius shrinkage:[164]

$$R_{CuO} = R - \frac{\varepsilon^2(t)}{4R} - \left(\frac{\rho_{Cu_2O} Z_{Cu_2O}}{MW_{Cu_2O}}\right)\left(\frac{MW_{CuO}}{\rho_{CuO} Z_{CuO}}\right)\tau \qquad \text{(a2.2)}$$

where,

ρ_x = density of material 'x'

MW_x = molecular weight of 'x'

Z_x = ratio of cation/anion in 'x', Z = 1 for CuO and Z = 2 for Cu_2O.

Compared to the original equation 4.5, we notice that in equation 4.6 an additional, negative third term is introduced which enhances the shrinkage rate of the NW. This term depends on the product of the thickness of the Cu_2O film (τ) and the ratio of densities and molecular weights of CuO and Cu_2O (using appropriate values for CuO and Cu_2O, this factor is 1.06). That is to say that Rayleigh instability can be enhanced in NWs with associated volume changes during the phase transformation.

Base on the above discussions, there are two factors which can enhance Rayleigh instability in a NW: 1) volumetric out diffusion of oxygen which continues to transform CuO → Cu_2O and stabilize the NW structure thus, preventing it from fragmenting and, 2) surface diffusion which continues to be driven by Rayleigh instability to decrease the surface energy.

Conclusions

An increase of the reduction temperature, the reduction rate can be significantly enhanced. In 1 hour at 400 ^oC, the CuO NWs can be completely reduced to Cu_2O. Longer reduction times (> 1 hour) do not reduce the Cu_2O to Cu but continues to reduce the CuO film below the NWs. Meanwhile, we see a surface morphology evolution for different reduction times. Periodical nodules grow when the CuO NWs are reduced Cu_2O for 1 hour. The periodicity and the shape of the nodules change with reduction conditions.

Crystallographic relationship of the nodules with respect to the NW show that the nodules have higher growth rates due to surface instability caused by surface reactions. The Cu_2O (100) and (110) planes have different energies, resulting in different growth rates. The NW shows a [110] growth direction and the nodules show a [100] growth direction. However, both of them terminated the surfaces with [110] planes. The growth of the periodical nodules is found to be induced by the Rayleigh instability, which is caused by the surface reduction reactions. This argument was shown to be consistent with kinetic and energetic considerations. An analytical equation is derived which predicts faster rate of Rayleigh induced shrinkage of NWs under phase transformations.

Appendix Ⅲ Visible light intensity

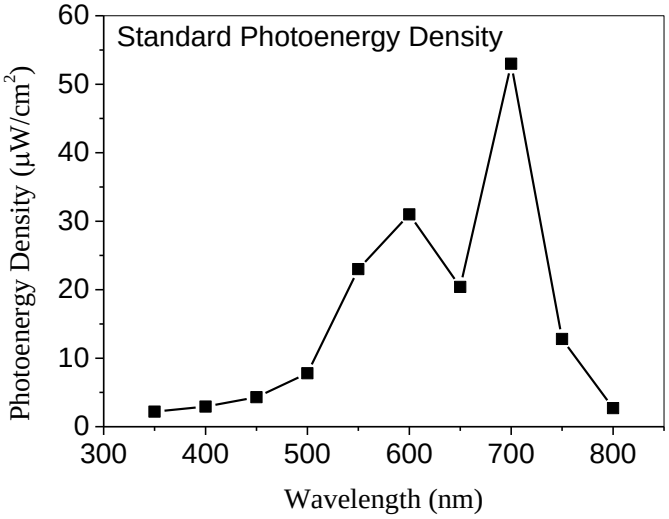

Figure A3.1. A light meter (PM100D Thor Labs) was used to measure the light intensity at specific wavelengths from 300 nm to 800 nm with 50 nm per step. There is very weak UV light intensity, indicating that the photoresponse observed in our experiment comes from visible light. The integrated white light power density is 5.7 mW/cm^2.

Appendix Ⅳ Surface conductivity of ultra-thin ZnO

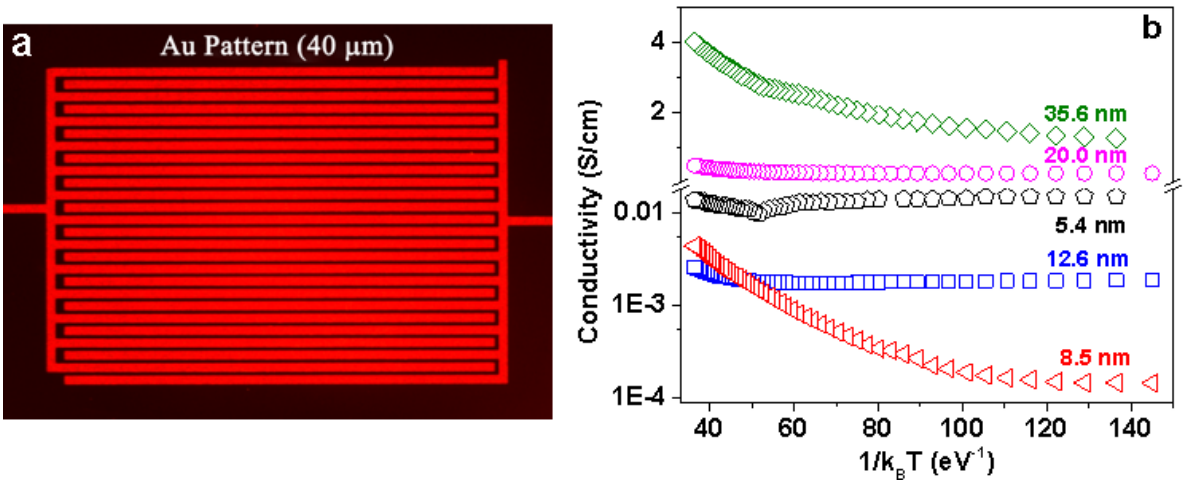

Figure A4.1. a) Au electrodes made by photolithography and lift-off techniques on the substrates of Si wafers with 300 nm thermal SiO_2, b) conductivity of ALD deposited ZnO on the Au electrodes shown in a) from 80 K to 320 K with a 5 K step.

Figure A4.1a shows the Au electrodes made on the Si wafer with 300 nm thermal SiO_2 on the surface. The channel length of the electrodes is 40 mm. Probes attached to terminals on both sides to measure the conductivity. **Figure A4.1b** displays the conductivity of ZnO deposited by ALD with a series of thicknesses: 5.4 nm, 8.5nm, 12.6 nm, 20.0 nm, and 35.6 nm. The conductivity of 5.4 nm ZnO is 0.016 S/cm at room temperature, which decreases to 0.0038 S/cm with an increase of the film thickness to 8.5 nm. A further increase of the film thickness to 12.6 nm continuously reduces the conductivity to 0.0023 S/cm. However, in a low temperature range from 80 K to 255 K the conductivity of 12.6 nm ZnO is much higher than the conductivity of 8.5 nm ZnO.

When the ZnO film is thicker than 12.6 nm, an increase of the thickness also create a dramatic improvement in conductivity. For example, the conductivity increases from 0.0023 S/cm of 12.6 nm ZnO to 0.44 S/cm of 20.0 nm ZnO and then to 3.85 S/cm of 35.6 nm ZnO at room

temperature. The thickness difference of the conductivity indicates that a surface to volume ratio difference plays an important role in affecting the conductivity of these ZnO thin films. 5.4 nm ZnO has a high surface to volume ratio of 185, which is 2.3 times higher than the ratio of 12.6 nm ZnO (78) and 6.6 times higher than the ratio of 35.6 nm ZnO (28). As a result, the high surface defects can dominate the conductivity with a film thickness less than 12.6 nm

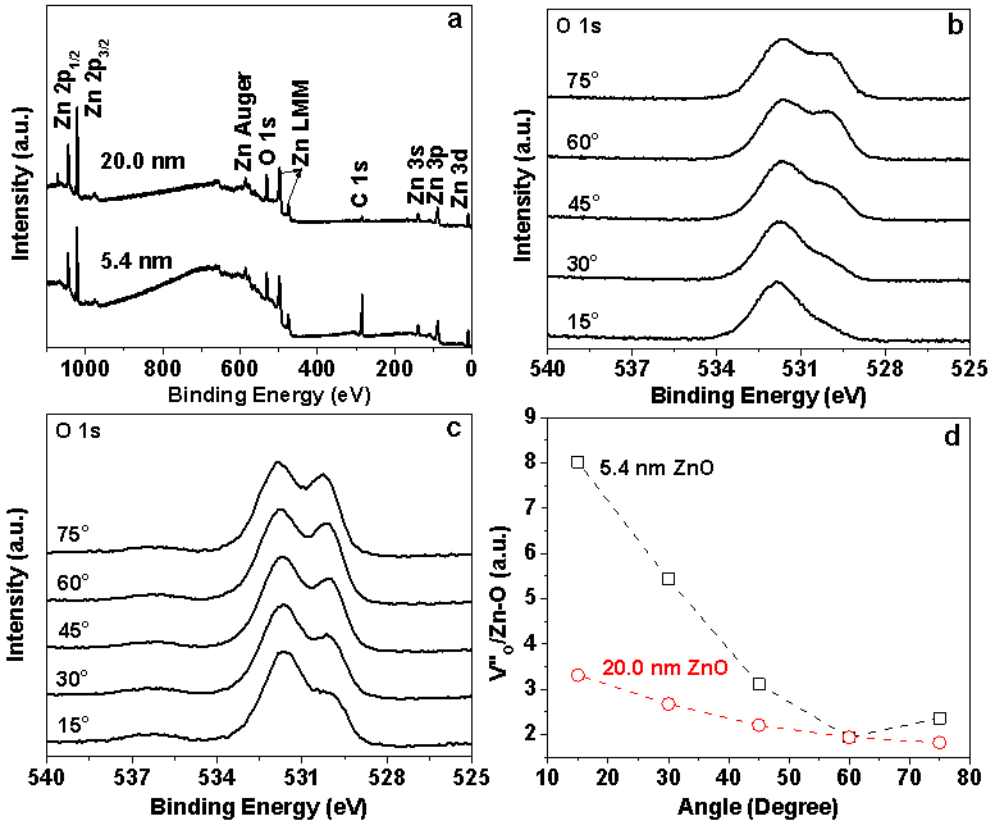

Figure A4.2. XPS spectrum of 5.4 nm ZnO and 20.0 nm ZnO with Zn terminated surfaces, a) survey scan from 0 eV to 1100 eV, b) angular scan from 15º to 75º of O 1s (5.4 nm), c) angular scan from 15º to 75º of O 1s (20.0 nm), d) the ratio of integrated VO" peak intensity at 531.8 eV over integrated lattice Zn-O peak intensity at 530.1 eV..

To characterize the surface difference between a thin ZnO film (5.4 nm) and a thick ZnO film (20.0 nm), ARXPS was employed to monitor the O vacancy ratio on the surfaces. The XPS survey spectrum are shown in **Figure A4.2a**. No impurities are observed except for Zn, O and C.

ARXPS O 1s spectrum are shown in **Figure A4.2b** with an angle at 15º, 30º, 45º, 60º and 75º. The lower the angle, the more information from the surface. The O 1s peak of 5.4 nm ZnO exhibits a strong peak at 531.6 eV and a shoulder at 530.0 eV, which are attributed to O vacancies (V_O") and lattice O (Zn-O), respectively.[206, 303] At a low angle, the O vacancies related surface defects peak intensity is dominant. The Zn-O lattice O 1s peak intensity increases when increasing the angle, demonstrating that defects on surface is prominent. We also collected angular XPS data from 20 nm ZnO, which is shown in **Figure A4.2c**.The O vacancy XPS peak and the O lattice peak both are obviously observed from low angle (15º) to high angle (75º).To quantitatively compare the surface defect density of the thin 5.4 nm ZnO film and the thick 20.0 nm ZnO film,

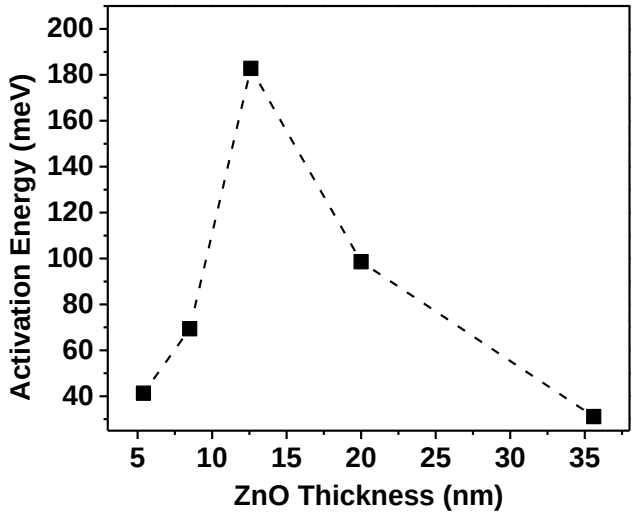

Figure A4.3. Activation energy extracted from **Figure A4.1b** and plotted vs. ZnO thickness.

the ratios of V_O" integrated XPS peak intensity to Zn-O integrated peak intensity from both samples are plotted in **Figure A4.2d**. At 15°, the V_O"/Zn-O ratio of 5.4 nm ZnO is 2.6 times higher than the ratio of 20 nm ZnO. Both of the ratios decreases when increasing the angle. Until 60°, both of the samples present similar values.

Angular XPS data indicate that the surface defect density of ZnO highly depends on the film thickness, especially with a thickness less than 20 nm. The thickness dependent conductivity results demonstrate that the conductive mechanism of the ZnO film with a thickness below and above 12.6 nm are different. Below 12.6 nm, the conductivity decreases with an increase of the thickness. In contrary, dramatic improvement of the conductivity is obtained with films thicker than 12.6 nm at room temperature. The activation energy of the conduction follows a similar trend under dark conditions in **Figure A4.3**. The activation energy of 5.4 nm ZnO film is 41.3 meV. It increases with film thickness and reaches the maximum value of 182.8 meV with a film thickness of 12.6 nm, and then continuously decreases to a value of 31.1 meV with a film thickness of 35.6 meV. The lower the activation energy, the higher the conductivity, which perfectly agrees with the conductivity results.

Appendix Ⅴ CuO NWs mass calculation

TGA (TA Instruments Q5000 IR with weight accuracy is ±0.1%) was employed during heating of a Cu foil in air at 500 ℃ for 30 min (see **Figure A5.1a**); the same conditions as used in the CuO photocatalyst synthesis, to determine mass gain. To fit into the TGA cell, the Cu foil was cut into small pieces (0.381×0.457 = 0.174 cm^2). After oxidation, the weight gain is 9.090 x 10^{-5} gm, which is the mass of oxygen reacted with Cu to form an oxide scale (**Figure A5.1a**). The mass

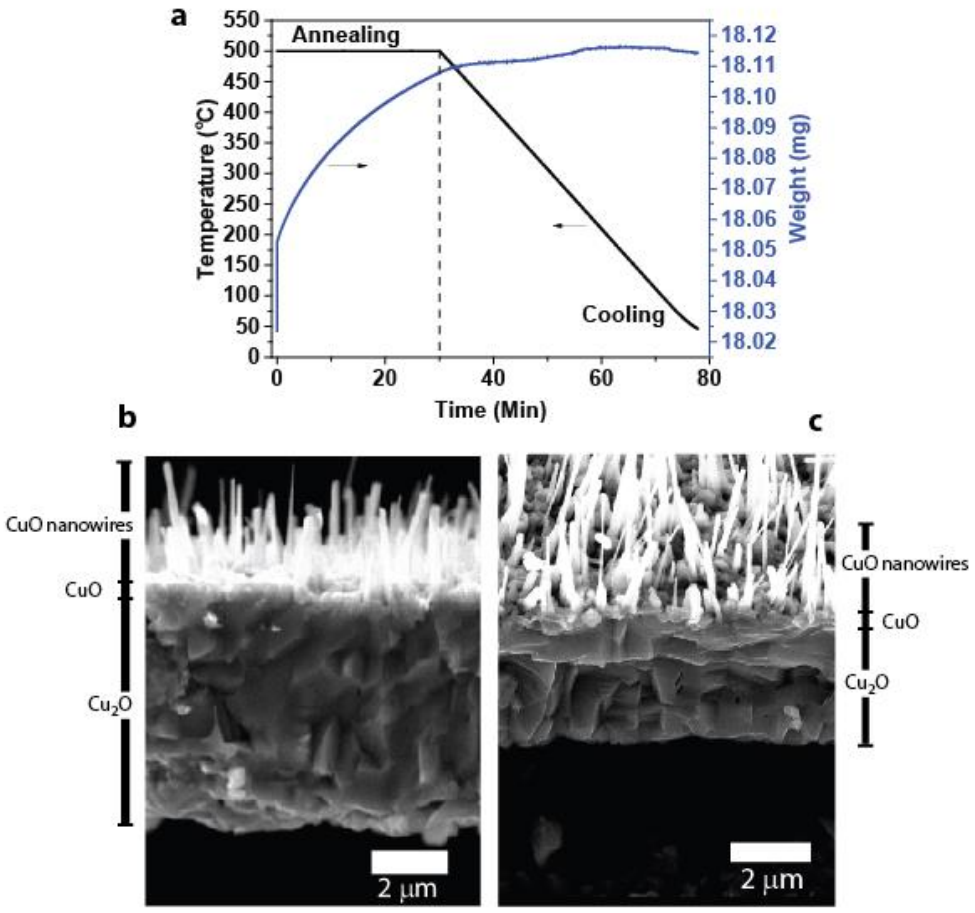

Figure A5.1. a) Curves of weight gain (blue) and temperature during the thermogravimetric analysis of the Cu foil in air. b) Representative cross section SEM of the top layer and c) Representative cross section SEM image of the bottom layer.

gain is 0.5% of the starting mass of Cu and is in line with other reports on copper oxidation to produce CuO nanowires.[145] The oxide scale consists of CuO nanowires over a bilayer oxide[304] of fine grained CuO on top of long, columnar Cu_2O grains which are in turn in direct contact with the Cu foil. The cross section of the TGA sample is shown **Figure A5.1b** (top of the foil) and **Figure A5.1c** (bottom of the foil).

In the calculations that follow, we assume that both CuO nanowires and the thin granular CuO film participate in the CO_2 photoreduction process. This is a reasonable assumption because the ALD ZnO deposits on the CuO nanowires and the exposed CuO film surface, activating both these surfaces. Thus, in order to calculate the mass of CuO nanowires + CuO film, we first determine the mass of Cu_2O film and subtract it from the total mass gain obtained from TGA.

Cross-section SEM analysis of top and bottom surfaces was conducted using Image J® software. Five images each, of the top and bottom cross-sections were analyzed and statistical averages and errors were calculated from 20 sets of thickness measurements. The Cu_2O thickness (mean ± standard error with 95% confidence) was found to be 4.83 ± 0.05 μm on the top and 2.81 ± 0.04 μm, on the bottom, respectively. The total volume of Cu_2O is $((4.83 \pm 0.05) + (2.81 \pm 0.04)) \times 10^{-4}$ x $0.381 \times 0.457 = (1.33 \pm 0.02) \times 10^{-4}$ cm^3. Given mass density of Cu_2O = 6.1 gm/cm^3, the mass of Cu_2O will then be $(8.11 \pm 0.12) \times 10^{-4}$ gm. The molecular weight of Cu_2O is 143 gm / mol. Therefore, the O component in Cu_2O weighs $(8.11 \pm 0.12) \times 10^{-4} \times 16/143 = (9.079 \pm 0.13) \times 10^{-5}$ gm. Subtracting this from the O gain observed from TGA, we obtain the O content in CuO nanowire + CuO thin film as, $9.090 \times 10^{-5} - (9.079 \pm 0.13) \times 10^{-5} = (1.078 \pm 13) \times 10^{-7}$ gm. Given that the CuO molecular weight is 79.5, converting the O gain in the CuO nanowire + CuO thin film into CuO mass, we obtain $(1.078 \pm 13) \times 10^{-7} \times 79.5/16 = (5.359 \pm 64.594) \times 10^{-7}$ gm. Recall

that the TGA sample area was 0.174 cm^2. However, for CO_2 photoreduction, the samples were 1 cm x 1 cm and thus, normalizing the CuO nanowire + CuO thin film area to 1 cm^2, we obtain the effective mass of the CuO nanowire and CuO thin film as, $(3.07 \pm 37.1) \times 10^{-6}$ gm. This data shows that the mass of the CuO nanowire + CuO film is dominated by the uncertainty of the thickness associated with the Cu_2O film, as determined by SEM cross sections. Since the uncertainty represents standard errors with 95% confidence interval, we claim that the mass of the CuO nanowire + CuO film is at the most 40.17×10^{-6} gm with 95% confidence.

The CuO nanowire + CuO film mass is distributed on two surfaces (top, **Figure 6.1b** and bottom, **Figure 6.1c**) whereas, only the top surface of the Cu foil was exposed to the CO_2 + H_2O mixture. Assuming the CuO thickness and therefore mass, is proportional to the Cu_2O underlying thickness[142, 244], we obtain a CuO mass of at most, $(40.17 \times 10^{-6}) \times 4.83 / (4.83 + 2.81) = 25.40 \times 10^{-6}$ gm. Based on this mass, we claim with 95% confidence, that the catalyst yield is *at least* 1.9 mmol /g-cat/hr or higher.

Appendix Ⅵ UV-vis of CuO NWs

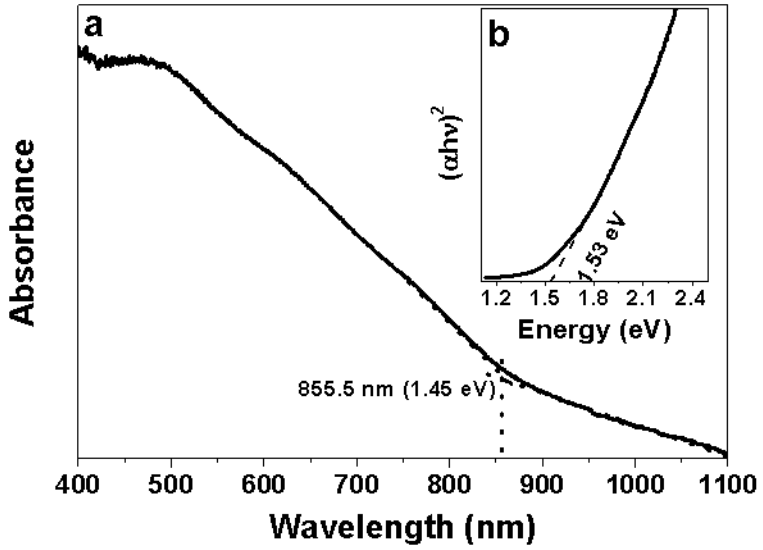

Figure A6.1. a) The UV-VIS-NIR spectrum of CuO NWs. Determination of bandgap of CuO NWs by using a least-squares fit of a line through the low energy edge of the transformed spectrum (inset, b).

Appendix Ⅶ Light spectrum of the Xe lamp

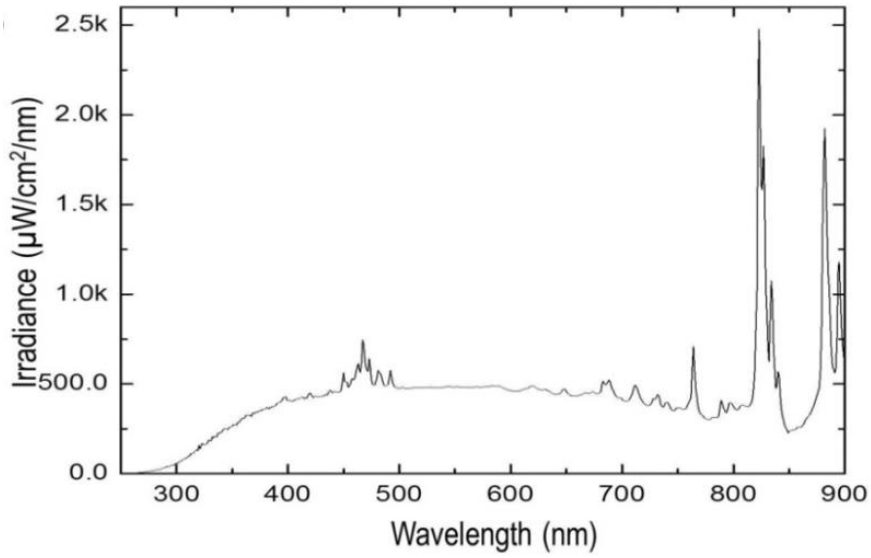

Figure A7.1. Light spectrum of the Xe lamp.

Appendix Ⅷ ALD ZnO thin film growth model

To gain deeper understanding the relationship between ZnO thickness and Cu2O reduction performance, we employed the island growth model to show surface morphology difference between ZnO films with a different thickness. While material addition in ALD is known to be one monolayer at a time, substrate inhibited growth is common, especially when there are a lack of chemical functional groups on a substrate. Single crystal substrates such as CuO nanowires are one such candidate where the lack of surface defects could present energetic barriers to film nucleation. Such substrates can induce incubation periods for film growth and result in a nucleation and island like growth mechanism to persist in the first few cycles of the ALD process. Schematic cross-section of a ZnO nuclei on CuO nanowire is shown in **Figure A8.1**.

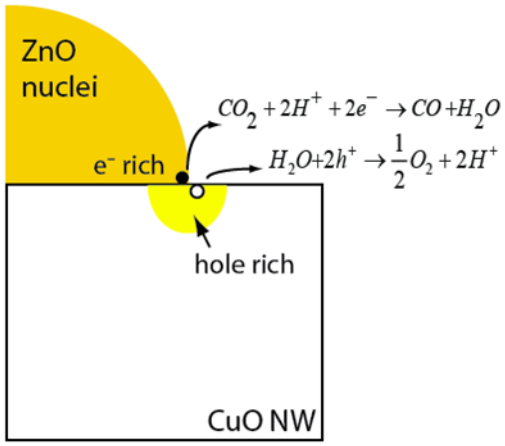

Figure A8.1. Schematic cross-section of a ZnO nuclei on CuO nanowire showing the region at the interface of the *n*-type ZnO / *p*-type CuO nanowire. The triple phase boundary i.e., the yellow region around the perimeter is modeled as the active reaction volume allowing for both h^+ (o) based oxidation of H_2O and e^- (•) based reduction of the CO_2.

Further assumptions in the model include –

1. ALD ZnO nuclei are assumed to be of circular cross section.
2. ALD ZnO nuclei deposit on CuO nanowire 'cells' with a density N, such that each cell has dimensions of $\frac{1}{\sqrt{N}}$ x $\frac{1}{\sqrt{N}}$.
3. The chain of reactions presenting electrons (e^-) and holes (h^+) consumption in the ZnO and CuO nanowires respectively occur very close to the surface. This means the triple-phase boundary involving the ZnO nuclei, CuO nanowire and ambient present the ideal location for the reactions to synergistically occur and result in the maximum CO_2 photoreduction rates.
4. Thus, the perimeter regions around ZnO nuclei are actively involved in the CO_2 photoreduction process.
5. Calculation of nuclei perimeters should trend with the CO_2 photoreduction rates.

The island growth model has two distinct stages. Initially, for a ZnO nuclei with radius *r*, the circumference, *p* (red dotted line in **Figure A8.2a-d**) is given as:

$$p = 2\pi r \text{ , for } r < R_{crit,1} \qquad \textit{Eq. 1}$$

Here, $R_{crit,1}$ is the radius at which adjacent nuclei impinge on each other. This is given as -

$$R_{crit,1} = \frac{1}{2\sqrt{N}} \qquad \textit{Eq. 2}$$

Where, N = nuclei number density (#/cm^2)

As the nuclei grow past $R_{crit,1}$ the perimeter starts to reduce and is given as

$$\chi = 4r(\frac{\pi}{2} - 2\alpha) + 8s \text{ , for } R_{crit,1} < r < R_{crit,2} \qquad \textit{Eq. 3}$$

Here, α is the 'overlap' angle of the nuclei given as –

$$\cos(\alpha) = \frac{R_{crit,1}}{R} \qquad Eq.\ 4$$

and *s* is the ZnO grain boundary formed due to two impinging nuclei (shown as the blue dotted line in **Figure A8.2c-d**). While it is expected that the grain boundary may not be an active site for CO_2 photoreduction, for very thin films (< 10 nm), grain boundary diffusion of the gas molecules will still contribute sufficient flux for the photoreduction reactions to take place, albeit with lesser efficiency.

Finally when all the nuclei have ceased to exist as independent ZnO islands at

$$R_{crit,2} = \frac{1}{\sqrt{2N}}, \qquad Eq.\ 5$$

the layer by layer characteristic growth of the ALD film takes over.

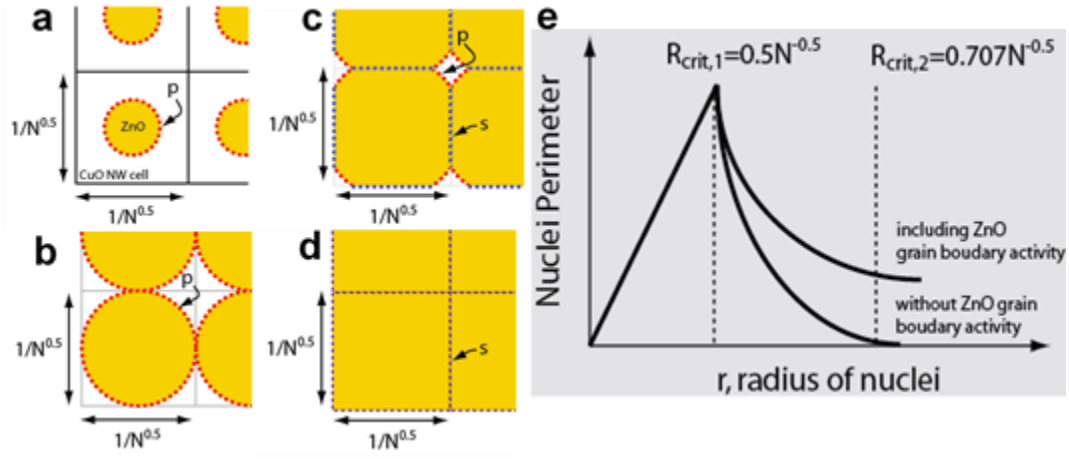

Figure A8.2. a-d) Schematic of the island growth model adopted for ALD ZnO deposition on CuO single crystalline nanowires. Calculation of nuclei perimeter, *p* consists of 2 regimes. One in which the nuclei are not impinging on each other. This occurs for $r < R_{crit,1}$. Beyond impingement, the nuclei perimeter decreases till p = 0 at $r = R_{crit,2}$. e). Depending on whether the ZnO grain boundary, *s* contributes to CO_2 photoreduction (or not), two scenarios of effective nuclei perimeter can be obtained as shown in the graph.

A schematic of the resultant variation of perimeter is given in **Figure A8.2e**. Two scenarios are presented for $r > R_{crit,1}$: One, without the ZnO grain boundaries contributing to any photoreduction reaction and the second, in which the ZnO grain boundaries contribute towards the photoreduction reaction with decreasing efficiency.

These equations have been used to fit the CO_2 photoreduction trend with ZnO thickness (**Figure 5.4b** in main text) using *only* N as an independent variable to obtain $N = 1.4 \times 10^{13}$ nuclei/cm^2. This gives $R_{crit,1}$=1.3 nm (based on *Eq*. 5) at which CO_2 photoreduction should peak. Thus, given the deposition rate of ALD ZnO is 0.17 nm/cycle, it only takes 8 cycles for the ZnO islands to merge and grow as a film and this incubation period is relatively small for an ALD based chemistry. However, remarkably enough, this makes a significant difference in CO_2 photoreduction rates.

Appendix Ⅸ Angle-Resolved X-ray Photoelectron Spectroscopy

Using angle resolved X-ray photoelectron spectroscopy (ARXPS), it is possible to characterize ultra-thin films. It is also a non-destructive surface analysis technique. Generally, the photoelectrons generated from a layer in the thin films with an emission angle normal to the surface follows Beer-Lambert Law: $I = I^{\infty}\exp(-t/\lambda)$, where I^{∞} is the photoelectron signal from the sample, t is the depth of the signal generation, and λ is the attenuation length of the photoelectron in the sample. If photoelectrons are collected at angles other than 90° with respective to the thin film surface, the photoelectrons penetration depth is decreased by a factor of sinθ. Then, the corrected Beer-Lambert Law at different angles becomes $I = I^{\infty}\exp(-t/\lambda\sin\theta)$.For example, O 1s ARXPS results are collected on 5.4 nm ZnO with Zn-terminated surfaces with angle from 15° to 75° in **Figure A9.1**. The O 1s peak can also be fitted into two peaks: 529.9 eV related to Zn-O lattice peaks and 531.4 eV related to O vacancy peaks. (**Chapter 5, Figure 5.4**) The higher the angle, the longer the detection depth, which also means that we can detect the very top surface layer at a low angle.

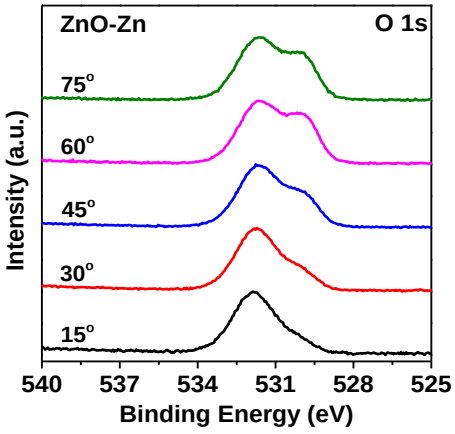

Figure A9.1. ARXPS of 5.4 nm Zn-terminated ZnO with take-off angle from 15° to 75°.

Related publications to the thesis

1. Fei Wu, Alireza Faghaninia, Cynthia Lo, Parag Banerjee, Observation of two dimensional metallic surface states and metal to semiconductor transition on low dimensional polar thin films, in preparation.
2. Fei Wu, Yoon Myung, Parag Banerjee, Indirect phase transformation pathway from CuO to Cu_2O in a nanowire, in preparation.
3. Fei Wu, Yoon Myung, Parag Banerjee, Surface defects tuned photoresponse of ZnO coated CuO nanowires, in preparation.
4. Weiming Wang*, Fei Wu*, Yoon Myung, Dariusz M Niedzwiedzki, Hyung Soon Im, Jeunghee Park, Parag Banerjee, Pratim Biswas, Surface Engineered CuO Nanowires with ZnO islands for CO_2 Photoreduction***, ACS Applied Materials & Interfaces,*** 2015**,** 7**,** 5685–5692. (* Co-first author)
5. Fei Wu, Yoon Myung, Parag Banerjee, Rayleigh instability driven nodular Cu_2O nanowires via carbothermal reduction of CuO nanowires, ***Crystal Growth & Design,*** 2015**,** 15, 1588-1595.
6. Fei Wu, Yoon Myung, Parag Banerjee, Unveiling the transient phases during thermal oxidation of copper for dense CuO nanowire growth, ***CrystEngComm,*** 2014, 16, 3264-3267.
7. Fei Wu, Limei Tian, Ravindra Kanjolia, Srikanth Singamaneni, Parag Banerjee, Plasmonic Metal-to-semiconductor switching in Au nanorod-ZnO nanocomposite films, ***ACS Applied Materials & Interfaces,*** 2013**,** 5, 7693-7697.

Related conference talks

1. Fei Wu, Sriya Banerjee, Yoon Myung, Parag Banerjee, Role of surface amorphization in CuO-Cu_2O core-shell nanowire array for photoelectrochemical water splitting, **2015, ECS 227th International Conference**, Chicago, USA (**Talk**).
2. Fei Wu, Yoon Myung, Parag Banerjee, Tuning photoresponse of ultrathin ZnO films using few angstrom Al_2O_3 overlayers, **2014, ECS 226th International Conference**, Cancun, Mexico (**Talk**).
3. Fei Wu, Wang, W-N., Myung, Y., Niedzwiedzki, D.M., Im, H-S., Park, J., Biswas, P., Banerjee, P., "At the Edge of Thickness: Few Angstrom ZnO on CuO NW for highly efficient CO_2 photoreduction", 2014, **14th International Conference of ALD**, Kyoto, Japan (**Talk**).
4. Fei Wu, Parag Banerjee, Composition and structure control of copper oxide (Cu_2O and CuO) nanowires via thermal routes, **2013, ECS 224th International Conference**, San Francisco, USA (**Talk**).
5. Fei Wu, Limei Tian, Ravindra Kanjolia, Srikanth Singamaneni, Parag Banerjee, Plasmon enhanced conductivity in ALD-enabled Au nanorod-ZnO nanocomposites**, 2013**, **13th International Conference of ALD**, San Diego, USA (**Talk**).